THESE DE DOCTORAT

NNT : 2025UPASP045

université PARIS-SACLAY

Arrays of single dysprosium atoms in optical tweezers to study collective light scattering

Chaines d'atomes uniques de dysprosium dans des pinces optiques pour étudier la diffusion collective de la lumière

Thèse de doctorat de l'université Paris-Saclay

École doctorale n°572 : ondes et matière (EDOM)
Spécialité de doctorat : physique
Graduate School : Physique. Référent : Institut d'Optique

Thèse préparée dans l'unité de recherche Université Paris-Saclay, Institut d'Optique Graduate School, CNRS, Laboratoire Charles Fabry, 91127, Palaiseau, France, sous la direction de **Antoine Browaeys**, directeur de recherche, la co-direction de **Igor Ferrier-Barbut**, chargé de recherche.

Thèse soutenue à Paris-Saclay, le 18 juin 2025, par

Damien Bloch

Composition du Jury

Membres du jury avec voix délibérative

Isabelle Bouchoule Directrice de recherche, Laboratoire Charles Fabry	Présidente
Robin Kaiser Directeur de recherche, Institut de Physique de Nice	Rapporteur & Examinateur
Sylvain Nascimbene Professeur, Laboratoire Kastler Brossel	Rapporteur & Examinateur
Caroline Champenois Directrice de recherche, Laboratoire Physique des Interactions Ioniques et Moléculaires	Examinatrice

université PARIS-SACLAY

ÉCOLE DOCTORALE
Ondes et matière
(EDOM)

Titre : Chaines d'atomes uniques de Dysprosium dans des pinces optiques pour étudier la diffusion collective de la lumière

Mots clés : physique quantique, atomes froids, pinces optiques, diffusion de la lumière collective, dysprosium, interaction dipôle-dipôle,

Résumé : Cette thèse porte sur la construction d'une expérience de pinces optiques avec des atomes de dysprosium pour étudier les interactions induites par la lumière. Le but est d'étudier des situations dans laquelle le champ électrique rayonné par un atome lorsqu'il se désexcite peut influencer un autre atome proche. Le travail présenté ici montre que les techniques développées pour imager et manipuler des atomes individuels dans des pinces optiques peuvent fournir de nouveaux outils expérimentaux pour étudier le problème de la diffusion collective de la lumière.

Une première partie de la thèse consiste en la conception et la construction d'une expérience de pinces optiques utilisant pour la première fois des atomes de dysprosium. Une fois le système construit, nous avons caractérisé le comportement des atomes de dysprosium dans les pinces optiques. En particulier, nous avons mesuré l'influence de la polarisation de la lumière du piège sur la polarisabilité de l'atome. Grâce à ces mesures, nous avons montré l'existence d'une polarisation magique qui rend possible l'imagerie non-destructive d'atomes uniques de dysprosium avec haute-fidélité.

Une fois ce but atteint, nous avons réalisé de premières expériences de diffusion de la lumière sur des ensembles atomiques ordonnés réalisés avec des pinces optiques. Pour ce faire, nous avons développé une technique de détection de l'état interne d'un atome unique sur une transition optique en utilisant la structure riche de l'atome de dysprosium. Grâce à cette technique, nous avons étudié comment le champ électrique rayonné par un atome sur un autre influence la mesure de la fréquence de la transition. Nous avons observé le décalage collectif du spectre en régime stationnaire dans l'approximation de dipôles rayonnants classiques.

Nous avons ensuite mesuré l'influence de ces interactions sur la spectroscopie de Ramsey. Cette situation ne peut être décrite dans une approximation classique et il est nécessaire de tenir compte de la discrétisation de l'état interne des atomes. Nous faisons également le lien entre les résultats obtenus dans ce régime et la limite classique.

Title: Arrays of single Dysprosium atoms in optical tweezers to study collective light scattering

Keywords: quantum physics, cold atoms, optical tweezers, dysprosium, collective light-scattering, dipole-dipole interaction

Summary: This thesis focuses on the development of an optical tweezer experiment with dysprosium atoms to study light-induced interactions. The goal is to investigate situations in which the electric field radiated by an atom as it de-excites can influence another nearby atom. The work presented here shows that the techniques developed to image and manipulate individual atoms in optical tweezers can provide new experimental tools to study the problem of collective light scattering.

The first part of the thesis involves the design and construction of an optical tweezer experiment using dysprosium for the first time. Once the system was built, we characterized the behavior of dysprosium atoms in optical tweezers. We measured the influence of the trap light's polarization on the atom's polarizability. Through these measurements, we demonstrated the existence of a magic polarization that enables high-fidelity, non-destructive imaging of individual dysprosium atoms.

Once this goal was achieved, we carried out some light scattering experiments on ordered atomic arrays created with optical tweezers. To do so, we developed a technique to detect the internal state of a single atom on an optical transition, leveraging the rich internal structure of the dysprosium atom. Using this technique, we studied how the electric field radiated by one atom can influence the measured frequency of the transition. We observed a collective shift of the spectrum in the steady-state regime, within the approximation of classical radiating dipoles.

We then measured the influence of these interactions on Ramsey spectroscopy. This situation cannot be described within a classical approximation and requires taking into account the discrete nature of the energy levels of the atoms. We also establish a connection between the results obtained in this regime and the classical limit.

Synthèse : Comprendre comment la lumière interagit avec un ensemble d'atomes est important pour expliquer de nombreux phénomènes. Le but de cette thèse est d'étudier les interactions induites par la lumière sur des chaines d'atomes avec un espacement comparable à la longueur d'onde de la lumière. Dans ce cas, le champ électrique rayonné par un dipôle atomique lorsqu'il se désexcite peut influencer un autre atome proche. Pour étudier cette situation, nous avons construit une nouvelle expérience de pinces optiques avec des atomes de dysprosium. Les expériences d'atomes froids ont fourni de nombreux outils pour étudier des systèmes atomiques en interaction. Le travail présenté ici montre que les techniques développées pour imager et manipuler des atomes individuels dans des pinces optiques peuvent fournir de nouveaux outils expérimentaux pour étudier le problème de la diffusion collective de la lumière par des chaines d'atomes.

Une première partie de la thèse consiste en la conception et la construction d'une expérience de pinces optiques utilisant pour la première fois des atomes de dysprosium. Pour cela, nous avons construit une chambre à vide pour produire des nuages d'atomes ultrafroids par refroidissement laser. Une fois les atomes refroidis dans un piège magnéto-optique avec à des températures de l'ordre de quelques microkelvins, nous avons construit un système optique pour générer des pinces optiques pouvant piéger des atomes uniques. Nous avons par la suite caractérisé le comportement des atomes de dysprosium dans les pinces optiques.

En particulier, nous avons mesuré l'influence de la polarisation de la lumière du piège sur la polarisabilité de l'atome. Cette interaction lumière-matière avec une forte anisotropie est spécifique aux atomes de dysprosium et nous avons dû la caractériser expérimentalement. Grâce à ces mesures, nous avons montré l'existence d'une polarisation magique pour laquelle l'état fondamental et l'état excite de la transition d'intercombinaison du dysprosium ressentent le même potentiel de piégeage dans une pince optique. Cette polarisation magique a rendu possible pour la première fois l'imagerie non-destructive d'atomes uniques de dysprosium avec haute-fidélité. Nous avons caractérisé quantitativement les propriétés et performances de cette détection d'atomes uniques.

Une fois que nous avons atteint ce but, nous avons réalisé de premières expériences de diffusion de la lumière sur des ensembles atomiques ordonnés réalisés avec des pinces optiques. Pour cela, nous avons utilisé une technique qui permet de déplacer les pinces optiques contenant chacune un atome pour réduire la distance les séparant jusqu'à environ un micromètre. Cette distance représente quelque fois la longueur d'onde d'une transition optique.

Nous avons ensuite développé une technique de détection de l'état interne d'un atome unique sur une transition optique en utilisant la structure riche de l'atome de dysprosium. Grâce à cette technique, nous avons la capacité de mesurer pour chaque atome s'il est dans l'état fondamental ou dans l'état excité de la transition d'intercombinaison. Avec cette méthode, nous avons étudié comment le champ électrique rayonné par un atome sur un autre influence la mesure de la fréquence de la transition. En mesurant le spectre lorentzien des atomes en régime de faible excitation, nous avons observé le décalage du spectre par les interactions induites par la lumière. Les résultats observés sont compatibles avec une théorie semi-classique approximant les atomes par des dipôles linéaires.

Nous avons ensuite mesuré l'influence de ces interactions dans un régime diffèrent en faisant une spectroscopie de Ramsey. Cette situation ne peut pas être décrite dans une approximation classique et il est nécessaire de tenir compte de la discrétisation de l'état interne des atomes. En particulier, nous avons mesuré un décalage de fréquence qui dépend de l'excitation atomique instantanée du système. Nous avons montré que les résultats obtenus sont compatibles avec une théorie de champ moyen. En particulier, lorsque les atomes sont faiblement excités, l'approximation par des de dipôles classiques est valide et nous retrouvons les résultats observés dans le régime classiques, ce qui permet de relier les régimes de faibles et fortes excitations.

Les résultats présentés dans cette thèse montrent l'intérêt des plateformes expérimentales utilisant des atomes uniques en combinaison avec des espèces atomiques complexes comme le dysprosium pour étudier le problème de la diffusion collective de la lumière.

Remerciements

Durant ces quatre ans de thèse, j'ai eu le plaisir de côtoyer des personnes extraordinaires, et sans qui cette thèse n'aurait pas été possible. Je voudrais ici remercier ces personnes avec qui j'ai passé une bonne partie de mon quotidien ces dernières années.

Merci tout d'abord à Igor pour m'avoir fait confiance pour démarrer ce projet, qui est aussi avant tout le tien. J'ai beaucoup appris de toi tout du long de la thèse, que ce soit sur de la physique fondamentale, sur des techniques expérimentales et sur plein d'autres sujets. J'ai grandement apprécié le temps que tu as passé au labo les premières années pour expliquer au thésard en herbe que j'étais comment construire une manip et comment faire de la physique en pratique. Ta présence, ta bonne humeur et les gâteaux que tu partageais à l'heure du goûter ont beaucoup contribué à la bonne ambiance en salle de manip. Une fois que la manip s'est lancée, tu nous as aussi fait confiance pour explorer plein de choses par nous-même, tout en apportant ton soutien et des explications lorsque nous buttions sur des difficultés. J'aurai bien du mal à imaginer un meilleur encadrement pour ma thèse.

Merci également à Antoine pour m'avoir fait confiance pour la thèse et pour m'avoir permis de rejoindre le groupe. J'étais initialement un peu intimidé par ta carrure scientifique, mais je me suis très vite rendu compte qu'en plus de tes qualités de physicien, tu présentes aussi de grandes qualités humaines et tu te soucies particulièrement du bien-être des thésards. Par exemple, tu venais souvent discuter et distribuer des carreaux de chocolat en salle de manip pour remonter le moral des troupes. J'ai beaucoup apprécié et appris des discussions que nous avons pu avoir, où tu remettais en contexte certaines découvertes en physique en racontant une histoire ou une anecdote rattachée : c'était très utile pour démystifier et lever le voile sur un grand nombre de concepts.

Je tiens aussi à remercier particulièrement les personnes qui ont passé beaucoup de temps avec moi au laboratoire et avec qui j'ai partagé une grande partie de ma thèse : Sam Cohen et Britton Hofer. Merci à Sam pour nous avoir rejoints et aidés durant la première année du projet. C'est en grande partie grâce à toi que l'expérience a pu se construire et avancer aussi vite. J'ai été très vite impressionné par tes connaissances sur l'état de l'art en physique quantique. Même si je n'ai pas tout compris à l'époque, j'ai beaucoup appris en discutant avec toi. Merci beaucoup aussi pour ton humour

au quotidien et ton entrain contagieux, même lorsque des difficultés se sont bien sûr présentées au cours d'un projet si complexe. En travaillant ensemble j'ai aussi appris que faire les chose de manière "banzai" à des avantages : c'est souvent une bonne idée d'essayer d'abord de faire l'expérience et de se faire du souci après, ça peut éviter bien des mots de tête.

Britton, ça a été un plaisir de travailler avec toi dès ton arrivée au laboratoire. Je suis très impressionné par la vitesse à laquelle tu t'es adaptée à une manip qui était déjà bien complexe quand tu es arrivée. Bien souvent en discutant ensemble, on s'est rendu compte qu'il y avait des points qui n'étaient clairs pour personne, et qu'il y avait de quoi creuser. J'ai aussi été très impressionné par ta résilience face aux difficultés, et ta capacité à rester optimiste dans les moments difficiles. Je me souviens particulièrement d'une période où nous galérions à aligner le réseau optique pendant des jours et jours; tout le monde était découragé et prêt à abandonner, mais un jour ou personnes d'autres n'était au labo, tu t'es retroussée les manches et le lendemain le problème était résolu. Merci beaucoup aussi pour avoir fortement contribué à la bonne ambiance du groupe, en organisant des soirées pub quiz (un jour j'espère pouvoir nommer toutes les chansons de Fleetwood Mac à l'oreille) et pleins d'autres activités. Pour sûr, ces années de thèse ne se seraient pas aussi bien passées sans toi.

Plus récemment, Giulio Biagioni, Nathan Bonvalet ont commencé à prendre le relai et vous avez déjà obtenu de nouveaux résultats. Les quelque temps que nous avons passés ensemble au labo ont été très agréables, et avec Théo Dardier qui vous a maintenant rejoint, j'ai hâte de voir ce que vous allez accomplir avec la manip dans les années à venir. J'espère qu'elle se comportera bien avec vous et que vous aurez autant de plaisir à travailler dessus.

Merci également à tous les autres membres du groupe et du laboratoire, avec qui j'ai pu partager de nombreux moments et qui ont contribué à rendre cette expérience inoubliable : Thierry Lahaye, Florence Nogrette, Guillaume Bornet, Gabriel Emperauger, Sara Pancaldi, Lucas Leclerc, Lukas Klein, Bastien Gely, Adrien Gavalda, Yuki Chew, Mu Qiao, Cheng Chen, Giovanni Ferioli, Daniel Barredo, Guillaume Tremblier, Romain Martin, Martin Poitrinal, Jamie Boyd et Olivia Rosenstein. Je garde de très bons souvenirs des pauses café le midi à discuter de tout et de rien, des parties de *Wordle* qui m'ont permis d'améliorer un peu mes connaissances en géographie (j'arrive encore à reconnaitre le Tchad par son contour), des séances jogging

et pizza le vendredi ainsi que des barbecues au bord du lac avec leurs parties de *Molkky*.

Enfin, j'aimerais remercier toutes les personnes qui nous ont aidé directement ou indirectement au cours de ce projet. En particulier, je voudrais remercier le service administratif de l'institut et le directeur du laboratoire, Patrick Georges, qui ont été d'un soutien énorme pour toutes les démarches administratives concernant la thèse et le projet. Merci aussi au service infrastructure et à l'accueil de l'institut pour nous avoir permis de travailler dans les meilleures conditions.

Pour finir, je voudrais également remercier mes amis et mes proches pour m'avoir supporté tout du long de ma thèse. En particulier, merci à ma sœur Hélène qui est aussi passée par là, et qui m'a donnée des conseils tout au long de la thèse. Mes derniers remerciements vont à mes parents pour leur soutien sans faille, et sans qui je ne serai jamais arrivé là où je suis. Sans pouvoir détailler ici tout ce que vous avez fait pour moi, je vous dis simplement merci pour tout !

Contents

Part I.

An optical tweezers experiment with dysprosium

Chapter 1

Introduction

Understanding how light interacts with an ensemble of atoms is key to explaining many phenomena. To give some examples, refraction bends light beams at a dielectric interface, scattering of sunlight in the atmosphere gives the sky its blue color, or diffraction of X-rays on atomic lattices are used to determine the structure of materials [WMS11]. These effects originate from the scattering of light by the medium: The oscillating electric field of the light induces an oscillating electric dipole moment in the atoms, that in turn radiates light. To understand many scattering phenomena, at least in dilute media, it is often enough to only consider the effect of light on a single emitter, and to assume that each atom is mainly driven by the incoming light and not by the field radiated by its neighbours. The total field radiated is the sum of the field emitted by all the atoms, and their interferences give rise to the observed effects.

However, there are some situations where it is not enough to simply consider the response of the individual atoms, but one has to take into account collective scattering. This is a much more complex problem [GRK17], and there are still open questions that arise, for example when trying to compute the optical index of a material [And+21] or when trying to understand how light propagates in disordered media [AL85; SSC13; Cot+19].

The situation becomes even more complex when considering the quantum nature of the atoms. Indeed, atoms cannot be described as classical dipoles, but instead must be described as quantum objects with discrete energy levels. An atom is in an excited state can now spontaneously decays back to its ground state by emitting a photon. Understanding the interaction between light and single atoms in the quantum regime has been very fruitful, and has given birth to the fields of quantum optics and applications such as laser cooling [Phi98].

When now taking into account both collective and quantum effects, new qualitatively different phenomena appear. One can expect non-classical effects such as entanglement to arise in the system. These effects manifest themselves in particular when the spacing between the emitters is small compared to the wavelength of the light

such that the field experienced by one atom from its neighbours is large. An example of such phenomena is the emergence of super-radiance and sub-radiance [Dic54]: Due to interactions, some atomic states spontaneously decay much faster or much slower than isolated atoms. There are today still many open questions on these effects, such as the role of entanglement [GH82; FT02] or the influence of atom number and geometry [BGA16b; Per+17; Sha+17].

To explore these effects, several experiments have been built to study the scattering of light by quantum emitters. In the case of atomic ensembles, there are for instance experiments that explore light-scattering in magneto-optical traps [Cha+11; GAK16; Roo+16; Ara+16]. In such situations, the spacing between the atoms is larger than the wavelength of the light, but collective effects are enhanced by the large number of atoms, ranging from millions to billions, leading to optically thick samples.

Another regime are hot atomic vapours [Kea+12; Pey+18]. With these setups, one can reach very high density with interparticle spacing between the atoms smaller than the wavelength of the light. The experiments are however more challenging to interpret due to collisions between atoms and large inhomogenous Doppler broadening because of the large temperature of the gas.

There are also experiments looking at both cold and dense samples, obtained by trapping atoms in small dipole traps [Fer+21]. The number of atoms is still relatively large, a few thousands, and the spacing between the atoms is comparable to the wavelength of the light, such that strong collective effects can be observed.

The experiments described above are performed with disordered ensembles of atoms and by measuring macroscopic quantities, such as the light transmitted or emitted by the atoms. In parallel to these developments, new experimental tools have appeared over the last decades to manipulate individual quantum objects. This kind of control has been realized with several systems, such as trapped ions [CZ95], superconducting qubits [HTK12; Kja+20], optical lattice with neutral atoms [GB21], Rydberg atoms in optical tweezers [BL20], or atoms near nanofibers [Vet+10]. In these experiments, the number of particles is usually small, from a few to hundreds, but one has a lot of control over the system. It is for example possible to control the coupling between the particles or the geometry of the ensemble [Bar+16], opening the way to studying collective light-scattering in ordered ensembles. New tools have also been developed to probe the microscopic properties of the system. It is now common to be able to measure the state of single particles, correlations between atoms, or even to perform

full quantum state tomography for small systems.

These tools could be used to explore different regimes of light-scattering from the ones described above, and a few experiments are now exploring such directions. There are for example experiments performed with ions [Mei+14], where collective effects where observed in small chains. However, for this platform, the geometry is not freely controllable, but is imposed by the electrostatic repulsion between the ions. Another approach is to load atoms in optical lattices using degenerate quantum gases [Rui+20]. This makes it possible to create perfect arrays with several hundreds atoms with subwavelength spacing. Coupled with single site imaging, this approach could bring new insights into collective light-scattering.

In this thesis, I will present one of the approaches considered in the Quantum Optics group at the Institut d'Optique, which is to adapt the optical tweezer platform to light-scattering experiments. This platform has several advantages; it provides a large degree of control over the geometry of the system, and makes it possible to control and measure the state of individual atoms. While subwavelength arrays are challenging to produce using this platform only, combined tweezer-lattice approaches are promising and could bring the best of both worlds [You+22; Tao+24].

I will explain in this manuscript the work I did during my PhD to build an optical tweezer setup to study collective light-scattering. One of the particularities of this experiment is the use of a relatively complex atomic species: dysprosium. This atom has a rich electronic structure that gives us additional tools for performing light-scattering experiments, compared to simpler species such as alkalies.

The manuscript is organized as follow. The first part presents the conception and building of the setup. In Chapter 2, I recall the main properties of dysprosium atoms that are relevant for this work. Chapter 3 explains the design of the vacuum system and the first cooling stages in magneto-optical traps. In Chapter 4, I present the optical setup that we built to create optical tweezers.

The second part explains the behavior of dysprosium atoms in optical tweezers. Chapter 5 describes how the anisotropic light-matter interaction of dysprosium plays a role in optical tweezers. It also contains the measurements we performed to characterize and quantify this effect. In Chapter 6, I explain how we go from several atoms per tweezer to a single atom by performing light-induced collisions. Chapter 7 explains the imaging of single dysprosium atoms in optical tweezers and the detection fidelity that we reached.

The third part is devoted to measuring collective light scattering effects in chains of atoms. In Chapter 8, after reviewing the formalism of collective light scattering in ordered atomic ensembles, I present how we prepare defect-free chains of atoms. In Chapter 9, I describe a technique we developed to measure the internal state of the atoms on an optical transition using the rich electronic structure of dysprosium. Using this technique, I present in Chapter 10 a steady-state spectroscopic measurement of the frequency of the atoms. When the atoms are close enough, and in the classical limit of low atomic excitation, we observe a frequency shift due to the collective diffusion of light by the atoms. Finally, in Chapter 11 I extend this study to Ramsey spectroscopy, which is not limited to the steady state regime and which is performed outside the low-excitation regime.

Chapter 2

Relevant properties of dysprosium

Contents

In this chapter, I give an overview of the main properties of dysprosium (Dy). I will only focus on the properties that are relevant for trapping and manipulating Dy atoms in optical tweezers. Reference [NF21] gives a more general overview about the use of lanthanides for cold atom experiments.

Dy is a rare earth lanthanide element now used in many cold atom experiments [Lu+11; Tan+19; Cha+20; Cho+22]. It has an atomic number $Z = 66$, with 12 more electrons than the previous noble gas, xenon.

It has several isotopes that are both stable and abundant in nature. Their properties are summarized in Table 2.1. In our experiment, we exclusively used the isotope ^{162}Dy. One of its particularities is that it has no nuclear spin I, and thus has no hyperfine structure. This makes it easier to understand the interaction of the atoms with light, and simplifies the first experiments with Dy in optical tweezers. We do not expect significant differences if other similar isotopes, like ^{164}Dy or ^{160}Dy, were used instead.

However, isotopes with a non-trivial hyperfine structure in the ground state could provide qualitatively different cooling mechanisms or spin manipulation techniques, but we have not explored these possibilities in the work presented here.

Due to its 12 outer electrons, Dy has a very rich electronic structure, and has many levels, as can be seen in Figure 2.1 a.

2.1 Ground state

Of particular interest is the ground state of Dy, since atoms populate this state by default. Its configuration is $[Xe]4f^{10}6s^2$, meaning it has an unfilled $4f$-shell containing

Isotope	Abundance [%]	Nuclear spin I
^{164}Dy	28.2	0
^{163}Dy	24.9	5/2
^{162}Dy	25.5	0
^{161}Dy	18.9	3/2
^{160}Dy	2.3	0

Table 2.1. – Properties of the most abondant isotopes of Dy. In the work presented here, we exclusively used the isotope ^{162}Dy.

ten electrons, as well as two valence electrons on an outer s-shell, as illustrated on Figure 2.1 b.

For this configuration, the angular momentum of the electrons can couple in many ways, resulting in several possible terms with different energies. To characterize the ground state of Dy, one can use Hund's rules, which empirically describe the coupling of the angular momentum of the electrons for the lowest energy level.

According to the first rule, the individual spins $\boldsymbol{s}_i$ of the electrons on an unfilled shell couple to give a total spin $\boldsymbol{S} = \sum_i \boldsymbol{s}_i$ with a magnitude S maximized for the lowest lying energy level. For Dy, this is achieved with four unpaired and aligned electrons in the $4f$ shell, resulting in a spin $S = 2$.

The second rule states that the magnitude L of the total angular momentum $\boldsymbol{L} = \sum_i \boldsymbol{l}_i$ of the electrons is maximized in the ground state. This translates to total orbital angular momentum $L = 6$.

The two angular momenta can add together through the spin-orbit coupling mechanism to give a total angular momentum $\boldsymbol{J} = \boldsymbol{L} + \boldsymbol{S}$ that takes values $|L - S| \leq J \leq |L + S|$. The third Hund's rule states that for Dy with a more than half-filled $4f$ shell, the lowest energy level is the one with the largest J, meaning $J = 8$.

This gives the final notation for the ground state of Dy as $G = 4f^{10}6s^2 \quad {}^5I_8$, where the last expression uses the spin-orbit coupling notation ${}^{2S+1}L_J$. The ground manifold of Dy is thus composed of $2J + 1 = 17$ states[1] that are degenerate in the absence of external field. These states can be labelled $|G, m_J\rangle$, where m_J represents the projection J_z of the spin $\boldsymbol{J}$ along a given quantization axis z and takes only integer values from $-J$ to J.

This large angular momentum in the ground state is very specific to lanthanide

[1] This only applies for isotopes without nuclear spin $\boldsymbol{I}$, otherwise, one would also have to take into account the hyperfine structure.

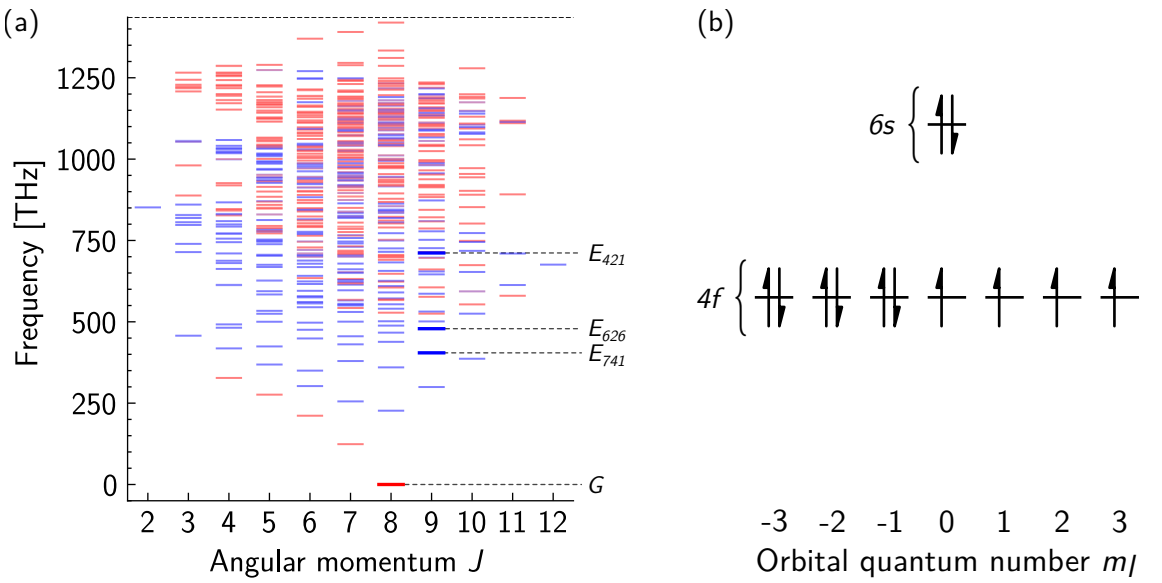

Figure 2.1. – (a) Energy levels of Dy [Ral+06]. Levels in red have even parity, while levels in blue have odd parity. The dashed black line indicates the ionization energy. Levels relevant for the transitions used in this work are highlighted. (b) Filling of the electronic shells for the ground state $G = 4f^{10}6s^2$ of Dy.

atoms, and it is usually the reason for using these species in cold atom experiments.

For example, the large angular momentum results in a large magnetic moment that leads to a strong magnetic dipole-dipole interaction between atoms[2]. This has been used to study many-body dipolar physics where the magnetic dipole-dipole interaction influences the behaviour of degenerated quantum gases [Cho+22].

Some experiments also make use of external fields to engineer interesting hamiltonians in the large manifold of the ground state in order to study the dynamics of large spin systems [Sat+21; Fab+22]. The influence of an external electric field on the internal degrees of freedom of Dy will be important for trapping in optical tweezers and will be discussed in detail in Chapter 5.

Two other species in the lanthanide family that are also commonly used in cold atom experiments are erbium (Er) and ytterbium (Yb). Er has a very similar electronic structure compared to Dy. It also presents an unfilled $4f$ shell and it has a large angular momentum in the ground state. However, while Yb technically belongs to the lanthanide family, its $4f$-shell is filled. It is thus more similar to alkaline-earth atoms, and is sometimes encompassed with them in the alkaline-earth-like family.

[2] In our case, since atoms in different optical tweezers are far appart ($> 1\,\mu m$), the magnetic dipole-dipole interaction is negligible ($< 1\,Hz$).

2.2 Excited states and transitions

While the physics that can be explored using the ground state properties of Dy is very rich, it is not the main reason for using this species in our experiment. Instead, we primarily want to make use of the various optical transitions that are available in Dy. Using these transitions, we want to cool and image the atoms and then perform light scattering experiments. For this purpose, it is advantageous to be able to choose from several optical transitions with different wavelengths or linewidths to best fit the requirements of the experiment.

Lanthanide species are particularly well suited for this, as there is a large number of transitions possible between the many energy levels. Even when only considering transitions from the ground state, as will be the case here, there are many available transitions. Depending on the energy of the excited levels and their coupling to the ground state, the associated transitions can have very different properties. Here I will give examples of such transitions by highlighting the ones we use in our experiment. Their properties are summarized in Table 2.2.

The most commonly used transitions of Dy are those where a $6s$ electron is excited to a $6p$ shell. Similar transitions are also present in alkaline-earth-like atoms, such as Sr or Yb, and many of the laser manipulation techniques developed for these atoms can thus be adapted to Dy [Coo18].

This is the case of the **421 nm transition** for which the excited level is $E_{421} = [4f^{10}(^5I_8)6s6p(^1P_1^o)]_9^o$. Here the angular momentum $J_1 = 8$ of the $4f$ shell electrons couples with the angular momentum $J_2 = 1$ of the $6p$ shell to give a total angular momentum $J = 9$. The superscript o indicates that the level has odd parity, which is required to have a dipolar electric transition with the ground state that has even parity.

This is a broad transition with a linewidth of $\Gamma_{421} = 2\pi \times 32.2\,\mathrm{MHz}$. Owing to this

Excited level	Wavelength λ [nm]	Linewidth $\Gamma/2\pi$ [s^{-1}]
$E_{421} = [4f^{10}(^5I_8)6s6p(^1P_1^o)]_9^o$	421.291	32.2×10^6
$E_{626} = [4f^{10}(^5I_8)6s6p(^3P_1^o)]_9^o$	626.082	135×10^3
$E_{741} = 4f^9(^6H^o)5d6s^2 \quad {}^5K_9^o$	740.964	1.8×10^3

Table 2.2. – Properties of the transitions of Dy used in the experiment.

large linewidth, this transition is commonly used as an efficient first cooling stage in a magneto-optical trap (MOT) or for fast imaging of the atoms [Su+25]. However, the temperature that can be reached with this transition is limited by the Doppler temperature, of the order of 1 mK, which is too large to load optical tweezers of reasonable depth.

In addition, this transition is not fully closed. Indeed, there are several lower lying levels with even parity and compatible angular momentum to which the atoms can decay [You+10]. It can happen that atoms that scatter light on the 421 nm transition end up decaying to these levels which have a long lifetime, and thus the atoms are lost from the cycling transition. This reduces the number of atoms that can be trapped in a magneto-optical trap using this transition, and I will discuss it in more detail in Chapter 3.

Another commonly used transition is the **626 nm transition**. Its excited level is $E_{626} = [4f^{10}(^5I_8)6s6p(^3P_1^o)]_9^o$, with a spin for the electron in the $6p$ shell of $S = 1$, and a total angular momentum $J = 9$. This transition links two states with different spin S and is called an *intercombination line*. Such spin flip is forbidden by the electric dipole selection rules, and the transition is thus much narrower than the 421 nm transition, with a linewidth of $\Gamma_{626} = 2\pi \times 135\,\mathrm{kHz}$[3]. Due to its low Doppler temperature of the order of 3 µK, this transition is commonly used to cool atoms in a second MOT stage [Mai+14]. It can also be used to perform non-destructive imaging of single atoms, as has been demonstrated in ytterbium which has a very similar transition [Sas19].

Besides the ground state, there is no other level with even parity and compatible angular momentum towards which the atoms can decay, and thus the transition is fully closed.

In addition to the transitions where a $6s$ electron is excited, there are also transitions where a $4f$ electron is excited to a higher shell. These transitions are specific to the lanthanides and can provide additional ways to manipulate the atoms.

This is the case of the **741 nm transition** that excite a $4f$ electron to a $5d$ shell. The excited state is $E_{741} = 4f^9(^6H^o)5d6s^2 \quad {}^5K_9^o$. Since the wavefunctions of the $4f$ and $5d$ shells have a small spatial overlap, both for the radial and angular part, the transition is very narrow with a linewidth of $\Gamma_{741} = 2\pi \times 1.8\,\mathrm{kHz}$. Here the angular

[3] The linewidth of the transition is not strictly zero because the excited state is not a pure $S = 1$ state, but has small admixture of $S = 0$ states due to relativistic corrections beyond the standard spin-orbit coupling term $\boldsymbol{L} \cdot \boldsymbol{S}$.

momentum of the $4f$ and $5d$ electrons give an orbital angular momentum $L = 7$, which then combines with the total spin $S = 2$ to give a total angular momentum $J = 9$. Such narrow transitions have for example been used to resolve motional sidebands of atoms in dipole traps and to cool them near the quantum motional ground state [Coo18; NYK18; Höl23].

These three transitions at 421 nm, 626 nm, and 741 nm are the ones we use in our experiment. They represent a sample of the variety of transitions that are available in Dy and why they can be interesting to trap and manipulate Dy atoms in optical tweezers. In the next chapters, I will explain more explicitly how these transitions are used in our setup, to realize magneto-optical traps, and then to cool and image single atoms in optical tweezers.

Chapter 3

Source of cold atoms

Contents

In this chapter, I will describe the parts of the experiment that are dedicated to the production of cold Dy gases. In the first section, I will give a global overview of the apparatus, and I will discuss the choice of design we made, highlighting especially the differences with more standard dysprosium experiments. In the following sections, I will provide more details on the first cooling stages of the experiment, namely the 2D MOT and 3D MOT. A succinct description of the setup is also given in [Blo+24]. The work presented here was done during the first year of my PhD, with the help of another student, Sam Cohen, who stayed in the lab for a year.

3.1 Design and overview

Cold atom experiments using dysprosium have become relatively common nowadays, motivated by the new possibilities offered by lanthanides. However, most of these experiments usually aim at studying the physics of degenerate quantum gases [Cho+22] and are optimized for this purpose. Indeed, they require very large MOTs in order to have sufficient atom number to perform efficient evaporative and reach quantum degeneracy. These requirements add significant complexity to the setup, and often increase the duration of the experimental sequence to several seconds or tens of seconds.

However, optical tweezer experiments have typically more modest requirements in terms of atom number, since in principle only a few atoms are required. In addition,

optical tweezers can be loaded even at relatively high temperature, and then lower temperatures can be reached in the tweezers with fast laser cooling techniques. As such, these experiments can be performed with simpler setups, and with a relatively high repetition rate of a few Hertz.

When we started this project, there were a few tweezers experiments using alkali-earth-like atoms such as Sr or Yb, but there was no such experiment using lanthanide atoms. We had to decide what kind of setup would allow us to do the experiments we planned, and then design a Dy setup that would fit these requirements.

For optical tweezers, a solution that proved to be quite versatile is to use a glass cell in combination with a microscope objective outside vacuum [Mad21; You23]. The glass cell provides large optical access, and there are now off-the-shelf microscope objectives with large numerical aperture designed to work with a glass cell. This glass cell solution is also a flexible setup that can be adapted as the requirements of the experiment evolve.

But, while there are existing Dy setups using glass cells [Dre17], there are some challenges that make this solution not as straightforward as for example with alkali species. Indeed, Dy needs to be heated up in an oven to very high temperatures, around 1000 °C, to produce a sufficient atomic flux. The hot atoms will then deposit on any cold surface in line of sight with the oven, and this surface will be permanently coated by a reflective layer of Dy. Because of this, it is not advisable to directly load a Dy MOT in a glass cell right at the oven output.

A typical solution to this problem is to load a MOT using a Zeeman slower, where the light used to slow down the atoms is reflected on an in-vacuum mirror that can become coated but remain reflective. It is however not easy to put a mirror inside a glass cell, and the atomic flux coming from the Zeeman slower may limit the lifetime of atoms in the MOT chamber. This is why usually the atoms are finally transported to a glass cell where the rest of the experiment takes place. This transport step significantly increases the complexity and duration of the experimental sequence, and we wanted to avoid it.

When looking at other species like Sr and Yb that face the same challenges, an appealing approach is to use a 2D MOT [Nos+17; Sas19; Bar+20; Esc+21]. In this case, a 2D MOT placed at the output of the oven cools and deflects the atoms directly towards the glass cell where they are trapped in a 3D MOT. This solution does not require to send light in the direction of the oven. In addition, the atomic flux to the

cell can be quickly stopped by tuning off the 2D MOT, thus allowing to have a long lifetime for the atoms in the glass cell. For these reasons, we decided to use this 2D MOT solution for our experiment. However, at the time, there was no 2D MOT setup using lanthanide with a complex spin structure like Dy or Er. A such, we had to adapt the 2D MOT setup for use with Dy.

The resulting apparatus that we built is shown in Figure 3.1. The whole setup is placed on a breadboard. Underneath the breadboard, we put several stripes of teflon tape, such that it can slide freely on the optical table. This way, it is possible to pull away the glass cell from the optics surrounding it, in case the apparatus needs to be baked again in the future. The vacuum chamber is adapted from a similar Sr design [Bar+20] and was built by the company LEOS. It consists of two parts separated by a differential pumping section.

In the first part, a high-temperature oven[1] loads a 2D MOT of Dy. The oven itself is made of two parts: an effusion cell and a hot lip. The effusion cell contains 70 g of small Dy chunks and is heated to 900 °C. The hot lip at the front of the oven is held at a higher temperature of 1200 °C. It prevents Dy from depositing at the output of the oven and clogging it.

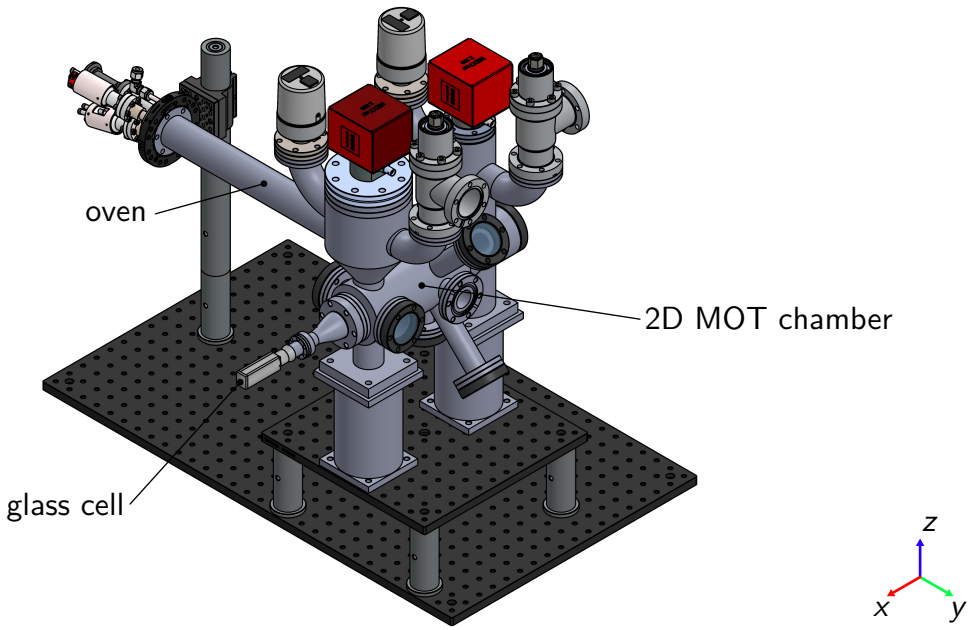

Figure 3.1. – Schematic of the vacuum chamber.

Atoms coming out of the oven are then cooled and trapped in a 2D MOT on the

[1] Createc DFC-40-25-WK-2

421 nm transition. The atoms are then sent to the second chamber part by accelerating them with a push beam through a 2 mm diameter differential pumping section. Once the atoms arrive in the glass cell, they are trapped in a 3D MOT and the rest of the experiment takes place. In the next sections, I will provide more details on these 2D MOT and 3D MOT stages.

The background pressure measured by the gauges mounted on the chamber is below 1×10^{-11} mbar both on the oven and glass cell sides. This relatively good vacuum quality is probably due to the dysprosium that continuously deposits in front of the oven and that acts as a getter for residual gasses.

3.2 2D MOT

3.2.1 Working principle

As mentioned above, there was no existing 2D MOT for Dy before, so I will explain here this part of the setup that I designed and built at the beginning of my PhD. At the same time we were designing our experiment, a similar 2D MOT setup was being developed in the group of Prof. Lauriane Chomaz [Jin+23], and we exchanged with them during the design phase.

A schematic view of the 2D MOT is shown in Figure 3.2 a. It uses the radiation pressure of light on the 421 nm transition to capture the atoms that come out flying of the oven with a typical thermal velocity of 300 m s^{-1} at 1200 °C. The 2D MOT is made of two pairs of counter-propagating beams that cross in the center of the chamber. This configuration is obtained by retro-reflecting light coming from a single fiber in a bow-tie configuration to avoid splitting the power between the two arms.

This configuration of counter-propagating beams cools the atoms in the YZ plane. Cooling occurs when the light is red-detuned from the transition, with a detuning $\Delta < 0$ [WI79; Phi98]. In this case, an atom with velocity $\boldsymbol{v}$ sees a laser beam l with an effective detuning $\Delta - \boldsymbol{k}_l \cdot \boldsymbol{v}$ due to the Doppler effect, where $\boldsymbol{k}_l$ is the wavevector of the beam. When the atom is moving against the beam, it sees light closer to resonance and scatters photons preferentially from this beam, and is thus slowed down. By sending beams in all directions in the YZ plane, the velocity of the atoms is damped in this plane. In the direction X, atoms still have a remaining velocity spread, but it is only a few meters per second thanks to the collimation by the oven tube.

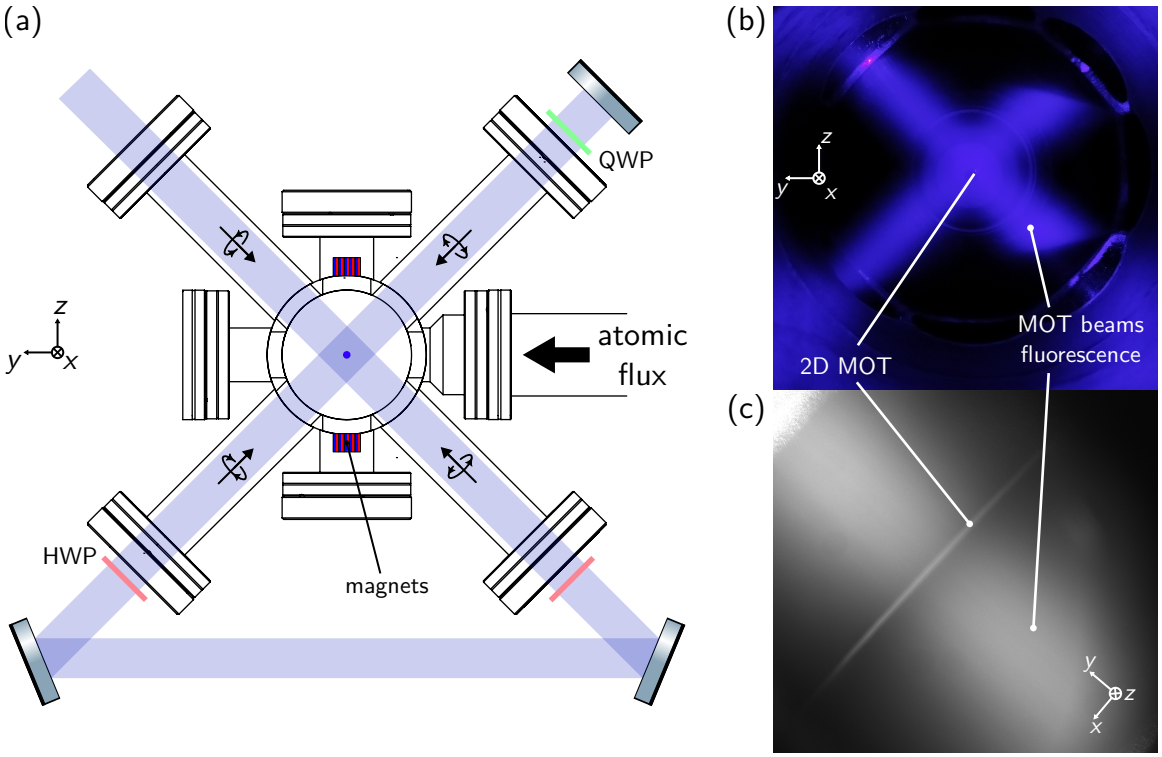

Figure 3.2. – (a) Schematic of the 2D MOT. Atoms come out of the oven on the right part of the figure and are trapped in the center of the chamber. (b) Front-facing picture of the 2D MOT. One can see the fluorescence of the two MOT beams forming a cross. At the intersection of the two arms, there is a small bright dot corresponding to the 2D MOT. (c) Picture from below of the 2D MOT. The 2D MOT is the bright line in the center of the picture, while the background light corresponds to the fluorescence of the atoms coming out of the oven.

As such, this configuration only provides a cooling force, but does not trap the atoms. To make a magneto-optical trap, one also adds a magnetic field gradient that provides a position-dependent force to trap the atoms at the center of the chamber [Raa+87; Foo05]. In our case, we produce this magnetic field gradient with permanent magnets placed around the chamber as shown in Figure 3.2 a. Using magnets allows us to produce large magnetic gradients of several tens of gauss per centimeter without the complexity of water-cooled coils. More details about the placement of the magnets and the characterization of the field they produce are given in Appendix A.1. Near the center of the chamber, they create a magnetic gradient of the form:

$$\boldsymbol{B}(x, y, z) = \begin{bmatrix} 0 \\ B'z \\ B'y \end{bmatrix} \tag{3.1}$$

where B' is the magnitude of the field gradient.

The polarization of the beams is chosen to be σ^- with respect to the quantization axis, given by the direction of the magnetic field. In this case, the light will mostly drive transitions between states $|G, m_g\rangle$ and $|E_{421}, m_e = m_g - 1\rangle$. The energy difference between these two states is shifted by the Zeeman effect by $\hbar\delta\omega_{m_g,m_e} = \mu_B(g_{E_{421}}m_e - g_G m_g)\|\boldsymbol{B}\|$, where μ_B is the Bohr magneton and $g_G = 1.241$ and $g_{E_{421}} = 1.22$ are the Landé factors of the ground and excited states respectively. As atoms move away from the center of the MOT, they become closer to resonance with beams that push them back towards the center.

With this setup, it is thus possible to cool and trap atoms in the YZ plane. The atoms then accumulate in a needle-shaped cloud along the X axis, as can be seen in Figure 3.2 b, c.

3.2.2 Optimal parameters

While the basic principles of the MOT are well understood, it is not straightforward to get quantitative predictions for the properties of a 2D MOT for an atom with so many Zeeman states as Dy. Here I will present the calculations I did to estimate the capture velocity of the 2D MOT. We used them to check for the viability of a 2D MOT solution for Dy, and to optimize numerically some of the parameters.

A relatively simple model that can capture some of the features of a Dy MOT is a rate equation model, where the atoms are described by their populations in the different Zeeman states. It is assumed that the coherences (both between ground and excited states and between Zeeman levels in a single manifold) are quickly damped and are at equilibrium with respect to the populations. This leads to the following set of equations on the populations in the ground states Π_{m_g} and excited states Π_{m_e} [Ste12]:

$$\frac{\mathrm{d}\Pi_{m_g}}{\mathrm{d}t} = +\sum_{l,m_e} \gamma^l_{m_g,m_e}(\Pi_{m_e} - \Pi_{m_g}) + \sum_{m_e} \Gamma_{m_e,m_g}\Pi_{m_e} \tag{3.2}$$

$$\frac{\mathrm{d}\Pi_{m_e}}{\mathrm{d}t} = -\sum_{l,m_g} \gamma^l_{m_g,m_e}(\Pi_{m_e} - \Pi_{m_g}) - \Gamma\Pi_{m_e} \tag{3.3}$$

Here $\Gamma_{m_e,m_g} = \Gamma \langle J_g\, m_g\,;1\, m_e - m_g \,|\, J_e\, m_e\rangle^2$ is the decay rate of the excited state m_e to the ground state m_g, where the last term is a Clebsch-Gordan coefficient between the states $|J_g, m_g\rangle$ and $|J_e, m_e\rangle$.

In addition, $\gamma^l_{m_g,m_e}$ is the rate of optical pumping between the states $|J_g, m_g\rangle$ and

$|J_e, m_e\rangle$ due to the laser l, and is given by:

$$\gamma^l_{m_g,m_e} = \frac{\left[\Omega^l_{m_g,m_e}\right]^2/\Gamma}{1 + 4\left(\Delta - \delta\omega_{m_g,m_e} - \boldsymbol{k_l}\cdot\boldsymbol{v}\right)^2/\Gamma^2} \tag{3.4}$$

where $\Omega^l_{m_g,m_e} = \Omega^l_{m_e-m_g}\,\langle J_g\, m_g\,;1\, m_e - m_g \,|\, J_e\, m_e\rangle$ is the Rabi frequency for the laser l on the transition between states m_g and m_e, and $\Omega^l_q = \Gamma\sqrt{\frac{s_l}{2}}(\boldsymbol{e}^*_q \cdot \boldsymbol{\epsilon}_l)$ is the q-th component of the total rabi frequency in the spherical basis for the considered quantization axis.

The average acceleration[2] experienced by the atom can be estimated by evaluating the momentum transfer between the atom and the different lasers [Eck+22]:

$$\boldsymbol{a} = \sum_l \frac{\hbar \boldsymbol{k_l}}{m} \sum_{m_g,m_e} \gamma^l_{m_g,m_e}(\Pi_{m_g} - \Pi_{m_e}) \tag{3.5}$$

With the previous equations on the populations and the acceleration, it is possible to estimate the trajectory of an atom in the MOT. To do this, one evolves the classical equations of motions for the position $\boldsymbol{r}(t)$ of the atom and its velocity $\boldsymbol{v}(t)$. At each time t, the acceleration $\boldsymbol{a}(t)$ is obtained by solving the steady-state rate equations assuming that the populations reach equilibrium much faster than the timescale of the motion of the atom. With this, it is possible to compute the trajectory of the atom across the MOT and check if it is captured or not. By finding the smallest initial velocity for which an atom is captured, one can estimate the capture velocity of the 2D MOT as is illustrated in Figure 3.3. In this plot, one sees for example that the capture velocity of the 2D MOT is about $100\,\mathrm{m\,s^{-1}}$.

It is worth noting that, as is, this model does not take into account the random force due to spontaneous emission, and thus, cannot estimate the temperature reached by the atoms in the MOT. In addition, this model obviously does not capture any mechanism involving coherences and thus ignores some possibly interesting sub-Doppler phenomena [DC89; YLL10]. In any case, we did not perform a detailed study of the temperature of the 2D MOT, and such effects should only have a small influence on the estimated capture velocity.

Using the simulations described above, one can numerically optimize the parameters of the 2D MOT. Among the parameters to tune, some of them are actually constrained by technical considerations, and there is no much insight to gain from simulations.

[2] Here we only take into account the radiation pressure force, and neglect other forces such as gravity or the magnetic force because they are negligible in a MOT on the broad transition.

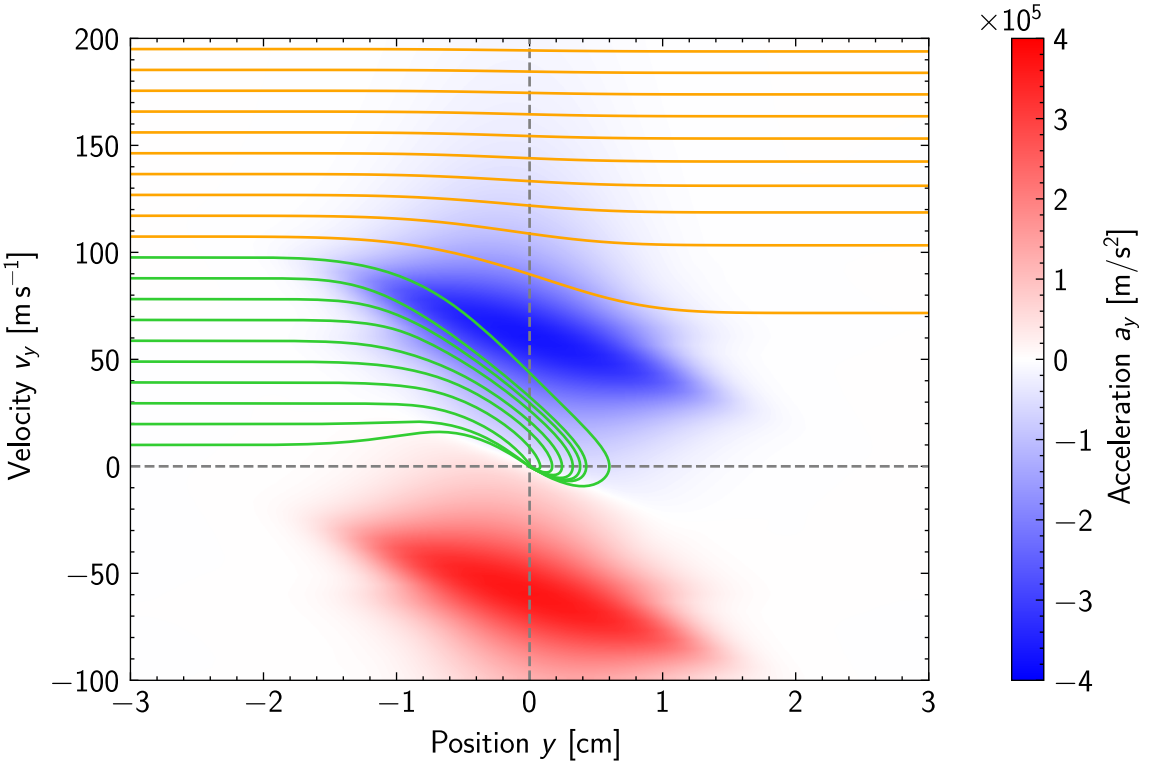

Figure 3.3. – Simulations of the phase-space trajectories of atoms in the 2D MOT for a detuning $\Delta = -3.2 \times \Gamma_{421}$ and a magnetic field gradient $B' = 23\,\mathrm{G\,cm^{-1}}$. The curve indicates the trajectories followed by atoms coming out of the oven. Trajectories in green represents atoms that are captured in the MOT, while trajectories in red represent atoms that are not captured. The color in the background represents the acceleration experienced by the atoms depending on their velocity and position.

For example, having large beams for the 2D MOT would increase the capture velocity of the 2D MOT, but the size of the viewports prevents us from having beams with a waist larger than $w = 8\,\mathrm{mm}$. Similarly, the power of the laser at the output of the fiber is limited to about 300 mW, yielding an intensity at the center of the beam $I = 5.3 \times I_{\mathrm{sat},421}$.

Still, without some numerical model, there is no obvious value to choose for the detuning Δ of the laser and the magnetic field gradient B'. Besides, these parameters are not easily tunable on the experiment in our case. Changing the magnetic gradient requires us to change the number of magnets, and to redo the alignment of the 2D MOT. Similarly, changing the detuning of the laser over a range comparable to the linewidth $\Gamma_{421} = 2\pi \times 32\,\mathrm{MHz}$ of the transition is not straightforward. For these reasons, I only performed simulations to find the best detuning and magnetic field gradient.

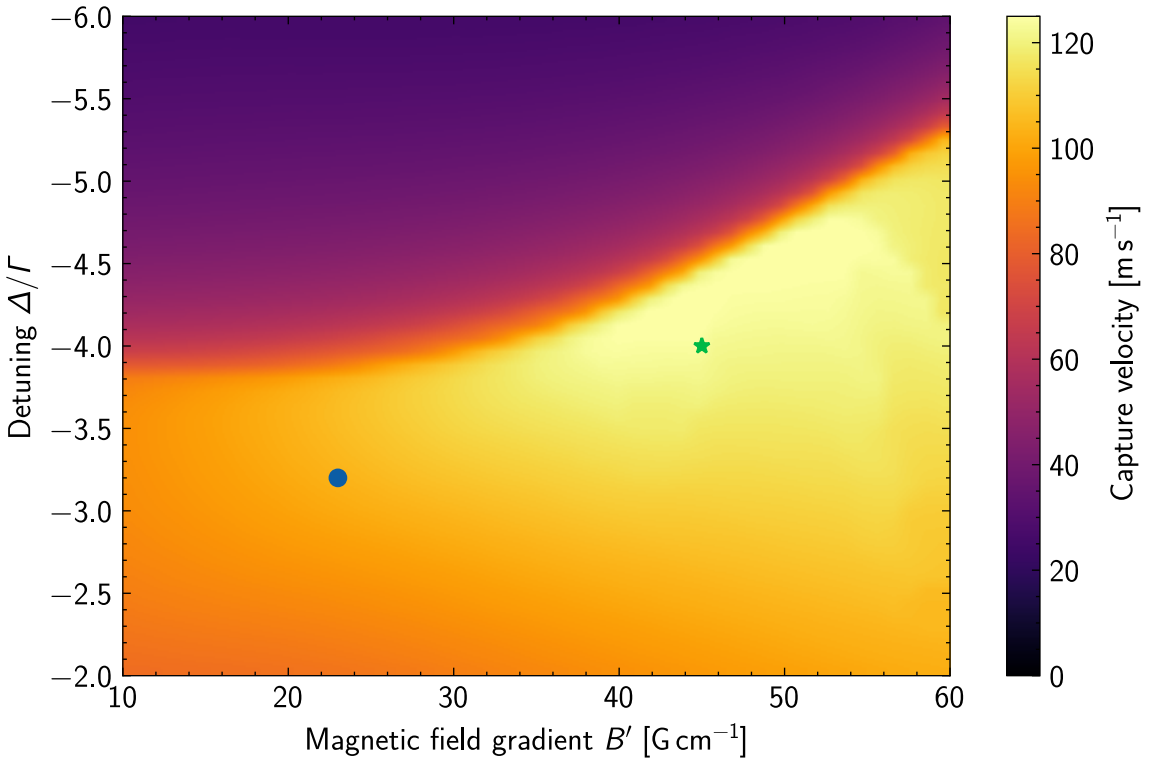

Figure 3.4. – Influence of the detuning and magnetic field gradient on the capture velocity of the 2D MOT. The blue point indicates the parameters currently used on the experiment, with a capture velocity of 105 m s^{-1}. The green star indicates a better set of parameters, $B' = 40\,\mathrm{G\,cm^{-1}}$ and $\Delta = -4\Gamma$, corresponding to a capture velocity of 125 m s^{-1}.

The results of the numerical analysis performed are shown in Figure 3.4. As one can see, it turns out that the capture velocity is relatively homogenous over a large range of detunings and magnetic field gradients. The largest capture velocity is expected to be at a detuning $\Delta = -4 \times \Gamma_{421}$ and a magnetic field gradient $B' = 40\,\mathrm{G\,cm^{-1}}$, with a capture velocity of $125\,\mathrm{m\,s^{-1}}$. For historical reasons, we are however not working in the optimal regime. Instead, we are currently using a detuning closer to resonance $\Delta = -3.2 \times \Gamma_{421}$ and a lower magnetic field gradient $B' = 23\,\mathrm{G\,cm^{-1}}$. Because of this, the expected capture velocity is only $100\,\mathrm{m\,s^{-1}}$. It would probably be worth to try to use the optimal parameters, but it requires a redesign of the 421 nm optical setup and a realignment from scratch of the 2D MOT, and we have not done it yet. The lower capture velocity in our current regime of parameters has been enough for our needs so far, as we do not require very large atom numbers to load optical tweezers. We did not perform any further study of loading rate for the 2D MOT, but a detailed experimental analysis of a similar 2D MOT setup is reported in [Jin+23].

By changing the frequency of the 421 nm laser to compensate for the isotopic frequency shift, other isotopes of Dy in the 2D MOT besides ^{162}Dy used in the rest of the thesis. This way, we managed to get a 2D MOT for the isotopes ^{162}Dy, ^{163}Dy and ^{164}Dy. Notably, we could not straightforwardly obtain a 2D MOT for the fermionic isotope ^{161}Dy, even though it has a large natural abondance. The complex hyper-fine structure of ^{161}Dy makes it more challenging to trap in a MOT, as explained in [You+10].

3.3 Push beam and 3D MOT

Once the atoms are trapped in the 2D MOT, we need to accelerate them towards the glass cell, in the X direction. To prevent the atoms from falling too much under gravity during their fly over the 30 cm between the 2D MOT and the glass cell, they must have a velocity larger than $15\,\mathrm{m\,s^{-1}}$. To reach this velocity, we use a beam on the 421 nm transition, with a waist of 1.2 mm and a detuning $\Delta_{\mathrm{push}} = -1.9 \times \Gamma_{421}$. This beam crosses the 2D MOT center, but it is angled by 5° with respect to the X axis such that it does not go through the differential pumping section and does not perturb the atoms in the glass cell. With less than 1 mW of power, we can accelerate the atoms to the required velocity. Similar results have been obtained with a push beam on the intercombination line at 626 nm [Jin+23].

We then capture the atoms coming from the 2D MOT in the glass cell using a 3D MOT. This 3D MOT works according to the same principle as the 2D MOT presented above, but provides cooling and confinement along all three directions of space. As depicted in Figure 3.5, we use a pair of coils in the anti-Helmholtz configuration in the vertical Z direction to produce a magnetic field gradient. Three pairs of compensation coils in the Helmholtz configuration are also present in all directions. They are used to create homogenous magnetic fields, for example to move the position of the MOT center. More details on the properties of these coils are given in Appendix A.2. In addition, three pairs of beams provide the cooling and trapping light.

One thing we had to decide is on which transition to operate the 3D MOT. Ideally, we would like to do the 3D MOT on the narrower 626 nm transition, as the typical temperature that can be reached in the MOT is of the order of the Doppler temperature $T_{\mathrm{Doppler}} = \hbar\Gamma/2k_B$. For the 626 nm transition, with its linewidth $\Gamma_{626} = 2\pi \times 135\,\mathrm{kHz}$, the Doppler temperature is $T_{\mathrm{Doppler},626} = 3.2\,\mu\mathrm{K}$. This is much lower than the Doppler

temperature of the 421 nm transition $T_{\text{Doppler},421} = 770\,\mu\text{K}$. We could then directly load optical tweezers with a trap depth of a few hundred microkelvins from the 3D MOT without additional cooling.

A drawback of a MOT on the intercombination line is its relatively low capture velocity. Indeed, the maximum acceleration that atoms can experience is limited by the scattering rate of the transition $a_{\max} = \hbar k\Gamma/2m$, even at very large laser power. Therefore, atoms can only be brought to a stop over a distance w if their velocity is lower than $v_c = \sqrt{\hbar k\Gamma w/m}$. Due to the small size of the glass cell, the size of the beams is limited to $w = 1\,\text{cm}$. The capture velocity of a 626 nm MOT is then at best $10\,\text{m}\,\text{s}^{-1}$, which is likely not enough to capture atoms coming from the 2D MOT. Techniques to broaden the line by modulating the laser frequency [Mai+14; Dre+17] would not solve this issue in our case, since they do not increase the actual scattering rate of the transition.

A common solution to overcome this problem is to implement a two-stage MOT. First, one would load a 3D MOT on the broad 421 nm transition, and then once enough atoms are trapped, switch to a MOT on the narrow 626 nm transition for further cooling. We initially implemented this scheme, but we observed a high loss rate on the 421 nm transition that prevented us from accumulating many atoms in a blue 3D MOT. This is because, as mentioned in Section 2.2, this transition is not fully closed, and atoms in the MOT can be lost in dark states. These states are not well-known, so it is difficult to add a repumper to bring the atoms back to the ground state. Even by adding a repumper, it is likely that losses due to light-assisted collisions would also prevent us from reaching high atomic density. As a result, we could not reach large atom numbers using a blue MOT alone.

To solve this issue, we instead decided to implement a *core-shell* MOT. This technique was first demonstrated for Yb [Lee+15]. The idea is to have a hollow MOT on the broad transition with at its center a MOT on the narrow transition. Atoms are slowed down by the broad transition on the outer shell, and then fall and accumulate in the narrow MOT inside. Atoms in the center are cooled down to the Doppler temperature of the narrow transition, and importantly, they are not exposed to the broad transition light for a long time, so losses are strongly reduced. This beam configuration is illustrated on Figure 3.5.

In our case, the 421 nm MOT has a waist of 1.5 cm and the center of the beams is blocked by masks with a diameter of 5 mm. We only use blue beams in the horizontal plane, since the velocity of the atoms coming from the 2D MOT is small in the Z

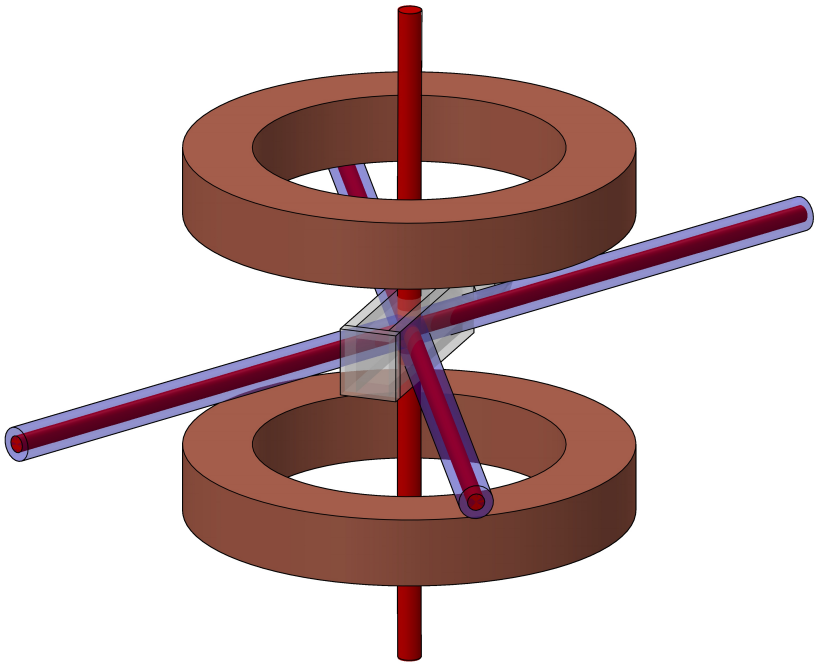

Figure 3.5. – Sketch of the beams and coils of the 3D MOT around the glass cell. In the horizontal direction, two hollow 421 nm beams surround the 626 nm beams, to increase the capture velocity of the MOT.

direction.

We empirically optimized the parameters of this core-shell MOT. Typically, we work at a magnetic field gradient of $B' = 5\,\mathrm{G\,cm^{-1}}$ along the strong axis of the coils. The detuning for the 626 nm MOT during the loading stage is $\Delta_{626} = -40 \times \Gamma_{626}$ and the intensity of each beam is $I_{626} = 100 \times I_{\mathrm{sat},626}$. The detuning of the 421 nm shell is $\Delta_{421} = -1.3 \times \Gamma_{421}$, with a power of about 5 mW per beam (including the blocked central part). It is important to be able to move the position of the MOT with the compensation coils in all three directions. Indeed, we found that the number of atoms that can be loaded in the MOT is only high when the magnetic zero is well inside the shadowed area of the 421 nm light. Alignment of the 421 nm beams is also crucial to ensure that the dark area is well-centered at the intersection of the beams.

With this technique, we are able to reach atom numbers one hundred times larger than with a blue 3D MOT alone. Again, we did not perform a quantitative study of the loading rate and atom number in the MOT, since it was enough to load optical tweezers.

After loading the core-shell MOT for 100 ms, we then switch off abruptly the 421 nm light to only keep a MOT on the 626 nm transition. In 50 ms, we then ramp the detuning of the beams to $\Delta_{626} = -7.4 \times \Gamma_{626}$, the intensity to $I_{626} = 3 \times I_{\mathrm{sat},626}$,

and the magnetic field gradient to $B' = 1.7\,\mathrm{G\,cm^{-1}}$. In this regime, the optical force becomes comparable in strength to gravity, and the MOT sags to a position a few millimeters below the magnetic field zero. In these conditions, the atoms are optically pumped to the $|G, m_g = -8\rangle$ state [Mai+14; Dre+17]. At this stage of the experiment, the atoms are ready to be loaded in optical tweezers.

Chapter 4

Optical tweezers setup

Contents

In this chapter, I will describe the setup we built to create optical tweezers and to image the atoms. I will only focus on the optical elements around the glass cell, and I will give a more detailed explanation about the physics of Dy atoms in optical tweezers in the next chapters. We built this setup at the beginning of the second year of my PhD, together with a starting PhD student, Britton Hofer.

4.1 Overview

To trap and manipulate single atoms, we use the dipole force exerted by off-resonant light. As will be discussed in more detail in chapter Chapter 5, the energy levels of Dy atoms are shifted proportionally to the intensity of the light. This so-called *light shift* can be expressed as [GWO00]:

$$\Delta U(\boldsymbol{r}) = -\frac{\alpha I(\boldsymbol{r})}{2c\epsilon_0} \tag{4.1}$$

where α is the polarizability of the considered atomic state, $I(\boldsymbol{r})$ the intensity of the light at the position of the atom, c the speed of light, and ϵ_0 the vacuum permittivity. If the polarizability α is positive, as will be the case for us here, atoms are attracted to regions of high intensity. We use this effect to create *optical tweezers* [Ash70]: focusing a laser beam on a small spot creates a potential well in which atoms are trapped.

In our case, we realize the traps using laser light at 532 nm. To transform a single beam into an array of traps, we use an acousto-optic deflector (AOD). The tweezer beams are then focused by an off-the-shelf microscope objective[1] that is designed to work through the 3.5 mm glass wall of the cell. This microscope has a relatively high numerical aperture $\eta = 0.5$, and therefore, focuses light on very small spots, with typical dimensions of a few hundreds of nanometers. This is illustrated on Figure 4.1. The resulting intensity at the focal point of the microscope is high, making it possible to create traps hundreds of microkelvin deep with only a few milliwatts of power.

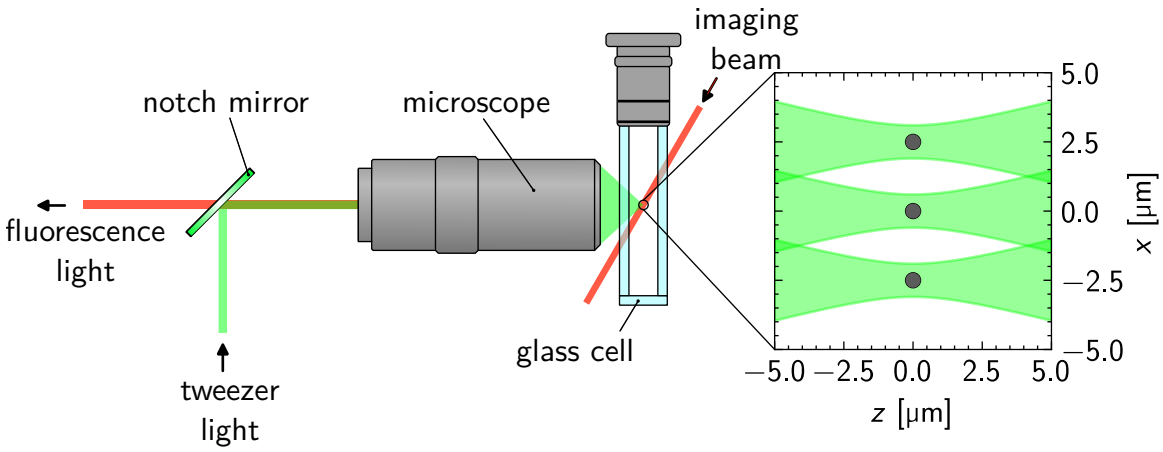

Figure 4.1. – Simplified illustration of the setup used to create optical tweezers and to image the atoms. The tweezer light is reflected by the notched mirror, before entering the microscope objective to create the traps in the glass cell. The atoms scatter light from the imaging beam at 626 nm and this light is collected by the microscope objective and goes through the notched mirror to be imaged. Inset on the right shows typical dimensions of the tweezers. Each tweezer has a waist of about 500 nm with a typical spacing of 2.5 µm.

To image the trapped atoms, we shine near-resonant light at 626 nm on them. The photons scattered are collected by the same microscope objective used to create the tweezers and are collected on a camera. A notch mirror[2] that reflects only light at 532 nm and transmits all other wavelengths is placed just before the microscope to

[1] Mitutoyo G Plan Apo 50x
[2] Semrock NFD01-532-25X36

separate the tweezer light from the fluorescence light. In the next sections, I will give more details on the optics used to generate the tweezer light and to image the atoms.

4.2 Tweezer optics

First, I will discuss the optical components used to generate the tweezers. The full tweezer path is shown in Figure 4.2. The 532 nm light is produced by a Verdi G laser system on a separate optical table. It is brought near the experiment using a high-power optical fiber[3] with about 1 W of light at the output. After a half waveplate (HWP) and a polarizing beam splitter (PBS) to clean the polarization, the beam goes through a zoom system[4] to expand its waist to $w_{\mathrm{AOD}} = 1.6\,\mathrm{mm}$.

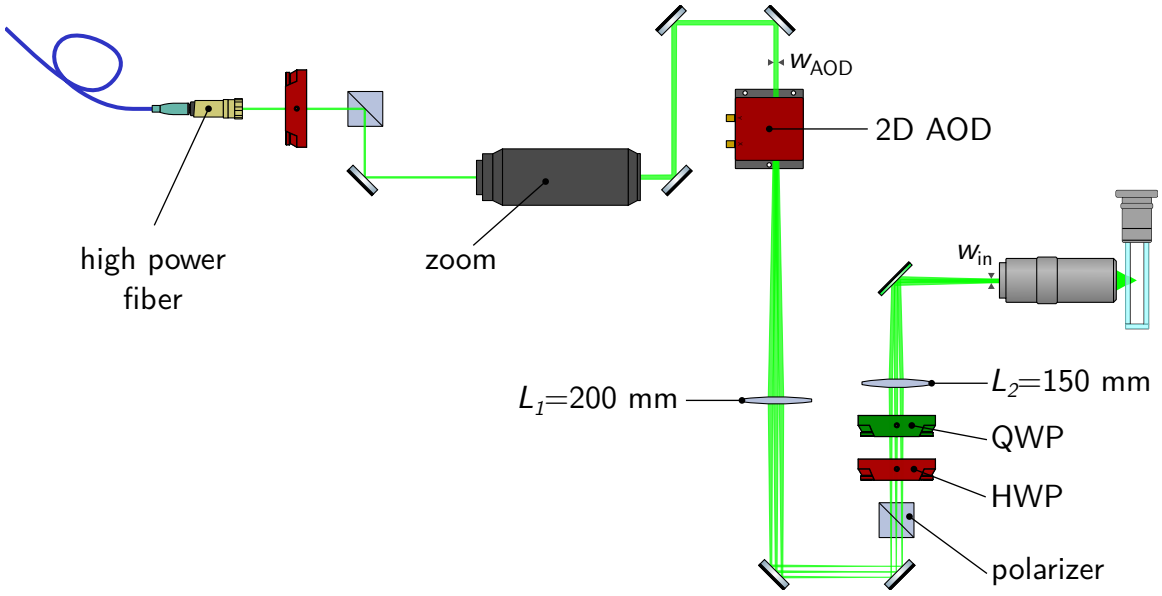

Figure 4.2. – Optical setup to create optical tweezers. The beam coming out of a high power fiber is expanded before going into the 2D AOD that creates the tweezers. The AOD is conjugated with the input aperture of the microscope objective using a telescope. Also present in the figure are polarization optics used to clean up and control the tweezer's polarization. Three beams are plotted at the output of the AOD, corresponding to one trap centered on the optical axis and two traps with the largest off-axis distance of 100 µm.

[3] NKT Photonics aeroGUIDE POWER
[4] Altechna VBE-1X-4X-0515-0532-B

4.2.1 Acousto-optic deflector

The beam then goes through a two-dimensional acousto-optic deflector[5] (2D AOD). The 2D AOD is made of two orthogonal crystals, one after the other. On each crystal, a piezoelectric transducer is glued. When the transducer is driven by an RF signal, it creates a traveling pressure wave in the crystal. The light then diffracts and is deflected by the resulting density grating inside the crystal.

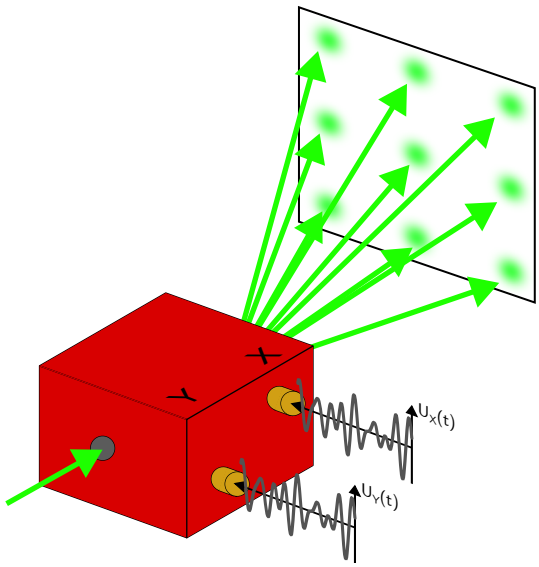

Figure 4.3. – Illustration of the working principle of the AOD. By driving the AOD with a multi-tone RF signal, it is possible to create grids of traps.

If the crystal is driven at frequency $\nu \simeq 100\,\mathrm{MHz}$, the light in the first diffraction order is deflected by an angle $\theta = \lambda\nu/v$, where λ is the wavelength of the light and $v = 650\,\mathrm{m\,s^{-1}}$ is the speed of sound in the crystal [BW99]. Changing the frequency ν of the signal thus steers the angle of the diffracted beam. In addition, when using a multi-tone RF signal containing several frequencies, it is possible to create an array of diffracted beams, where each frequency component corresponds to a different tweezer. After the beam is split in a horizontal array by the first crystal, it is split again in the vertical direction by the second crystal. One can thus create a grid of traps, with controllable spacing between rows and columns. This is illustrated in Figure 4.3. More information on how the RF signal is generated is given in Chapter 8, and also in Appendix C. It is worth noting that in addition to a direction change, the diffracted light also experiences a frequency shift equal to the frequency of the RF signal. In most cases, this has no effect on the atoms since the light is far-detuned from atomic

[5] AA Opto-electronic DTSXY-400-532-002

transitions.

The AOD is conjugated with the microscope objective using a telescope made of two lenses $L_1 = 200\,\text{mm}$ and $L_2 = 150\,\text{mm}$ with magnification $G = L_2/L_1 = 3/4$. There are two different ways to conjugate the AOD with the microscope, either with *pupil conjugation* or with *back focal plane conjugation*. In the first case, the beams from different tweezers all cross on the input pupil of the microscope, to make use of its full numerical aperture. This is illustrated in Figure 4.4 a. In the second case, the beams cross before the microscope, at a distance given by its effective focal length $f = 4\,\text{mm}$. In this case, the numerical aperture of the microscope is not fully used, but the tweezers all come out parallel at the output of the microscope, as illustrated in Figure 4.4 b.

It is worth noting that there is a separation of 2 cm between the two rotation axes along X and Y of the AOD. Because this distance is larger than the effective focal length of the microscope, it is not possible to correctly conjugate both axes with the microscope. For our current setup, we use pupil conjugation for the X axis of the AOD.

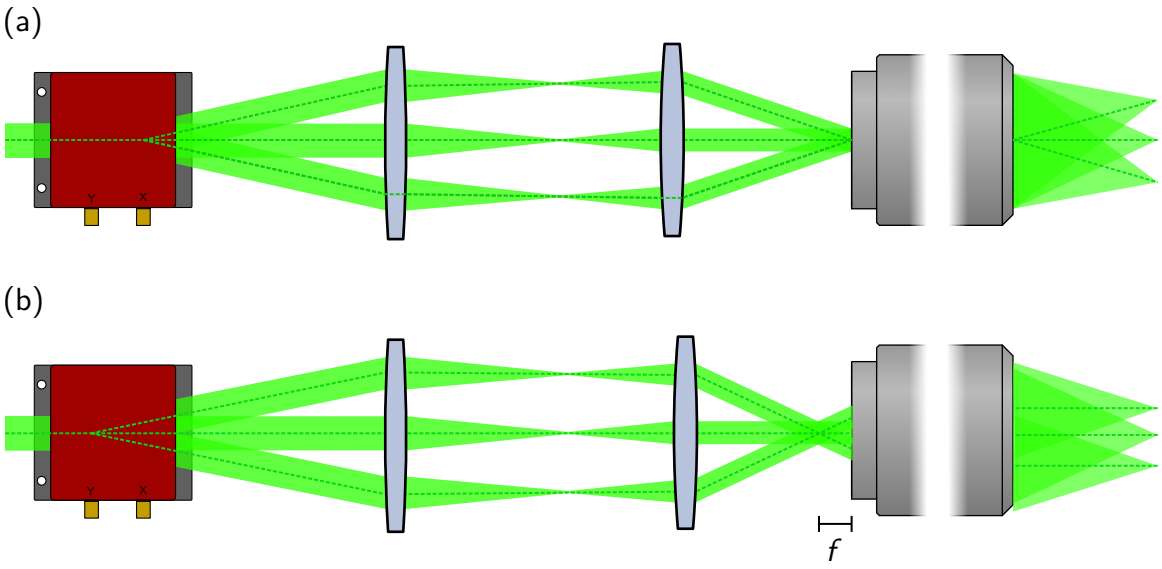

Figure 4.4. – (a) Illustration of the conjugation of the X axis of the AOD with the input pupil of the microscope. The tweezers come out of the microscope with different optical axes. (b) Illustration of the conjugation of the Y axis of the AOD with the back focal plane of the microscope. The tweezers come out of the microscope parallel. The angles are exaggerated for clarity.

The angular range of the AOD $\Delta\theta = \lambda\Delta\nu/v$ is limited by its RF bandwidth $\Delta\nu = 50\,\text{MHz}$. This eventually limits the maximum size of the arrays that can be

created. This size is given by:

$$D = f\lambda\Delta\nu/Gv \tag{4.2}$$

In our case $D = 200\,\mu\text{m}$. Also, the AOD cannot resolve infinitely small angles. This is because the diffracted gaussian beam with waist w_{AOD} already has a non-zero angular spread $\delta\theta = \lambda/\pi w_{\text{AOD}}$. Because of this, the number of traps that can be resolved by the AOD is at most $\Delta\theta/\delta\theta \approx 200$ in each direction, but this is enough for our purposes.

4.2.2 Choice of parameters

Given the constraints of the microscope and the AOD, there are two free parameters to choose when designing the optical system: the waist w_{AOD} of the beam inside the AOD and the scaling factor of the telescope G. On theone hand, w_{AOD} should be small enough to avoid clipping on the AOD aperture, but it should be large enough to not reduce the angular resolution of the AOD. On the other hand, the waist at the input of the microscope $w_{\text{in}} = G \times w_{\text{AOD}}$ should be comparable to the radius of the microscope input pupil $R = 2\,\text{mm}$. If w_{in} is much larger than R, a large fraction of the input power P_{in} is lost by clipping on the aperture. However, if w_{in} is much smaller than R, we do not make use of the full numerical aperture of the objective and the tweezers are not as focused as they could be. To quantify the influence of the input waist on the tweezer shape, in Appendix B, I calculate the peak intensity I_0 at the bottom of the trap using paraxial optics [BW99]. Ideally, one wants to maximize this intensity since it is directly proportional to the trap depth. Similarly, the intensity curvatures, both in the radial and axial direction $\partial_\perp^2 I$ and $\partial_\parallel^2 I$, characterize the confinement strength of the trap, and should be maximized. The values of these parameters depend strongly on the beam waist at the input of the microscope as plotted in Figure 4.5.

They indicate that the ideal waist should be the same size as the radius of the microscope input. For the values of w_{AOD} and G quoted above, we have $w_{\text{in}} = 1.2\,\text{mm} = 0.6R$. As such, it seems that a larger value for w_{in} would be beneficial, as we could get deeper traps for the same input laser power. This could be obtained by increasing either the waist w_{AOD} of the beam before the AOD or the magnification G of the telescope. However, another point to consider is that the largest array size D is inversely proportional to G according to Equation 4.2. Increasing G to have a larger waist on the microscope would thus be detrimental since it reduces the extent of the arrays that we can create. In retrospect, it might have been better to use a

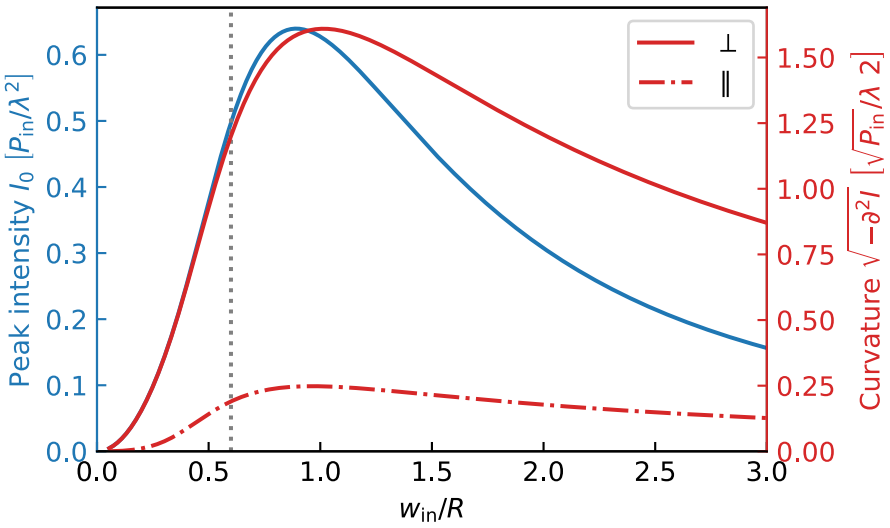

Figure 4.5. – Intensity and curvature of the intensity profile at the bottom of a trap as a function of the input waist on the microscope. These curves are obtained for a microscope objective with numerical aperture $\eta = 0.5$. The vertical-dashed line indicates the current waist used in the experiment.

larger waist w_{AOD} inside the AOD, even at the cost of small clipping losses on the AOD aperture.

4.2.3 Polarization control

As will be explained in more detail in the next part, the polarization of the tweezers strongly influences the performance of the imaging scheme due to the anisotropic polarizability of Dy. It is thus crucial to have good control over the polarization of the trapping light.

For this reason, we placed a Glan-Thompson polarizer after the AOD to ensure that all the beams have the same well-defined polarization. After the polarizer, the beam goes through a half-wave plate and a quarter-wave plate. These wave plates are mounted on motorized rotation stages[6] to be able to rotate them remotely and with good repeatability, below a fraction of a degree. With the two degrees of freedom of the wave plates, one can create any polarization state at the input of the microscope.

These polarization elements are placed as close as possible to the microscope, since any intermediate optics could change the polarization. The only element before the microscope that could change the polarization is the notched mirror on which the

[6] Thorlabs ELL14

tweezer light is reflected. We measured the polarization change induced by the notched mirror and found that it was negligible for our purposes[7].

Another effect to consider is the modification of the polarization by the high numerical aperture microscope. It can be shown that the breakdown of the paraxial approximation can lead to small gradients in the longitudinal component of the polarization *across a single tweezer* [RWG97]. We did not observe any influence of such effect for the experiments presented in this thesis, but it could be an issue for future work, as the effect can couple the internal and motional degrees of freedom of the atom [Tho+13].

However, we observe another issue coming from our choice to use input pupil conjugation between the AOD and the microscope as explained above. In this configuration, the tweezers coming out of the microscope make an angle with the optical axis proportional to their distance from the axis, as illustrated on Figure 4.4 a. Since the polarization of a tweezer is perpendicular to its direction of propagation, this causes a small gradient of polarization across the tweezers that can induce inhomogeneity in the array [Bia+25]. This effect can probably be removed when using back focal plane conjugation, as in that case, the tweezers all come out parallel of the objective, as shown on Figure 4.4 b.

4.3 Imaging setup

To image the atoms, we built the setup in Figure 4.6 a. When shining near-resonant 626 nm light on the atoms, they re-scatter photons in random directions. This fluorescence light is collected by the microscope objective, goes through the notched mirror, and is imaged on a camera to obtain pictures of the atoms in the tweezers, such as the ones shown in Figure 4.6 b and Figure 4.6 c.

In all the experiments presented in this thesis, we exclusively used the transition at 626 nm to image the atoms. But, since the notched mirror transmits all light besides 532 nm, it is in principle possible to use other transitions to image the atoms. One could for example use the broad transition at 421 nm to take pictures of the atoms in a few microseconds, as has been demonstrated for erbium atoms [Su+25; Grü+24].

[7] This is not necessarily true for other dichroic mirrors, as they can in general introduce a dephasing between the S and P components of the reflected polarization.

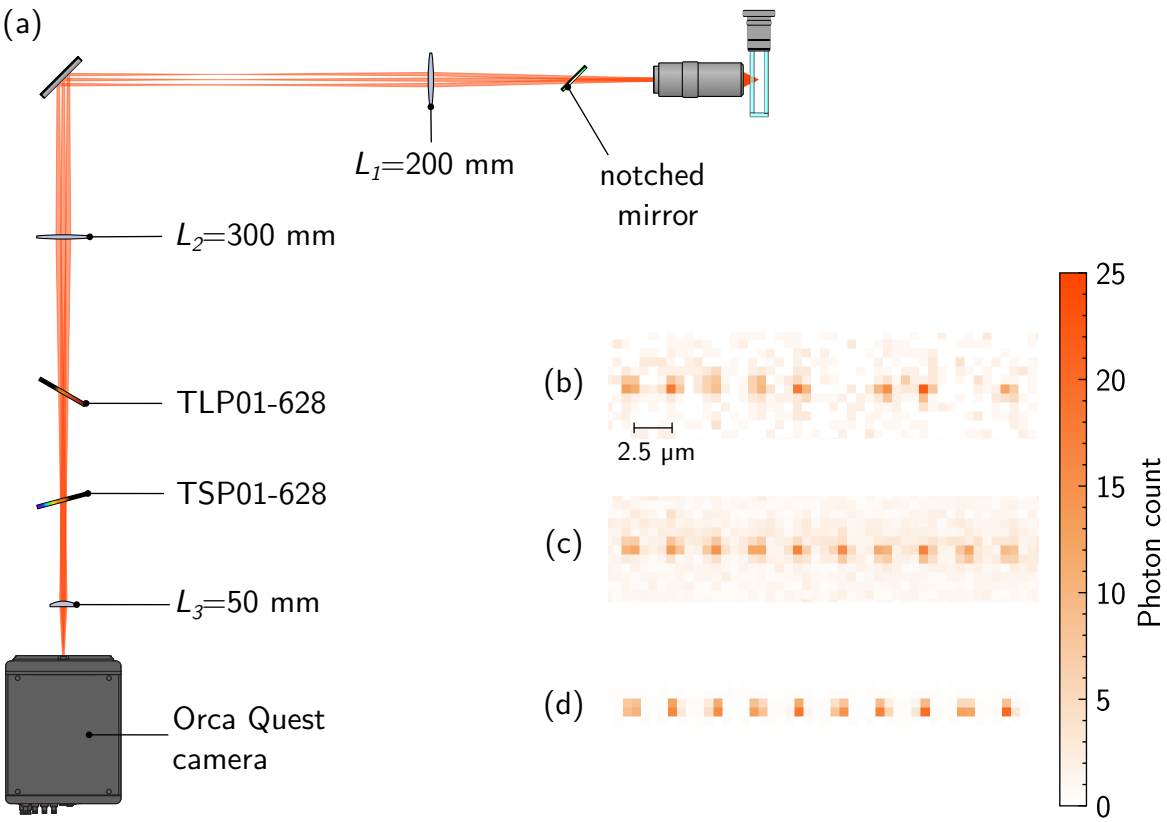

Figure 4.6. – (a) Optical setup to collect fluorescence light from the atoms. The fluorescence beam path is shown for three traps, one centered on the optical axis, and two corresponding to tweezers that are 100 µm off-axis. (b) Single shot picture of the atoms in the traps. The scale in the figure represents the physical distance between atoms and not the distance on the camera sensor. (c) Average imaging of the atoms in the traps. (d) Simulated image of the point spread function of the atoms on the camera.

4.3.1 Microscope objective

The first element in the imaging path is the microscope objective whose goal in this case is to collect as much light as possible from the atoms without introducing aberrations. Our commercial microscope is guaranteed to be diffraction limited as long as it is well aligned to the glass cell. To ensure a correct alignment of the microscope, we first retro-reflected a laser beam on the glass cell. This beam is then used as a reference for the microscope objective mount. More details on the alignment procedure can be found in [Hof22].

An important point to consider is the collection efficiency of the microscope that increases with the numerical aperture η of the objective. To estimate this parameter, one also needs to know the angular distribution of the light scattered by the atoms.

This distribution is not necessarily isotropic but depends on the direction of oscillation of the atomic dipole. In our case, the imaging light drives the transition between the states $|G, m_J = -8\rangle$ and $|E_{626}, m_J = -9\rangle$ for a quantization axis pointing along the direction of the optical axis of the microscope. As a result, the atomic dipole oscillates circularly in the plane perpendicular to the objective. The light is thus preferentially emitted in the two directions aligned with the microscope, with an angular intensity dependency [Ste12]:

$$D(\theta, \phi) = \frac{3}{16\pi}\left(1 + \cos^2\theta\right) \tag{4.3}$$

where θ and ϕ are respectively the polar and azimuthal angles in spherical coordinates aligned with the microscope axis, as shown in Figure 4.7 b. This configuration

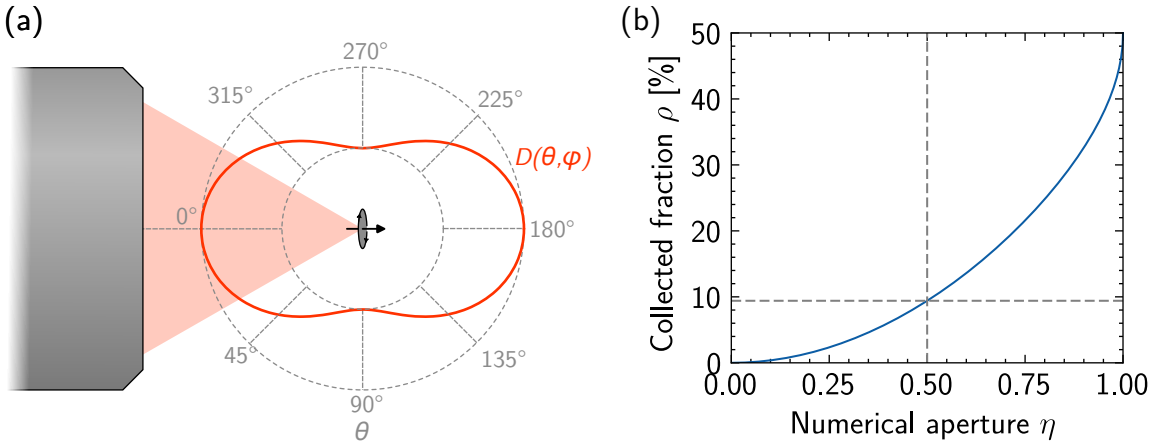

Figure 4.7. – (a) Radiation pattern of a circular atomic dipole. Only the light emitted in the colored area is collected by the microscope. (b) Fraction of collected light as a function of the numerical aperture of the microscope. Dashed lines indicate the values for our current microscope objective.

is particularly favorable for imaging, as most of the light is directed towards the microscope, as opposed for example with a quantization axis perpendicular to the optical axis of the microscope, for which only about half of the light would be collected. The fraction of light collected is:

$$\int_0^{2\pi}\int_0^{\arcsin(\eta)} D(\theta, \phi)\sin\theta \mathrm{d}\theta\mathrm{d}\phi = \frac{1}{2} + \sqrt{1-\eta^2}\left(\frac{\eta^2}{8} - \frac{1}{2}\right) \tag{4.4}$$

In our case with a numerical aperture of $\eta = 0.5$, this corresponds to a collection efficiency of about 10 %, as shown in Figure 4.7 b.

4.3.2 Magnification optics

The fluorescence light coming out of the objective is transmitted by the notched mirror and then goes through a magnification system. As illustrated on Figure 4.6 a, this is a telescope made of two lenses $L_1 = 200\,\text{mm}$ and $L_2 = 300\,\text{mm}$ that rescales the aperture of the microscope with radius $R = 2\,\text{mm}$ by a scaling factor $G = L_2/L_1 = 1.5$. This telescope conjugates the output aperture of the microscope with the object plane of the last lens $L_3 = 50\,\text{mm}$ that focuses the light on the camera. This way, the plane of the atoms is conjugated with the camera plane, with an overall magnification $f_3/fG = 8.3$.

The intensity spot that a point-like atom creates on the camera is commonly called the *point spread function* (PSF) of the imaging system. In the paraxial approximation, the intensity profile on the camera is an Airy disk (see Appendix B):

$$I(r) = I_0 \left(\frac{2J_1(ar)}{ar} \right)^2 \tag{4.5}$$

where J_1 is the first order Bessel function of the first kind. The diameter of this spot is $7.66a = 6.3\,\mu\text{m}$ with $a = f_3/kGR$.

We chose the parameters f_3 and G such that the spot size of an atom on the camera is comparable to the pixel size of $4.6\,\mu\text{m}$. We want to avoid spreading the light of an atom over too many pixels, since the readout noise increases with the number of pixels. Making the spot size much smaller than a pixel would make it difficult to separate the light of two neighboring atoms, which is why we choose this magnification.

A simulated image of the atoms using Equation 4.5 for the PSF is shown in Figure 4.6 d. As can be seen, the measured spot size on Figure 4.6 c is ever so slightly larger than expected, and seems to present a halo around the traps. This could be due to several experimental imperfections, such as aberrations in the optical setup, vibrations of the camera between acquisitions, or the presence of atoms outside the imaging plane. It is also worth noting that the apparent size of the PSF varies from site to site, depending on the position of the traps with respect to pixel boundaries. It could be advantageous in future work to tweak the positions of the traps such that the spots are always centered on a pixel.

The discussion above using paraxial optics does not include the effect from the size of the optics. However, this can significantly influence the quality of the images, and one needs to use lenses with the correct size. In a first version of the setup, we used lenses with a one-inch diameter for L_1 and L_2. This is not an issue when imaging traps that lie on the optical axis because the microscope aperture is anyway much smaller than the lenses. It becomes problematic when imaging off-axis traps, as the light of these traps comes out of the microscope with a significant angle with respect to the optical axis as shown in Figure 4.6 a. In our case, the light of the off-axis traps was clipped by the lenses, reducing the effective field of view of the imaging system.

4.3.3 Camera and sources of noise

The camera used to image the atoms is a critical element of the setup as it needs to detect the few photons scattered by a single atom. The camera we use is the qCMOS Hamamatsu Orca Quest. Compared to EMCCD cameras, it has a fast readout speed that lets us take consecutive pictures with a delay of only a few milliseconds[8]. One of its other advantages is its large quantum efficiency in the visible range, about 80 % at 421 nm and 65 % at 626 nm, which is particularly suitable for Dy.

Another specificity is its ability to take images in *photon-resolving mode*. Indeed, this camera has a very low readout noise of about 0.27 photon-electron per pixel, even for large photon counts. This is small enough that it is possible to count the number of photons in each pixel of the camera with small error rate. For us, this translates to negligible readout noise, and the fluctuation in the number of photons collected in each pixel is only due to the shot noise. The probability to detect a given number of photons n in a pixel then follows a Poisson distribution and only depends on the average number of photons $\mu = \langle n \rangle$:

$$P_p(n|\mu) = \frac{\mu^n}{n!} e^{-\mu} \tag{4.6}$$

The standard deviation of the number of photons detected in a pixel is $\sqrt{\mu}$, meaning that the signal-to-noise ratio goes down with the number of photons detected.

[8] The exact duration between two pictures depends on several factors, such as the size of the sensor area being read and the noise level.

One would ideally collect as many photons per atom as possible, but as will be explained in more detail in the next chapters, we can only collect a few tens of photons per atom without losing it. In this situation, it is particularly important to identify and minimize any source of background light that reaches the camera.

One possible source of background light is the scattering of the imaging beam into the microscope objective. This becomes increasingly difficult to avoid for large numerical aperture microscopes, since the available optical access is reduced. To avoid this, we do not use the MOT beams to image the atoms in the tweezers, but instead use a single dedicated imaging beam. This beam is angled and not retro-reflected such that no reflection on the glass cell can enter the microscope.

For us, the main source of background light is actually the fluorescence of the glass elements making up the microscope. Indeed, when shinning several hundreds of milliwatts of light at 532 nm on the microscope, the glass elements absorb a fraction of the light and re-emit it by fluorescence at longer wavelengths. In particular, there is some background light at our imaging wavelength of 626 nm[9]. For a total power in the microscope of 300 mW at 532 nm, we measure about 50 background photons per pixel on the camera.

To reduce this issue, we put two tunable dichroic filters[10] in front of the camera. The cutoff wavelength of these filters can be tuned by changing their angle, and we set them up to only transmit light centered on 626 nm. This reduces strongly the background light we measure, to about 0.7 photons per pixel in similar conditions, but still, it does not remove it completely. Since we sum the fluorescence of 10 pixels around each trap, we typically have an offset photon count of about 7 photons. This reduces a bit the imaging fidelity that we can reach, but we are still able to image atoms in the traps. It was not a significant limitation for the experiments we performed.

Summary

In this chapter, I have presented the optical tweezers setup we built to trap and image Dy atoms. Most of the components used here, such as the AOD, the microscope, or the camera, are now standard elements for such experiments and are not specific to Dy. One mostly has to adapt the parameters of the optical elements to the specific requirements of the experiment. Thanks to the relative simplicity of this kind of setup, it was possible to build it in a short time. The more challenging aspect came from

[9] When imaging with a wavelength shorter than the trapping wavelength this issue can be avoided.
[10] Semrock TLP01-628 and TSP01-628

understanding the physics of Dy atoms in optical tweezers to image single atoms with high fidelity. I will discuss this in the next chapters.

Part II.

Dysprosium atoms in optical tweezers

Chapter 5

Anisotropic light shift

Contents

After the tweezer setup was built, we were ready to try imaging atoms in the tweezers. While it is relatively easy to trap atoms, it was initially difficult to image them, as they scattered very few photons before being lost. We assumed that the atoms were heated up by the imaging light, whether we used the 421 nm or 626 nm light. To be able to collect enough photons, we had to understand the effect of the light on the trapped atoms and see if it was possible to find a way to cool the atoms during the imaging.

We decided to focus on the 626 nm transition, since thanks to its narrow linewidth, it should be possible to reach lower temperature than with the 421 nm transition. However, the energy shift of the tweezer light on the atomic levels can be larger than the linewidth of this transition, so we had to characterize it. In particular, for Dy, the effect of the trapping light is expected to be anisotropic, with a strong dependency on the the light polarization and the angular momentum of the atom [LWD14; Bec+18; Cha+18; Kre+21].

In this chapter, I will start by showing the formalism used to describe this interaction, and then I will present the measurements we performed to characterize it. Most of the discussion presented here can also be found in [Blo+24].

5.1 Light shift hamiltonian

5.1.1 Expression

Within the dipole approximation, the interaction between an atom and the classical electric field of the trapping light $\boldsymbol{E}(t) = \mathrm{Re}\{\boldsymbol{E_0} e^{-i\omega t}\}$ is described by the hamiltonian:

$$\hat{H}_d(t) = -\hat{\boldsymbol{d}} \cdot \boldsymbol{E}(t) \tag{5.1}$$

where $\hat{\boldsymbol{d}}$ is the atomic dipole operator coupling ground and excited states. When the driving frequency ω if far from any transition, the dipole hamiltonian can be treated as a perturbation, and one can use perturbation theory to estimate the energy shift of the levels.

For Dy, its large electronic angular momentum and the large number of states in each fine structure manifold make the situation more complex than an idealized two-level atom. Indeed, each level is actually a manifold M with angular momentum J_M containing $2J_M + 1$ states, degenerated in the absence of external magnetic or electric fields. These states can be labeled $|M, m\rangle$ where m is an integer between $-J_M$ and $+J_M$ representing the projection of the angular momentum along an arbitrary quantization axis. These states form one possible basis of the considered manifold, but they are not necessarily appropriate to the symmetries of the perturbating hamiltonian. Because of this, the states $|M, m\rangle$ can mix strongly even for infinitesimally small laser field, if nothing else breaks the degeneracy. Instead of simply computing an energy shift, it is necessary to take this into account by computing a perturbative light-shift hamiltonian $\hat{H}_{ls}$ inside each manifold. At second order of perturbation theory, it is given by [Ste12]:

$$\langle M, m_1|\hat{H}_{ls}|M, m_2\rangle = \sum_{\substack{N\neq M \\ -J_N\leq n\leq +J_N}} \left[\left(\frac{1}{\hbar(\Delta\omega_{M,N} + \omega)} + \frac{1}{\hbar(\Delta\omega_{M,N} - \omega)}\right) \langle M, m_1|\hat{\boldsymbol{d}} \cdot \boldsymbol{E_0}|N, n\rangle \ \langle N, n|\hat{\boldsymbol{d}} \cdot \boldsymbol{E_0^*}|M, m_2\rangle\right] \tag{5.2}$$

where the sum covers the other fine structure manifolds N with $2J_N + 1$ angular momentum states $|N, n\rangle$.

Equation 5.2 gives us in principle the desired result since by diagonalizing $\hat{H}_{ls}$, one

can link the intensity and polarization of the applied electric field to the energy shift of the states $|M, m\rangle$. However, it is not necessarily the most tractable form to work with, as it does not make explicit the overall rotational symmetry of the system. Instead, $\hat{H}_{ls}$ is usually rewritten using the Wigner-Eckart theorem. It allows us to rewrite the angular dependency of the dipole matrix element as such:

$$\langle M, m|\hat{\boldsymbol{d}} \cdot \boldsymbol{E_0}|N, n\rangle = \frac{\langle M||d||N\rangle}{\sqrt{2J_M + 1}} \sum_q \boldsymbol{e}_q^* \cdot \boldsymbol{E_0} \, \langle J_N \, n \, ; 1 \, q \, | \, J_M \, m\rangle \tag{5.3}$$

where $\langle M||d||N\rangle$ is the *reduced dipole matrix element* and $\boldsymbol{e}_q$ are the spherical basis vectors: $\boldsymbol{e}_\pm = \mp(\boldsymbol{e}_x \pm i\boldsymbol{e}_y)/\sqrt{2}$ and $\boldsymbol{e}_0 = \boldsymbol{e}_z$. The reduced dipole matrix element is an intrinsic value to the transition $M \leftrightarrow N$ and is independent of the light polarization and the m and n numbers. It can in principle be calculated by an integral over the electronic wavefunctions and is related to the spontaneous decay rate $\Gamma_{M,N}$ from the higher state to the lower state by:

$$|\langle M||d||N\rangle|^2 = \frac{3\pi\epsilon_0\hbar c^3}{\Delta\omega_{M,N}^3}(2J_N + 1)\Gamma_{M,N} \tag{5.4}$$

With a bit of effort, one can rewrite the light-shift hamiltonian as the sum of three irreducible terms: a *scalar* part, a *vectorial* part and a *tensorial* part [LSR13; CD72].

$$\hat{H}_L = \hat{H}_S + \hat{H}_V + \hat{H}_T \tag{5.5}$$

When introducing the light intensity $I = c\epsilon_0|\boldsymbol{E_0}|^2/2$ and the complex polarization $\boldsymbol{\epsilon} = \boldsymbol{E}_0/||\boldsymbol{E}_0||$, the three parts are:

$$\hat{H}_S = -\alpha_S \frac{I}{2c\epsilon_0} \tag{5.6}$$

$$\hat{H}_V = -\alpha_V \frac{I}{2c\epsilon_0} i\,(\boldsymbol{\epsilon}^* \times \boldsymbol{\epsilon}) \cdot \frac{\hat{\boldsymbol{J}}}{2J} \tag{5.7}$$

$$\hat{H}_T = -\alpha_T \frac{I}{2c\epsilon_0} \frac{3\{\boldsymbol{\epsilon} \cdot \hat{\boldsymbol{J}}, \boldsymbol{\epsilon}^* \cdot \hat{\boldsymbol{J}}\} - 2\hat{\boldsymbol{J}}^2}{2J(2J-1)} \tag{5.8}$$

where $\hat{\boldsymbol{J}}$ is the atomic spin operator inside the manifold M[1]and $\{\hat{A}, \hat{B}\} = \hat{A}\hat{B} + \hat{B}\hat{A}$ is the anti-commutator between two operators $\hat{A}$ and $\hat{B}$.

The three values α_S, α_V and α_T do not depend on the laser light or the Zeeman state of the atom, but instead are intrinsic constants for the considered manifold.

[1] I will drop the index M when focusing on a single manifold to simplify the notation.

They are respectively called the scalar, vector and tensor polarizability, and are given by:

$$\alpha_S = \frac{2}{3(2J_M+1)} \sum_{N \neq M} \frac{\Delta\omega_{M,N} |\langle M||d||N\rangle|^2}{\hbar(\Delta\omega_{M,N}^2 - \omega^2)} \tag{5.9}$$

$$\alpha_V = \sqrt{\frac{6J_M}{(J_M+1)(2J_M+1)}} \sum_{N \neq M} (-1)^{J_M+J_N+1} \begin{Bmatrix} 1 & 1 & 1 \\ J_M & J_M & J_N \end{Bmatrix} \frac{\Delta\omega_{M,N} |\langle M||d||N\rangle|^2}{\hbar(\Delta\omega_{M,N}^2 - \omega^2)} \tag{5.10}$$

$$\alpha_T = \sqrt{\frac{40J_M(2J_M-1)}{3(J_M+1)(2J_M+1)(2J_M+3)}} \sum_{N \neq M} (-1)^{J_M+J_N} \begin{Bmatrix} 1 & 1 & 2 \\ J_M & J_M & J_N \end{Bmatrix} \frac{\Delta\omega_{M,N} |\langle M||d||N\rangle|^2}{\hbar(\Delta\omega_{M,N}^2 - \omega^2)} \tag{5.11}$$

where the terms in brackets are Wigner-6j symbols.

This way of writing the light shift hamiltonian helps to understand its influence on the different angular momentum levels $|m\rangle$. For instance, the scalar part is fully isotropic: it has no dependency on the light polarization, nor on the m number.

The vector hamiltonian, however, depends on the polarization through $\boldsymbol{u} = i(\boldsymbol{\epsilon}^* \times \boldsymbol{\epsilon})$. This term is non-zero only if the polarization has some elliptical component, and cancels out for linearly polarized light. The eigenvectors of the vector hamiltonian are the angular momentum states with a quantification axis $\boldsymbol{u}$. They have energies proportional to m.

The tensor component also has a dependency on the polarization of the light through the anti-commutator $\{\boldsymbol{\epsilon} \cdot \hat{\boldsymbol{J}}, \boldsymbol{\epsilon}^* \cdot \hat{\boldsymbol{J}}\}$. When the polarization is linear, it is diagonal in the angular momentum basis defined by the polarization, and its energies have a quadratic dependency on m.

To illustrate this, the typical energy shifts are plotted in Figure 5.1, both for the ground state $M = G$ and the excited state of the 626 nm transition $M = E_{626}$.

It is worth noting that the total light shift hamiltonian can only be diagonalized in an angular momentum basis in the case of purely linear or purely circular polarization. Indeed, when using trapping light with any other polarization, there is no axial symetry for the system. In this case, if one wants to find the eigenstates of $\hat{H}_{ls}$, it is typically necessary to perform numerical diagonalization.

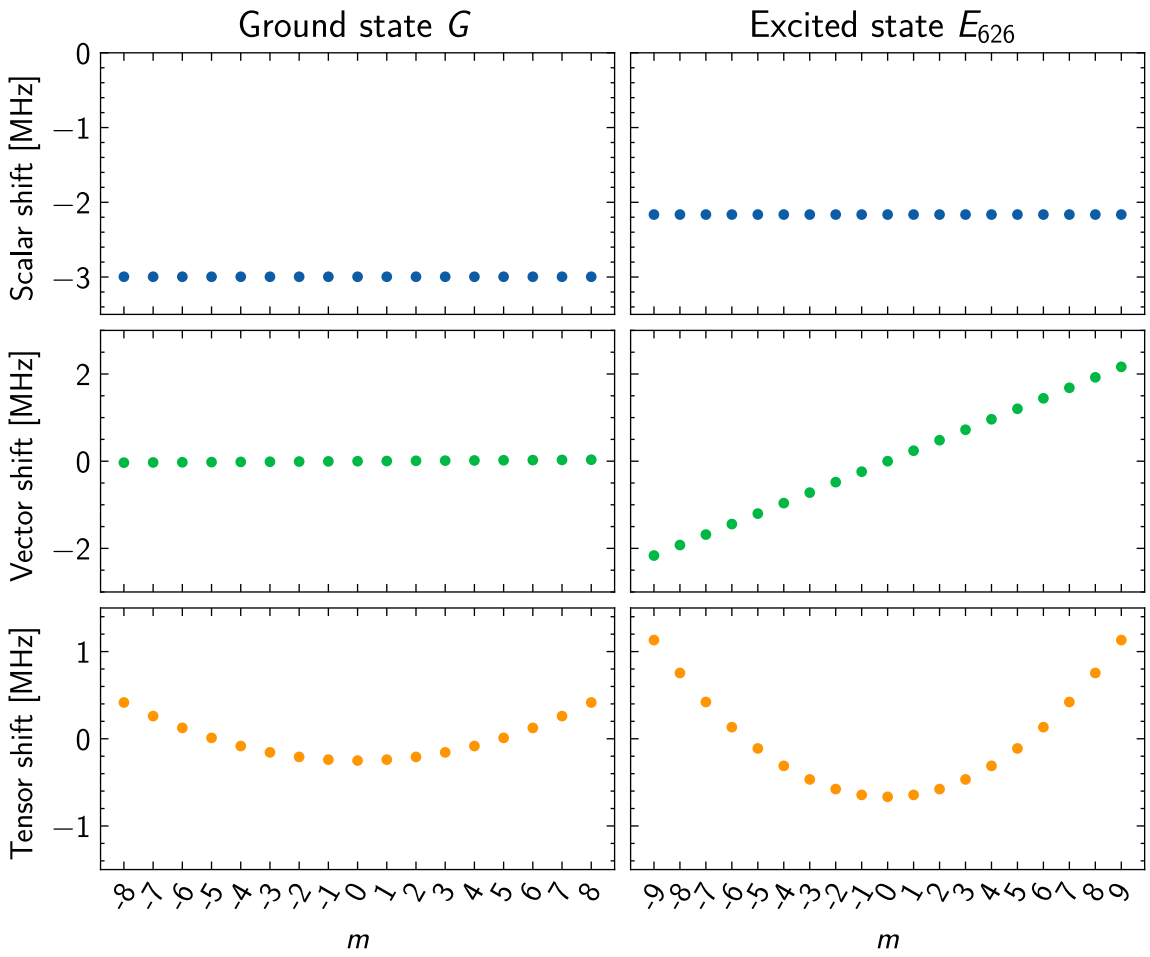

Figure 5.1. – Energy shift due to the different components of $\hat{H}_{ls}$. The left column is for the ground state manifold G while the right column is for the excited state of the intercombination line E_{626}. The first row corresponds to the scalar shift that has no dependency on m. The second row corresponds to the vector shift for a purely circular polarization. It has has a linear dependency on m. The slope is very small for the ground state as its vector polarizability is almost zero. The third row corresponds to the tensort shift for a linear polarization and has a quadratic dependency on m. The numerical values are the typical ones for Dy in an optical tweezer at 532 nm with a power of 2 mW.

5.1.2 Interaction with a magnetic field

In the presence of a magnetic field $\boldsymbol{B}$, as is the case for our experiments, it is also necessary to include the Zeeman hamiltonian:

$$\hat{H}_Z = g\mu_B \hat{\boldsymbol{J}} \cdot \boldsymbol{B} \tag{5.12}$$

where g is the Landé factor for the considered manifold. In general, this hamiltonian does not commute with the light shift hamiltonian and the eigenstates of the system depend on the angle between the magnetic field and the polarization of the light, as well as their relative intensity.

It is typically easier to work in a regime where the magnetic field is dominant with respect to the light shift. This is the case when the Zeeman splitting $g\mu_B\|\boldsymbol{B}\|$ is significantly larger than the anisotropic components $\alpha_{V,T}I/2c\epsilon_0$. In this case, one can assume that the eigenstates of the total hamiltonian are still to first order the Zeeman states $|m\rangle$, satisfying $\boldsymbol{b}\cdot\hat{\boldsymbol{J}}\,|m\rangle = m\,|m\rangle$, where $\boldsymbol{b} = \boldsymbol{B}/\|\boldsymbol{B}\|$ is the normalized magnetic field direction. Then the energy of the state $|m\rangle$ is linearly shifted as:

$$\Delta E \simeq \langle m|\hat{H}_{ls}|m\rangle = -\frac{\alpha_{\text{eff}}I}{2c\epsilon_0} \tag{5.13}$$

where

$$\alpha_{\text{eff}} = \alpha_S + \alpha_V\frac{m}{2J}i(\boldsymbol{\epsilon}^*\times\boldsymbol{\epsilon})\cdot\boldsymbol{b} + \alpha_T\frac{3m^2 - J(J+1)}{2J(2J-1)}\left(3\|\boldsymbol{\epsilon}\cdot\boldsymbol{b}\|^2 - 1\right) \tag{5.14}$$

One recovers a simple expression for the light shift, with the condition to use now an effective polarizability α_{eff} that depends on the state $|m\rangle$ and the light polarization.

In all the work presented in this thesis, we always apply magnetic fields between 7 G to 10 G, such that $\mu_B B/h \sim 10$ MHz. As such, we are always in a regime where the magnetic field is dominant compared to the anisotropic light shift shown in Figure 5.1, and Equation 5.13 and Equation 5.14 apply.

5.1.3 Calculating the polarizabilities

As can be seen on Figure 5.1, in optical tweezers, the magnitude of the light shift is of the order of a megahertz. This is large compared to the linewidth of the intercombination line at 626 nm of only 135 kHz. To be able to manipulate the atomic state on this transition, it is crucial to accurately quantify these shifts. This boils down to knowing the exact values of α_S, α_V and α_T. In principle, by using Equations 5.9, 5.10 and 5.11, also called the *sum-over-states* formulas, one could predict the values of the different polarizabilities *ab-initio*. Indeed, if one knows the energy of all states and the dipole matrix elements between them, the exact values of the polarizabilities can be computed by summing the contribution of each state. For simple atoms with only a few excited states, like alkali or alkali-earth species, this approach is tractable.

However, for Dy with its large number of excited states, this method is significantly more challenging. One needs to catalog the several dozens of states that play a role and then compute their coupling to the ground state. This requires a good understanding of the structure of the excited states of Dy, and is a work for experts [Cha+18; Li+16].

In Figure 5.2, I just show the result of such calculation performed by Maxence Lepers. In this plot, the polarizabilities of the ground state and the excited state of the 626 nm transition around 532 nm are plotted. As one can see, there are several poles for the polarizabilities, corresponding to the many transitions that exist near this wavelength. The width of the transitions is not necessarily well-known, in particular if they have not yet been observed. The uncertainty on their width quickly adds up, and as a result, there are large error bars on the predicted polarizability values. This makes it impossible to rely solely on these predictions, as some experimental quantities depend finely on the exact values. This issue is less problematic when using trapping wavelengths in the infrared, since there are fewer transitions nearby that can contribute to the polarizability [Rav+18].

5.2 Measurement

Since we expect the anisotropic polarizabilities to have a significant impact when sending near resonant light on the narrow 626 nm transition, we decided to measure them at our wavelength of interest of 532.208 nm. To do so, the general idea is to find an observable that can be related to the effective polarizability. Then by measuring how this observable changes for different polarizations of the trap light and magnetic field, it is possible to extract the irreducible components of the polarizability.

5.2.1 Ground state polarizabilities

Trap frequencies

A possible observable to measure the ground state polarizabilities is the oscillation frequency of the atoms in the dipole trap. If the trap is approximated by a harmonic potential:

$$U(\boldsymbol{r}) = -U_0 + \sum_{\mu=x,y,z} \frac{1}{2} m\omega_\mu^2 r_\mu^2 \tag{5.15}$$

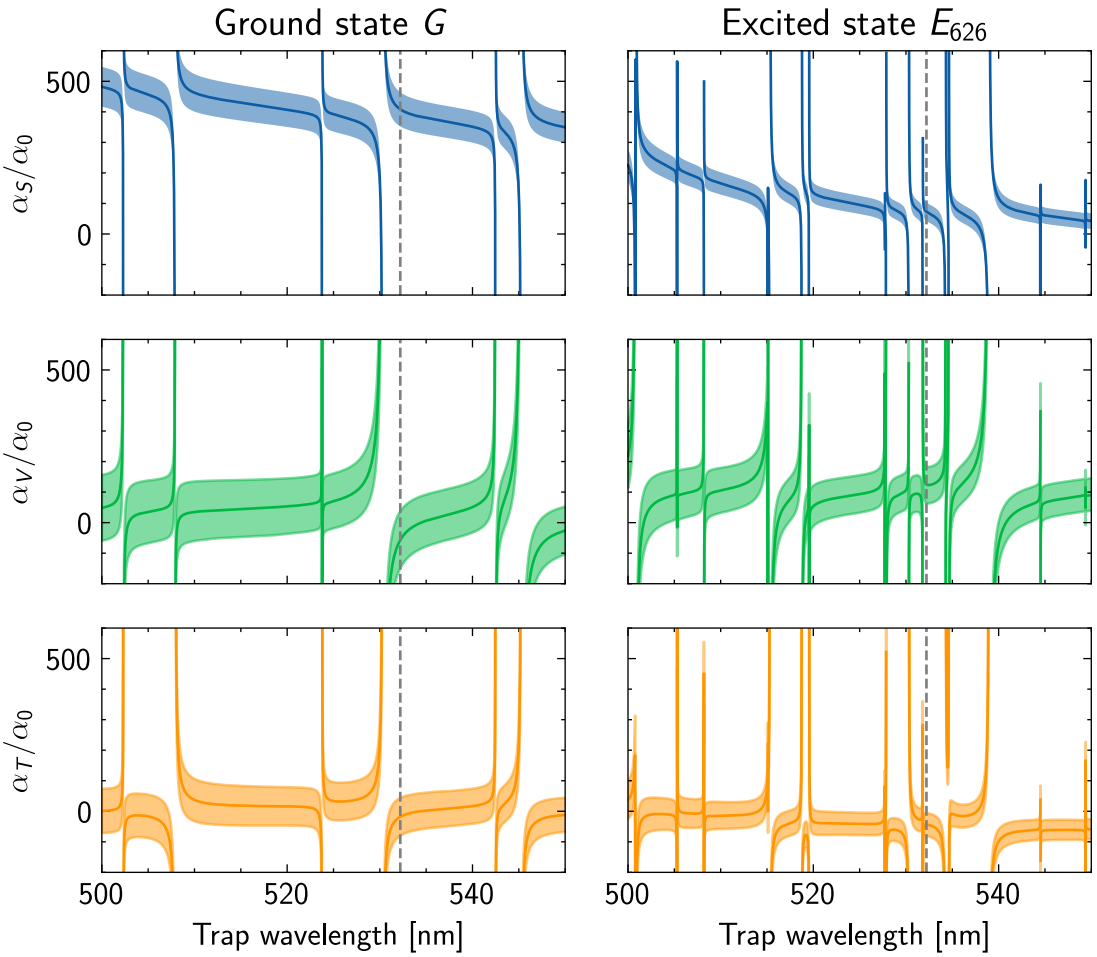

Figure 5.2. – Predicted polarizabilities of the ground and excited states of Dy. Curves with their error bars are theoretical predictions obtained by the sum-over-states formula. These values are provided by Maxence Lepers [Blo+24]. The dashed line indicates our working wavelength 532.208 nm.

then the trap depth and trap frequencies depend on the effective polarizability as:

$$U_0 = \frac{\alpha_{\text{eff}} I_0}{2c\epsilon_0} \tag{5.16}$$

$$\omega_\mu = \sqrt{-\frac{\alpha_{\text{eff}}}{2mc\epsilon_0}\frac{\partial^2 I}{\partial r_\mu^2}} \tag{5.17}$$

For the experiments presented here, we performed the measurement with large dipole traps containing many atoms loaded from the MOT. The experiment is easier to perform in this case because the fluorescence signal from the atoms is larger and the loading is less sensitive to the trap polarization. To increase the trap size, we simply put an iris in front of the microscope objective to reduce its effective numerical

aperture to $\eta_{\text{eff}} \simeq 0.2$. Using the paraxial optic calculation in Appendix B, one finds that the peak intensity and trap depth are:

$$I_0 = \frac{P k^2 \eta_{\text{eff}}^2}{4\pi} \tag{5.18}$$

$$U_0 = \frac{\alpha_{\text{eff}} I_0}{2c\epsilon_0} \tag{5.19}$$

and the radial and axial trap frequencies are:

$$\omega_\perp = k\,\eta_{\text{eff}} \sqrt{\frac{U_0}{2m}} \tag{5.20}$$

$$\omega_\parallel = k\,\eta_{\text{eff}}^2 \sqrt{\frac{U_0}{24m}} \tag{5.21}$$

To experimentally measure the trap frequencies, we use parametric heating by modulating the trap intensity by 10 % of its nominal value for 50 ms, at variable frequency. When the modulation frequency is twice the trap frequency, atoms are heated up and eventually spill out of the trap [SOT97]. A typical measurement of the remaining atom number after modulation as a function of modulation frequency is shown in Figure 5.3 showing dips at twice the axial (a) and radial (b) frequency of the trap.

Uncertainties For all experimental values given here, there is some uncertainty on their exact value. Every time, we quote two uncertainties: the first one coming from statistical fluctuations and that goes down with the number of repetitions of the measurement, and the second one that attempts to take into account systematic errors. For example, the power in the tweezer for the measurements presented in this part is $P = (14.0 \pm 0.7 \pm 3.0)$ mW. Here there are about 0.7 mW fluctuation in the tweezer power from day to day and there is a systematic uncertainty of 3 mW coming from the estimated transmission of the optical system.

Similarly, for the measured trap frequencies, in addition to the statistical uncertainty, there might be some systematic errors. Indeed, the atoms are not trapped precisely at the trap bottom, especially when they are heated out of the trap. Since the trap is not perfectly harmonic, they might experience an effectively lower trapping frequency [Rav+18]. To take this into account, we estimate to have a 10 % systematic error for the measured values of the trap frequencies[2].

[2] To reduce this possible error, it would have been better to apply a smaller modulation of the trap power, and to measure a heating rate instead of a loss from the trap.

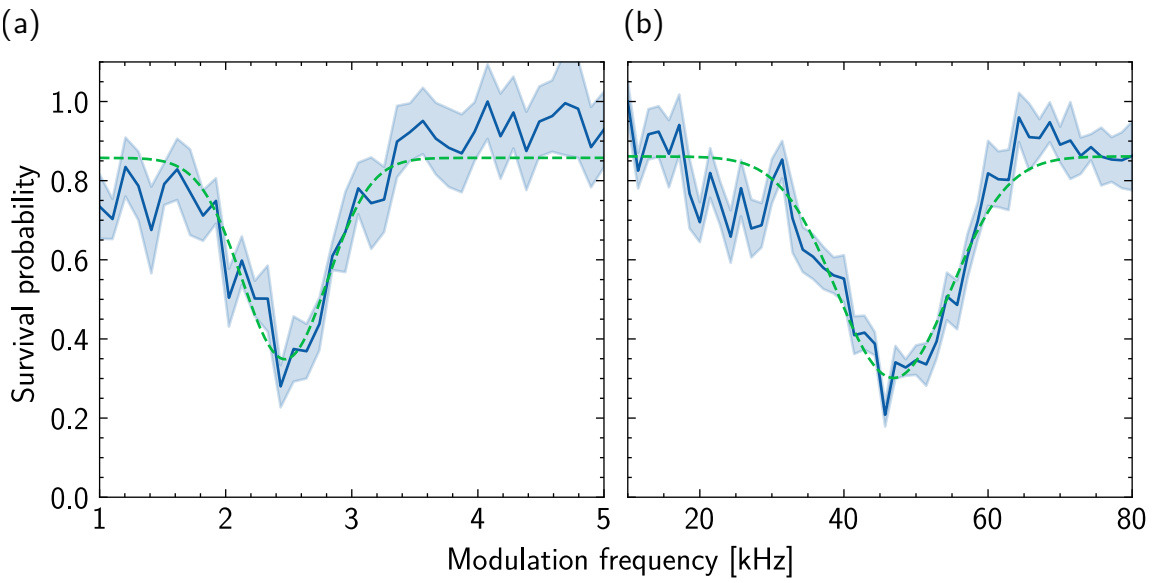

Figure 5.3. – Measurement of the axial (a) and radial (b) oscillation frequencies in the ground state using parametric heating for a tweezer power $P = 14\,\mathrm{mW}$. The dashed lines are fits to Gaussian dips in order to locate the resonant modulation frequency. We measure significant losses when we modulate the trap intensity at $(2.47 \pm 0.02 \pm 0.07)\,\mathrm{kHz}$ and $(47 \pm 1 \pm 5)\,\mathrm{kHz}$, corresponding respectively to twice the axial frequency and twice the radial frequency.

Another possible unknown is the exact trap shape, or in another word η_{eff}. While it can be predicted from the iris size used to clip the tweezer beam, it is better to estimate it from an atomic signal in case aberrations are present in the optical path. To do so, we use the ratio of the radial and axial frequencies. Assuming that Equation 5.20 is valid, we have:

$$\eta_{\mathrm{eff}} = 2\sqrt{3}\omega_{\parallel}/\omega_{\perp} = 0.182 \pm 0.006 \pm 0.020 \tag{5.22}$$

This is in agreement with our expectation given the size of the iris we put before the microscope.

Scalar and tensor polarizabilities To extract the polarizabilities of the ground state, we first perform experiments with a linear trap polarization $\boldsymbol{\epsilon}$. In this case, the vector contribution to the light-shift vanishes and the potential experienced by an atom in $|G, m = -8\rangle$ is:

$$U^G_{\mathrm{lin}}(\boldsymbol{r}) = -\frac{I(\boldsymbol{r})}{2c\epsilon_0}\left(\alpha^G_S + \frac{\alpha^G_T}{2}[3\cos^2(\theta) - 1]\right) \tag{5.23}$$

where θ is the angle between the polarization of the trapping light and the magnetic field $\boldsymbol{B}$. We change the value of the parameter θ by rotating the magnetic field with

respect to a fixed tweezer polarization. For each angle we measure the axial trap frequency, as shown in Figure 5.4 a, and we fit the data obtained to:

$$\omega_{\parallel} = \omega_{\parallel,0}\sqrt{1 + \frac{\alpha_T^G}{2\alpha_S^G}[3\cos^2(\theta) - 1]} \tag{5.24}$$

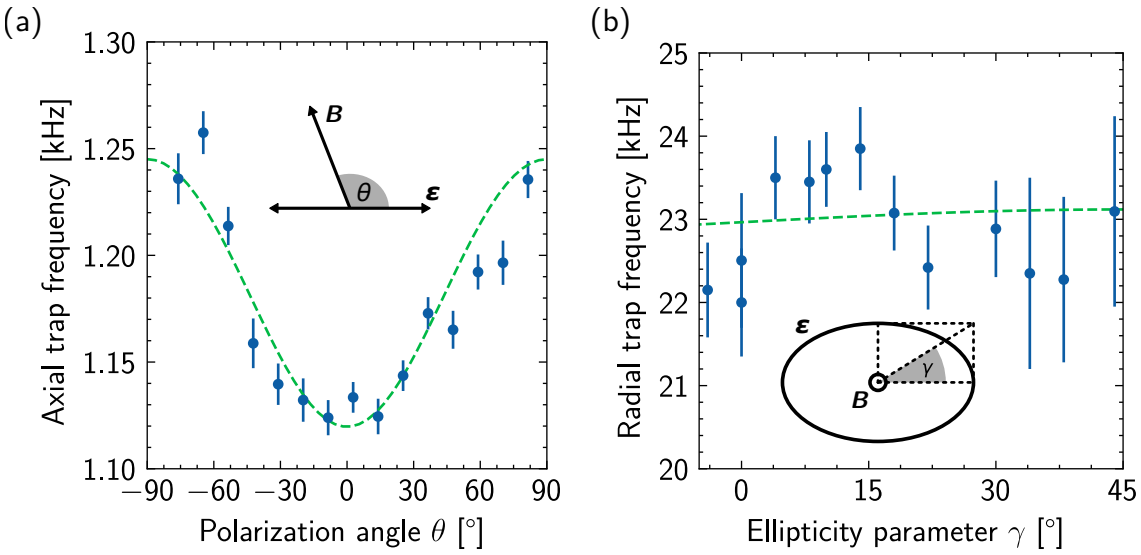

Figure 5.4. – Variations of the trap mechanical frequencies depending on the trap polarization. (a) Axial frequency as a function of the angle between a linear trap polarization and the magnetic field. Blue points are the frequencies measured, and the green dashed line is a fit to Equation 5.24. (b) Radial frequency as a function of the degree of ellipticity parameter for the trap polarization. Blue points are the frequencies measured, and the green dashed line is a fit to Equation 5.27.

From this analysis, we find $\omega_{\parallel,0} = 2\pi \times (1.21 \pm 0.02 \pm 0.10)\,\mathrm{kHz}$. This yields $\alpha_S^G = (150 \pm 30 \pm 100) \times \alpha_0$, with $\alpha_0 = 1.649 \times 10^{-41}\,\mathrm{C^2m^2J^{-1}}$ being the atomic unit of polarizability. Similarly, the fitted curve gives us $\alpha_T^G/\alpha_S^G = -0.14(6)$. It is worth noting that despite a large systematic error for the absolute polarizabilities, due to the large uncertainty on the light intensity at the position of the atoms, the ratio of the two polarizabilities is quite precise.

Vector polarizability To measure the vector polarizability α_V^G, the trap polarization must have a circular component. We use an elliptical polarization in the plane perpendicular to the magnetic field $\boldsymbol{B} = B\boldsymbol{e}_z$ aligned to the tweezer axis:

$$\boldsymbol{\epsilon} = \cos(\gamma)\boldsymbol{u}_x + i\sin(\gamma)\boldsymbol{u}_y \tag{5.25}$$

By scanning the parameter γ from 0° to 45°, the polarization can be changed from linear to circular. The potential experienced by atoms in the $|G, m = -8\rangle$ state is:

$$U_{\mathrm{el}}^{G}(\boldsymbol{r}) = -\frac{I(\boldsymbol{r})}{2c\epsilon_0}\left(\alpha_S^G - \frac{\alpha_T^G}{2} + \frac{\alpha_V^G}{2}\sin(2\gamma)\right) \tag{5.26}$$

The ellipticity parameter is controlled with the quarter waveplate placed before the microscope objective. We repeat the measurement of the trap frequencies for different ellipticity parameters γ by rotating the quarter waveplate, and we fit the resulting radial trap frequencies shown in Figure 5.4 b to:

$$\omega_\perp = \omega_{\perp,0}\sqrt{1 + \frac{\alpha_V^G}{2\alpha_S^G - \alpha_T^G}\sin(2\gamma)} \tag{5.27}$$

The dependence of the trap frequency on γ is smaller than experimental uncertainties, yielding a vector polarizability in the ground state compatible with zero: $\frac{\alpha_V^G}{2\alpha_S^G - \alpha_T^G} = 0.01(4)$.

This set of measurements in principle allows us to extract the values of the polarizabilities in the ground state. Unfortunately, while the measurements of the polarizability ratios are relatively accurate, there is more uncertainty on their absolute value. Indeed, when using the measured frequencies to retrieve the absolute polarizability, we find a scaling on the effective numerical aperture $\alpha_{\mathrm{eff}} \propto \omega_\perp^2/\eta_{\mathrm{eff}}^4$ when using the perpendicular frequency and $\alpha_{\mathrm{eff}} \propto \omega_\parallel^2/\eta_{\mathrm{eff}}^6$ when using the axial frequency. Because of the large exponents on η_{eff}, even a moderate uncertainty on the effective numerical aperture results in a large uncertainty on the polarizability.

Trap depth

To estimate the ground state polarizabilities more accurately, we decided to also measure the trap depth U_0. Indeed, the polarizability then scales as $\alpha_{\mathrm{eff}} \propto U_0/\eta_{\mathrm{eff}}^2$ and could give more precise results. In this section, we also go back to using the full microscope numerical aperture to check if the values we found previously are reproducible with a different trap intensity profile.

To measure the trap depth, we rely on the fact that the tweezers'position is controllable in real time by the acousto-optic deflector that produces the traps. We perform a sequence where we place an atom in a tweezer, then we adiabatically accelerate the trap to a given velocity v_g. After this acceleration, the atom is at rest in the moving

frame of the tweezer, but has velocity v_g in the lab frame. We then abruptly stop the tweezer. The atom now has kinetic energy $E_K = \frac{1}{2}mv_g^2$ in the trap frame. If E_K is smaller than the trap depth U_0, the atom will remain in the trap. However, if E_K is larger than U_0, the atom will be expelled from the trap. The trajectory followed by the traps is shown in Figure 5.5 a, but its exact shape is not important as long as the acceleration is smooth. Typically, the distance covered by the trap in this time is $\Delta x = 43(1)\,\mu\text{m}$, and we change the velocity v_g reached at the end of the motion by scanning the acceleration time t_a between 1 ms and 5 ms. One can then look for the threshold in velocity v_g for which the atoms remain in the trap.

In practice, the threshold is broadened by the non-zero atomic temperature. The initial velocity v of the atom along the direction of motion follows the Boltzmann distribution:

$$P(v) = \sqrt{\frac{m}{2\pi k_B T}} \exp\left(-\frac{mv^2}{2k_B T}\right) \tag{5.28}$$

After the trap has stopped, the atom then has kinetic energy $E_K(v) = \frac{1}{2}m(v + v_g)^2$. The probability that the atom remains in the trap is then:

$$P_S(v_g) = \int \Theta(U_0 - E_K(v))P(v)\mathrm{d}v \tag{5.29}$$

$$= \frac{1}{2}\left[\text{erf}\left(\sqrt{\frac{U_0}{k_B T}} + \sqrt{\frac{mv_g^2}{2k_B T}}\right) + \text{erf}\left(\sqrt{\frac{U_0}{k_B T}} - \sqrt{\frac{mv_g^2}{2k_B T}}\right)\right] \tag{5.30}$$

By measuring P_S for different values of v_g as shown in Figure 5.5 b, one can extract the trap depth and temperature by fitting the data to Equation 5.30.

For a tweezer power of 1.7(3) mW, we find a trap depth $U_0 = k_B \times (119 \pm 1 \pm 7)\,\mu\text{K}$ and a temperature $T = 5.5(4)\,\mu\text{K}$. Using the expected intensity from Figure 4.5, we find an effective polarizability $\alpha_{\text{eff}} = (204 \pm 5 \pm 40) \times \alpha_0$. This measurement was taken with an elliptical trap polarization similarly to 5.2.1, with an ellipticity parameter $\gamma = 6.5°$. Using the values of the atomic polarizability ratios from the previous section, we get a more accurate estimate of the ground state scalar polarizability $\alpha_S^G = (180 \pm 10 \pm 35) \times \alpha_0$. This value is compatible with the one obtained in the previous section that was obtained in a different trap, in principle ruling out a large systematic error not taken into account.

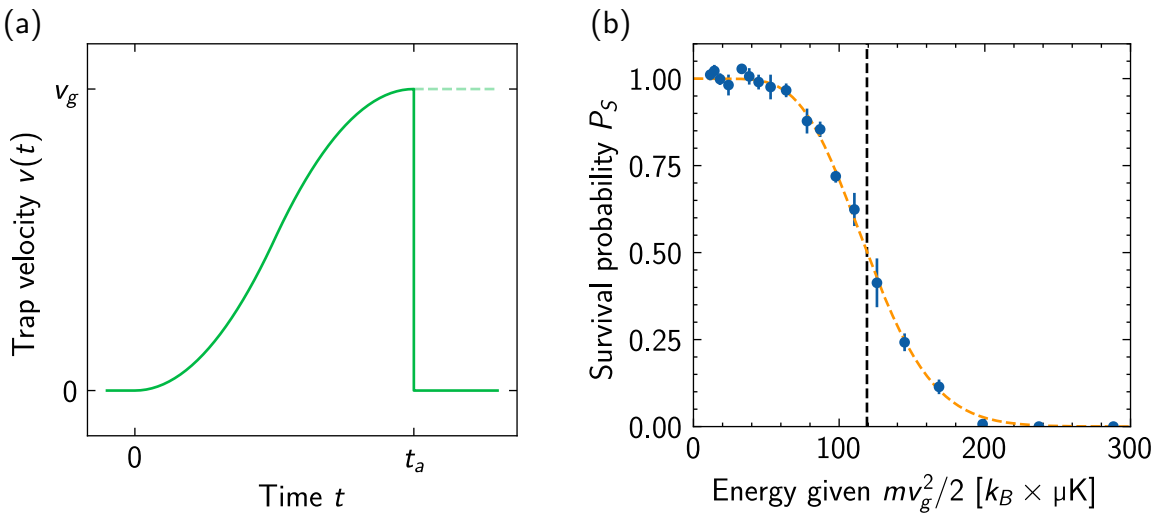

Figure 5.5. – (a) Trap velocity as a function of time for the acceleration profile used to measure the trap depth. The trap initially at rest is accelerated up to a speed v_g in a time t_a and is then abruptly brought to a stop. (b) Survival probability as a function of the energy given U_g. Blue points are experimental results, while the dashed orange line is a fit using Equation 5.30. The dashed vertical line marks the estimated trap depth U_0.

Comparison with predictions

By combining the polarizability ratios obtained with the frequency measurements and the more precise absolute polarizability value obtained with the trap depth method, we can give estimates for all three polarizability components in the ground state. These values are given in Table 5.1 next to their predicted values.

Component	Experiment	Theory
α_S^G	180(36)	408(56)
α_V^G	4(15)	-57(93)
α_T^G	-25(12)	-18(61)

Table 5.1. – Measured and predicted values for the polarizabilities of the ground state G of Dy at 532 nm. All values are given in multiple of α_0.

As one can see, despite the rather large uncertainties, the experimental polarizabilities that we obtained do not all agree with theoretical expectations. In particular, the disagreement is significant for the scalar polarizability, with the experimental value half lower than predicted. This result is particularly surprising, and it is difficult to find an explanation for this. Indeed, as seen in Figure 5.2 a, the ground state scalar polarizability presents a large positive trend around 532 nm since these wavelengths

are red-detuned with respect to the wavelengths of the broad transitions of Dy near 400 nm. The scalar polarizability can only be lower than expected if there was a nearby transition with a wavelength longer than 532 nm[3]. No such transitions has been observed, and if it existed, it would contribute to increase the magnitude of the vector and tensor polarizabilities, which is incompatible with the measured values.

A more likely explanation is that the systematic errors one the setup are not correctly estimated. It is possible that the intensity profile at the bottom of the tweezers is very different from what we expect, for instance, if the optical setup presents significant aberrations. While we were careful to check for the consistency of the values obtained, we cannot fully rule out such imperfections in our setup. To fully explain the origin of this discrepancy would require further investigations, maybe by measuring the polarizabilities in a larger trap with a better control of its shape. Ongoing measurements using the optical lattice presented in Chapter 8 give a value for the scalar polarizability $\alpha_S^G = 257(15) \times \alpha_0$, slightly closer to the theoretical value, but still in disagreement. Because of this potential issue, numerical values that rely on the exact trap shape should be taken with caution. Ratiometric quantities or values obtained from atomic signals such as trap frequencies or trap depth should still be correct regardless.

5.2.2 Excited state polarizabilities

Once the polarizabilities of the ground state G have been measured, we use these values to deduce the polarizabilities of the intercombination line excited state E_{626} as it is the one we will use for imaging single atoms. To do this, we measure the differential polarizability between the ground state and the excited state by measuring the transition frequency as a function of the tweezer polarization. When shining 626 nm light on many atoms in the trap, losses are induced when the light frequency is resonant with a transition. These losses are due to heating when scattering resonant photons and to two-body light-assisted losses.

By measuring the fluorescence signal of the remaining atoms in the trap as a function of the light frequency, it is possible to determine the frequency of the atomic transitions. An example of such measurement is shown in Figure 5.6. Similarly to the measurement of the trap frequencies we used a large trap containing many atoms. The effective

[3]It would have been interesting to measure the polarizability as a function of the trapping wavelength to try to look for such transition, but the laser we used is unfortunately not tunable.

numerical aperture $\eta_{\text{eff}} = 0.182$ used for these measurements is the same as above, and the power of the dipole trap beam is $P = (33 \pm 1 \pm 6)\,\text{mW}$. The light intensity is $I \simeq 5I_{\text{sat},626}$ and is applied for 20 ms. We also apply a magnetic field of 3 G to split the different Zeeman levels. This is why one can see three dips in the fluorescence signal, corresponding to the three projections σ_-, π and σ_+ of the light polarization along the quantization axis. Since the atoms are initially in the state $|G, m = -8\rangle$ from the MOT, only the σ_- transition with the state $|E_{626}, m = -9\rangle$ is cycling. That is why the corresponding peak is narrower than for the other polarizations that depump the atoms to larger m states. We therefore only rely on the frequency difference $\Delta\nu$ of the σ_- transition between $|G, m - 8\rangle$ and $|E_{626}, m = -9\rangle$ to extract the differential polarizability.

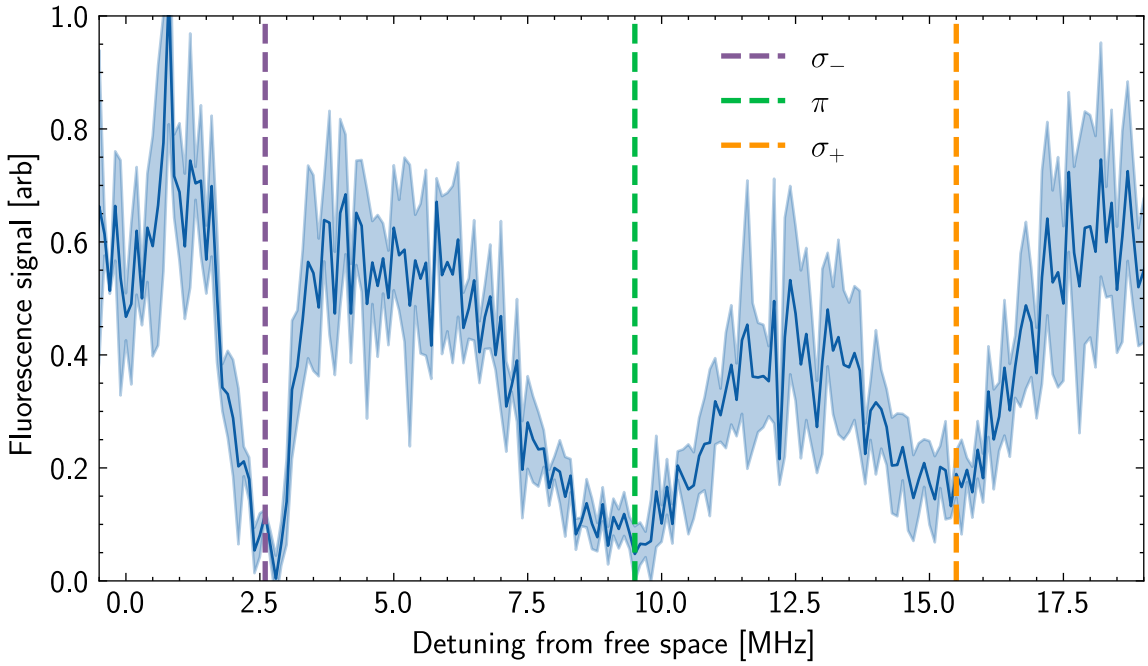

Figure 5.6. – Induced losses in the fluorescence signal from the dipole trap after shining 626 nm light with variable frequency. The three dips in the signal correspond to the projection of the light polarization on the quantization axis.

Scalar and tensor differential polarizabilities Similarly as for the trap frequency, we measured $\Delta\nu$ for different angles θ between the magnetic field direction and a linear trap polarization. This lets us access differential scalar and tensor polarizabilities $\Delta\alpha_S = \alpha_S^E - \alpha_S^G$, $\Delta\alpha_T = \alpha_T^E - \alpha_T^G$, since the frequency follows:

$$\Delta\nu = \frac{U_{\text{lin}}^E - U_{\text{lin}}^G}{h} = \Delta\nu_0 \left[1 + \frac{\Delta\alpha_T}{2\Delta\alpha_S}\left(3\cos(\theta)^3 - 1\right)\right] \tag{5.31}$$

By fitting the values shown in Figure 5.7 a to this equation, we find $\Delta\nu_0 = 2.83(3)$ MHz and $\Delta\alpha_T/\Delta\alpha_S = 0.86(3)$. Since $\Delta\nu_0 = -\Delta\alpha_S I_0/2hc\epsilon_0$, and using Equation 5.18 for the peak intensity, we obtain $\Delta\alpha_S = (-50 \pm 3 \pm 14) \times \alpha_0$.

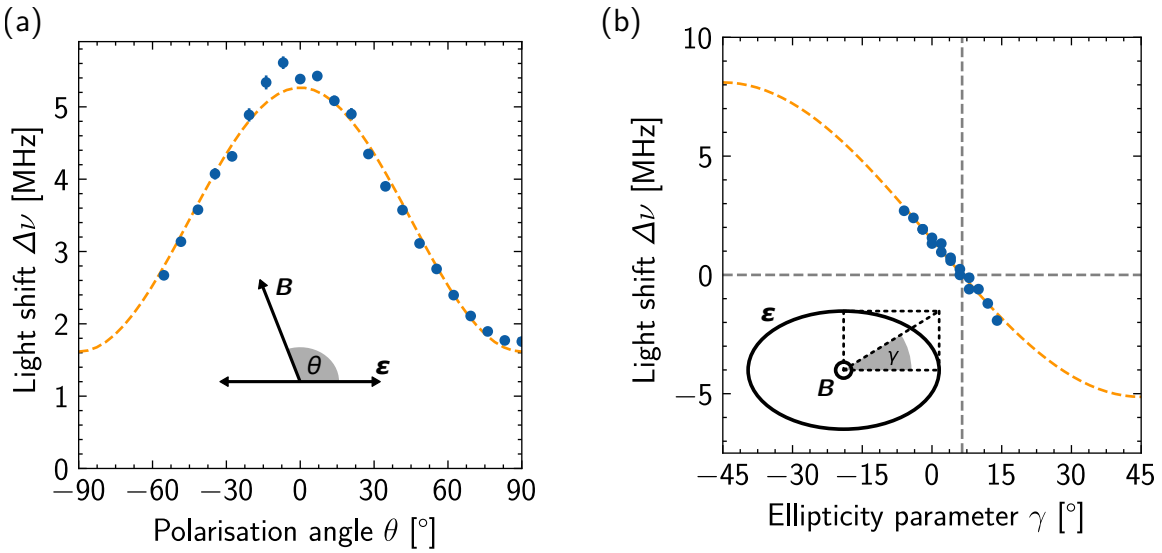

Figure 5.7. – Frequency of the transition $|G, m = -8\rangle \leftrightarrow |E_{626}, m = -9\rangle$ for various polarization of the tweezer. (a) Frequency of the transition as a function of the angle between the linear trap polarization and the magnetic field. The orange dashed line is a fit to Equation 5.31. (b) Frequency of the transition as a function of the ellipticity parameter for the trap polarization. The orange dashed line is a fit to Equation 5.32. The dashed grey lines indicate a *magic ellipticity* for which the differential polarizability cancels.

Vector differential polarizability To measure the differential vector polarizabilities $\Delta\alpha_V = \alpha_V^E - \alpha_V^G$, we perform a similar measurement, now changing the ellipticity parameter γ of the trap polarization. This is again done in a configuration where the polarization ellipse is perpendicular to the magnetic field. The values obtained are plotted in Figure 5.7 b and are fitted to:

$$\Delta\nu = \frac{U_{\text{el}}^E - U_{\text{el}}^G}{h} = \Delta\nu_0 \left[1 + \frac{\Delta\alpha_V}{2\Delta\alpha_S - \Delta\alpha_T} \sin(2\gamma)\right] \tag{5.32}$$

with $\Delta\nu_0 = -(\Delta\alpha_S - \Delta\alpha_T/2)I_0/2hc\epsilon_0 = 1.48(5)$ MHz and $\Delta\alpha_V/(2\Delta\alpha_S - \Delta\alpha_T) = -4.46(1)$.

Similar to the polarizability measurements in the ground state, the relative values of the polarizabilities are fairly accurate. However, it is challenging to get their

absolute value due to the uncertainty on the intensity at the bottom of the traps. In addition, these results obtained by estimating the transition frequency only give us the differential polarizabilities. The values obtained for the excited state depend thus strongly on what is measured in the ground state, and thus are susceptible to the measurement errors in the ground state.

Comparison with predictions

With these considerations in mind, it is still possible to provide values for the excited state polarizabilities. They are given in Table 5.2, next to their predicted values.

Component	Experiment	Theory
α_S^E	130(40)	73(30)
α_V^E	260(80)	125(60)
α_T^E	-68(18)	-44(38)

Table 5.2. – Measured and predicted values for the polarizabilities of the excited state E_{626} of the intercombination line of Dy at 532 nm. All values are given in multiple of α_0.

Both experimental and theoretical values are attached to large uncertainties, and the agreement between the two is limited. This is somewhat not surprising because it is very difficult to predict the polarizabilities of the excited state due to the unknown on its coupling with other excited levels.

Polarization tunability and magic condition

From the estimation of the polarizabilities, one can see that the trap light shift depends strongly on the polarization of the tweezer. This is particularly true for the excited states for which the vector and tensor components are comparable in magnitude to the scalar part. Simply by changing the polarization of the light, it is thus possible to change significantly the trapping potential experienced by the atoms. Such strong dependency on polarization, even in the ground state, is typical for lanthanide species. This gives us the possibility to change the differential polarizability over a large range from $\alpha_{\text{eff}}^E/\alpha_{\text{eff}}^G = -0.7$ to 2.2. For other species, such large variations are typically only possible by changing the trapping wavelength. It is a significant benefit to have this additional tunability knob, and it allows us to explore different regimes when trying to cool and image the single atoms.

In particular, there exists a specific elliptical polarization parameter γ_{magic} for which

the differential polarizability vanishes, as can be seen in Figure 5.7 b. This is a situation called a *magic condition*, for which the ground and excited states have the same effective polarizability. As a result, the two states experience the same trapping potential whatever the intensity of the trapping light. It turns out that having a magic condition is crucial to cool and image single atoms using the narrow intercombination line [Yam+16; Sas19]. This is maybe not surprising since in the absence of magic condition, the atoms would experience a detuning that vary greatly depending on their position in the trap.

In our case, we indeed observe that the atoms can be cooled without losses using 626 nm light only when the tweezer's polarization is close to the magic condition. The temperature reached when shining red-detuned light on the atoms is about 5.5 µK, measured using time-of-flight thermometry, and it is comparable to the Doppler temperature of the transition. While the influence of the differential light-shift on laser cooling has been studied both theoretically [Taï+94; IG11] and experimentally [Mon+95; Coo18; Höl23], most studies are done in the *sideband resolved* regime, where the linewidth of the transition is smaller than the trap frequencies. This is however not the regime we operate in. The linewidth of the 626 nm transition of Dy is 135 kHz, and is larger than the tweezer's frequencies of 45 kHz and 7 kHz in the radial and axial direction respectively. For this reason, there is yet no clear understanding why cooling is only efficient in the magic regime, and further studies would be required to provide a complete explanation.

Summary

In this chapter, I have presented the influence of the anisotropic polarizability of dysprosium on the light-shift the atoms experience in the tweezers. This effect has a strong influence on the differential light-shift on the narrow 626 nm transition. As a result, it is possible to significantly change the trapping strength of the excited state by changing the trap polarization or the magnetic field direction. In particular, there exists a particular *magic* elliptic polarization of the tweezers for which the ground state and excited state are equally trapped. This is the condition we will use in the next chapters to image single atoms.

Chapter 6

Multiple atoms in a tweezer

Contents

After understanding how the anisotropic polarizability of Dy influences the light-shift in the tweezers, we moved on to try to get single atoms in the tweezers. From the MOT, we typically load a few atoms in each trap with an atom number following a Poisson distribution. We then need an experimental step that removes the extra atoms.

6.1 Light-induced collisions

6.1.1 Pairwise losses

The mechanism leading to single atoms in a tweezer is two-body loss induced by near-resonant light. This is a very general effect that occurs in cold atom samples when the density is high enough [Fuh+12; Chr+19]. When near-resonant light is shone on the atoms, it can induce pair-wise losses that expel a pair of atoms from the trap. This radiation induced loss mechanism usually prevents laser cooling atoms to large densities. In our case, it can be used to ensure that at most a single atom is present in a tweezer [Sch+01; FSA16].

To illustrate this effect experimentally, we take a "video" of the process as shown on Figure 6.1. This figure shows the number of photons collected for a given trap during continuous illumination with the 626 nm light. To measure this, we take 30 quick successive pictures, each with an exposure time of 4 ms[1]. Each subplot corresponds to a different realization of the experiment, with a different initial atom number.

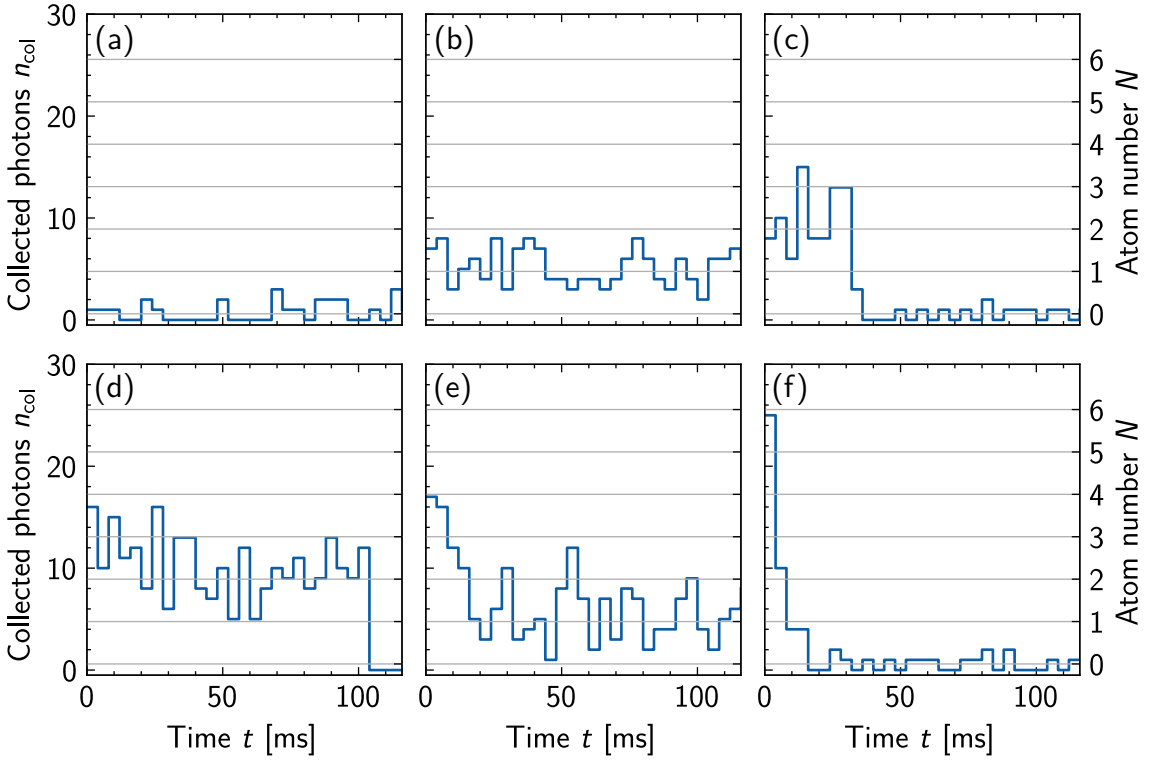

Figure 6.1. – Single shot fluorescence traces over time for a tweezer. (a) corresponds to a situation where no atom was initially loaded in the trap. In this case the fluorescence remains at the background level. (b) corresponds to a situation where a single atom is initially present in the trap. The fluorescence is larger, and remains roughly constant over time. (c, d) correspond to a situation where two atoms are initially present in the trap. The number of collected photons is initially twice as large as for a single atom, and suddenly drops to the background level. (e) corresponds to a situation where three atoms are initially present in the trap. The number of collected photons is initially about three times as large as for a single atom, and then drops to the level of a single atoms after a pair is removed. (f) corresponds to an initially large even atom number. After a large burst of collected photons, the fluorescence drops to the background level.

One can see on Figure 6.1 a that when no atom is initially present in the trap, the fluorescence level is small, corresponding to background levels.

[1]The camera has a delay of a few milliseconds between two pictures, so we actually perform this measurement in stroboscopic mode, where light is only shone on the atoms when the camera is exposing.

Since the level of background light is mainly due to the induced fluorescence of the microscope glass by the tweezer light, as explained in Section 4.3.3, we reduced the number of tweezers and their intensity to a minimum for this measurement.

In Figure 6.1 b, the number of photons collected fluctuates around a value that does not change over time. This corresponds to the situation where one atom is initially present in the trap and remains there during the full imaging process. Here the fluctuations are due to the photon shot noise present even at fixed atom number. In Figure 6.1 c, d, one can see that the fluorescence level starts initially at twice the value where a single atom is in the trap, and then suddenly drops to background level at some time. This is the situation where two atoms are initially present in the trap, and the pair is then ejected by light-induced collisions. In Figure 6.1 e, there is initially a large number of collected photons, which quickly drops to single atom level. This probably corresponds to a situation with initially three atoms, and where one pair is then ejected. In the last subplot, Figure 6.1 f, there is initially a large burst of collected light at short times, then the number of collected photons quickly drops to zero. This is a situation where there was initially an even number of atoms in the trap, but then all pairs are removed until no atoms remain.

To prepare single atoms after having loaded the tweezers from the MOT, we thus simply have to shine 626 nm light on the atoms. After a time long enough that all pairs have been removed, there is thus either zero or one atom remaining in the tweezer, depending if the trap initially contained an even or odd number of atoms [Sch+01]. As this process conserves the parity of the atom number, it is also sometimes called *parity projection*. It is a stochastic process, as one does not control the parity of the initial atom number in the trap. This leads to a random filling of the traps, with only one out of two traps containing an atom. This limitation is usually overcome by rearranging the tweezers to produce defect-free arrays, as will be discussed in Chapter 8.

When using a broad transition for the MOT, for example for alkali species, the rate of light-induced losses can often be larger than the loading rate of atoms from the MOT. This is because the atoms scatter many photons that can induce losses. It means that as soon than a second atom is loaded in the tweezer, the pair is immediately lost, and there can never be more than one atom in the tweezer. This is also called the *collisional blockade regime* [SRG02].
We do not operate in this regime when using the narrow 626 nm transition of Dy. The tweezers are typically not magic for this transition during the loading from the MOT because of the different magnetic field direction. When atoms end up in the tweezers, the light-shift makes the MOT light far-detuned from the transition, thus shielding the atoms from light-induced collisions. Because of this, more than one atom can be loaded in a tweezer, and it is necessary to perform an additional step to remove the extra atoms.

6.1.2 Origin of the effect

Since this effect comes from the interaction between a pair of atoms and light, we can understand it by reviewing the interaction between a pair of atoms. The main interaction between two atoms in a tweezer is the electric dipole-dipole interaction. I will give a more detailed description of this interaction in Chapter 8 when presenting the formalism of light scattering. At small distances, this interaction reduces to the electrostatic interaction between two dipoles:

$$V_{\mathrm{dd}}(r) \approx \frac{d_1 d_2}{4\pi\epsilon_0 r^3} \tag{6.1}$$

where d_1 and d_2 are the electric dipole of each atom and r is the distance between them. For two atoms in the ground state, there is no direct coupling between them: $\langle gg|\hat{V}_{\mathrm{dd}}|gg\rangle = 0$. The interaction energy between two atoms in the ground state is thus a second order effect and scales as C_6/r^6 [Li+16; KP11]. It is also called the Van der Waals interaction, and it is plotted in Figure 6.2 b. As one can see, for distances larger than a few tens of nanometers, this interaction is negligible compared to other energy scales. It only plays a role in direct collisions between atoms and contributes

to redistributing kinetic energy through elastic collisions[2]. For the problem considered here, it is common to ignore this interaction and to consider that two atoms in the ground state do not interact.

Instead, what is significant is the interaction between two atoms when one of them is in an excited state: $\langle eg|\hat{V}_{\mathrm{dd}}|ge\rangle \simeq \hbar\Gamma/(kr)^3$, where Γ is the linewidth of the considered transition. Depending on the orientation and relative phase between the two electric dipoles, this interaction corresponds either to an attractive molecular state $|a\rangle$ or repulsive state $|r\rangle$. The energy of these two states for the 626 nm transition that will interest us here is plotted in Figure 6.2 a. As one can see, at distances of a few tens of nanometers, the energy of these states becomes very large compared to the other energy scales in a tweezer.

The interpretation of light-induced collisions is then the following: when shinning near resonant light red detuned light on the atoms, as one would do to cool them, an atomic pair initially in the ground state $|gg\rangle$ can be excited to the attractive molecular state $|a\rangle$, as depicted in Figure 6.2. The two atoms then accelerate towards each other and gain a large kinetic energy in their center of mass referential. In and of itself, this does not mean that the atoms acquire energy, as the potential is conservative. However, the atoms can spontaneously deexcite while they are moving towards each other. In this case, the atoms are suddenly brought back to the ground state where they experience no attractive potential, while keeping their large velocity. The kinetic energy acquired is typically much larger than the trap depth, and the two atoms fly out of the tweezer.

6.2 Extracting the two-body loss rate

When trying to produce and image single atoms in tweezers, it is important to have some idea of the dynamics of the light-induced losses. For example, we need to be sure that we start our experiments with only a single atom in each tweezer. If the timescale of the light-induced collisions is slower than expected, we could end up with several atoms per trap, which would make the following steps invalid. To gain a better understanding of this process, I will discuss in this section some measurements we performed to characterize the light-induced losses. Here, we only performed a detailed analysis using the 626 nm transition, but we also observed that the 421 nm and 741 nm transitions have similar effects, albeit with very different timescales.

[2]This picture is a bit muddier for Dy, as one needs also to account for the magnetic dipole interaction which also plays a role in ground-state scattering.

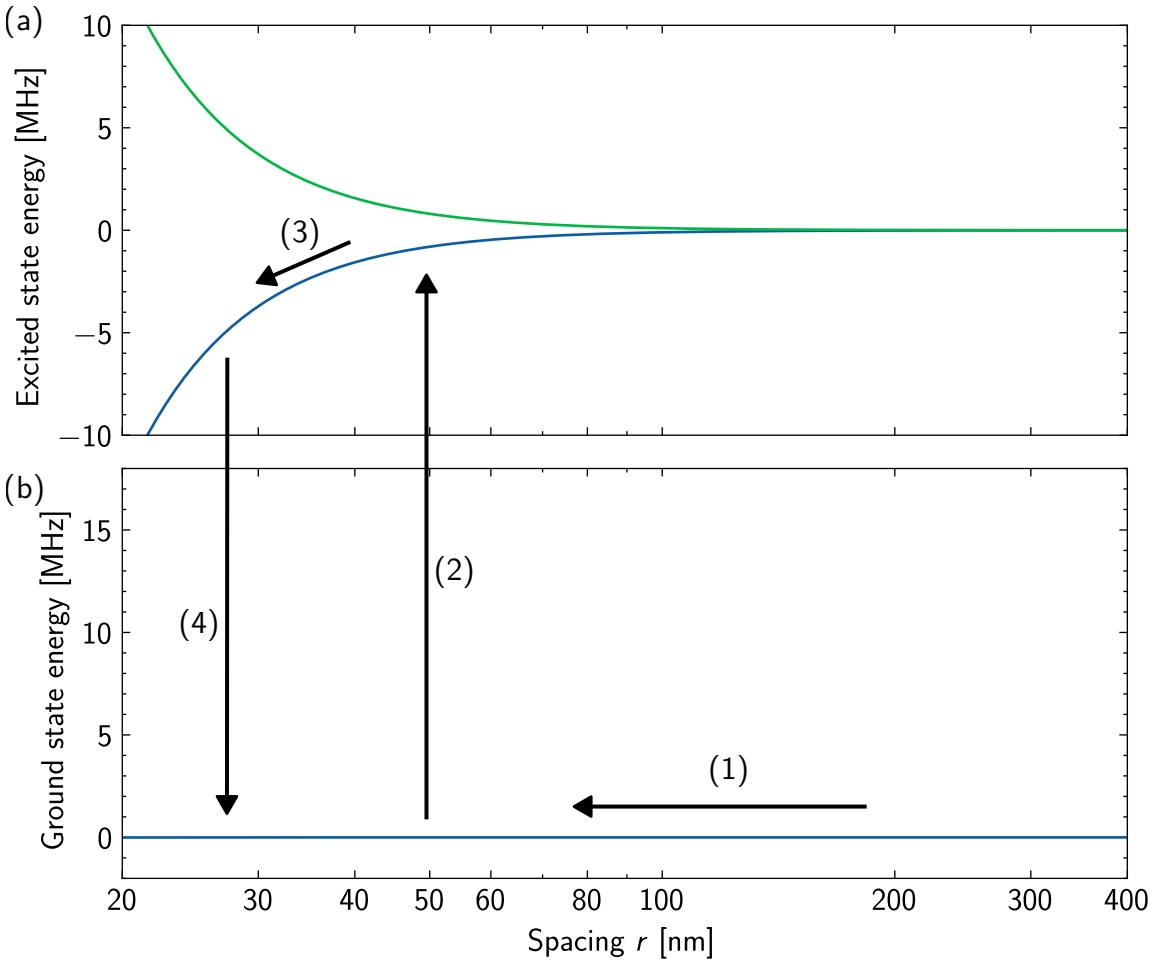

Figure 6.2. – Illustration of the light-induced collision mechanism. (1) Two atoms in the ground state get close to each other. (2) They are excited to an attractive molecular state by absorbing a photon. (3) They accelerate towards each other and gain a large velocity. (4) They spontaneously deexcite and end up in the ground state with a velocity much larger than the trap depth.

To quantify the effect of light-assisted collisions, we need to be able to look at the evolution of the number of atoms over time. For this, we can average the traces presented in Figure 6.1 over many experimental realizations to get the mean number of collected photons at a time t: $\langle n_{\mathrm{col}}(t)\rangle$. For exposure times much shorter than the dynamics of light-induced collisions, the mean number of collected photons is proportional to the mean number of atoms in the trap $\langle N(t)\rangle$:

$$\langle n_{\mathrm{col}}\rangle = n_{\mathrm{atom}} \times \langle N\rangle + n_{\mathrm{bg}} \tag{6.2}$$

where n_{atom} and n_{bg} are respectively the mean number of collected photons for a single atom and for the background. By calibrating n_{atom} and n_{bg}, it is thus possible to get

the mean number of atoms in the trap from the mean number of collected photons. One needs to be careful that Equation 6.2 is, however, only valid when the exposure time is short compared to the timescale of the light-induced losses. If the exposure time is too long, the number of atoms will decrease during the picture, and it will be challenging to interpret the results.

An example of such measurement is plotted in Figure 6.3 a. We see that there are initially, on average, about 3 atoms in the trap. Under the effect of the light, the atom number then decreases in a few tens of milliseconds to an average value of 0.5. This corresponds to the situation described above where half of the time the initial atom number is even and no atom remains in the trap, and half of the time the initial atom number is odd and a single atom survives in the trap [Fuh+12].

We can be more quantitative about this and extract the two-body loss rate β' from the data. If there were always exactly two atoms, the mean atom number would decrease exponentially at a rate β', but here the situation is slightly more complicated due to fluctuation in the initial atom number. To model this, let us introduce the probability $P_N(t)$ to have N atoms in the trap at a given time t. We assume that the initial atom number follows a Poisson distribution with mean N_0:

$$P_N(0) = P_p(N|N_0) = e^{-N_0}\frac{N_0^N}{N!} \tag{6.3}$$

The mean atom number at any time is given by:

$$\langle N(t)\rangle = \sum_{N=0}^{\infty} N P_N(t) \tag{6.4}$$

One then has to know how the different probabilities P_N evolve over time [Sor+12]:

$$\frac{\mathrm{d}P_N}{\mathrm{d}t} = -\beta'\frac{N(N-1)}{2}P_N + \beta'\frac{(N+2)(N+1)}{2}P_{N+2} \tag{6.5}$$

Here, the population corresponding to N atoms in the trap decays at a rate $\beta' N(N-1)/2$ due to light-induced losses and feeds into the population at $N-2$. It is worth noting that the decay rate is increased by $N(N-1)/2$ corresponding to the number of pairs in the tweezer. In particular, the populations P_0 and P_1 do not decay but only accumulate population from the higher N states. This encapsulates the fact that the atom number decreases initially fast when there are many atoms in the trap, but then reaches a plateau when only zero or one atoms remain.

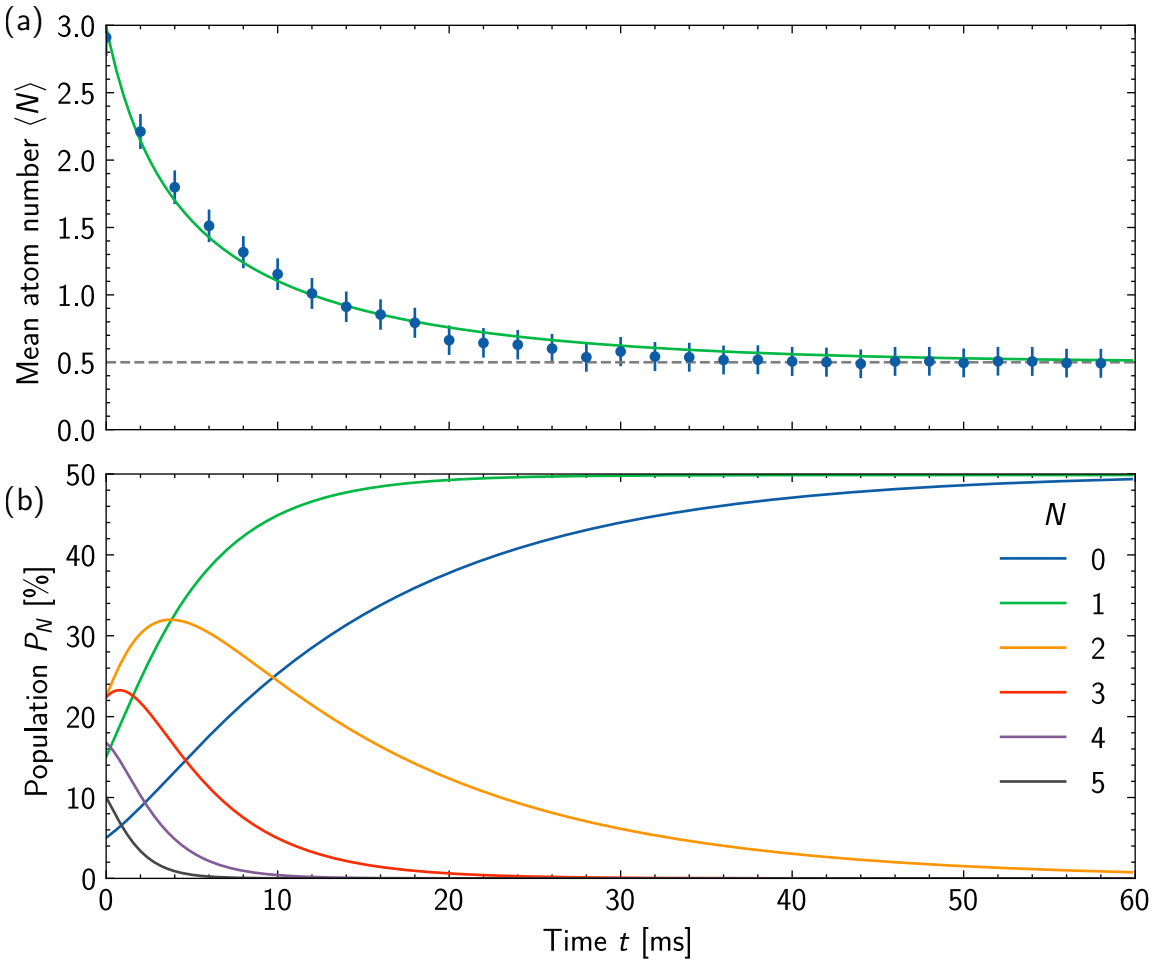

Figure 6.3. – (a) Evolution of the mean atom number over time in the presence of two-body light-induced losses. These values are obtained for a magic trap with a detuning $\Delta = -2.5 \times \Gamma_{626}$ and an intensity $I = 0.57(5) \times I_{\text{sat},626}$. (b) Evolution of the calculated probabilities to have N atoms in the trap at a given time.

It is possible to add one body loss rate to the model:

$$\frac{\mathrm{d}P_N}{\mathrm{d}t} = -\alpha N P_N + \alpha(N+1)P_{N+1} \tag{6.6}$$

This could include, for example, the effect of collisions with the residual gas in the chamber. In our case, the timescale of these losses is about 300 s and its contribution to losses is negligible compared to the two-body light-induced losses. Similarly, one could include one body loss rate due to the light [Fuh+12], but this is also negligible in the regime considered here of negative detuning and low intensity.

By fitting the mean atom number using this model as shown in Figure 6.3 a, we

can extract the initial mean atom number $N_0 = 2.9(1)$ and the two-body loss rate $\beta' = 63(8)\,\mathrm{s}^{-1}$ in these specific conditions. In Figure 6.3 b, I calculate the evolution of the probability P_N for the value of the parameters extracted from the fit. As seen, the probability to have more than one atom in the trap decreases over time, while the probabilities to have one or zero atoms both increases to 50 %. With this measurement, we can then determine at which point only single atoms are present in the tweezers. In typical experiments, we prefer to work with smaller detuning $\Delta = -1.5 \times \Gamma_{626}$ where the loss rate is larger $\beta' = 310(70)\,\mathrm{s}^{-1}$, and we reach the single atom regime in less than 30 ms.

It might at first seem unnecessary to introduce the model over P_N to get the evolution of $\langle N \rangle$. Indeed, in the dilute gas regime, it is usual to find the following equation for the evolution of the mean atom number:

$$\frac{\mathrm{d}\langle N \rangle}{\mathrm{d}t} = -\beta n \langle N \rangle \tag{6.7}$$

where β is the density loss rate coefficient and n is the atomic density. Instead of solving for $\langle N \rangle$ using Equation 6.5, it would be tempting to write directly:

$$\frac{\mathrm{d}\langle N \rangle}{\mathrm{d}t} = -\beta' \langle N \rangle^2 \tag{6.8}$$

with $\beta = V\beta'$, where $V = (4\pi k_B T/m\bar{\omega}^2)^{3/2}$ is the thermal volume of the tweezer, and $\bar{\omega} = (\omega_x \omega_y \omega_z)^{1/3}$. This equation does *not* give the correct result in our case. Indeed, by multiplying each side of Equation 6.5 by N and summing all the terms, we find [Fuh11]:

$$\frac{\mathrm{d}\langle N \rangle}{\mathrm{d}t} = -\beta' \left[\langle N \rangle^2 - \langle N \rangle + \mathrm{Var}\,(N) \right] \tag{6.9}$$

We recover Equation 6.8 only if $\mathrm{Var}\,(N) = \langle N \rangle$. This is no longer the case after light-induced collisions have removed pairs of atoms and the distribution is no longer Poissonian.

6.3 Comparison with numerical models

In addition to learning how to produce single atoms, we can also use the values of the loss rate from the previous section to test if the explanation for the light-induced collisions given in Section 6.1.2 is indeed the correct one. In this section, I will compare

the experimental data to some numerical models to test this hypothesis.

6.3.1 Gallagher and Pritchard model

While it is possible to come up with analytical formulas for the loss rate, it usually comes at the cost of large simplifications, such as the influence of the tweezer shape or the role of more complex interaction potentials. To have the possibility to easily change the model used, I instead performed semi-classical Monte-Carlo simulations of a pair of atoms in a tweezer, following more recent approaches [Som+13; Pam+25]. It is worth noting that compared to the case of alkali atoms, Dy is not necessarily more complex. Indeed, we do not have to deal with a hyperfine structure in the case of bosons, and we start from a polarized Zeeman state, which hopefully makes the situation simpler.

In the simulations I performed, the positions $\mathbf{r}_1$, $\mathbf{r}_2$ and velocities $\mathbf{v}_1$, $\mathbf{v}_2$ of two atoms evolve according to the classical equation of motions in the gaussian potential of the tweezer. At the temperature considered here, it might not be fully valid to neglect the spread of the atomic wavefunctions, but I will still make this assumption to keep the problem tractable.

At some time during their evolution, the pair of atoms can be excited to the attractive molecular state $|a\rangle$ by the 626 nm light. To model this, the first approach I used is the Gallagher and Pritchard model [GP89]. In this case, the rate of excitation of the pair is chosen to be the value reached in steady state for the optical Bloch equations in the low Rabi frequency limit:

$$\Gamma_{\text{asso}} = \frac{\Omega_a^2/\Gamma_a}{1 + 4\left(\frac{\Delta_{\text{loc}}(\boldsymbol{r})}{\Gamma_a}\right)^2} \tag{6.10}$$

where $\mathbf{r} = \mathbf{r}_1 - \mathbf{r}_2$ is the position difference between the atoms and $\Delta_{\text{loc}}(\boldsymbol{r}) = \Delta - E_a(\boldsymbol{r})/\hbar$ is the local detuning between $|gg\rangle$ and $|a\rangle$. The energy of the attractive state $|a\rangle$ is:

$$E_a(\mathbf{r}) = \langle a|\hat{V}_{\text{dd}}|a\rangle = -\lambda_a \frac{\hbar\Gamma_{626}}{(kr)^3} \tag{6.11}$$

where λ_a is a value of the order of one. Here, the lifetime Γ_a and the Rabi frequency Ω_a are the ones corresponding to the attractive excited state $|a\rangle$, and are *a priori* different from the single atom case. In particular, the values λ_a, Ω_a and Γ_a in principle depend on the orientation between the atoms, and Ω_a and Γ_a also depend on the

spacing between them. However, in the tweezer the relative position between the atoms is not controlled, so we can expect this dependency to average out. That is why for the rest of the discussion, I will take an isotropic potential with $\lambda_a = 3/4$, which is the value obtained by averaging over all orientations, and I will also use the single atom values $\Omega_a = \Omega$ and $\Gamma_a = \Gamma_{626}$. With this approximation, the value of Γ_{asso} is plotted in Figure 6.4 a for different detunings Δ. As one can see, for small detuning, the excitation region becomes delocalized over a large range of distances, and the pair of atoms can get excited even for large separation. On the opposite, when the detuning is large, the excitation region becomes localized around a distance R_C where $E_a(R_C) = \hbar\Delta$, and is thus:

$$R_C = \frac{1}{k}\left(\lambda_a \frac{\Gamma_{626}}{|\Delta|}\right)^{1/3} \tag{6.12}$$

The separation where this occurs is called the Condon radius R_C.

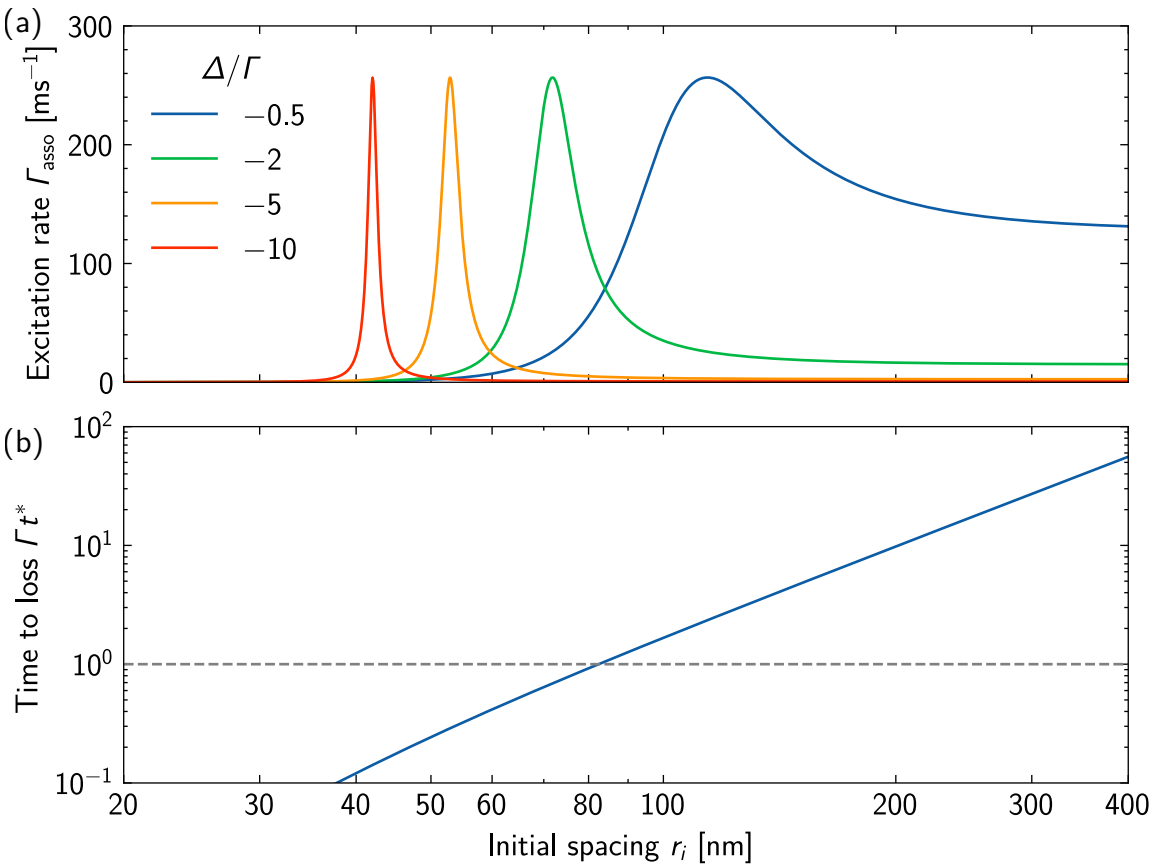

Figure 6.4. – (a) Excitation rate of a pair of atoms as a function of their distance from Equation 6.10. The different curves correspond to different light detunings. (b) Time after which a pair of atoms excited at a distance r_i reach a separation such that the excess energy exceeds the trap depth.

In the simulation, once the atoms are excited, the attractive interaction between them is included, and the atoms are strongly accelerated towards each other, thus acquiring a large kinetic energy. After a random time dictated by the lifetime Γ_a of the state $|a\rangle$, the pair spontaneously deexcites while keeping their large kinetic energy[3]. If this energy is larger than the trap depth, the pair is expelled from the trap. This depends strongly on the distance between the atoms when they get excited. If the atoms are too far apart, they barely accelerate towards each other in a time comparable to the lifetime of the excited state since the dipole-dipole potential is very flat. It is only if their initial separation is small enough that a loss is likely to occur.

To get some idea of the distance at which the losses become important, we can compute the evolution of the pair of atoms in the excited state. Neglecting the initial kinetic energy and angular momentum of the atoms, we find that atoms starting with a separation r_i, will reach the separation r_f after a time:

$$t(r_i, r_f) = \frac{\sqrt{m}}{2} \int_{r_f}^{r_i} \frac{\mathrm{d}r}{\sqrt{E_a(r_i) - E_a(r)}} = \sqrt{\frac{m r_i^2}{4E_a(r_i)}} \int_{r_f/r_i}^{1} \frac{\mathrm{d}u}{\sqrt{1/u^3 - 1}} \tag{6.13}$$

Let us introduce the final position $r_f^*(r_i) = (1/r_0^3 + 1/r_i^3)^{-1/3}$ for which the acquired energy is larger than the trap depth $U_0 = E_a(r_0)$. We can then define the time at which excited atoms reach a separation such that their kinetic energy is larger than the trap depth $t^*(r_i) = t\left(r_i, r_f^*(r_i)\right)$. This time is plotted in Figure 6.4 b for different initial separations r_i. If the separation between atoms is larger than about 100 nm, the pair will deexcite before having acquired enough energy to be lost. It is only if the atoms have an initial separation of some tens of nanometers that they will be ejected. From this, we can see that three contributions determine the rate of two-body losses:

- The excitation rate Γ_{asso}, which depends on the detuning and intensity of the light.
- The probability that excited atoms are lost when deexciting that depends on the trap depth and their initial separation.
- The density of pairs at a given spacing that depends on the temperature and on the tweezer volume.

To take into account the last point, I repeat many simulations for a large number of pairs (typically 10 000) with different starting positions and velocities sampled from a

[3] We ignore the momentum change from the spontaneously emitted photon, as the recoil energy is much smaller than the change from the dipolar interaction.

thermal distribution. By counting the fraction of simulations where the pair is lost, we can extract the loss rate.

The values of the parameters used in the simulations are the same as the experimental ones:

- Radial trap frequency: $\omega_\perp = 2\pi \times 50\,\mathrm{kHz}$
- Axial trap frequency: $\omega_\parallel = 2\pi \times 6.5\,\mathrm{kHz}$
- Trap depth: $U_0 = k_B \times 120\,\mu\mathrm{K}$
- Temperature: $T = 9(1)\,\mu\mathrm{K}$. This is the temperature after loading the tweezers from the MOT and without additional cooling. The temperature might change slightly when shinning the 626 nm light on the atoms, but this does not affect the two-body loss rate significantly.
- Single atom Rabi frequency: $\Omega = 0.55(5) \times \Gamma_{626}$. This is the typical value we use when performing light-induced collisions.

The loss rate as a function of detuning in this situation is plotted in Figure 6.5. Blue points represent the experimental data, while the orange line is the result of the simulations using the Gallagher and Pritchard model described here.

The numerical values obtained have indeed the same magnitude as the ones measured, which already hints that this model successfully captures a large part of the process of light-induced losses. Some deviations between the simulations and the data are still present: the measured loss rate is strongly reduced at small detuning, while the simulations predict a value that reaches a plateau at zero detuning. In addition, the experimental loss rate decreases faster at larger detuning than the simulated one. A possible limitation of the Gallagher and Pritchard model is that it considers a frozen picture when making the steady state assumption for the excitation rate Γ_{asso}. However, it is not obvious that the motion of the atoms is slow compared to the evolution of their internal state; Atoms that become excited at a distance r_i smaller than 100 nm will be attracted before they reach steady state, as shown on Figure 6.4 b. It is thus not clear if Equation 6.10 applies. One might instead expect that the relative velocity between the atoms might play a role in the excitation rate.

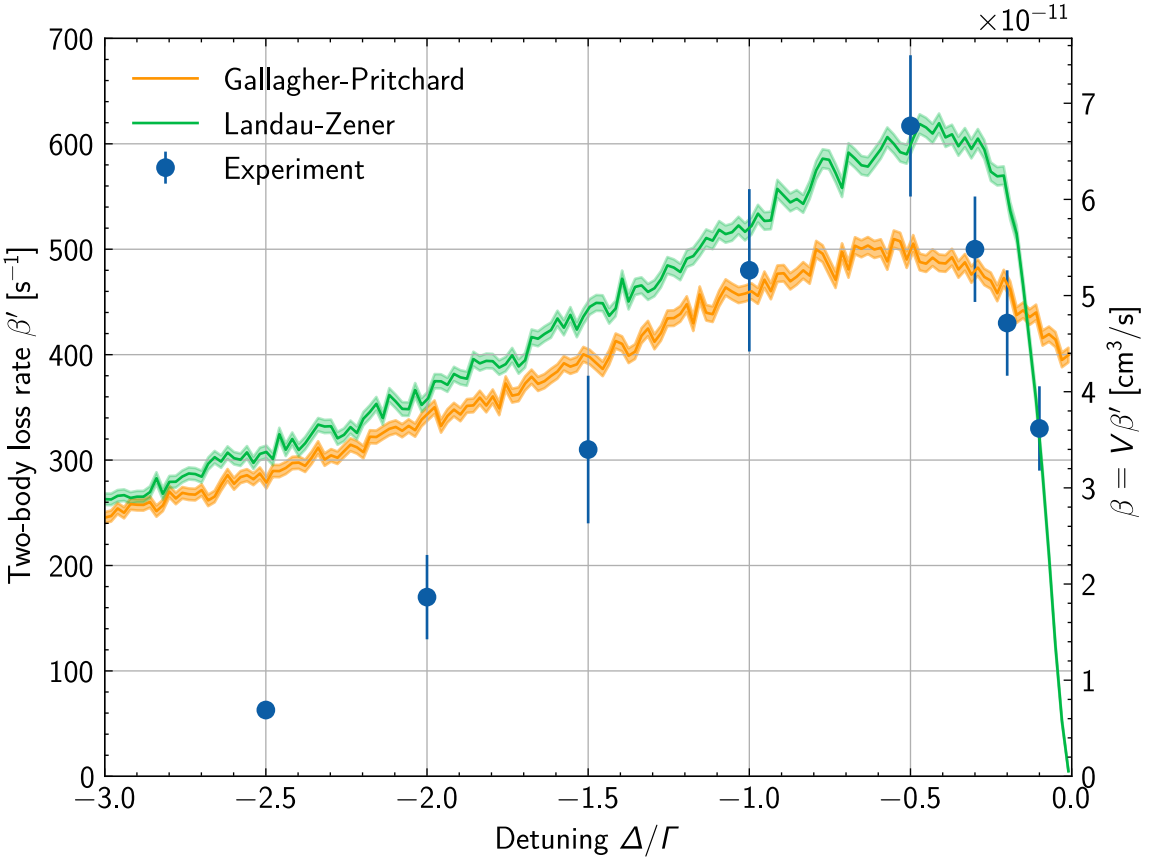

Figure 6.5. – Two body loss rate in a tweezer as a function of detuning. Blue points are the experimental data, while the lines correspond to the result of the simulations. The orange line is obtained using the Gallagher and Pritchard model, and the green line is obtained using the Landau-Zener model. For the numerical simulations, no fitting parameter is introduced, and the necessary parameters are directly measured on the experiment.

6.3.2 Landau-Zener model

Here I will describe a model that attempts to account for the dynamical nature of the excitation process, also called the Landau-Zener model [Suo96]. To illustrate this model, it is convenient to plot the energy levels in the rotating frame of the laser light. In this case, the singly excited states $|a\rangle$ and $|r\rangle$ have energy $-\hbar\Delta$ when the atoms are far apart. As the distance between the atoms decreases, the energy of the attractive state crosses the energy of the ground state as shown in Figure 6.6.

This crossing occurs when the separation between the two atoms reaches the Condon radius R_C. At the intersection, the two states $|gg\rangle$ and $|a\rangle$ mix under the effect of the

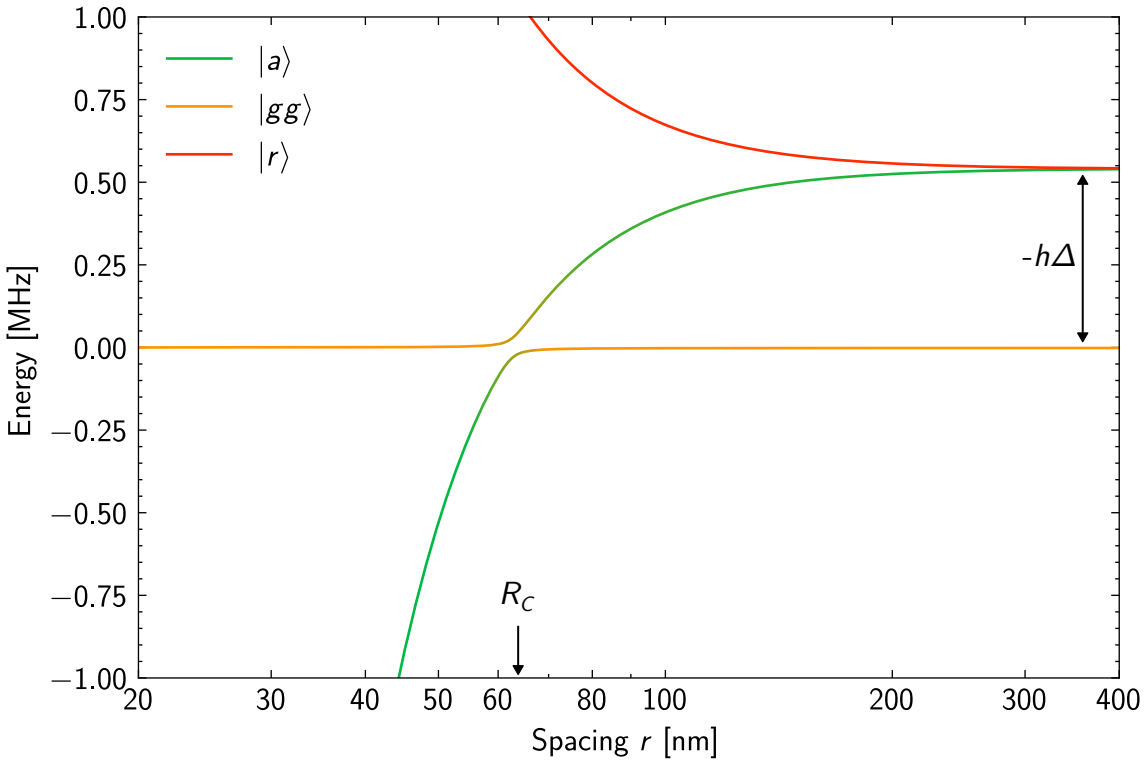

Figure 6.6. – Illustration of the avoided crossing between $|gg\rangle$ and $|a\rangle$ in the case of negative detuning.

laser light, resulting in an avoided crossing with a splitting:

$$\langle gg|\hat{H}_L|a\rangle = \frac{\hbar\Omega_a}{2} \tag{6.14}$$

Incoming atoms in the ground state $|gg\rangle$ will become excited when coming close to each other only if they stay in the instantaneous ground state of the system. If their relative velocity is too large, the process will not be adiabatic and the pair will not be excited. The Landau-Zener theory gives us a way to calculate the probability of such diabatic transition [Joy94]:

$$P_{\mathrm{LZ}} = \exp\left[-\frac{2\pi}{\hbar}\frac{\left|\langle gg|\hat{H}_L|a\rangle\right|^2}{\left|\frac{\mathrm{d}}{\mathrm{d}t}[E_a(t) - E_{gg}(t)]\right|}\right] = \exp\left[-\frac{\pi}{2}\frac{\hbar\Omega_a^2}{|\boldsymbol{v}\cdot\boldsymbol{\nabla}E_a(\boldsymbol{r})|}\right] \tag{6.15}$$

We can then perform very similar simulations to the ones described in the previous section, but now the excitation of pair only occurs when the separation between the atoms reaches R_C. When this happens, we randomly excite the pair with the probability $1 - P_{\mathrm{LZ}}$. We see that now the probability to be excited depends explicitly

on the relative velocity $\boldsymbol{v}$ between the two atoms, so we might hope to have a better representation of the dynamics. The atoms then again evolve under the dipole-dipole potential with the same spontaneous decay rate Γ_a, and the same probability to be ejected from the trap when they deexcite.

When using analytical formulas, the Landau-Zener probability needs to be corrected to take account multiple passages; If two atoms do not get excited when their distance becomes smaller than R_C, they have a chance to become excited again when they separate, and their distance equals R_C again. This is readily included in the simulations by taking into account all events where the distance between the atoms reaches R_C whether it is from above or from below. In the conditions of the experiment, this effect has little influence on the calculated loss rate.

The results of these simulations are again plotted in Figure 6.5 for this model. Unlike the Gallagher-Pritchard model and its delocalized excitation picture, it seems somewhat able to capture the reduced value of the loss rate at small detuning. Unfortunately, it does not seem to fare better than the Gallagher and Pritchard model at large detuning, and appears to give very similar results in this case.

It might seem surprising that the two models give similar results at large detuning. Indeed, the two models use a different formula for the excitation probability of the pair of atoms. The Landau-Zener has an exponential form that includes the relative velocity of the atoms which at first seems irreconcilable with the frozen lorentzian of the Gallagher-Pritchard model. It is actually known that the two models are equivalent [Suo96]. To demonstrate it, let us consider the probability that two atoms do not get excited between the times t_1 and t_2 in the Gallagher-Pritchard model:

$$P_{\mathrm{GP}} = \exp\left[-\int_{t_1}^{t_2} \Gamma_{\mathrm{asso}}(t)\,\mathrm{d}t\right] \tag{6.16}$$

When the detuning Δ becomes large, $\Gamma_{\mathrm{asso}}(t)$ is only significant when the atoms are near the Condon radius, as illustrated on Figure 6.4 a. We can then replace the lorentzian in the association rate with a Dirac delta function around the time of the crossing t_C:

$$\Gamma_{\mathrm{asso}}(t) \simeq \frac{\pi\Omega_a^2}{2\Gamma_a}\delta(\Delta_{\mathrm{loc}}(t)/\Gamma_a) = \frac{\pi\Omega_a^2}{2}\frac{\delta(t-t_C)}{\left|\left.\frac{\mathrm{d}\Delta_{\mathrm{loc}}}{\mathrm{d}t}\right|_{t_C}\right|} \tag{6.17}$$

We then obtain the probability that the atoms do not get excited in the Gallagher-Pritchard model:

$$P_{\mathrm{GP}} \simeq \exp\left[-\frac{\pi\Omega_a^2}{2\left|\left.\frac{\mathrm{d}\Delta_{\mathrm{loc}}}{\mathrm{d}t}\right|_{t_C}\right|}\right] = \exp\left[-\frac{\pi}{2}\frac{\hbar\Omega_a^2}{|\boldsymbol{v}\cdot\boldsymbol{\nabla}E_a(\boldsymbol{r})|}\right] = P_{\mathrm{LZ}} \tag{6.18}$$

At large detuning, both models thus have the same excitation probability and are indeed equivalent.

Since the two models give the same results at large detuning and fail to reproduce the experimental data, it seems that something is missing in the description of the problem. This may be expected since larger detuning probes smaller separation between the atoms, which is harder to model. A similar result was observed when quantifying two-body losses in a MOT on the intercombination line of Dy, with a measured loss rate higher than the one predicted by analytical predictions [Dre+17]. It is difficult to conclude on the origin of the discrepancy without further experiments and analysis. Without being exhaustive, here are some explanations that could explain the difference observed:

- The difference between the lifetime Γ_a and Rabi frequency Ω_a of the excited state from the isolated atoms case might play an important role.
- The molecular potentials at short distances might not be well represented by the simple model presented here.
- The classical approximation for the atomic trajectory might not be valid at the temperature considered here.
- The Rabi frequency is too large, and one has to consider more elaborate models [Suo96].

Summary

In this chapter, I have explored the mechanism of light-induced collisions that we rely on to be sure to have no more than one atom per tweezer. When shining red-detuned light on a pair of atoms, they are excited in an attractive molecular state. If the atoms deexcite as they are attracted towards one another, the released kinetic energy is enough to expel the atoms from the trap.

We have measured the timescale at which these light-induced collisions occur and compared it to numerical Monte-Carlo simulations using simple models for the interaction between the atoms. The simulations and measured data are in relatively good agreement, and further exploration might give additional insights in the details of this phenomenon. In particular, it could be that at the small distances considered here, the lifetime and coupling to the light-field differ significantly for a pair of atoms than for isolated atoms.

In the discussion presented here, I only considered the case of red-detuned light. It could be interesting to also explore the case of blue-detuned light. In this situation, instead of exciting an attractive molecular state, the repulsive one is excited. As a result, the atoms cannot get too close, and the kinetic energy they acquire in the excited state is bounded by the detuning of the light [Suo+95]. It has been demonstrated that it is then possible to fine-tune light-induced collisions to eject only one atom from the trap, and that this approach can be used to load tweezers with a filling fraction larger than 0.5 [Grü+10; Bro+19; Jen+22]. We have not explored this approach in the work presented here, but it could be an interesting possibility to explore in the future.

Chapter 7

Imaging single atoms

Contents

In the previous chapter, we have seen how to produce single atoms in optical tweezers. Here, I will discuss in more detail the performance of the imaging process, as this will determine our ability to detect single atoms with good fidelity in a single shot. I have presented similar results in [Blo+23], but following improvements in the imaging setup, I will here provide improved data and analysis since the publication.

7.1 Fluorescence imaging

7.1.1 Photon count histogram

As explained in Chapter 4, to image atoms, we collect the fluorescence light scattered on a camera. The inset in Figure 7.1, contains a typical single shot fluorescence image. We analyze this image by summing the number of received photons x in a small region around each trap. Our goal is to use this information to infer the presence of an atom

in the trap. Indeed, since the tweezers loading is stochastic, as we do not control the initial atom number parity, we expect the number of atoms in the trap to be random each shot. The number of photons x is then expected to be larger when an atom is present than when the trap is empty. This is illustrated in Figure 7.1 that shows the typical histogram of the number of collected photons after many repetitions of the experiment. It is obtained with an exposure time $T = 30\,\mathrm{ms}$, a detuning $\Delta = -1.6\,\Gamma_{626}$ in the magic condition regime, and an intensity $I = 1.4\,I_{\mathrm{sat},626}$ One can see two peaks, one with a low photon count corresponding to the absence of an atom in the trap, and one with a larger photon count corresponding to an atom present in the trap. While the two peaks do not have the same width, as the photon shot noise increases with the number of photons, it turns out that they have roughly the same area. This bimodal distribution is a characteristic signature of the presence of single atoms [Sch+01]. Being in the near-magic regime turned out to be critical to observe it, as it has been observed for Yb [Sas19; Hui+23]. Indeed, in this regime, the imaging light also cools the atoms and does not risk heating them out of the trap during the picture.

It seems thus straightforward to link the number of photons to the presence of an atom. For example, by putting a threshold somewhere around $x_t = 18$, we could simply say that an atom is present if $x > x_t$ and absent otherwise. In a large majority of cases, we can then correctly infer the presence of an atom. Still, there is still a small overlap between the two peaks. It seems that the situation is sometimes ambiguous, and there could be some events where we would collect the same number of photons whether there is an atom in the trap or not. This would eventually limit our imaging fidelity since there would be no way to distinguish between the two situations. To try to see if the situation could be improved, we need to quantify and investigate the influence of the imaging parameters. For example, maybe a longer exposure time or a larger light intensity would be better to separate the two peaks?

7.1.2 Losses between pictures

In Figure 7.2 a,b, I show a comparison of two histograms obtained respectively with 30 ms and 60 ms exposure time. In the second case, the number of collected photons is indeed twice as large and the peaks are more separated. Still, one can see a "bridge" that remains and connects the two peaks. It seems that even for very large exposure times, there will always be some events where the number of photons collected falls between the two peaks. To understand what this means, it is useful to look at two consecutive pictures of the same trap. This is done in Figure 7.2 c, d that contains 2D

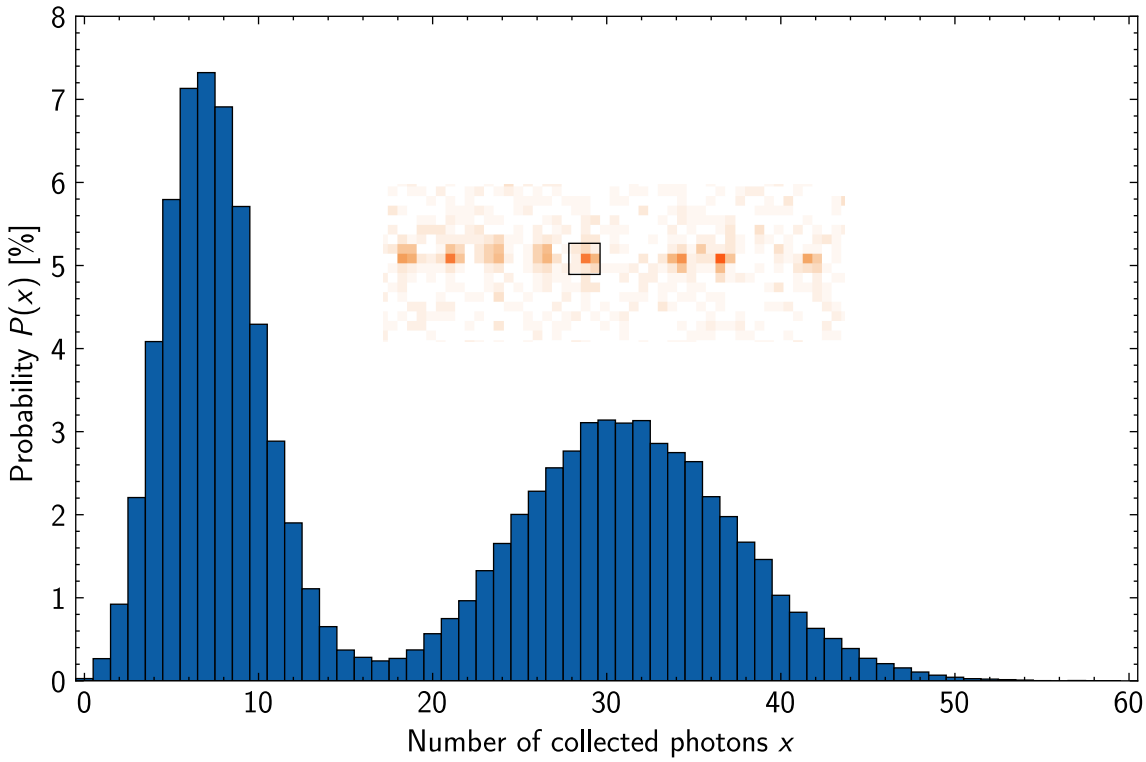

Figure 7.1. – Fluorescence histogram of a single trap. The peak around 7 photons corresponds to no atom in the trap, while the peak around 30 photons corresponds to an atom in the trap. These values are obtained for an exposure time of 30 ms, a detuning $\Delta = -1.6 \times \Gamma_{626}$ and an intensity $I = 1.4 \times I_{\text{sat},626}$. Inset shows the integration region around a trap for a typical array with spacing of 2.5 µm.

points corresponding to the number of photons collected in a first and second picture. The two pictures are separated by a few milliseconds, and the loading from the MOT is disabled, such that we would expect a strong correlation between the fluorescence of the two pictures. For example, if no atom is initially present in the trap, we expect to collect few photons in both pictures. This corresponds to the set of points in the lower left corner. Conversely, if an atom is present in the trap in both pictures, we expect to collect many photons in both pictures. The set of points in the upper right corner corresponds to this situation. For increasing exposure times, the two clouds of points become more separated, but one can also see a set of trailing points in the bottom right corner of Figure 7.2 d. These points correspond to the situation where some photons are collected during the first picture, but nothing is detected in the second picture. We interpret these events as an atom initially present in the trap but that disappears in the middle of the imaging. When an atom disappeared during imaging, it scattered a number of photons in between the zero and one-atom counts

during the first picture, and no photons in the second picture.

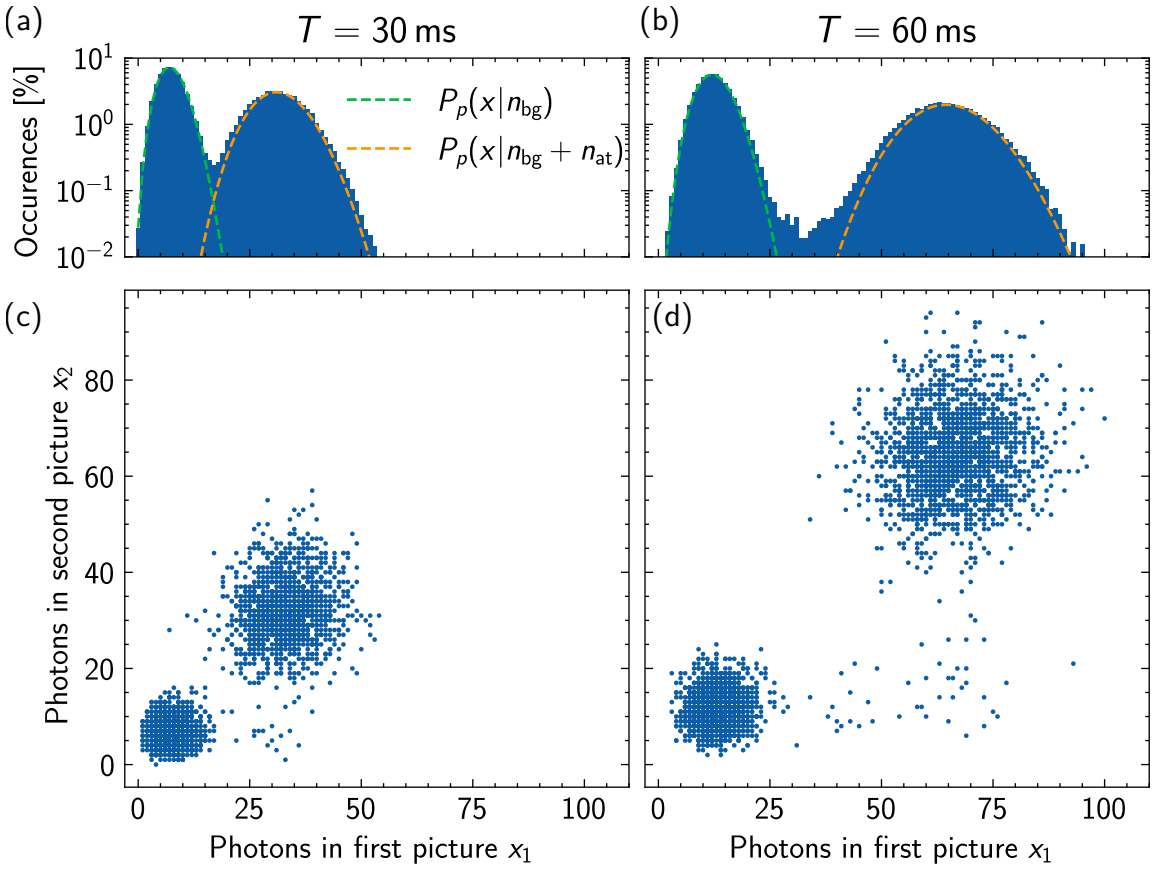

Figure 7.2. – (a, b) Fluorescence histograms of a single trap for an exposure time of 30 ms and 60 ms respectively. By increasing the exposure, the zero and one-atom peak are more separated, but a bridge between the two peaks remains. Dashed lines indicate the Poisson distribution for the number of expected photon depending if the trap contains one or zero atoms. (c, d) Joint events of the number of photons collected in two consecutive pictures respectively for 30 ms and 60 ms exposure time. In addition to the two clouds in the bottom left and top right corresponding to situations were the atom number does not change between pictures, there are also events in the bottom right of the plot. These events correspond to a loss of atom in the middle of a picture.

As we increase the exposure time, the number of events where an atom disappeared in the middle of a picture increases. Because of this, it is not obvious if trying to separate the two peaks would improve the imaging fidelity or if it would instead cause more of these losses.

On the joint plots of Figure 7.2 c, d, we sometimes see events in the upper left corner of the plot. They correspond to the situation where no light is scattered in the first picture, but some light is collected in the second picture. These events could be caused, for example, by remaining atoms from the MOT that gravitate around the tweezers and only end up trapped after sending a pulse of imaging light. In typical experiments, and in the plots for Figure 7.2 c, d, we remove such events by shinning the imaging light a few milliseconds before taking the first picture.

7.2 Quantitative analysis

7.2.1 Model of the imaging process

To quantify the losses observed and their effect on the performance of the imaging, it is fruitful to formalize a bit the problem. For a single image, let us define the probability $P(x, z)$ to detect x photons and to have an atom presence z during the picture. In the discussion to come, I will use the following notation for z:

- $z = \bigcirc$, when the trap is empty and never contains an atom
- $z = \bullet$, when the atom is present for the full duration of the picture
- $z = \CIRCLE$, when the atom is initially present but is lost before the end of the picture

I will not consider events where an atom appears in the trap during the picture, as this is very unlikely to happen in our situation. For smaller tweezer spacing, it might also be necessary to consider atoms hopping from one trap to another, but we do not observe it for out typical spacing of 2.5 µm.

In this problem, the presence of an atom z is called a *latent* or *hidden variable* as we cannot observe it directly. We instead only have access to the number of photons x in the image. Formally, we have a set of fluorescence counts x_i for each repetition i of the experiment, and we want to infer their associated z_i, as well as the parameters of the model. The problem can be generalized when considering two consecutive pictures, and we then have to infer the couple of events $(z_{1,i}, z_{2,i})$ from the two fluorescence counts $x_{1,i}$ and $x_{2,i}$.

For a single picture, one can define the probability of each situation as:

$$P(z) = \sum_{x=0}^{+\infty} P(x,z) = \begin{cases} P_{\text{empty}} & \text{if } z = \bigcirc \\ P_{\text{full}}(1 - P_{\text{loss}}) & \text{if } z = \bullet \\ P_{\text{full}} P_{\text{loss}} & \text{if } z = \text{◐} \end{cases} \tag{7.1}$$

Here P_{empty} is the probability that the trap is initially empty and $P_{\text{full}} = 1 - P_{\text{empty}}$ is the probability that the trap is initially occupied by an atom. P_{loss} is the probability that the atom does not survive the full duration of the imaging. To model P_{loss}, I will assume that for every photon the atom scatters, it has a small probability to be lost. This model is the one that matches best the data observed, and its justification will become clearer after understanding the origin of the losses[1]. Assuming a constant loss rate α during the imaging, the loss probability can be written as:

$$P_{\text{loss}} = \alpha \int_0^T e^{-\alpha t_l} \, \mathrm{d}t_l = 1 - e^{-\alpha T} \tag{7.2}$$

where the integral runs over the time at which the atom is lost.

The probability of each event can then be extended to two consecutive pictures 1 and 2:

$$P(z_1, z_2) = \begin{cases} P_{\text{empty}} & \text{if } z_1 = \bigcirc, z_2 = \bigcirc \\ P_{\text{full}}(1 - P_{\text{loss}})^2 & \text{if } z_1 = \bullet, z_2 = \bullet \\ P_{\text{full}}(1 - P_{\text{loss}}) P_{\text{loss}} & \text{if } z_1 = \bullet, z_2 = \text{◐} \\ P_{\text{full}} P_{\text{loss}} & \text{if } z_1 = \text{◐}, z_2 = \bigcirc \\ 0 & \text{otherwise} \end{cases} \tag{7.3}$$

In addition to the above probabilities, we also need to know the conditional probability $P(x|z)$ to detect x photons given the presence z of the atom. When the atom number does not change during the imaging, this probability is simply given by the Poisson distribution:

$$P(x|z) = \begin{cases} P_p(x|n_{\text{bg}}) & \text{if } z = \bigcirc \\ P_p(x|n_{\text{bg}} + n_{\text{at}}) & \text{if } z = \bullet \end{cases} \tag{7.4}$$

where $P_p(x|n) = e^{-n} n^x / x!$ is the probability density function for a Poisson distribution with an average of n photons. n_{bg} is the average number of background photons, and

[1] For example, if the losses were instead due to recoil heating from the imaging light, the atom would then be lost after a fixed number of scattered photons.

n_{at} is the average number of photons scattered by an atom.

The case where the atom is lost in the middle of the picture is a bit more involved, as we need to integrate the probability to detect x photons for all possible loss times t_l:

$$P(x|\text{◐}) = \frac{\alpha}{P_{\mathrm{loss}}} \int_0^T e^{-\alpha t_l} P_p(x|n_{\mathrm{bg}} + n_{\mathrm{at}} t_l/T)\,\mathrm{d}t_l \tag{7.5}$$

In our case, the losses are small enough such that the loss time is uniform during the exposure, i.e. $\alpha T \ll 1$, and we can simplify the probability to detect x photons when the atom is lost by replacing the exponential tail with a uniform distribution:

$$P(x|\text{◐}) \approx \frac{1}{n_{\mathrm{at}}} \int_{n_{\mathrm{bg}}}^{n_{\mathrm{bg}}+n_{\mathrm{at}}} P_p(x|n)\,\mathrm{d}n = \frac{Q(x+1, n_{\mathrm{bg}}) - Q(x+1, n_{\mathrm{bg}} + n_{\mathrm{at}})}{n_{\mathrm{at}}} \tag{7.6}$$

where in the last term, Q is the regularized upper incomplete gamma function. $P(x|\text{◐})$ is the probability density function for the number of collected photons is the case of an atom that is lost in the middle of the picture. It is a smooth plateau that bridges the two peaks in the histogram. This is illustrated in Figure 7.3 that shows the different contributions to the probability $P(x)$ to detect x photons. This last probability is simply given by:

$$P(x) = \sum_z P(x|z)P(z) \tag{7.7}$$

The conditional probability in the case of two consecutive images is simply the product of the single picture probabilities for physically realizable z_1 and z_2:

$$P(x_1, x_2|z_1, z_2) = P(x_1|z_1)P(x_2|z_2) \tag{7.8}$$

To summarize, these are the hypotheses made in the model presented above:

- The number of photons scattered by an atom follows a Poisson distribution.
- We only consider loss of atoms, events where an atom appears in the trap are ignored.
- Losses occur only during imaging, with a constant rate.
- The magnitude of the losses is small for the exposure times considered here.

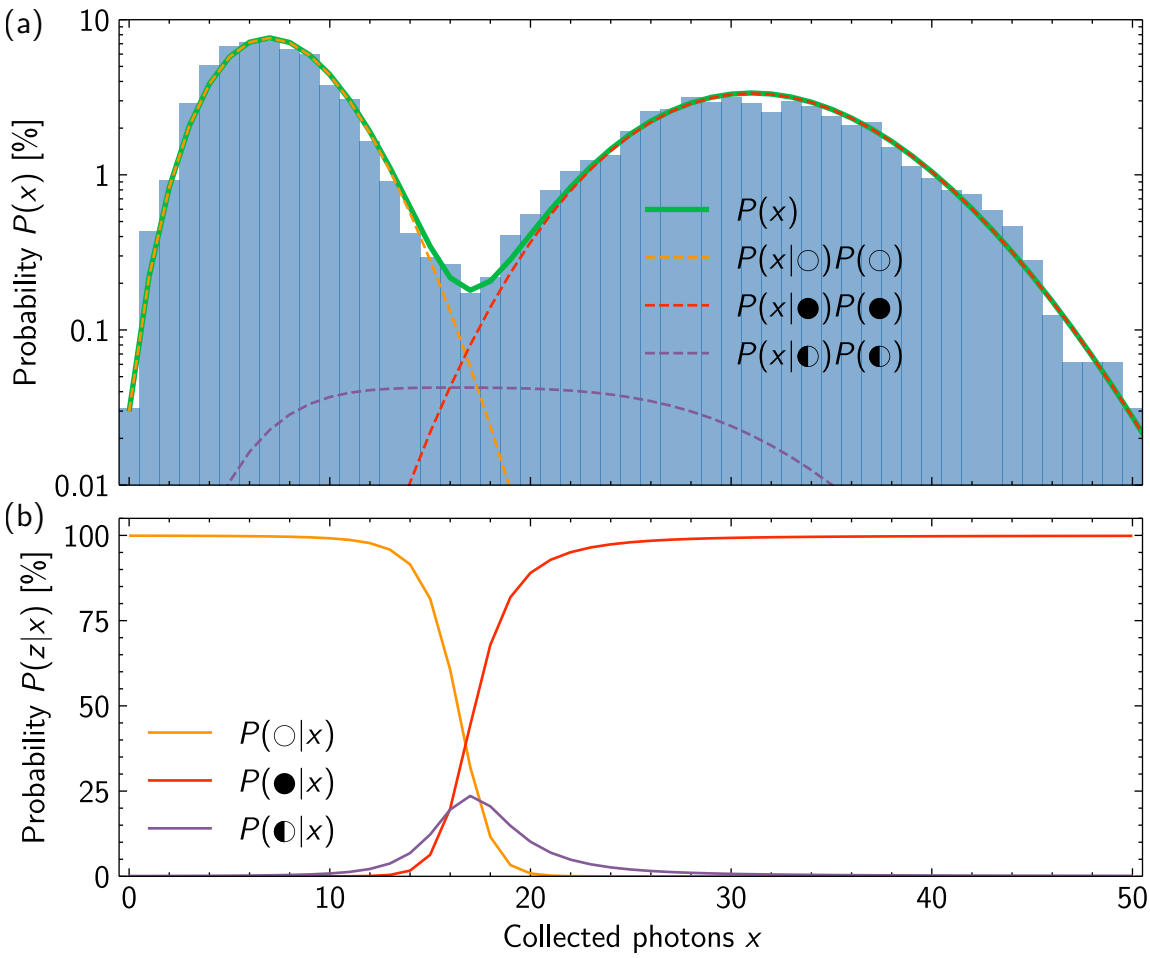

Figure 7.3. – (a) Contributions of the probability to detect x photons for the different situations z. The histogram is obtained from experimental data for an exposure time of 30 ms. The full curve represents the total probability $P(x)$ to detect x photons using parameters extracted from experimental data. Dashed curves are the different contributions $P(x|z)P(z)$. (b) Probability that detecting x photons corresponds to the presence of an atom in the same conditions. For small (large) x, the situation most likely corresponds to no (one) atom in the trap. In between the two peaks, the situation is ambiguous and can correspond to any event with different probability.

7.2.2 Parameter estimation

In the model presented above, the values of the different probabilities depend on some unknown experimental parameters: n_{bg}, n_{at}, P_{empty} and P_{loss}. In the discussion below, I will encompass all these parameters in a single vector $\boldsymbol{\theta} = [n_{\mathrm{bg}}, n_{\mathrm{at}}, P_{\mathrm{empty}}, P_{\mathrm{loss}}]$. If we can extract these parameters, we can then estimate any quantities of interest, for example the fidelity of the imaging process.

However, to do so, there is a chicken-and-egg problem: Knowing the true values of

the parameters, we could compute the probability that a measured fluorescence count corresponds to the presence of an atom using Bayes' theorem:

$$P(z|x) = \frac{P(x|z)P(z)}{P(x)} \tag{7.9}$$

These conditional probabilities are for example plotted in Figure 7.3 b. With this, we could determine the most likely event z for a given photon count x and determine the probability to be correct. But initially, we do not know what are the values of the unknown parameters. If instead we knew the correct label z_i on each fluorescence count x_i, we could then estimate the best value of $\boldsymbol{\theta}$. One way to do so would be to use the *maximum likelihood estimation* algorithm. In this case, we estimate the value of $\boldsymbol{\theta}$ by choosing the value that maximizes the probability of seeing the observed events z_i and x_i:

$$\hat{\boldsymbol{\theta}} = \arg\max_{\boldsymbol{\theta}} \prod_i P(x_i, z_i; \boldsymbol{\theta}) \tag{7.10}$$

with $P(x, z) = P(z)P(x|z)$. In practice, we would actually maximize the logarithm of this quantity, since it has nicer mathematical properties and it is more stable numerically:

$$\hat{\boldsymbol{\theta}} = \arg\max_{\boldsymbol{\theta}} \sum_i \log P(x_i, z_i; \boldsymbol{\theta}) \tag{7.11}$$

However, do to this we need to know the values of z_i, which is the goal of the problem. To solve this circular dependency issue, we use an iterative approach also called the *expectation-maximization* algorithm [DLR77]. We start with an initial guess for the unknown parameters $\boldsymbol{\theta}^t$. We then find a better guess $\boldsymbol{\theta}^{t+1}$ assuming that the z_i follow a distribution given by the current guess:

$$\boldsymbol{\theta}^{t+1} = \arg\max_{\boldsymbol{\theta}} \sum_i \left[\sum_{z_i} P(z_i|x_i; \boldsymbol{\theta}^t) \log P(x_i, z_i; \boldsymbol{\theta}) \right] \tag{7.12}$$

This formula is similar to the maximum likelihood estimation Equation 7.11, but instead of having a definite label for z_i, we instead attribute a weight for each possible value of z_i depending on how likely it is given our current estimation. We then repeat this step several times until $\boldsymbol{\theta}^t$ converges to the correct values of the parameters.

To keep the notations simpler, I presented the algorithm considering only a single picture per shot. However, in this case, the algorithm has trouble converging when the two peaks start to overlap and it is very sensitive to the initial parameter guess. Instead, the method is much more robust when taking two consecutive pictures each

shot. The method is straightforward to extend in this case, we just have to consider two data points for each repetition of the experiment:

$$\boldsymbol{\theta}^{t+1} = \arg\max_{\boldsymbol{\theta}} \sum_i \left[\sum_{z_{1,i}} \sum_{z_{2,i}} P(z_{1,i}, z_{2,i} | x_{1,i}, x_{2,i}; \boldsymbol{\theta}^t) \log P(x_{1,i}, x_{2,i}, z_{1,i}, z_{2,i}; \boldsymbol{\theta}) \right] \quad (7.13)$$

This is the method that we use to estimate the parameters of the imaging process. In Figure 7.3 a, the curves representing the different contributions to the probability $P(x)$ are obtained using this method.

7.3 Detection performance

7.3.1 Figures of merit

Now that we have a way to estimate the parameters of the imaging process, we can use this to determine its performance. There are several competing goals that we want to achieve. First, we want to minimize the probability P_{loss} of losing the atom during the picture. If the losses are too large, every time we take a picture, we will end up with fewer atoms to work with. This is particularly problematic when trying to realize large ensembles of atoms without defects.

However, this is not the full story: if we sent no light on the atoms, we would indeed have $P_{\text{loss}} = 0$, but we also get no information about the presence of the atom in the trap. That is why, in addition to minimizing P_{loss}, we also want to maximize the *fidelity* of the imaging process. This is the probability to correctly detect the presence of the atom. There are two main ways to define the fidelity of the imaging process in our case. The first one that I will call F_1 is the probability that we are correct in our labeling when considering a single image. In this case, we only care about the presence of the atom at the beginning of the image. An atom initially present but lost in the middle of the image is not an issue. We just need to know whether the atom was here. This is useful for instance when taking the last image in a shot. This single image fidelity is given by:

$$F_1 = P(+|\bullet)P(\bullet) + P(+|\half)P(\half) + P(-|\circ)P(\circ) \quad (7.14)$$

where the $+$ and $-$ signs correspond to positive and negative detection of an atom respectively.

The second way to define the fidelity, is the probability F_2 that the label we attributed in the first image is correct in a following picture. Here is an atom is lost in the middle of the picture, we would rather consider it not detected, and the fidelity is defined as:

$$F_2 = P(+|\bullet)P(\bullet) + P(-|\circledcirc)P(\circledcirc) + P(-|\circ)P(\circ) \tag{7.15}$$

It is better to have a large F_2 when we want to take multiple successive pictures of the atoms, for example to rearrange the traps. Depending on the application, we might want to maximize one or the other fidelity. However, in typical conditions, the optimal parameters are similar for both fidelities. It is worth noting that when the loss probability is negligible, the two definitions of the fidelity are indeed equal.

To detect if an atom is present, we compare the collected fluorescence to a predetermined threshold x_t. The probability of a positive detection is then:

$$P(+|z) = \sum_{x>x_t} P(x|z) \tag{7.16}$$

To determine the best threshold, we minimize the infidelity $1 - F$ as a function of the threshold position using the estimated parameters of the imaging. Typical values are shown in Figure 7.4. As one can see, depending on which fidelity we want to maximize, the optimal threshold is different. If we want to maximize F_1, we should choose a threshold at the right edge of the zero-atom peak to include the atoms lost. If instead, we do not want to detect the atoms lost and to maximize F_2, we should rather place the threshold on the left edge of the single atom peak. This distinction is mainly necessary when the two peaks are largely separated. In typical conditions, the difference between the two cases is small.

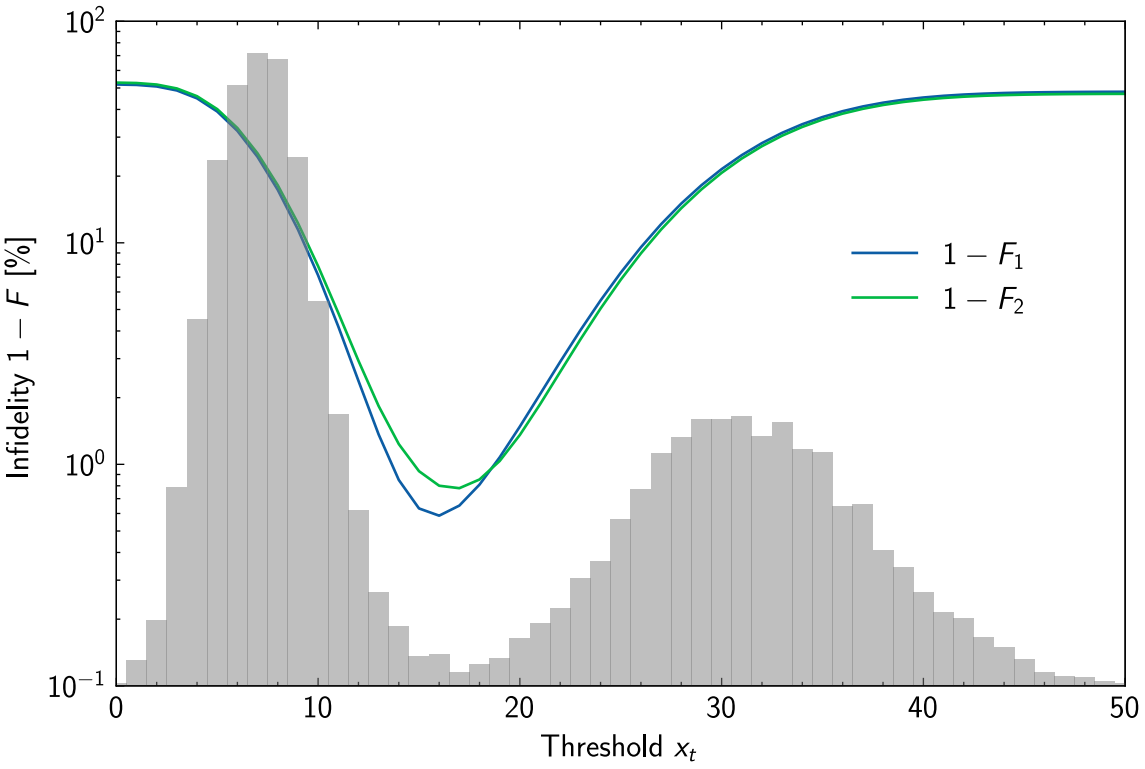

Figure 7.4. – Expected imaging fidelity as a function of the position x_t of the detection threshold in typical conditions. The optimal threshold is chosen to maximize the fidelity of interest.

Instead of maximizing the fidelity, we could also choose to minimize the probability of false negatives or false positives depending on the situation. For instance, if we wanted to have no defects after rearanging an array, we could decide to put the threshold on the right side of the loss plateau $x_t \approx 30$. In that case, we would be sure that all atoms detected were not lost and will be there for the next steps of the experiment. The tradeof is that we would discard many atoms that survived the imaging but did not scatter enough photons to be distinguished from a loss. We have not explored this possibility in detail, as the experiments presented here can tolerate a few deffects, but it could be useful in other situations.

7.3.2 Influence of the imaging parameters

The procedure described above allowed us to optimize the imaging parameters. For example, we looked at the influence of the imaging exposure time, as shown in

Figure 7.5 a. As one could expect, the number of collected photons n_{at} increases linearly with the exposure time. This is also the case for P_{loss} that follows the same trend. It confirms the hypothesis made before that the loss rate is constant during the imaging. In addition, this also shows that the losses are proportional to the number of collected photons. In other words, for each photon that an atom scatters, it has a small probability to be lost.

In Figure 7.5 b, the infidelity is plotted. It is large at short exposure when the two peaks are not well separated, but reaches a plateau after about 40 ms. At large exposure, the zero and one atom peak no longer overlap, but the infidelity still does not reach zero. What limits the fidelity is now the overlap between the two peaks and the loss plateau. In other words, if the loss occurs at the very beginning or end of a picture, it is not possible to distinguish an atom loss from a trap always empty or an atom that survived the full exposure. We usually work with exposures close to 30 ms as there is not much gain to choose a larger exposure time, and it would only increase losses and increase the duration of the experiment.

Compared to our published work [Blo+23], we achieve here comparable fidelity with about three times fewer losses. This is due to the improvement of the imaging setup explained in Chapter 4 that allows us to collect more photons. We can then work with fewer scattered photons and still have similar fidelity.

We also measured the influence of the trap power on these parameters as shown in Figure 7.5. In the magic regime, one would expect the trap depth to have little influence on the imaging performance as long as the trap is deep enough to hold the atoms. However, this is not what is observed, as shown in Figure 7.6. In this plot, for a trap power larger than about 1.5 mW, the losses per photon scattered $P_{\mathrm{loss}}/n_{\mathrm{at}}$ increase linearly with the trap depth. I will come back to this point in the next section. Still, it is clear that there is no point trying to image in deeper traps, as it will just result in larger losses. Instead, we prefer to image atoms in shallow traps with a tweezer power of 2 mW corresponding to a trap depth of 120 µK.

7.4 Origin of losses

The loss of atoms during a picture is the main limitation of the imaging process. It prevents us from scattering more photons to detect the atom. From the results of the

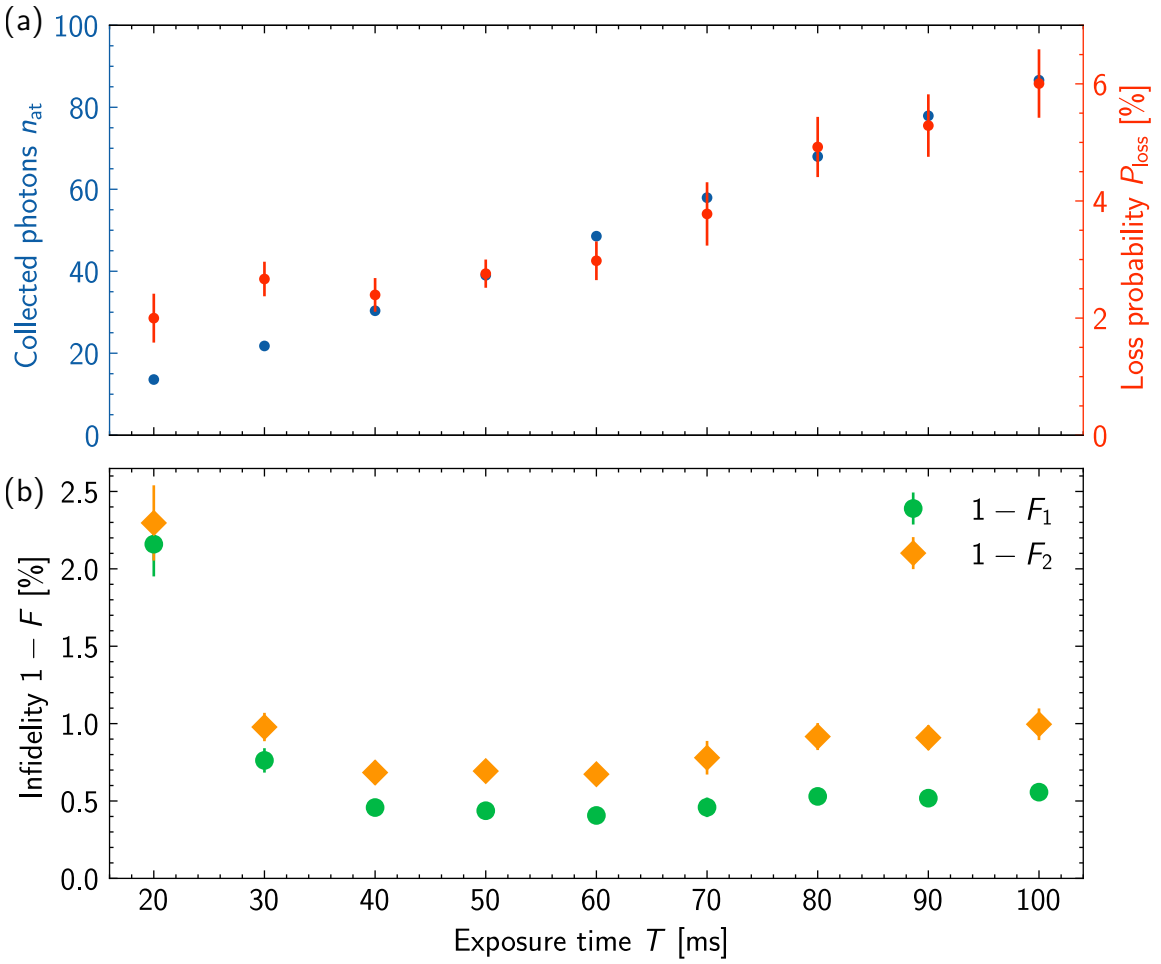

Figure 7.5. – (a) Influence of the exposure on the number of collected photons and the fraction of lost atoms. Both show a linear dependency with exposure time. (b) Influence of the exposure on the fidelity of the imaging. The data in this plot is taken for a power per tweezer of 2 mW.

previous section, the losses increase for each 626 nm photon scattered by the atom.

A possible explanation for the loss mechanism could have been that the imaging transition is not closed. If it were the case, atoms in the excited state would have a small probability to decay to other states than the ground state, and to be lost from the imaging cycle. This would be a plausible explanation if we were using the 421 nm transition for imaging as there are many states to which the atoms could decay from the excited state. However, the 626 nm transition we are using is fully closed since, apart from the ground state, there are no states to which the atom could decay without violating the dipole selection rules [Mai+14].

Instead, we attribute the losses to a *two-photon process*, which has also been observed

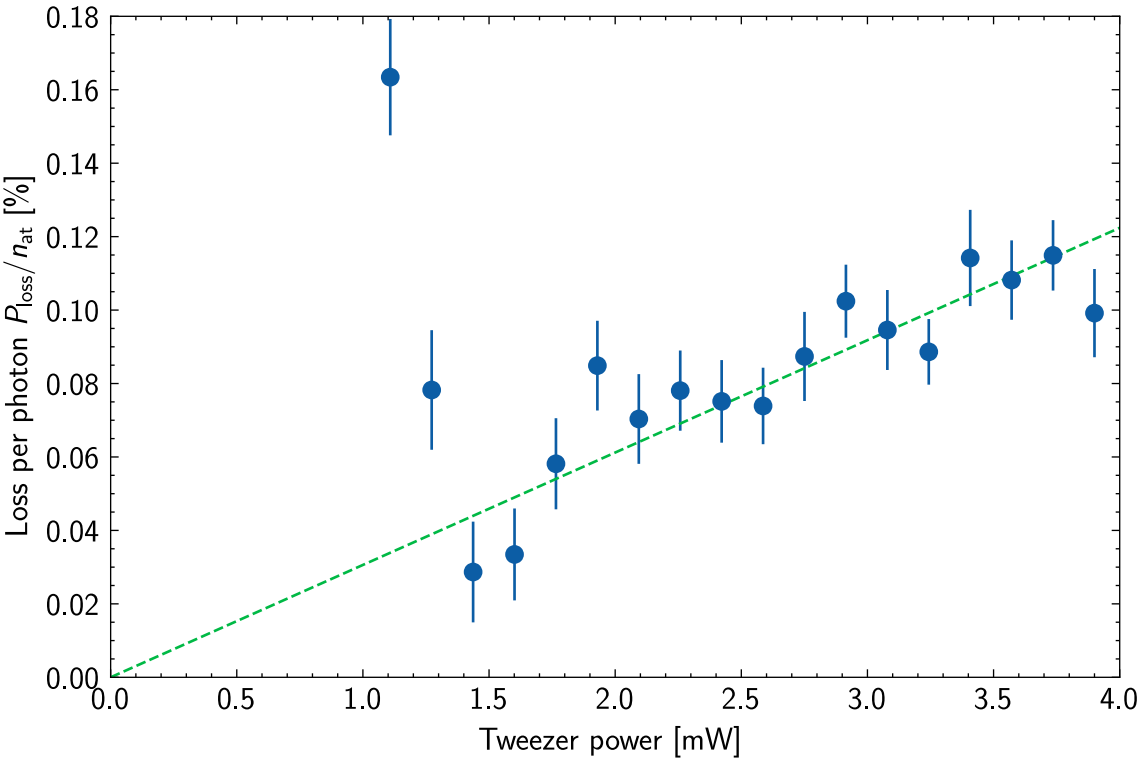

Figure 7.6. – Loss per photon scattered as a function of the tweezer power. Blue points are experimenal data, and the green dashed line is a linear fit. For low tweezer power, the trap is too shallow to hold the atoms during the imaging and they are lost after scattering a few photons. For power larger than 1.5 mW, the losses per scattered photons increase linearly with the trap power.

for Yb [Sas19]. This process is illustrated in Figure 7.7 a. When the atom is in the excited state E_{626} of the 626 nm transition, it has a small probability to absorb a trap photon at 532 nm and to be sent in a highly excited state E'. Indeed, for Dy with its large number of excited states there are some possible candidates E' whose energy is close to the sum of the energy of a 626 nm photon and a 532 nm photon. For example, there is a state $4f^{10}5d6p$ with $J = 10$ and energy 34 776.04 cm^{-1}, that lies only about 400 GHz away from the sum of the two laser frequencies. If an atom is sent to one of these highly excited states, it can then deexcite through many decay channels, some of which contain states M with very long lifetime. Atoms that end up in one of these metastable states M then stop being visible with the 626 nm imaging light and the event is registered as a loss. This explanation is consistent with the fact that the losses increase linearly with the trap power observed in Figure 7.6.

After an atom is sent to a metastable state, two things can happen at long time. Either the state M_a is not trapped at 532 nm and the atom is definitively lost, or the

state M_t is trapped and once the atom deexcites back to the ground state, it can be reimaged again. To confirm this hypothesis, we performed continuous imaging of the atoms for several seconds, without reloading the tweezers when an atom disappears. A typical fluorescence trace during this experiment is shown in Figure 7.7 b. An atom initially bright suddenly stops scattering light and becomes dark. After some time, the atom decays from its shelved state M_t and reappears. The cycle repeats possibly several times, until the atom is sent to a non-trapped state M_a and is lost. Even though we have not directly confirmed the presence of these dark states, this experiment leads us to believe that this phenomenon is the cause of the observed losses.

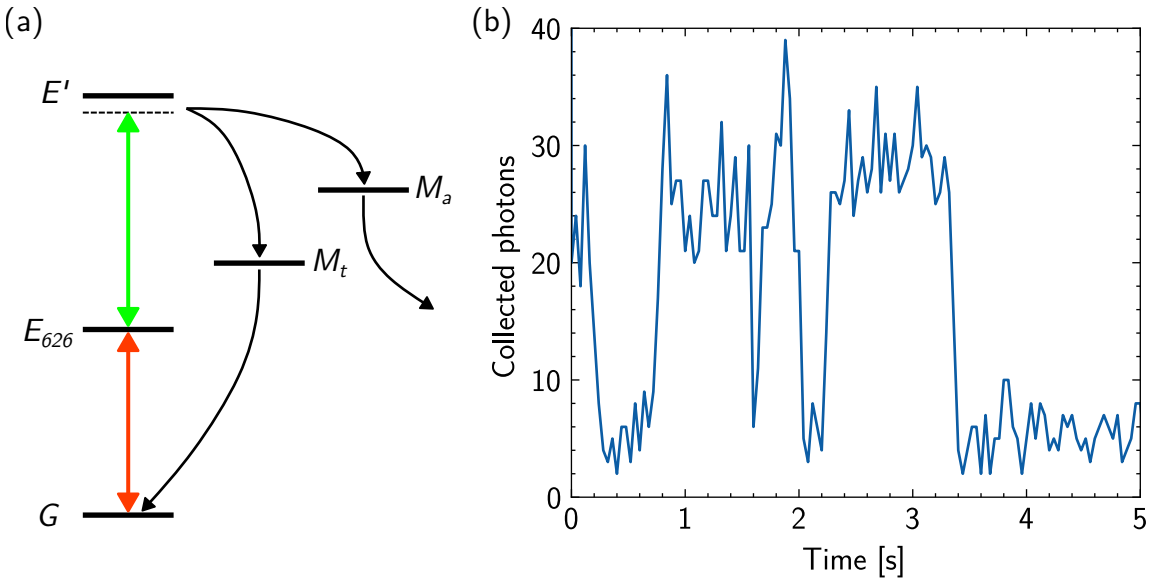

Figure 7.7. – (a) Illustration of the two-photon process leading to losses. See the main text for an explanation of the process. (b) Collected photons from a trap containing an atom under continuous imaging. After a few pictures, the atom is suddenly depumped to a dark state and stops scattering light. The atom then deexcites back to the ground state and reappears. This process repeats several times until the atom is eventually lost.

A way to mitigate this issue could be to repump the atoms shelved in metastable states back to the group state. This technique has been successfully applied for Sr for which the leakage channels are well known [Cov+19]. At the moment for Dy, it is not fully understood which are the dark states in which the atoms end up. It could be that some of the metastable states are not trapped at 532 nm, making it impossible to repump the atoms before they are lost.

Summary

In this chapter, I have shown how we image and detect single atoms in fluorescence pictures. The imaging fidelity is currently limited by losses to dark states when the atoms scatter photons on the 626 nm and 532 nm transitions.

In the future, we plan to replace our current microscope objective with 0.5 numerical aperture by one with a 0.7 numerical aperture. The collection efficiency would be almost doubled, which means that we expect to be able to reduce the losses by half and to increase the fidelity.

While it would be beneficial to reduce the imaging losses further and to increase the detection fidelity, the performances we were able to reach are good enough to enable us to do some light-scattering experiments. This will be the focus of the last part of this thesis.

Part III.

Collective light scattering in ordered ensembles

Chapter 8

Towards light-scattering experiments in ordered ensembles

Contents

In the previous chapters, I have explained how we trap and image individual atoms. With this, we are able to produce 1D chains of up to 75 traps randomly filled, and containing atoms with a temperature of about 5 µK. In this chapter, I will first explain how the interaction mediated by light between two atoms depends on the separation between the atoms, and why controlling the geometry is important. I will then show how we prepare ordered chains of atoms to move towards light-scattering experiments in ordered ensembles. The work presented here was mostly done during the third year of my PhD, together with another PhD student: Britton Hofer.

8.1 Light-scattering formalism in atomic ensembles

8.1.1 Classical dipole-dipole interaction

To derive the interaction mediated by light between two atoms in free-space, let us start by considering the classical case. When an oscillatory electric field $\boldsymbol{\mathcal{E}}(t) = \mathrm{Re}\{\boldsymbol{E}e^{-i\omega t}\}$ with frequency ω is applied on an atom, it induces a dipole moment that oscillates at the same frequency $\boldsymbol{\mathcal{D}}(t) = \mathrm{Re}\{\boldsymbol{d}e^{-i\omega t}\}$.

Such an oscillating dipole thus in turn radiates an electric field at a position $\boldsymbol{r}$ given by [Jac99]:

$$\boldsymbol{E}(\boldsymbol{r}) = -\frac{k^3}{4\pi\epsilon_0}e^{ikr}\left[\frac{\boldsymbol{d}-3\boldsymbol{u}_r(\boldsymbol{d}\cdot\boldsymbol{u}_r)}{(kr)^3} + i\frac{3\boldsymbol{u}_r(\boldsymbol{d}\cdot\boldsymbol{u}_r)-\boldsymbol{d}}{(kr)^2} + \frac{\boldsymbol{u}_r(\boldsymbol{d}\cdot\boldsymbol{u}_r)-\boldsymbol{d}}{kr}\right] \tag{8.1}$$

Here $k = \omega/c$ is the wave number of the light, and $\boldsymbol{u}_r = \boldsymbol{r}/r$ is the unit vector in the direction $\boldsymbol{r}$. The oscillatory term e^{ikr} represents retardation effects as the field radiated by the atom propagates at the speed of light. There are then terms that decay respectively as $1/(kr)^3$, $1/(kr)^2$ and $1/(kr)$. For distances small compared to the wavelength of the light, the near-field electrostatic $1/(kr)^3$ term dominates. On the opposite, at large distances, the term $1/kr$ dominates, and it causes the atom to radiate energy away.

When considering two atomic dipoles $\boldsymbol{d}_1$ and $\boldsymbol{d}_2$ placed respectively at $\boldsymbol{r}_1$ and $\boldsymbol{r}_2$, the second atomic dipole interacts with the field radiated by the first atom through the dipole-dipole interaction $-\boldsymbol{d}_2\cdot\boldsymbol{E}_1$:

$$V_{\mathrm{dd}}(\boldsymbol{r}) = \frac{k^3}{4\pi\epsilon_0}e^{ikr}\left[\frac{\boldsymbol{d}_1\cdot\boldsymbol{d}_2-3(\boldsymbol{d}_1\cdot\boldsymbol{u}_r)(\boldsymbol{d}_2\cdot\boldsymbol{u}_r)}{(kr)^3} + i\frac{3(\boldsymbol{d}_1\cdot\boldsymbol{u}_r)(\boldsymbol{d}_2\cdot\boldsymbol{u}_r)-\boldsymbol{d}_1\cdot\boldsymbol{d}_2}{(kr)^2} + \frac{(\boldsymbol{d}_1\cdot\boldsymbol{u}_r)(\boldsymbol{d}_2\cdot\boldsymbol{u}_r)-\boldsymbol{d}_1\cdot\boldsymbol{d}_2}{kr}\right] \tag{8.2}$$

Equation 8.2 represents the interaction energy between the two atoms. It is a complex number that takes into account collective dissipation between the two atoms; This interaction modifies the rate at which the dipole moment of the atoms decays by radiating energy.

8.1.2 Master equation

To generalize Equation 8.2 to quantum emitters, one has to write the combined hamiltonian between the atoms and the modes of the electromagnetic field, and then trace over the field degrees of freedom. This is a relatively tedious calculation that I will not reproduce here, but instead I will just give the equation that dictates the evolution of the internal degrees of freedom for two-level atoms [Leh70].

Since the atoms can emit energy in the environment by spontaneous emission, the system is dissipative, and one has to replace the Schrödinger equation by the Lindblad master equation over the density matrix of the system $\hat{\rho}$ [Ase+17]:

$$\frac{\mathrm{d}\hat{\rho}}{\mathrm{d}t} = \frac{1}{i\hbar}\left[\hat{H}, \hat{\rho}\right] + \mathcal{L}[\hat{\rho}] \tag{8.3}$$

Here $\hat{H}$ describes the coherent part of the evolution and is given by:

$$\hat{H}/\hbar = \sum_i \left[-\Delta\hat{\pi}_i^e + \frac{\Omega_i}{2}\hat{\sigma}_i^+ + \frac{\Omega_i^*}{2}\hat{\sigma}_i^-\right] + \sum_{i\neq j} J_{ij}\hat{\sigma}_i^+\hat{\sigma}_j^- \tag{8.4}$$

$\mathcal{L}[\hat{\rho}]$ represents the dissipative part of the evolution, and is given by:

$$\mathcal{L}[\hat{\rho}] = \sum_i \Gamma\left[\hat{\sigma}_i^-\hat{\rho}\hat{\sigma}_i^+ - \frac{1}{2}\left\{\hat{\sigma}_i^+\hat{\sigma}_i^-, \hat{\rho}\right\}\right] + \sum_{i\neq j}\Gamma_{ij}\left[\hat{\sigma}_i^-\hat{\rho}\hat{\sigma}_j^+ - \frac{1}{2}\left\{\hat{\sigma}_i^+\hat{\sigma}_j^-, \hat{\rho}\right\}\right] \tag{8.5}$$

In the previous equations, there are single body terms represented by a sum over the index i of the atoms.

The term $-\Delta\hat{\pi}_i^e$ represents the energy of the excited state in the rotating frame of the laser field, where Δ is the detuning of the laser with respect to the frequency of the two-level transition considered and $\hat{\pi}_i^e = |e_i\rangle\langle e_i|$ is the population operator for the excited state.

The terms $\Omega_i\hat{\sigma}_i^+/2$ and its complex conjugate represent the coupling between the laser field and the atoms. Here $\hat{\sigma}_i^+ = |e_i\rangle\langle g_i|$ and $\hat{\sigma}_i^- = |g_i\rangle\langle e_i|$ are respectively the rising and lowering operators for the transition, while Ω_i is the Rabi frequency of the atom i. In particular, Ω_i includes the position-dependent phase of the laser such that $\Omega_i = \Omega e^{i\boldsymbol{k}\cdot\boldsymbol{r}_i}$, where $\boldsymbol{k}$ is the wavevector of the laser, $\boldsymbol{r}_i$ is the position of the atom and Ω is a real number proportional to the amplitude of the laser field.

In the dissipative part, the term proportional to the transition decay rate Γ represents spontaneous decay of the excited state, where $\{\widehat{A}, \widehat{B}\} = \widehat{A}\widehat{B} + \widehat{B}\widehat{A}$ is the

anti-commutator between two operators.

In addition to the single body terms, what will interest us particularly are the two-body terms. In the coherent part, there are indeed spin exchange terms $J_{ij}\hat{\sigma}_i^+\hat{\sigma}_j^-$ while in the dissipative part, there are terms proportional to Γ_{ij}, similar to the single body decay, but that mix operators on two atoms.

The coupling terms J_{ij} and Γ_{ij} are related to the complex interaction potential introduced in Equation 8.2. First, let us introduce the dipole-dipole interaction operator obtained simply by promoting the dipoles $\boldsymbol{d}_i$ and $\boldsymbol{d}_j$ of the two atoms to operators:

$$\hat{V}_{\mathrm{dd}}(\boldsymbol{r}_i-\boldsymbol{r}_j)=\frac{k^3}{4\pi\epsilon_0}e^{ikr}\left[\frac{\hat{\boldsymbol{d}}_i\cdot\hat{\boldsymbol{d}}_j-3(\hat{\boldsymbol{d}}_i\cdot\boldsymbol{u}_r)(\hat{\boldsymbol{d}}_j\cdot\boldsymbol{u}_r)}{(kr)^3}\right.$$
$$\left.+i\frac{3(\hat{\boldsymbol{d}}_i\cdot\boldsymbol{u}_r)(\hat{\boldsymbol{d}}_j\cdot\boldsymbol{u}_r)-\hat{\boldsymbol{d}}_i\cdot\hat{\boldsymbol{d}}_j}{(kr)^2}+\frac{(\hat{\boldsymbol{d}}_i\cdot\boldsymbol{u}_r)(\hat{\boldsymbol{d}}_j\cdot\boldsymbol{u}_r)-\hat{\boldsymbol{d}}_i\cdot\hat{\boldsymbol{d}}_j}{kr}\right] \tag{8.6}$$

The coupling terms are then given by:

$$J_{ij}=\frac{\mathrm{Re}\{V_{ij}\}}{\hbar}\quad\text{and}\quad\Gamma_{ij}=-2\frac{\mathrm{Im}\{V_{ij}\}}{\hbar} \tag{8.7}$$

with

$$V_{ij}=\langle eg|\hat{V}_{\mathrm{dd}}(\boldsymbol{r}_j-\boldsymbol{r}_i)|ge\rangle \tag{8.8}$$

V_{ij} depends on the spacing r between the two atoms, but also on the orientation between the dipoles. In our case, we will only consider a σ^- polarized transition between two stretched Zeeman $|g\rangle=|G,m=-8\rangle$ and $|e\rangle=|E,m=-9\rangle$. In this case, one can use Wigner-Eckart theorem introduced in Section 5.1 to show that:

$$V_{ij}=\frac{3\hbar\Gamma}{8}e^{ikr}\left[\left(3\cos^2\theta-1\right)\left[\frac{1}{(kr)^3}-i\frac{1}{(kr)^2}\right]-\frac{1+\cos^2\theta}{kr}\right] \tag{8.9}$$

where θ is the angle that makes the line joining the two atoms with the quantization axis of the dipoles. In Figure 8.1, I plot the coupling terms in this situation for $\theta=0$.

Deep in the subwavelength regime, $r\ll\lambda$, Γ_{ij} reaches a constant value equal to Γ, while J_{ij} diverges proportionally to $1/(kr)^3$. In this case the coherent part of the interaction becomes much larger than the dissipative part. This is the regime we explored when looking at light-induced collisions in Chapter 6.

The remaining chapters will instead be done in the large distance regime $r>\lambda$.

In this case J_{ij} and Γ_{ij} decay as $\cos(kr)/(kr)$ and $\sin(kr)/(kr)$ respectively; The interactions have a long-range extent and oscillate with the distance. We thus expect their effect to depend strongly on the spatial arrangement of the atoms. If the atoms are distributed randomly, one could expect the contributions from different atoms to average out. Instead, if some spatial structure is present, the interactions could be enhanced [FJR16; BGA16a; Sha+17]. For example, it might be interesting to consider chains or grids of atoms. Such systems have been prepared using optical lattices [Rui+20], but here I will show how we can instead use the optical tweezer toolbox. This technique is more versatile than optical lattices with a fixed geometry, and allows us in principle to prepare a larger variety of configurations. In the rest of this chapter, I will present the experimental techniques we implemented to be able to prepare such ensembles.

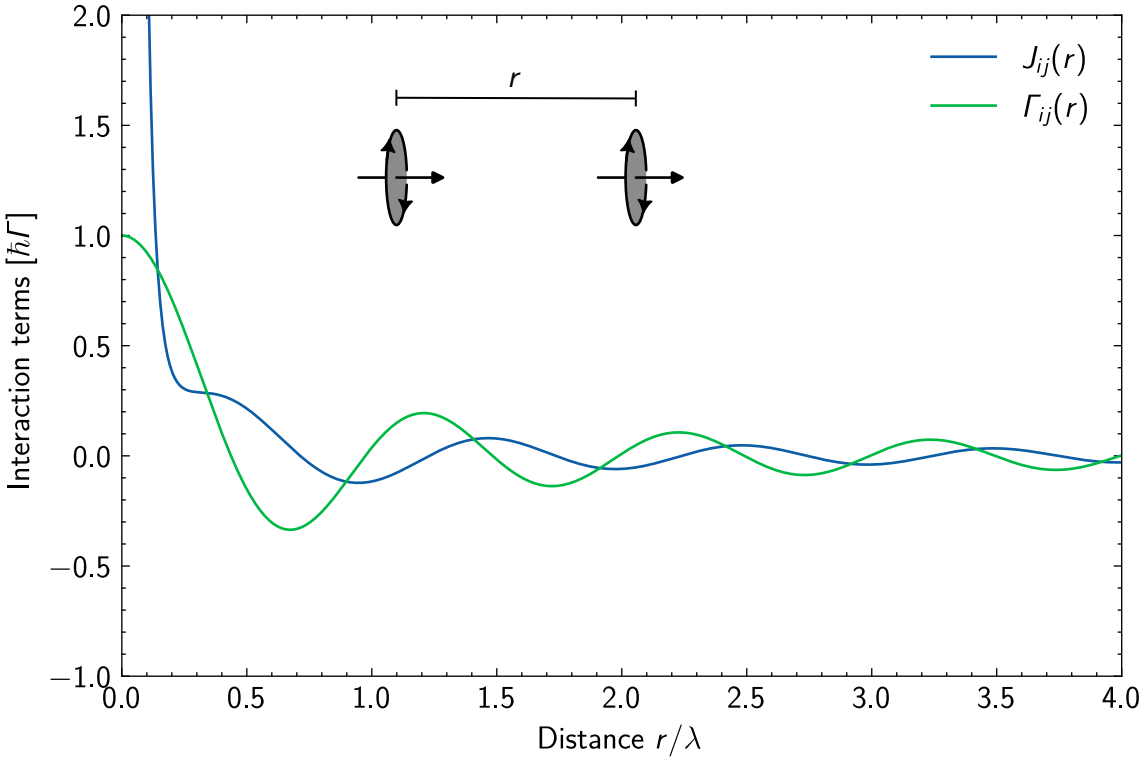

Figure 8.1. – Coherent and dissipative interactions as a function of the distance between two atoms. This corresponds to the situation of stretched circular dipoles aligned along their quantization axis.

8.2 Defect-free arrays

8.2.1 Arrays of traps

In the work presented in this thesis, we will consider only the simplest ordered system: A 1D chain of atoms with inter-atomic spacing d. To create this configuration, we generate multiple tweezers using the acousto-optic deflector (AOD). To do so, we drive the AOD with a multi-tone signal $V(t)$:

$$V(t) = \sum_i A_i \sin(\phi_i(t)) \tag{8.10}$$

where A_i and $\phi_i(t)$ are respectively the amplitude and the phase of the tone corresponding to trap i. The position of the trap is proportional to the frequency of the tone, as explained in Section 4.2.1. Therefore, to create an array of traps, we drive the AOD with a frequency comb:

$$\phi_i(t) = 2\pi\nu_i t + \varphi_i \quad \text{with} \quad \nu_i = \nu_0 + i\Delta\nu \tag{8.11}$$

The spacing between the traps is $d = \Delta\nu \times 2.45\,\mu\text{m}\,\text{MHz}^{-1}$, and can be changed by modifying the frequency difference $\Delta\nu$. This allows us to create arrays of traps with a controlled number of sites and spacing. There are some subtleties to this procedure, for example, how to choose the amplitudes A_i to have traps with equal depth, or how to choose the relative phases φ_i to limit the amplitude of the total signal $V(t)$. These are explained in more details in Appendix C.

8.2.2 Rearranging the tweezers

Even when generating a perfect array of traps, we also still have the issue of the stochastic loading of the tweezers. After loading them from the MOT and performing the light-induced collision step, each tweezer only has half-probability to contain an atom, as explained in Chapter 6. This is doubly detrimental: First because the inter-atomic distance is random, and second because the average spacing between the atoms is twice the trap spacing. To circumvent this limitation, we perform a *rearrangement* step of the traps, illustrated on Figure 8.2. The procedure is very similar to the one demonstrated in [End+16]. We start by taking a first picture of

the atoms after the light-induced collision step to know which traps are occupied, as shown in Figure 8.2 a. From this picture we determine how to move the traps to remove the empty sites. For 1D geometries, this is a simple problem: We turn off the empty traps and pack the occupied ones to the center of the array. Once the required moves are known, we compute the signal to send to the AOD to perform the rearrangement. The signal for each tone has a frequency $\nu_i(t)$ that smoothly interpolates over time between the initial frequency and the target frequency. Since the instantaneous frequency is given by the derivative of the phase, we then need to compute the following signal for each tone:

$$s_i(t) = A_i(t)\sin(\phi_i(t)) \quad \text{with} \quad \phi_i(t) = \phi_i(0) + 2\pi \int_0^t \nu_i(t')\,\mathrm{d}t' \tag{8.12}$$

There are some technical details to ensure that the phases reconnect correctly at the end of the move. This is explained in Appendix C.2. We move all the traps in parallel in about 500 µs, as illustrated on Figure 8.2 e that shows the spectrogram of the signal sent to the AOD. The shape of the trajectories in this diagram is simply a cosine curve, and it is what we use routinely on the experiment. We have tried other shapes, such as ones minimizing acceleration or jolt, but there was no noticeable improvement as long as the trajectory is smooth[1]. Once the rearrangement is done, we take a second picture of the atoms to check if the rearrangement was successful, as illustrated on Figure 8.2 d.

This signal for the rearrangement cannot be computed ahead of time, since we do not know which traps will be occupied after the loading step. For every shot of the experiment, we then need to recompute it after the first picture has been taken. This can be computationally expensive due to the large sampling rate of the arbitrary waveform generator (AWG) of about 600 MHz. Typically, for a chain of 75 traps and a move duration of 500 µs, we need to compute about 20 MSa of the form given by Equation 8.12. To speed up this computation, we perform it on a GPU. This way, the samples for all the time points can be evaluated in parallel, and it is significantly faster than if the computation was done on a CPU. Using a cheap GPU[2], the computation takes about 20 ms for a chain of 75 traps. There is still some technical jitter between the time when the picture is read from the camera and the time when the signal is sent to the AWG. Because of this, we typically wait 50 ms to 100 ms between the first picture and the rearrangement. This time is short enough to not be a major issue,

[1] The only trajectory to avoid is a linear ramp, since it causes large acceleration spikes at the start and end of the move, which heats up the atoms.
[2] NVidia Geforce RTX 3060

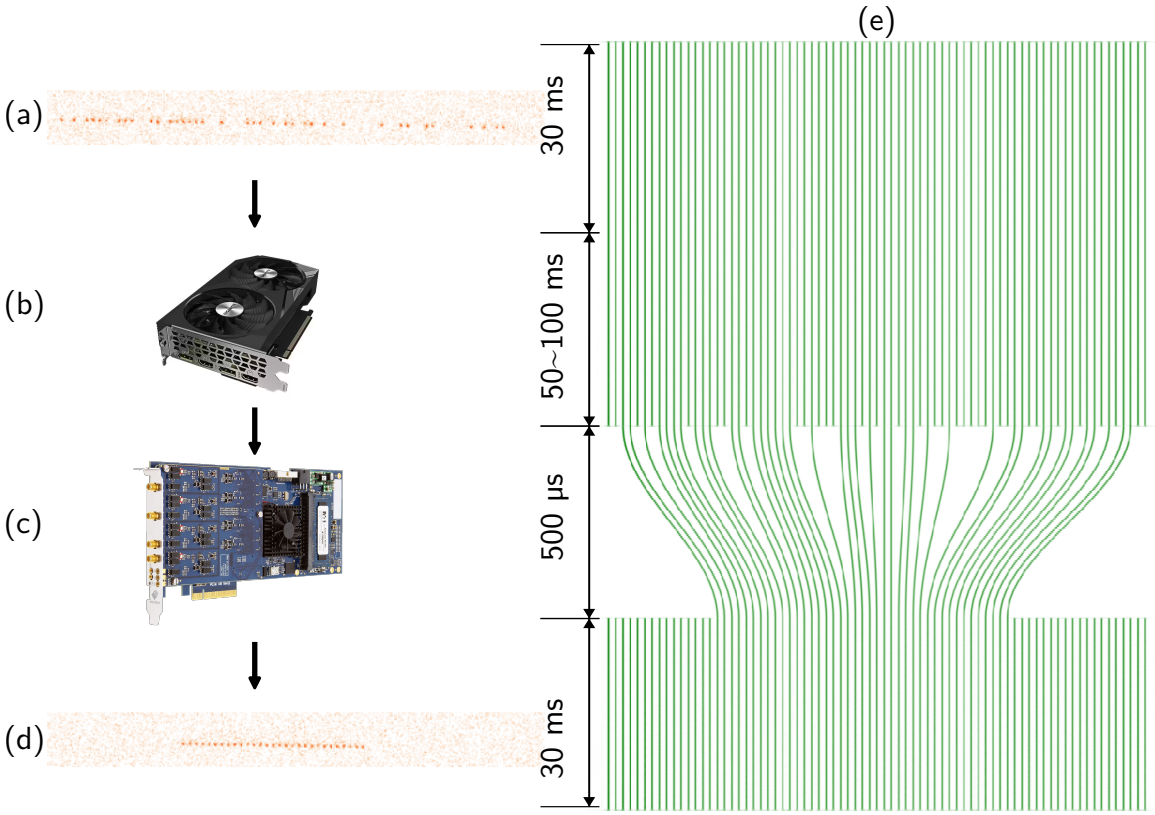

Figure 8.2. – Illustration of the rearrangement process. (a) Picture of the atoms with an initial random filling. (b) RF signal for the moves is computed on the GPU. (c) Signal is transfered from the GPU to the AWG driving the AOD. (d) Picture of the atoms after the move. (e) Spectrogram of the RF signal sent to the AOD.

but it starts to become a limitation when the repetition rate of the experiment is a few Hertz. This latency probably has a software origin, and it should be possible to reduce it in future experiments.

This reactive rearrangement procedure is incorporated in the experiment control software that I wrote from scratch for our experiment during my PhD. I will not describe the software in detail in this manuscript, but instead I point the interested reader to the documentation and sources of the project[3].

8.2.3 Rearrangement performances

The procedure described above allows us in principle to generate defect-free 1D arrays of atoms. In practice, some factors limit the fidelity of the rearrangement. For example, since we cannot detect the atom's presence in the first picture perfectly

[3] https://github.com/light-scattering-io/caqtus

reliably, we make errors in the moves we generate. In addition, even if an atom is correctly detected, it might be lost during the imaging or during the move, resulting in an empty trap after the rearrangement.

In practice, we observe that losses during imaging are the limiting factor. To show this, I plot on Figure 8.3 the filling fraction of the tweezers as a function of position in the chain after the rearrangement. In this experiment, we move the atoms to fill in priority the traps on the left edge of the chain. These traps have a filling fraction $1 - P_{\text{loss}} = 98\,\%$, which is the number of atoms that survive the first picture. The atoms on the right edge of the chain have a filling fraction that drops to 0 for i larger than 35. This is because, for an initial array of traps $N_t = 75$, there are not always enough atoms to fill more than $N_t P_1$ traps, where P_1 is initial filling fraction after the light-induced collision step.

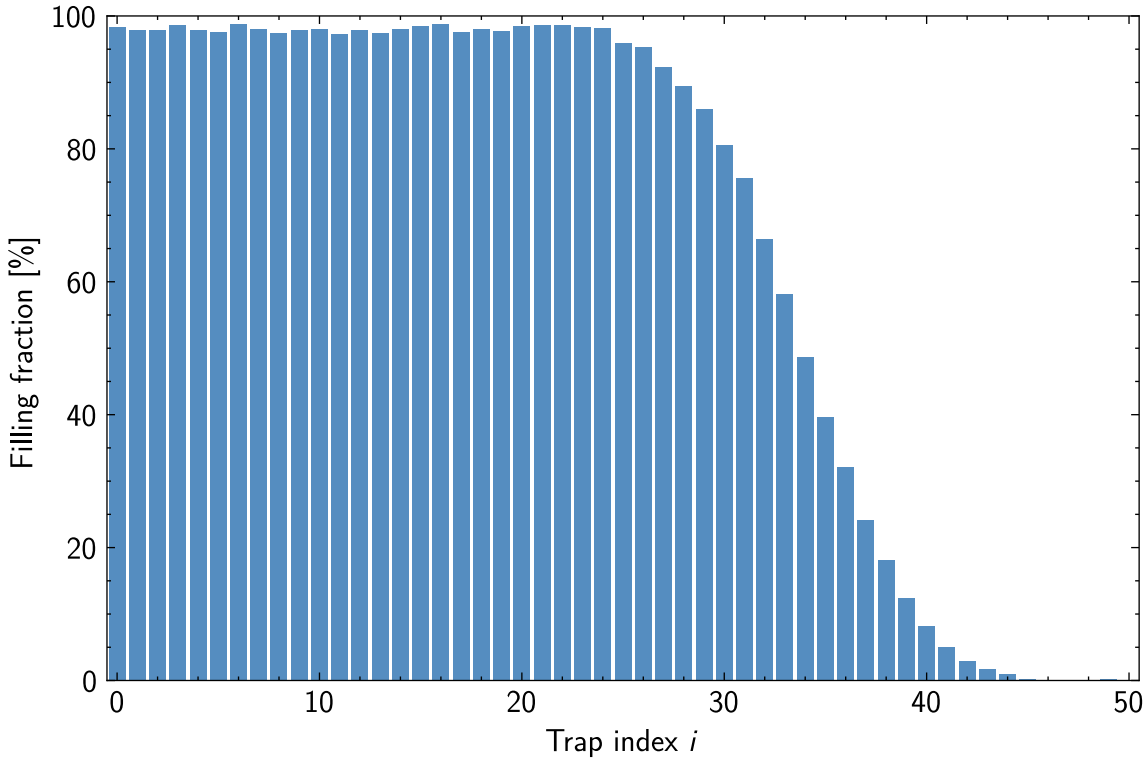

Figure 8.3. – Filling fraction of the tweezers after rearrangement. In the left side of the chain, the filling fraction is limited by the imaging fidelity. On the right side of the chain, the filling fraction drops because we do not always have enough atoms to fill all the traps.

As long as the move duration is long enough, we do not observe any loss from the move itself, and all losses are dominated by the imaging. The moves in themselves thus seem to not heat up or expel atoms. Still, the probability to prepare perfect arrays drops quickly with the target atom number N because of the imaging losses. Assuming

that we initially have more than N atoms before rearrangement, the probability to have a perfect array is $(1 - P_{\text{loss}})^N$. For $N = 30$, we thus only prepare a perfect array about half of the time. It turns out that the experiments presented here are resilient to a few defects, so this is not a major issue. However, it could become a limitation if some of the future experiments require perfect arrays. Hopefully, the imaging fidelity, which is the limiting factor, can be improved in the future by using a larger numerical aperture microscope objective, as planned on the experiment.

8.3 Small spacing arrays

In addition to having defect-free arrays, we also need the atoms to be close to each other. This is because the interaction strength scales as $\hbar\Gamma/kd$ for large enough distances. If we want the interaction to be comparable to the natural lifetime Γ of the excited state, we need the atoms to be at a distance d of the order of the wavelength of the light. All the experiments presented here are performed with the 626 nm transition, so we would like to bring the atoms below a few micron distances.

To do so, we bring the tweezers close to each other by dynamically reducing the frequency spacing $\Delta\nu$ between the different tones. With this technique, we can bring the distance between the atoms down to about 1 µm. This is possible thanks to the small trapping wavelength of 532 nm that allows us to create tweezers with a small diffraction limit. At this distance, the atoms can no longer be resolved individually when taking fluorescence images. This is not an issue since we can perform the experiment when the atoms are close, and then bring the tweezers far apart to image them afterward.

There is some limit to how close we can bring the tweezers, as shown in Figure 8.4. In this figure, I plot the fraction of atoms remaining in the traps after changing the spacing to a given value, waiting some time, and bringing the tweezers far apart again to take a picture. As one can see, for spacings smaller than about 1 µm, the number of atoms remaining in the traps decays the longer the traps are held close to each other. In addition, the initial fraction of remaining atoms goes down sharply at small spacings. This can be due to several reasons. At these distances, the traps overlap significantly, as plotted on Figure 8.5, which reduces their effective depth, allowing atoms to potentially move between traps. For the temperature we have, these events rarely occur and are not the main source of losses. Instead, the culprit is likely to be

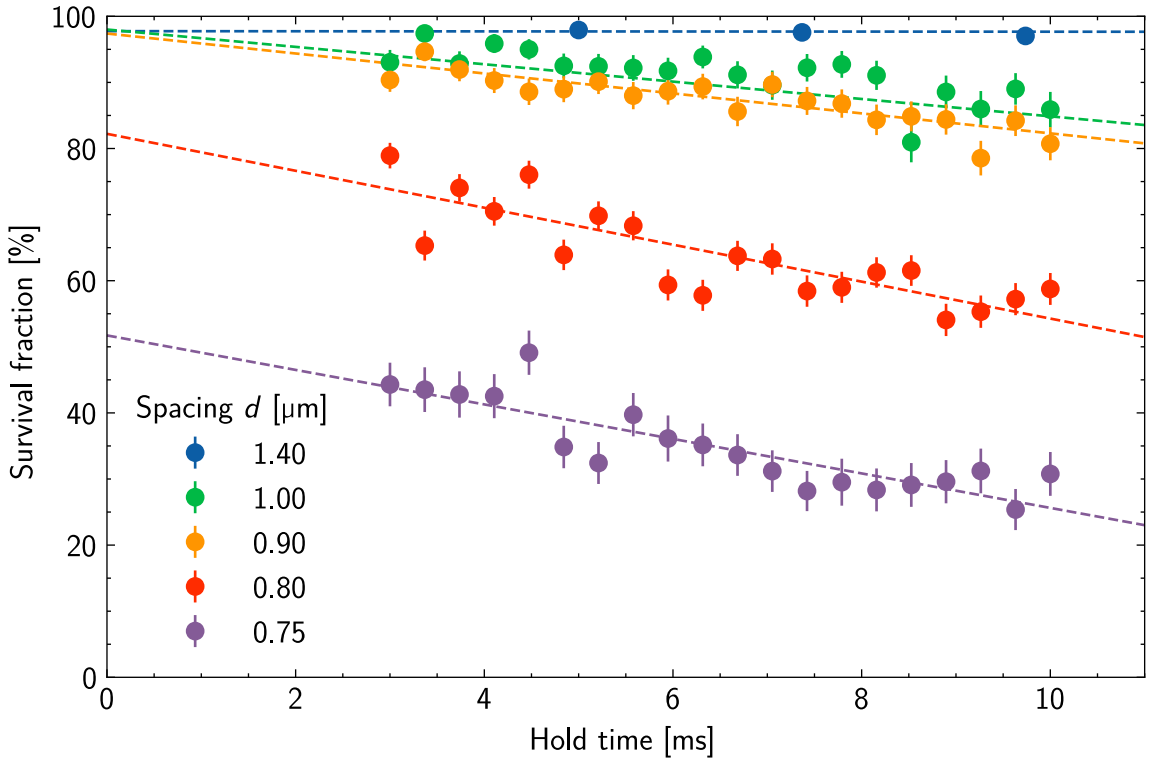

Figure 8.4. – Fraction of surviving atoms as a function of the duration for which the traps are held close together for different tweezer's spacings. Points are experimental data, while dashed line are linear fits. When the spacing is reduced, the loss rate of atoms increases, and the initial surviving fraction decreases.

an intensity beat between two neighboring tweezers. Indeed, two neighboring traps have a frequency difference $\Delta\nu$ of the order of a few hundreds of kilohertz when the traps are close. When the intensity profiles of two traps start to overlap, as shown in Figure 8.5, it results in an intensity modulation of the trap intensity at frequency $\Delta\nu$. This frequency is close enough to the atom's motional frequencies to cause heating and losses, and eventually prevents us from bringing the tweezers closer.

The intensity beat between neightboring traps can also be observed when performing spectroscopy in non-magic conditions. In this case, the intensity beat results in a modulation of the tweezer's light-shift at frequency $\Delta\nu$. This is equivalent to modulating the detuning of the light with the same frequency. This creates sidebands in the spectrum, split by $\Delta\nu$ from the central peak. When the transition is magic, a modulation of the tweezer's intensity does not cause a modulation of the light-shift and we do not observe sidebands.

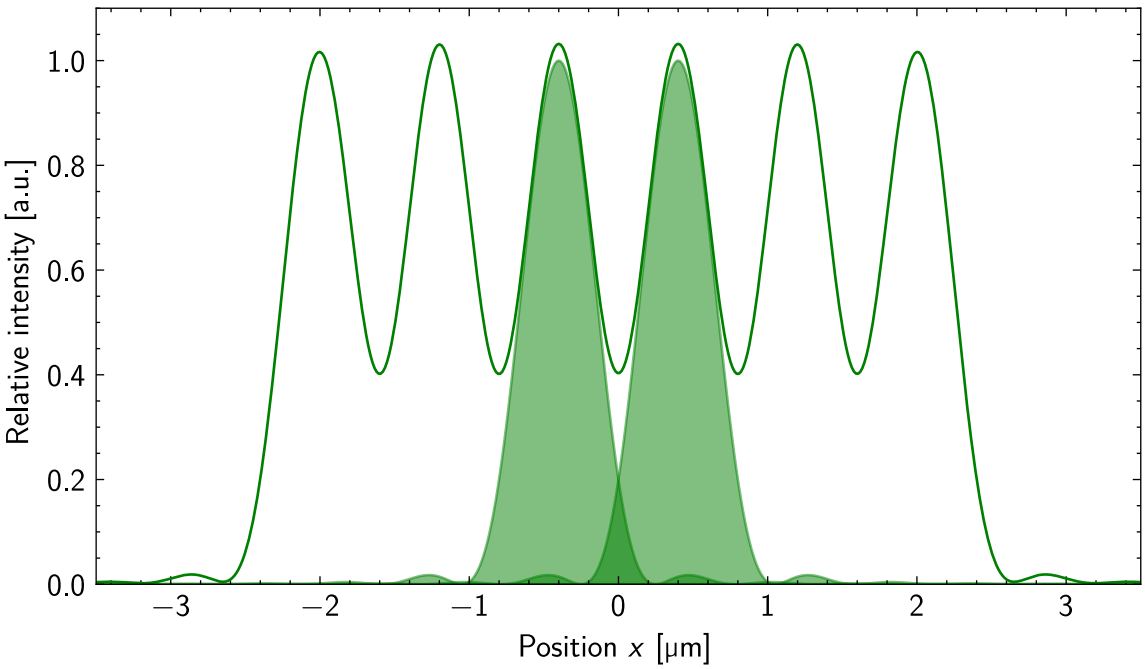

Figure 8.5. – Illustration of the overlapp between tweezers at spacing $d = 0.8\,\mu\text{m}$. The green line represents the total intensity from all tweezers, while the two filled areas represent the intensity profile of two neighboring tweezers. Each profile has some wings that start to overlap with the next tweezer. The intensity profile is obtained from Appendix B.

Using this technique, we can create chains with a spacing d as small as $d = 1\,\mu\text{m} = 1.6\lambda_{626}$, or $kd \simeq 10$. This is small enough that collective light scattering effects become noticeable, and I will discuss the experiments we performed in this regime in the next chapters. Still, it would be interesting to go to even smaller spacings, ideally below the wavelength of the light. A possibility would be to use a transition with a larger wavelength, for example, the one at 741 nm or even infrared transitions. Such transitions are usually narrower than the one at 626 nm, and using them for light scattering is not without challenges. Another option could be to interleave another tweezer array with the first one, using for example a second AOD with its frequency shifted to avoid the intensity beat. Using this technique, it might be possible to divide the minimum spacing by two, and go down just below 626 nm. A third solution could be to use the tweezers to load an *accordion lattice* with dynamically tunable spacing [Vil+17; Su+25]. Such a lattice can be loaded with a filling fraction close to unity using the tweezers, and then its spacing can be reduced below the wavelength of the light. These are some of the future improvements that will be implemented on the setup to reach the sub-wavelength regime.

8.4 Axial lattice

8.4.1 Positional disorder

Even though we are able to prepare near-perfect arrays of traps with small spacing, the atoms are actually not perfectly placed along a chain. This is because of the thermal disorder that causes the atoms to explore a range of positions around the tweezer's center. Indeed, an atom at temperature T in a harmonic oscillator of frequency ω has a position spread σ given by[4]:

$$\sigma = \sqrt{\frac{k_B T}{m\omega^2}} \tag{8.13}$$

For the tweezers with typical radial frequency $\omega_\perp = 2\pi \times 45\,\mathrm{kHz}$ and axial frequency $\omega_\parallel = 2\pi \times 6.5\,\mathrm{kHz}$, at a temperature of $5.5\,\mu\mathrm{K}$, this gives $\sigma_\perp = 50\,\mathrm{nm}$ and $\sigma_\parallel = 400\,\mathrm{nm}$. The axial position spread is significantly larger than the radial one because of the weaker confinement provided by the tweezers in this direction. This disorder is illustrated in Figure 8.6 a, where one can see the range of positions explored by the atoms when they are placed in tweezers at a spacing $d = 1.5\,\mu\mathrm{m}$. The amplitude of the disorder in the axial direction of the tweezers is actually comparable to the spacing between the atoms.

Since the interaction between two atoms separated by a distance r scales as $\hbar\Gamma e^{ikr}/(kr)$, we expect disorder to wash down the interaction if the fluctuation in distance δr is such that $k\delta r > 1$. The radial disorder in the direction of the chain causes a first order effect in the distance between the atoms. The magnitude of this fluctuation is $k\delta r = k\sqrt{2}\sigma_\perp \approx 0.7$ for the 626 nm transition, where the factor $\sqrt{2}$ comes from the fact that we consider the position difference between two atoms. This is actually not negligible and can reduce the effects we want to observe. Even worse is the influence of the axial disorder. It is a second order effect since the displacement occurs in the direction perpendicular to the chain, but since the axial confinement is weak, it still has a large magnitude $k\delta r = k\sqrt{2}\sigma_\parallel^2/d \approx 2.3$ for $d = 1\,\mu\mathrm{m}$.

To reduce axial disorder, one could try to increase the confinement of the tweezers such that their axial frequency goes from $\omega_{\parallel,1}$ to a larger value $\omega_{\parallel,2}$. The issue is that increasing the trap frequencies this way also results in significant adiabatic heating of the atoms. Indeed, under the assumption of adiabaticity $k_B T/(\hbar\bar{\omega})$ is constant

[4] I neglect here the zero-point motion. This is valid in the axial direction of the tweezers for which $k_B T/\hbar\omega_\parallel \approx 20$, but might not be totally correct in the radial direction since $k_B T/\hbar\omega_\perp \approx 2.5$.

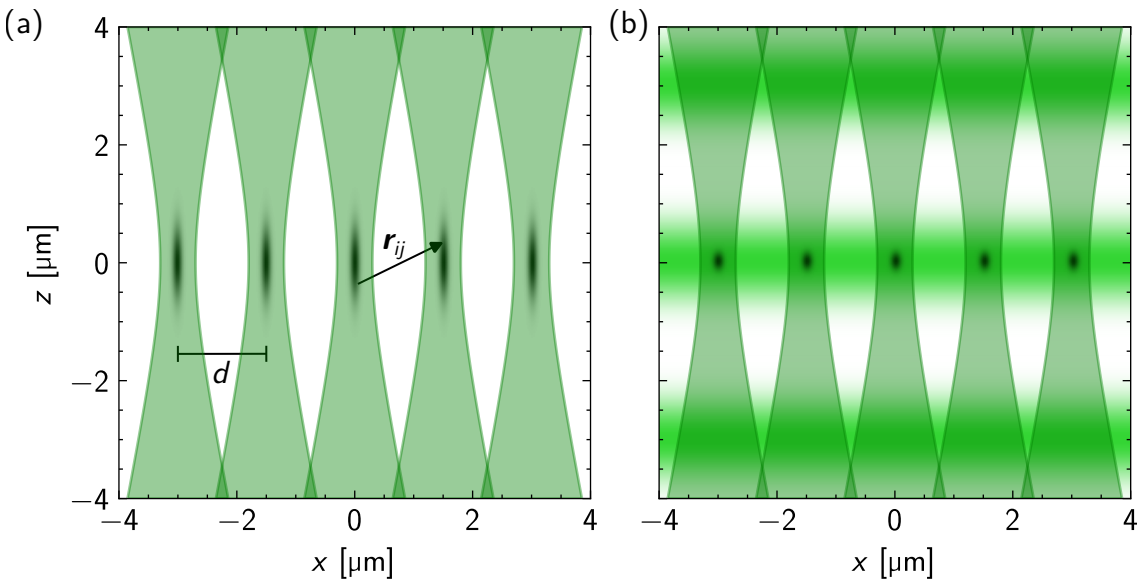

Figure 8.6. – (a) Positional disorder of the atoms in the tweezers for a spacing $d = 1.5\,\mu\text{m}$. The dark green areas represent the intensity profile of the tweezers, and the black areas represent the probability density function of the atoms. (b) Positional disorder in the combined potential of the tweezers and axial lattice. The bright green stripes represent the axial lattice intensity profile.

during the compression, where $\overline{\omega} = (\omega_\perp^2 \omega_\parallel)^{1/3}$. As such, the temperature increases by $\omega_{\parallel,2}/\omega_{\parallel,1}$. Therefore, the axial position spread only scales as $(\omega_{\parallel,1}/\omega_{\parallel,2})^{1/2}$, thus requiring a prohibitively large increase in tweezer power to reduce disorder to tolerable levels. In addition, if the temperature increases too much, it makes it impossible to perform experiments in time-of-flight as the hot atoms start to spread a lot when the tweezers are off.

To solve the issue, we decided to add a lattice to provide stronger confinement, but only in the axial direction of the tweezers. In this case, when the axial frequency increases from $\omega_{\parallel,1}$ to $\omega_{\parallel,2}$, the temperature only rises by $(\omega_{\parallel,2}/\omega_{\parallel,1})^{1/3}$, thus resulting in a reduction of the axial disorder by $(\omega_{\parallel,1}/\omega_{\parallel,2})^{6/5}$. This is a better solution to increase the axial confinement without heating the atoms too much, and it is the one we implemented on the experiment.

Our goal is to increase the axial frequency from $\omega_\parallel = 2\pi \times 6.5\,\text{kHz}$ to about $\omega_\parallel = 2\pi \times 30\,\text{kHz}$. In this case, the temperature would rise from 5.5 µK to about 9 µK. The positional spread in the radial direction would increase a bit to $\sigma_\perp = 70\,\text{nm}$ due to this adiabatic heating, but the axial spread would decrease to $\sigma_\parallel = 90\,\text{nm}$. Such a situation is illustrated on Figure 8.6 b, and as one can see, it would help a lot to reduce the disorder in the chain.

8.4.2 Lattice setup

To implement the solution presented above, we added a shallow angle lattice at $\lambda_{\text{lat}} = 532\,\text{nm}$ to the setup, as illustrated on Figure 8.7. Sending two coherent beams with a half-angle θ on the atoms results in an interference pattern with fringe spacing $d_{\text{lat}} = \lambda_{\text{lat}}/2\sin(\theta)$. There are several competing goals when choosing the lattice spacing. A small spacing provides strong confinement, which is beneficial. However, if the spacing is too small, we are not guaranteed that the atoms will be loaded in a single sheet of the lattice when ramping it up. To ensure that this is the case, we need the lattice spacing to be larger than the axial spread of the atoms in the tweezers. In addition, a small spacing requires a large angle between the lattice beams. This reduces the area over which the two lattice arms overlap, and makes it difficult to have homogeneous confinement over large arrays. The compromise we chose is to have an angle $\theta = 5°$, corresponding to a spacing $d_{\text{lat}} = 3\,\mu\text{m}$.

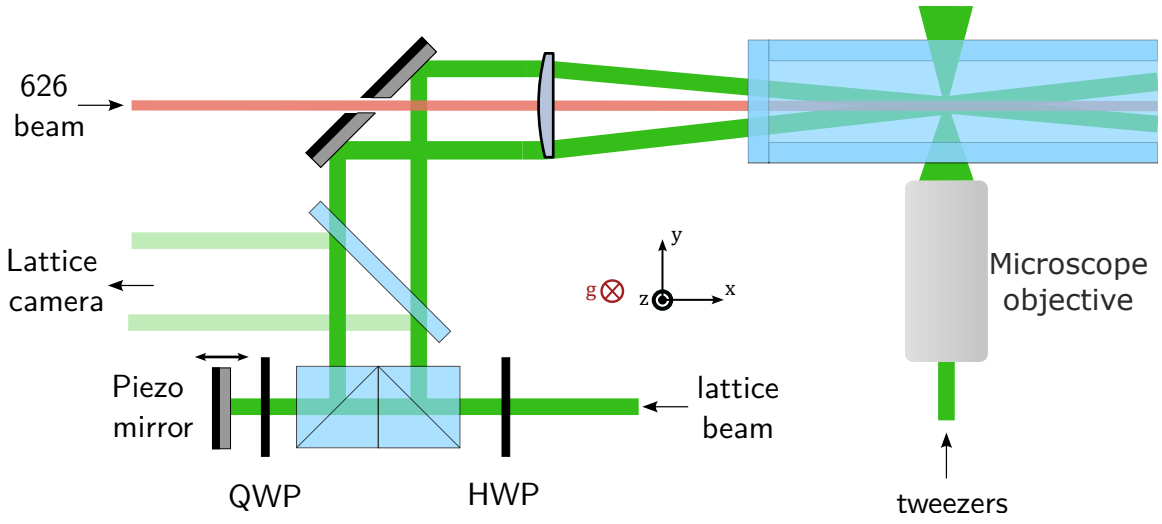

Figure 8.7. – Schematic of the lattice setup used to increase the axial confinement in the tweezers. See text for an explanation of the different components.

The light of the lattice is produced by the same laser as the tweezer's, but its frequency is shifted by a few hundred megahertz with an AOM to avoid interferences with the tweezers. The lattice is created by splitting a single beam into two parallel beams using two PBS mounted side-by-side, as demonstrated in [Vil+17]. The power balance between the two arms is controlled with a half-wave plate (HWP) before the cubes, such that there is typically 0.5 W in each arm. One beam is reflected on a piezo

mirror, making it is possible to control the path difference between the two beams and to move the fringe position along y. The two beams then reflect on a mirror drilled in its center. The hole in the mirrors allows us to send additional beams, for example at 626 nm, along the direction of the atomic chain x.

To ensure that the two arms interfere, they must have the same polarization. The easiest situation is when each arm has linear polarization along the z direction such that the polarization is not modified when the beams are going through the focusing lens. Because of this condition, the lattice is not magic for the 626 nm transition. Due to the finite overlap area between the two beams, the lattice intensity is not perfectly homogeneous across the chain of tweezers. This makes it difficult to cool efficiently in the lattice using the 626 nm transition since the detuning of the cooling light varies significantly between different atoms. For this reason, we do not cool the atoms once the lattice is turned on.

8.4.3 Alignment

Due to the small waist of the lattice beams, it is rather tricky to align them on the atoms when coming from the direction perpendicular to the tweezer beams. To perform the procedure, we initially aligned each beam independently. To do so, we started by sending precursor resonant beams at 421 nm instead of the 532 nm beams. Indeed, it is easier to see the effect of a resonant beam on the atoms, since it will have a strong effect, either on the MOT or on the atoms in the tweezers. Once this beam is known to pass through the atoms, we align the 532 nm beam onto it. To fine-tune the alignment of each lattice beam on the atoms, we then look at fluorescence images. When a lattice beam is well aligned on the atoms, it light-shifts the imaging transition, since it does not have a magic polarization. We thus optimize the lattice alignment by making the atoms disappear from the images. We do this for both arms of the lattice independently, such that we know that they cross on the chain of atoms.

After this first alignment step, a useful diagnostic is to measure the light-shift applied by the lattice. To do this, we adiabatically ramp up the lattice over 5 ms, while keeping the tweezers on, and then take regular fluorescence images for 30 ms. We then scan the imaging frequency and measure at which frequency the atoms fluoresce. An example of this is shown on Figure 8.7 a. As one can see, the light-shift takes a maximum value around $x = -30\,\mu$m, corresponding to the location where the two lattice arms cross. This is not exactly centered in the middle of the chain, but it can

be easily corrected by changing the position of the lens focusing the two beams that is mounted on a translation stage such that the beams cross at $x = 0\,\mu m$.

What is more surprising is the existence of two branches in the spectrum, on each side of the position $x = 20\,\mu m$. This effect is due to the misalignment between the plane of the lattice fringes and the axis of the chain defined by the tweezers. This is illustrated on Figure 8.8 b. When the lattice is ramped up, the atoms move in the y direction towards a bright fringe of the lattice. They then end up in the fringe closest to their initial position, which is different depending on their position in the chain, as illustrated on Figure 8.8 c. Since the fringes all have a different intensity, we see a discontinuity in the spectrum at the location where the atoms switch from one fringe to the other. By changing the relative phase between the two beams, we observe that the position of the discontinuity changes (not shown here). Depending on the length of the array and the misalignment between the lattice and the tweezers, there can even be more than one discontinuity. We then walk the lattice beams to make this discontinuity disappear, until we know that all atoms in the chain end up in the same fringe when the lattice is turned on.

However, the procedure described above is not sufficient to have the best alignment between the line of tweezers and the lattice fringes. Indeed, even if all atoms fall down in the same fringe, there might still be a slight misalignment between the lattice and the chain of tweezers. To solve this issue, we perform a procedure similar to the one explained in [You23]. Instead of looking at the light-shift of the atoms, we perform parametric heating by modulating the tweezer's potential to probe the mechanical frequency of the lattice in the y direction. The idea is that when atoms are located in a bright fringe that coincides with the center of the tweezers, modulating the tweezers only adds a quadratic potential on top of the lattice. In this case, modulating the tweezer's intensity is similar to modulating the lattice intensity, and we do not expect to see heating at the lattice frequency, but instead at twice this value. This situation is illustrated on Figure 8.9 e. However, if the tweezer's bottom is not aligned with a bright fringe, modulating the tweezer's power adds a linear perturbating potential that induces losses when the modulation is done at the lattice frequency. Crucially, there are no losses when modulating at twice the lattice frequency. This corresponds to the situations illustrated in Figure 8.9 f, g.

We thus perform an experiment where we measure the survival of the atoms after a modulation of the tweezer's power by 20 % for 100 ms. The result is shown in Figure 8.9 a. We observe losses when modulating at the lattice frequency only for

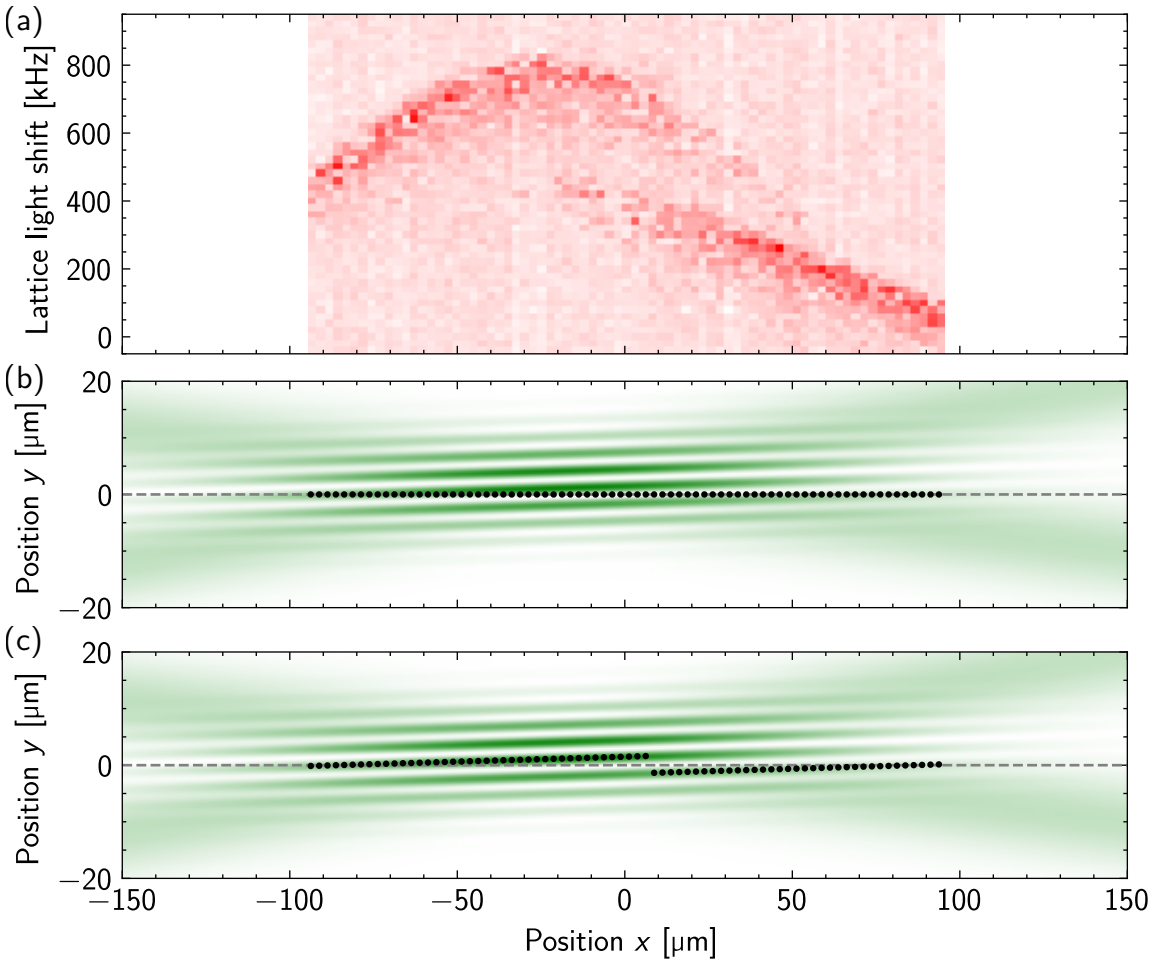

Figure 8.8. – (a) Fluorescence spectrum of the atoms in the lattice after the initial alignment as a function of the position along the chain. Each column corresponds to the signal from an atom, and each row corresponds to a probe frequency. The colormap corresponds to the number of collected photons. (b) Illustration of a misalignment of 1° between the lattice plane and the chain of the tweezers. The green image represents the lattice intensity profile, and the black dots represent the initial position of the atoms in the tweezers before the lattice is ramped up. The position $y = 0$ corresponds to the center of the tweezers in their axial direction. (c) In this case, the black dots represent the position where the atoms settle to after the lattice is ramped up.

the atoms on the left and right side of the chain. Atoms in the center survive the modulation since the tweezer's bottom coincides with a bright fringe of the lattice. These atoms are only lost when modulating at twice the lattice frequency, which is not visible on this plot. The fact that the atoms are lost on the sides when the modulation is resonant, but not in the center, indicates that the lattice is not well aligned with the tweezers, as shown in Figure 8.9 b.

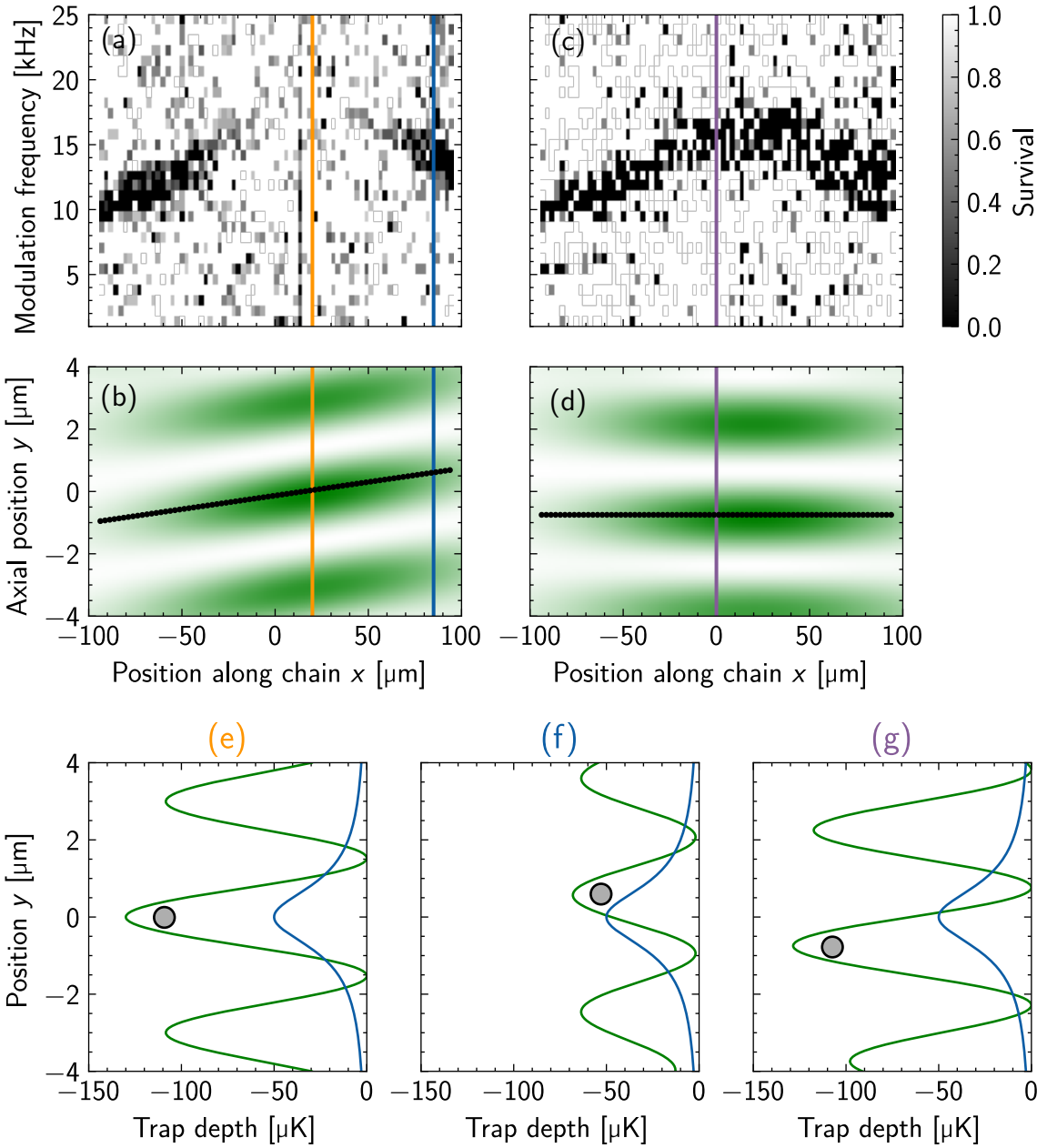

Figure 8.9. – (a) Induced losses in the lattice when modulating the tweezer's power. The columns correspond to the traps along the chain, and the rows correspond to different modulation frequencies. When the lattice and tweezers coincide along y, we observe no losses when modulating at the lattice frequency (vertical orange line), while we observe losses when they do not coincide (vertical blue line). Here, the power in each arm is 0.15 W instead of the typical 0.5 W. (b) Illustration of a 0.5 degree misalignem ent between the lattice and tweezers. (c) Similar loss curve to (a), but after alignment of the lattice. We observe homogeneous losses at the lattice frequency when the lattice is displaced by half an interfringe with respect to the tweezer's center. (d) Illustraction of the lattice potential well aligned to the tweezers. (e) Potential of the lattice (green curve) and of a tweezer (blue curve) as a function of the axial position for a position x along the chain where the tweezer center coincides with the bright fringe. (f, g) Illustration of the potentials when the lattice has an offset from a tweezer center.

To align the lattice, we then walk one of its arms until the loss curve is the most homogeneous as shown in Figure 8.9 c. In this case, we know that the relative displacement between the tweezer's centers and the fringes containing the atoms is the same for all positions x along the chain. After this procedure, the lattice is well aligned on the tweezer chain. We measured the mechanical frequency of the lattice now by modulating the lattice power and observing losses at twice the lattice frequency. The measured frequencies as function of the position in the chain are shown in Figure 8.10.

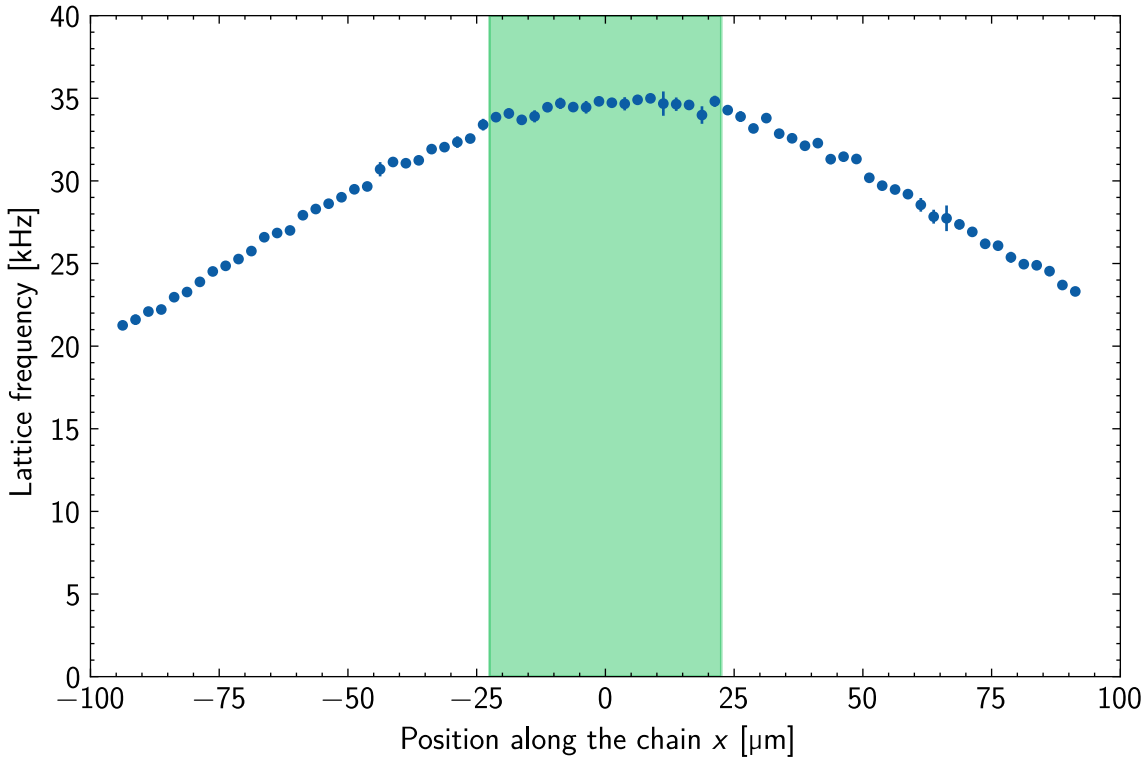

Figure 8.10. – Mechanical frequency in the lattice along the y direction as a function of the position along the chain. Blue points are the measured frequencies, and the green area indicates the extent that a chain of 30 atoms with 1.5 µm covers.

While the frequency is not constant over the whole 200 µm position range accessible with the AOD, we can ensure to put the atoms in the region where the frequency is the highest. We also measured the temperature of the atoms after the lattice has been ramped up by performing a release-and-recapture measurement. We observe an increase of temperature from 5.5(5) µK to 8(1) µK which is compatible with the expected adiabatic heating of the lattice. In these conditions, the axial disorder is reduced from 400 nm to 90 nm.

8.4.4 Fringe stabilization

Even after the lattice beams are well aligned on the tweezers, we still need to ensure that the position of a bright fringe coincides with the tweezer's center along y. If the tweezers are on a lattice saddle point, they might end up in different fringes once the lattice is ramped up. To check that the fringe offset is correct, we abruptly flash the lattice potential on the atoms in the tweezers. If the tweezer's center coincides with a bright fringe, the atoms experience almost no force from the lattice. However, if the tweezers are on the side of a fringe, the atoms are violently pulled by the lattice potential. This is illustrated on Figure 8.11, where the survival fraction is plotted after flashing the lattice for different voltages of the piezo mirror that controls the fringe's position.

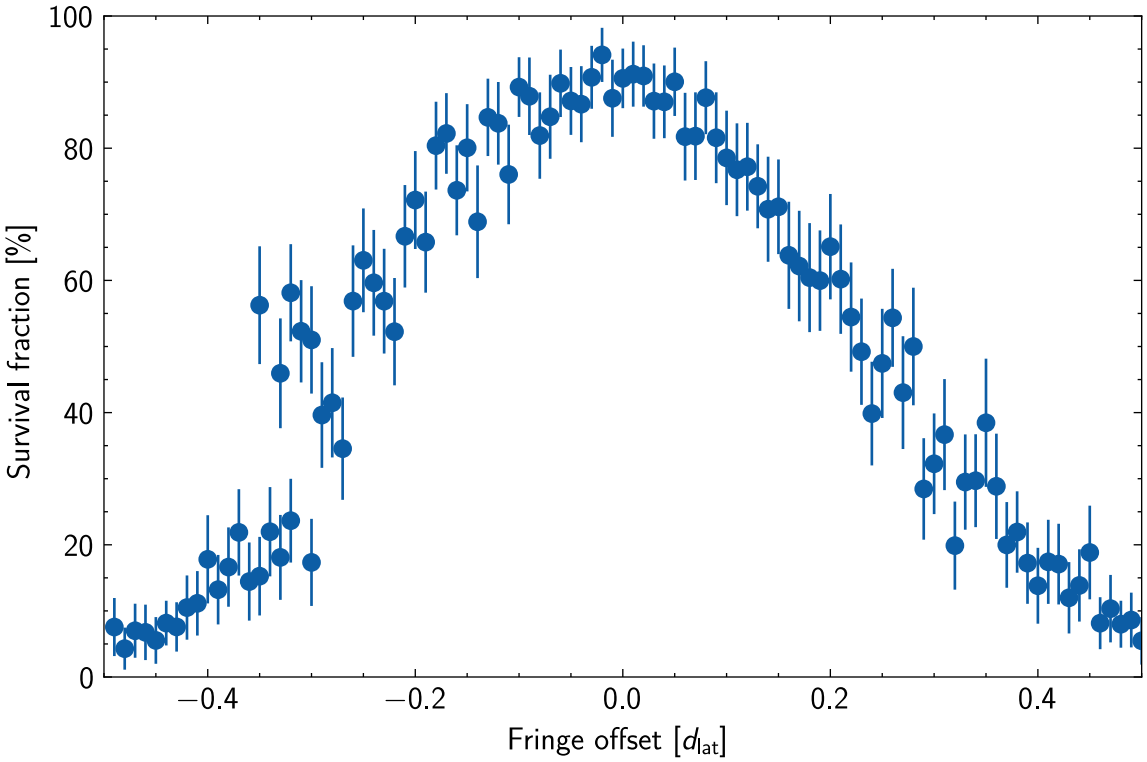

Figure 8.11. – Survival fraction of the atoms when flashing the lattice for different relative position between the bright fringes and the tweezers. When a bright fringe coincides with the center of the tweezers along y, we observe almost no losses.

We want to be in the situation corresponding to the maxima of this curve. By scanning the piezo voltage, we can find the optimal value to choose. The issue is that the fringe position tends to drift over time. If the optical path difference between the lattice arms changes by a fraction of a wavelength, the optimal piezo voltage will be

different. We initially observed a significant drift of the fringe position over the atoms over several tens of minutes. This drift is directly correlated with the temperature fluctuations of the optical table.

To reduce fluctuations, we installed a better temperature regulation system for the air conditioning in the room to stabilize the temperature over the optical table. This scheme was developed in the team of Marc Cheneau at the Institut d'Optique, and more details can be found in [Fai24]. With this system, we were able to reduce the temperature fluctuations over the optical table to about 0.1 °C. While it improved the stability of the lattice fringes significantly, it was not enough to reach the required stability. So in addition, we implemented a feedback loop on the piezo voltage controlling the fringe position. To do so, we image the lattice on a separate camera by picking up a small fraction of the lattice light with a beam-splitter and imaging it on the camera. We extract the position of the fringe on the monitoring camera and use a software proportional-integral controller to stabilize it. With these improvements, the position of the lattice is stable by about 10 % of the fringe spacing over more than a day, which is satisfactory to perform most of the experiments presented in the next chapters[5].

Summary

With the techniques presented in this chapter, we are able to prepare chains of up to 30 atoms with a filling fraction of 98 % using optical tweezers. Still in the tweezers, we are able to reach inter-atomic spacing as small as 1 µm. While this is still larger than an optical wavelength, it is small enough that the light-mediated interaction between atoms scaling as $\hbar\Gamma e^{ikr}/(kr)$ has observable effects.

One limitation of using optical tweezers is the weak confinement in their axial direction, resulting in a large positional disorder. To avoid this issue, we added an optical lattice on top of the tweezers to increase the axial confinement and reduce the disorder.

[5] The feedback directly on the fringe position also has the benefit to bypass hysteresis effects from the piezo.

Chapter 9

State readout for light-scattering

Contents

9.1 Two-level transition

To perform collective light-scattering experiments on our Dy platform, we first need to pick an optical transition to work with. In our case, two potential candidates are the 626 nm one with an excited state lifetime $\tau_{626} = 1/\Gamma_{626} \approx 1.2\,\mu s$ and the 741 nm transition with $\tau_{741} = 1/\Gamma_{741} \approx 88\,\mu s$. These two transitions have relatively long wavelength in the red, meaning that the ratio d/λ can be larger than if using a shorter wavelength transition like the 421 nm. In addition, the two transitions have convenient lifetimes, such that it is possible to manipulate the internal state of the atoms both for times shorter and longer than the transition lifetime. With these two points, the 741 nm transition seems at first to be the best candidate: it has a slightly larger wavelength and does not require sub-microsecond pulses to manipulate the atoms.

However, its narrow linewidth makes it more challenging to use for light-scattering experiments. Besides requiring a better frequency lock, the long lifetime of the 741 nm transition also means that the atoms need to be trapped during the experiment to prevent them from spreading out. This requires the tweezers to be magic for this transition to avoid inhomogenous broadening if the tweezer depth is slightly different from trap to trap. However, it turns out that this transition is not magic for our 532 nm tweezers [Bia+25]. Even if the tweezers where magic, since the tweezer's mechanical frequencies are larger than the lifetime of the 741 nm, one also has to

consider the influence of the fast atomic motion on the internal state dynamics. This can make the analysis of the results more complex [RSC21].

For the 626 nm transition, the situation is simpler. Since its lifetime is much shorter, even if the tweezers or the lattice are not magic, we can still perform the experiments in time-of-flight with the tweezers turned off. In addition, since the linewidth of the 626 nm transition is larger than the trap frequencies, the position of the atom can be considered nearly frozen during the experiment[1]. For these reasons, we decided to perform the first experiments using the 626 nm transition.

Now, we want to isolate a two-level transition. We want to drive the σ^- transition between the state $|g\rangle = |G, m = -8\rangle$ in which the atoms initially are, and the state $|e\rangle = |E_{626}, m = -9\rangle$. This is because this transition is closed: Once atoms are excited to $|e\rangle$, they can only decay back to $|g\rangle$. To ensure that atoms always stay in the states $|g\rangle$ and $|e\rangle$, we need to make sure that we do not drive the π or σ^+ transitions from $|g\rangle$. For example, if we sent atoms from $|g\rangle$ to $|E_{626}, m = -8\rangle$, they could decay to $|G, m = -7\rangle$, and leave the two-level transition. For the narrow 626 nm transition, it is easy to split the three transitions σ^-, π and σ^+ by applying a moderate magnetic field. Indeed, the frequency difference between two states $|G, m_G\rangle$ and $|E_{626}, m_E\rangle$ is given by:

$$\Delta\nu = \frac{\mu_B B}{h}(g_E m_E - g_G m_G) \tag{9.1}$$

where μ_B is the Bohr magneton, B is the magnitude of the magnetic field, and $g_G = 1.241$ and $g_E = 1.29$ are the Landé factors respectively for the ground and excited states. The frequencies of the different transitions for our working magnetic field $B = 7\,\mathrm{G}$ are shown in Figure 9.1. When we shine a laser close to resonance with the $|g\rangle \leftrightarrow |e\rangle$ transition indicated by the red line, this light is detuned by more than $10\,\mathrm{MHz} \approx 70\Gamma_{626}$ from the π and σ^+ transitions. Thanks to this, even if the polarization of the laser is not perfectly σ^-, we still drive only the σ^- transition. Therefore, as long as the Rabi frequency of the laser is smaller than the detuning from the π transition, we can consider the transition $|g\rangle \leftrightarrow |e\rangle$ as a closed two-level system.

[1] This assumption stops becoming valid when the atoms are too close such that the dipole-dipole potential attracts or repels the atoms strongly, as in the case for light-induced collisions [Ber97].

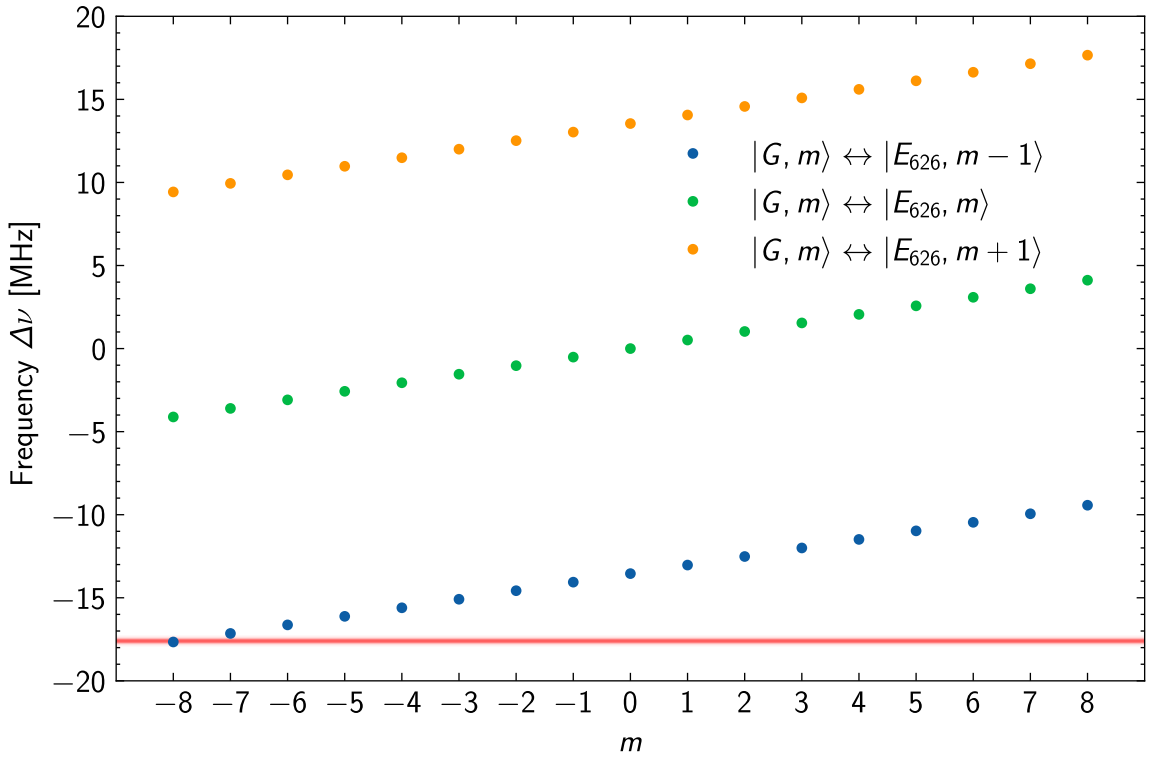

Figure 9.1. – Frequency of the transitions between different Zeeman states for the 626 nm transition as a function of the Zeeman number in the ground state. These values are for a magnetic field of 7 G. The red line has vertical position corresponding to the frequency of the transition $|G, -8\rangle \leftrightarrow |E_{626}, -9\rangle$. Its shading indicates the linewidth of the transition.

9.2 State readout

9.2.1 Optical shelving

After isolating our two-level transition, we need to measure the state of the system. As stated in Chapter 1, most experiments studying light scattering look at the photons emitted by the system to infer properties of the atoms. While this approach is fruitful to characterize the state of the emitted light, it is not always straightforward to use this information to extract the underlying atomic state [Fer+24; Ros+24]. Here I will present the approach we use to measure the atomic state directly.

We want to be able to determine if a given atom is in the ground state $|g\rangle$ or in the excited state $|e\rangle$ in a single realization of the experiment. If we are able to do so, we can use this information to access a lot of information on the system. For example, this would give us access to the average value of single body operators, such as the mean

excitation fraction $\rho_i^{ee} = \langle \pi_i^e \rangle$. We could also measure the mean coherence of an atom $\left\langle \sigma_i^X \right\rangle$ or $\left\langle \sigma_i^Y \right\rangle$ by applying rotation pulses before the measurement. In addition to single body observables, it would also let us measure two-body observables like $\left\langle \pi_i^e \pi_j^e \right\rangle$ or $\left\langle \sigma_i^X \sigma_j^X \right\rangle$ by measuring coincidence probabilities. Having the possibility to access such quantities has been very useful to understand collective behaviors in interacting Rydberg atom systems [BL20; Sem+21; Bor+23], and adapting this technique to light-scattering experiments could be fruitful.

To measure the internal state of the atoms $|g\rangle$ or $|e\rangle$, we use an *optical shelving* technique. The excited state $|e\rangle = |E_{626}, m = -9\rangle$ acts as a metastable state, while we map atoms in $|g\rangle = |G, m = -8\rangle$ to other Zeeman states $|G, m = -7, -6, -5, \ldots\rangle$ using the 421 nm transition. More precisely, we shine a pulse of 421 nm light with Rabi frequency $\Omega_{421} = 2\pi \times 50\,\text{MHz}$ for a duration $T_{421} = 100\,\text{ns}$ on the atoms. This light is π polarized such that it drives transitions between the states $|G, m\rangle$ and $|E_{421}, m\rangle$. Once atoms have been excited to $|E_{421}, m\rangle$, they decay preferentially to $|G, m-1\rangle$. After a few cycles, the atoms in the ground state $|g\rangle$ have been depumped to other Zeeman ground states $|G, m \geq -7\rangle$. This process is illustrated in Figure 9.2 a.

During the pulse of 421 nm light, the atoms in the excited state of the 626 nm transition are not affected, and remain in $|e\rangle$. After the pulse, we let the atoms that were in $|e\rangle$ decay to $|g\rangle$. This way, we have mapped the state $|g\rangle$ to other ground states $|G, m \geq -7\rangle$, while the atoms that were in $|e\rangle$ have been mapped to $|g\rangle$. The 626 nm imaging that we perform after is sensitive to the ground state m number. To take a picture of the atoms, we use the procedure described in Chapter 7: We send a pulse of near-resonant 626 nm light on the $|g\rangle \leftrightarrow |e\rangle$ transition, and collect the scattered photons. Atoms that have been mapped to a Zeeman state $|G, m \geq -7\rangle$ are out of resonance with this light by a few times Γ_{626}, as shown on Figure 9.1. As a result, they do not scatter photons and are not imaged. This scheme allows us to tell for each atom if it was initially in the state $|g\rangle$ or $|e\rangle$: Only atoms that where in $|e\rangle$ are detected in the following pictures, while atoms in $|g\rangle$ have been sent to dark Zeeman states and are not detected. The pulse sequence is illustrated on Figure 9.2 a, with the resulting picture shown on Figure 9.2 b.

To produce the pulse of 421 nm light, we use an acousto-optic modulator (AOM) followed by an electro-optic modulator (EOM). The AOM allows us to have a large extinction to ensure that no 421 nm light is present while we shine the 626 nm light. This is crucial, otherwise the 421 nm light can induce decoherence on the 626 nm

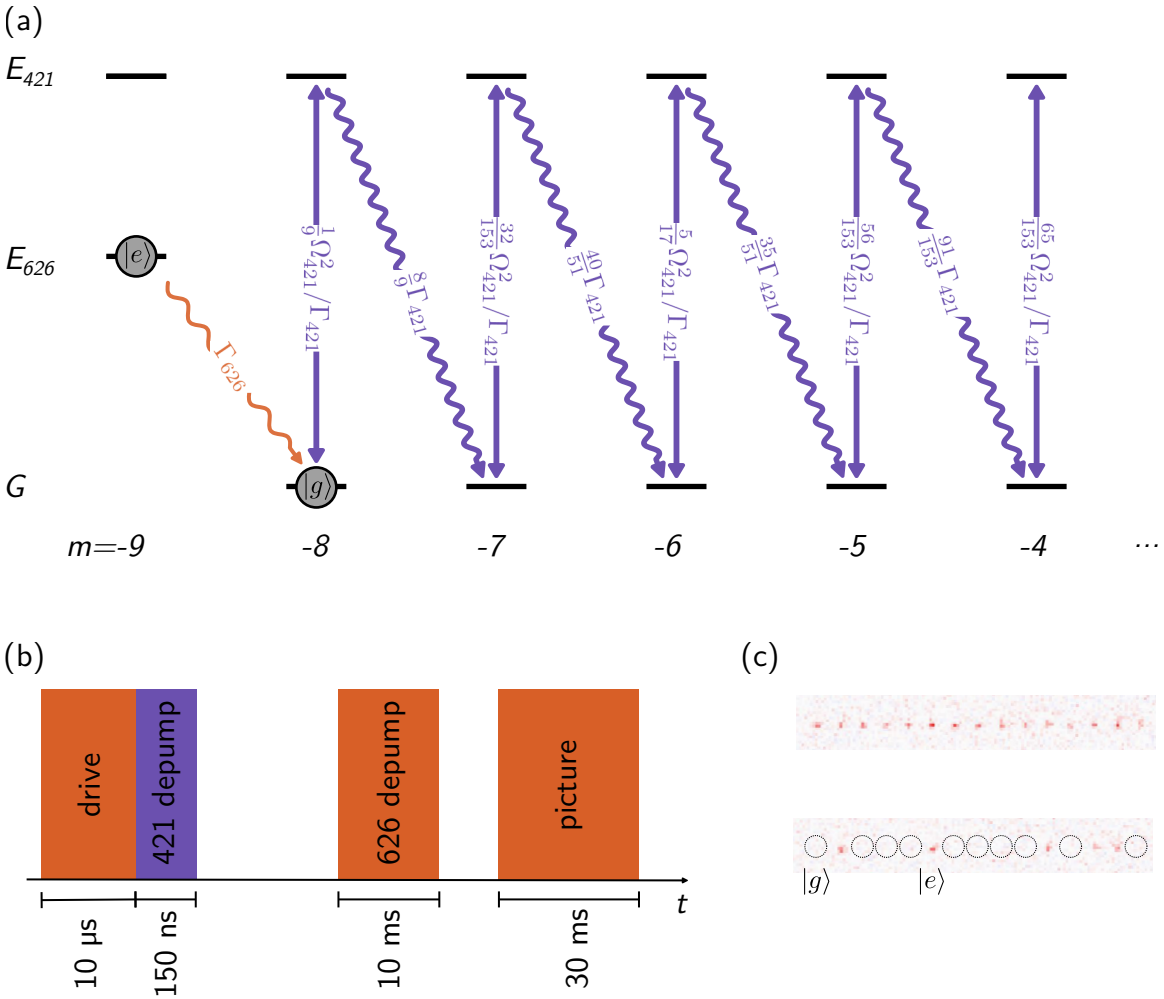

Figure 9.2. – (a) Illustration of the population transfer rates between the different states during the depumping with the 421 nm light. (b) Experimental sequence used to measure the internal state of the 626 nm transition. After driving the atoms for about 10 µs, we project the internal state by applying a short pulse of 421 nm light. Following an optional depumping pulse of 626 nm light, we image the atoms. (c) Example of single shot picture for the state detection scheme. Atoms detected after the 421 nm pulse were initially in $|e\rangle$, while atoms not reimaged were in $|g\rangle$.

transition. However, the AOM has a slow rise time of about 200 ns, making it difficult to produce short pulses. Instead of relying on the AOM for pulse shaping, we turn it on 200 ns before the 421 nm pulse, and then use the EOM to switch the light quickly. The EOM has a rise time of 15 ns and allows us to produce short square pulses of light.

9.2.2 Performances

To quantify the fidelity of this state discrimination, let us start by estimating the number of false positives: Starting with atoms in the ground state $|g\rangle$, what is the probability $P(+|g)$ that they will be reimaged after the pulse? The orange squares in Figure 9.3 show the fraction of ground state atoms reimaged as a function of the duration of the 421 nm pulse. As one can see, this fraction of atoms decays quickly over some tens of nanoseconds, as the atoms are sent to dark Zeeman states with $m \geq -7$. In this plot, I also show the evolution of the populations in the ground state using the rate equations presented in Section 3.2. Under the influence of the depumping 421 nm light, the population of the state $|g\rangle$ decays exponentially, while transferring to the other states $|G, m \geq -7\rangle$.

Still, the orange diamonds do not follow exactly the simulated population of the state $|G, m = -8\rangle$. Indeed, this population decays significantly faster than the orange points. After 150 ns, we expect to have almost no atoms left in the $|G, m = -8\rangle$ state, while we actually reimage about 10 % of the atoms. In other words, the probability of false positives is about 10 %.

The issue is that atoms sent to the states $|G, m = -7\rangle$ (and to a lesser extent also in $|G, m = -6\rangle$) have a chance to still scatter a bit of the imaging light. Indeed, the imaging light is only detuned from the transition $|G, m = -7\rangle \leftrightarrow |E_{626}, m = -8\rangle$ by a few linewidths, as shown on Figure 9.1. If atoms in the supposedly dark state $|G, m = -7\rangle$ scatter a few photons of the imaging light, they can be repumped to $|g\rangle$ where they are imaged. To avoid this issue, before imaging the atoms, we apply a 10 ms pulse of 626 nm light on the σ^+ transition $|G, m = -7\rangle \leftrightarrow |E_{626}, m = -6\rangle$. This way, atoms in the state $|G, m = -7\rangle$ are sent to even larger Zeeman states $|G, m = -6, -5, ...\rangle$, where they are not affected by the imaging light. With this additional step, we can reduce the number of false positives to 2 % for 100 ns of 421 nm light. This corresponds to the blue dots on Figure 9.3.

Now, let us consider the probability of false negatives $P(-|e)$, which is the probability that an atom in $|e\rangle$ is not reimaged after the sequence. To measure the probability of false negatives, we apply a long pulse of 626 nm light with a Rabi frequency much larger than the linewidth of the transition. In this saturated regime, once the evolution of the populations has reached steady-state, the population inversion is zero: $\rho_{ee} = \rho_{gg} = 1/2$.

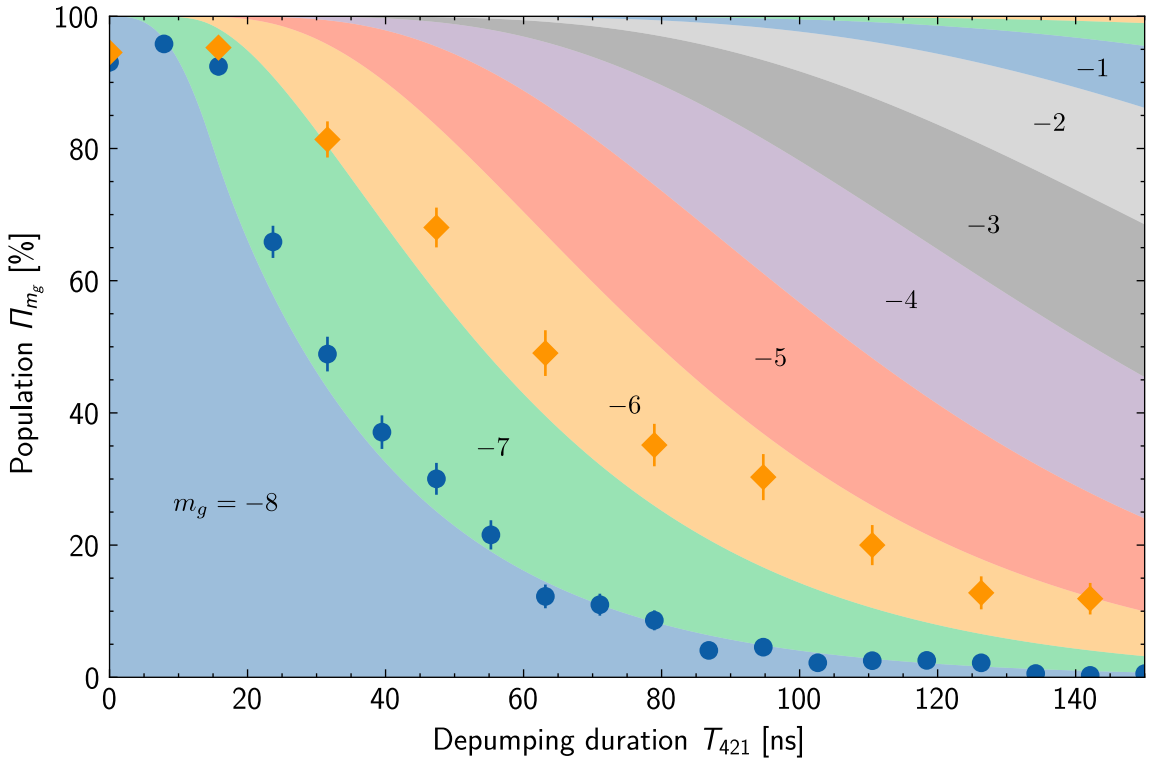

Figure 9.3. – Evolution of the resulting ground state populations as a function of depumping time for an atom initially in the state $|g\rangle = |G, m = -8\rangle$. These values correspond to a Rabi frequency $\Omega_{421} = 2\pi \times 50\,\text{MHz}$. The orange squares and blue points correspond respectively to the situation without and with additional depumping 626 nm light before taking the picture. Note that what is plotted are the populations after applying the 421 nm light and letting the atom decay from the excited states. The initial plateau for Π_{-8} is due to the finite rise time of the EOM.

The probability that we detect an atom is thus:

$$P(+) = P(+|g)\rho_{gg} + P(+|e)\rho_{ee} = \frac{P(+|g) + P(+|e)}{2} \tag{9.2}$$

By measuring $P(+)$ in this situation, and knowing the probability of false positives $P(+|g)$ from the previous paragraph, we obtain the probability of false negative $P(-|e) = 1 - P(+|e) = 8\,\%$.

The main contribution to this error is the decay of the atom initially in $|e\rangle$ during the 421 nm pulse. In that case, the atom will be sent to dark states and will not be reimaged latter. The probability of such events is roughly $1 - e^{-\Gamma_{626} T_{421}}$. For a duration $T_{421} = 100\,\text{ns}$, this indeed corresponds to the 8 % measured. This is the main source of error in typical conditions. It could be made smaller by reducing T_{421}, but then the probability of false positives would increase instead. All the results presented in this

thesis are done in the above conditions with $T_{421} = 100\,\text{ns}$ and $\Omega_{421} = 2\pi \times 50\,\text{MHz}$, but for future experiments, it would be interesting to find a way to improve the readout fidelity. A potential way to reduce the false negatives would be to increase the Rabi frequency of the 421 nm such that T_{421} can be reduced without affecting the probability of false positives.

This scheme for discriminating the internal state on a narrow transition can also be applied to the 741 nm transition. In that case, since Γ_{741} is much smaller than Γ_{626}, the number of false negatives drops drastically. One would thus expect this scheme to work very well for measuring the state on the 741 nm transition.

Summary

In this chapter, I explained how we isolate a two-level system on the 626 nm transition. Using an optical shelving scheme with the 421 nm transition, we are able to measure in a single shot if a given atom is in the ground or excited state. This detection scheme has a fidelity of about 90 %. While this might not be enough for some applications, it is sufficient for our purposes, and with it, we performed the light-scattering experiments presented in the following chapters.

It is also worth noting that this measurement is non-destructive. During the 421 nm pulse, atoms are not lost, but are simply sent to dark states. In principle, we could repump the atoms back to the state $|g\rangle$ after the measurement to redo the experiment and gain time by not having to reload the MOT every time. We have not explored this option in detail for the results presented here, but ongoing experiments are producing promising results.

Chapter 10

Collective steady-state spectrum

Contents

We now have all the tools to perform light-scattering experiments on chains of atoms. We want to use these tools to see how dipole-dipole interaction influences the collective response of the system. In this chapter, I will explore one of the simplest situations: What happens when driving a chain of atoms for a time much longer than the lifetime of the excited state? In this case, the system reaches a steady-state, where the driving by the laser is balanced by dissipation to the environment. For multiple atoms, this steady-state is modified by the action of the radiating dipoles on each other. This situation is easier to understand than time-dependent experiments, and will give a first insight into the effects we can expect.

This situation has already been explored in the group at the Institut d'Optique using chains of rubidium atoms with random filling [Gli+20]. Here we will realize a cleaner implementation of the system, and we will also extend the results, in particular in the next chapter when considering Ramsey spectroscopy.

10.1 Measuring the global spectrum

We first performed a measurement of the "spectrum" of the atoms, meaning that we measure the mean excitation of an atom in steady-state as a function of the detuning Δ of the driving light. It is faster to measure this quantity when averaging over all atoms in the chain, so we usually measure the average excitation:

$$\rho_{ee} = \frac{1}{N}\sum_{i=1}^{N}\rho_i^{ee} = \frac{1}{N}\sum_{i=1}^{N}\langle\pi_i^e\rangle \tag{10.1}$$

To access this quantity, we drive the atoms for $7\,\mu s \approx 6/\Gamma_{626}$ on the 626 nm transition and then perform the 421 nm state projection described in the previous chapter.

In the case where the atoms are far enough that the interaction between them is negligible, we expect to observe a lorentzian line centered on the bare transition frequency. By introducing the Rabi frequency of the laser Ω and its detuning Δ, we have:

$$\rho_{ee} = \frac{\Omega^2/\Gamma^2}{1 + 2\Omega^2/\Gamma^2 + 4\Delta^2/\Gamma^2} \tag{10.2}$$

This is a lorentzian spectrum centered on $\Delta = 0$, and with a power-broadened width $\Gamma_\Omega = \sqrt{\Gamma^2 + 2\Omega^2}$. We want to see how this spectrum changes when the atoms are brought close together.

To increase the effect of interactions between the atoms, we want them to radiate preferentially in the direction along the chain. Since we use the σ^- transition, the radiation pattern of the atoms has a "peanut" shape, aligned with the quantization axis given by the magnetic field. This is contained in the angular dependency of the interaction potential in Equation 8.9. Before performing the light-scattering experiment, we therefore rotate the direction of the magnetic field in the direction X of the chain. This way, collective effects are about twice larger than if the magnetic field were perpendicular to the chain. This is illustrated on Figure 10.1 a, b.

The extreme case is the one of a linearly polarized dipole, for example when using a π transition. The radiation pattern of the atoms has a donut shape, and in particular, the atoms do not radiate in the direction of the quantization axis. In that situation, if the magnetic field is aligned with the chain, only non-radiating terms in $1/(kr)^2$ and $1/(kr)^3$ remain and collective effects are strongly suppressed.

After the atoms have been rearranged in a regular chain, we dynamically bring the tweezers to a smaller spacing d to enhance interactions. We then adiabatically ramp up the lattice to increase the axial confinement of the atoms over a millisecond. We turn off the tweezers and the lattice for 7 µs during which we drive the atoms to steady-state with 626 nm light. The experiment is performed in time-of-flight since neither the confining lattice nor the tweezers are magic for this magnetic field configuration, and might otherwise cause inhomogeneous broadening. After the internal state of the atoms has reached steady state, we project the state with a 421 nm pulse of light before retrapping the atoms in the tweezers and lattice potentials. We then ramp down the lattice again and go back to standard imaging configuration to take a picture of the atoms that were in the state $|e\rangle$ when the measurement with the 421 nm light was performed. This sequence of steps is illustrated on Figure 10.1 c, d.

By averaging the probability to reimage an atom over several tens of repetitions, we get ρ_i^{ee} after driving the atoms. By performing this measurement for different values of the detuning Δ, we obtain the spectrum of the atoms, as illustrated on Figure 10.2. In this figure, the blue points correspond to the case where the atoms are far apart, while the orange points correspond to the case where the atoms are at a close distance $d = 1.25\,\mu\text{m}$. Both cases are taken with the laser driving the atoms aligned with the chain, which is important as will be explained latter.

One can see that the spectrum when the atoms are close is slightly shifted to the left from the reference case where the atoms are far apart. Such effects have been observed on a similar experiment in a 1D chain with random filling and without single-atom resolution [Gli+20].

When trying to measure small frequency shifts, it is critical that the driving intensity does not depend on the frequency. For example, if the AOM used to control the light frequency has a diffraction efficiency that depends on the frequency, it could lead to a deformation of the spectrum. This effect would result in an apparent shift of the spectrum since the applied Rabi frequency Ω would then have a dependence on the detuning Δ. To be sure to avoid this effect, we use an AOM with large bandwidth compared to the frequency range we use, and we make sure to work in the center of its bandwidth.

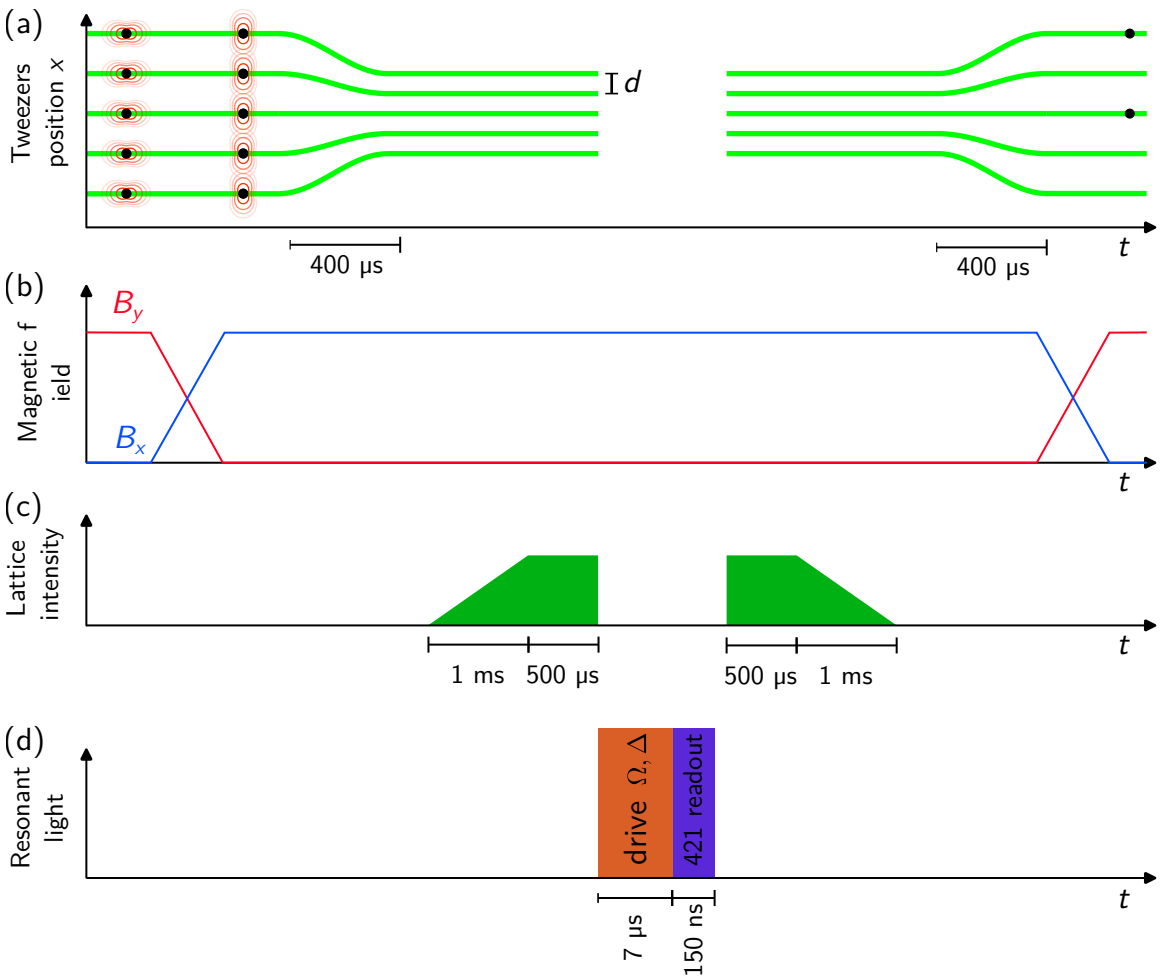

Figure 10.1. – Sequence of steps used to peform light-scattering experiments. (a) Positions of the tweezers over time. Before performing the experiment, we brind the atoms to a spacing d. (b) Magnetic field during the experiment. We rotate the magnetic field in the direction of the chain to align the radiation pattern of the atoms with the chain. (c) Lattice intensity. We ramp up the lattice to increase the axial confinement of the atoms. (d) Pulses of light for the light-scattering experiment. After driving the atoms with 626 nm light to steady-state, we perform readout with the 421 nm light.

10.2 Classical regime

10.2.1 Linear coupled dipoles

To understand the origin of the frequency shift observed, it is useful to consider the limiting case in which the atoms are treated as classical dipoles. This approximation is only valid in the weak excitation regime $\rho_{ee} \ll 1$, or $\Omega \ll \Gamma$. We are not exactly in this regime, since $\rho_{ee} \sim 0.1$, but it can still give us a first picture that can be refined

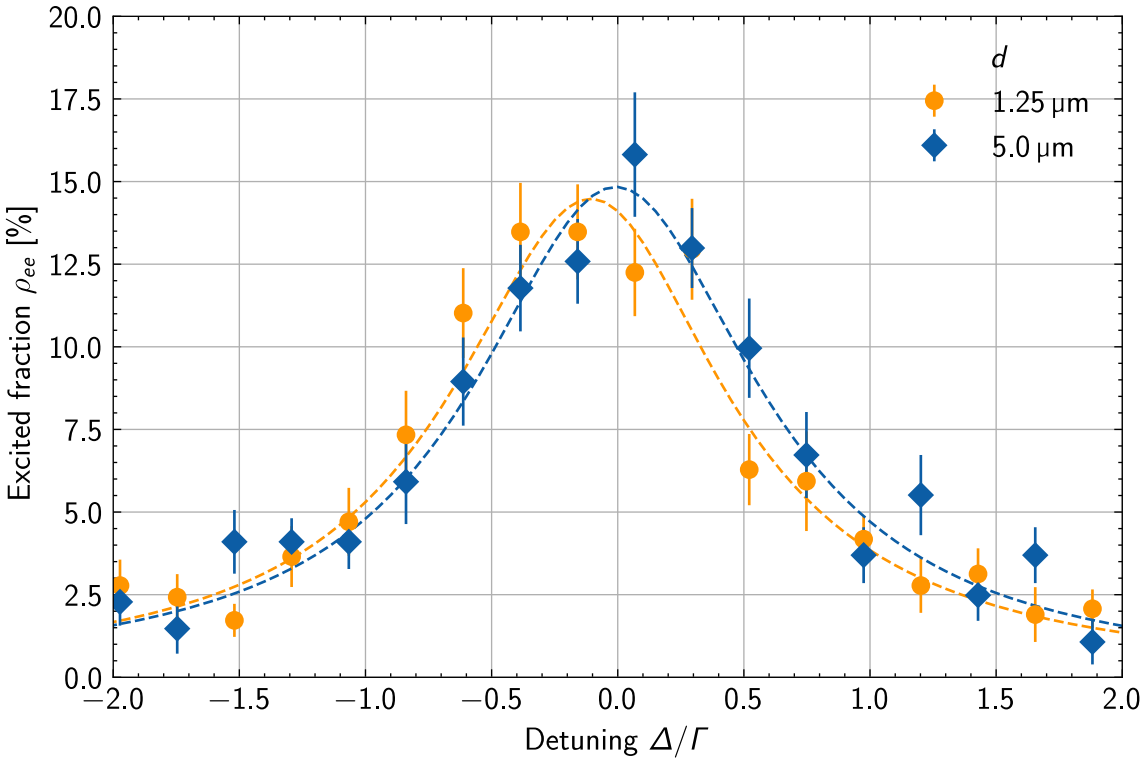

Figure 10.2. – Collective spectrum on the chain for a driving direction parallel to the chain. Blue points correspond to the case of 15 atoms separated by 5 µm, while the orange points correspond to the case of 30 atoms separated by 1.25 µm. Dashed curves are fit using the function given in Equation 10.26.

latter.

Let us consider a laser driving field, oscillating at frequency ω and with a wavevector $\boldsymbol{k}$:

$$\boldsymbol{\mathcal{E}}_l(\boldsymbol{r},t) = \mathrm{Re}\Big\{\boldsymbol{\epsilon} E_l(\boldsymbol{r}) e^{-i\omega t)}\Big\} \quad \text{with} \quad E_l(\boldsymbol{r}) = E_0 e^{i\boldsymbol{k}\cdot\boldsymbol{r}} \tag{10.3}$$

Here $\boldsymbol{\epsilon}$ is the complex polarization of the field, and E_0 is its amplitude, which is related to the Rabi frequency by $\Omega = -\langle e|\boldsymbol{\epsilon}\cdot\hat{\boldsymbol{d}}|g\rangle E_0/\hbar$. We then look for the dipole moment of the atom i as:

$$\boldsymbol{\mathcal{D}}_i(t) = \mathrm{Re}\Big\{\boldsymbol{\epsilon} d_i(t) e^{-i\omega t}\Big\} \tag{10.4}$$

where $d_i(t)$ is the complex amplitude of the dipole moment.

To derive how the dipole evolves when driven by the laser, we can use the Lorentz model, as done for example in [Ste12]. We assume that the dipole moment of the atom is due to a fictional localized charge q with mass m and a displaced position from equilibrium $\boldsymbol{r}$, such that $\boldsymbol{\mathcal{D}} = q\boldsymbol{r}$. The equation of motion for the charge is given

by:

$$\ddot{\boldsymbol{r}}(t) + \Gamma\dot{\boldsymbol{r}}(t) + \omega_0^2\boldsymbol{r}(t) = \frac{q\boldsymbol{\mathcal{E}}_l(\boldsymbol{r}_i, t)}{m} \tag{10.5}$$

In addition to oscillation at the natural frequency ω_0, the charge also looses energy by radiation at a rate Γ, and is driven by the laser field $\boldsymbol{\mathcal{E}}_l$. We can rewrite Equation 10.5 for the complex dipole moment d_i, with the assumption that it evolves much more slowly than the driving field ($\ddot{d}_i \ll \omega^2 d_i$):

$$\dot{d}_i = \left(i\frac{\omega^2 - \omega_0^2}{2\omega} - \frac{\Gamma}{2}\right) d_i + i\frac{q^2 E_l(\boldsymbol{r}_i)}{2m\omega} \tag{10.6}$$

If the driving field is close to resonance with the transition, i.e. $\Delta = \omega - \omega_0 \ll \omega_0$, we can rewrite Equation 10.6 as:

$$\dot{d}_i = \left(i\Delta - \frac{\Gamma}{2}\right) d_i + \frac{3i\pi\epsilon_0\Gamma E_l(\boldsymbol{r}_i)}{k^3} \tag{10.7}$$

where we assume that the decay rate is given by the Larmor formula: $\Gamma = q^2\omega_0^2/6\pi mc^3\epsilon_0$. This equation fully describes the time evolution of a single dipole, and can be solved to get the spectrum of an isolated atom in the classical limit.

Now we need to extend this when several atoms are present. In this case, the field seen by an atom is the sum of the laser field and the field radiated by the other atoms:

$$E(\boldsymbol{r}_i) = E_l(\boldsymbol{r}_i) + \sum_{j\neq i} G_{ij} d_j \tag{10.8}$$

with $G_{ij} = -V_{ij}k^3/3\pi\epsilon_0\hbar\Gamma$ where V_{ij} is the dipole-dipole interaction potential defined in Chapter 1. Rewriting Equation 10.6 gives us:

$$\dot{d}_i = \left(i\Delta - \frac{\Gamma}{2}\right) d_i + \frac{3i\pi\epsilon_0\Gamma}{k^3}\left[E_l(\boldsymbol{r}_i) + \sum_{j\neq i} G_{ij} d_j\right] \tag{10.9}$$

This is a set of first order coupled linear differential equations. It can be solved, for example numerically, to get the evolution of the dipole for each atom. This equation is also sometimes called the *linear coupled dipole equation*.

In steady-state, this equation reduces to:

$$d_i = \epsilon_0\alpha\left[E_l(\boldsymbol{r}_i) + \sum_{j\neq i} G_{ij} d_j\right] \tag{10.10}$$

where I introduced the polarizability of the atoms:

$$\alpha = -\frac{3\pi\epsilon_0\Gamma}{k^3}\frac{1}{\Delta + i\Gamma/2} \tag{10.11}$$

The polarizability is the proportionality constant that relates the induced dipole to the total driving field. The polarizability changes sign with the detuning; When the frequency of the driving field is lower than the natural oscillation frequency, $\Delta < 0$, the induced dipole oscillates in phase with the driving field. However, when the driving frequency is larger than the natural frequency, $\Delta > 0$, the dipole lags behind the driving field and is in opposition of phase with it.

Equation 10.10 is a time-independent linear set of equations that can be solved in several ways, that I will describe below. To link the solutions of this equation to the excitation probability ρ_i^{ee} that we measure experimentally, we can notice that in the classical limit, the Larmor formula gives the power radiated by an isolated dipole:

$$P_{\text{rad}} = \frac{\omega_0^4 |d_i|^2}{12\pi\epsilon_0 c^3} \tag{10.12}$$

while for a two-level system:

$$P_{\text{rad}} = \hbar\omega_0\Gamma\rho_i^{ee} \tag{10.13}$$

Thus, if we solve d_i using Equation 10.10, we can then compute the excitation probability using:

$$|d_i|^2 = \frac{12\pi\epsilon_0\hbar\Gamma}{k^3}\rho_i^{ee} \tag{10.14}$$

10.2.2 Eigenmodes

One way to solve Equation 10.10 is to rewrite it in matrix form:

$$\Delta\begin{bmatrix} d_1 \\ d_2 \\ \vdots \\ d_N \end{bmatrix} + \begin{bmatrix} i\Gamma/2 & -V_{12}/\hbar & \dots & -V_{1N}/\hbar \\ -V_{21}/\hbar & i\Gamma/2 & \dots & -V_{2N}/\hbar \\ \vdots & \vdots & \ddots & \vdots \\ -V_{N1}/\hbar & -V_{N2}/\hbar & \dots & i\Gamma/2 \end{bmatrix} \cdot \begin{bmatrix} d_1 \\ d_2 \\ \vdots \\ d_N \end{bmatrix} = -\frac{3\pi\epsilon_0\Gamma}{k^3}\begin{bmatrix} E_l(\boldsymbol{r}_1) \\ E_l(\boldsymbol{r}_2) \\ \vdots \\ E_l(\boldsymbol{r}_N) \end{bmatrix} \tag{10.15}$$

We can then look at the eigenvalues λ_ζ and eigenvectors $\boldsymbol{u}_\zeta$ of the matrix M given above [BGA16b]:

$$M\boldsymbol{u}_\zeta = \lambda_\zeta \boldsymbol{u}_\zeta \quad \text{with} \quad M_{i,j} = \begin{cases} i\Gamma/2 & \text{if } i = j \\ -V_{ij}/\hbar & \text{if } i \neq j \end{cases} \tag{10.16}$$

One has to be careful that M is a symmetric *complex* matrix. Therefore, its eigenvectors, while forming a basis, are not in general orthogonal. When decomposing a vector $\boldsymbol{w}$ on the eigenvectors $\boldsymbol{u}_\zeta$ as $\boldsymbol{w} = \sum_\zeta w_\zeta \boldsymbol{u}_\zeta$, the contribution of each eigenvector is given by:

$$w_\zeta = \frac{\boldsymbol{u}_\zeta^* \cdot \boldsymbol{w}}{\sum_\zeta \boldsymbol{u}_\zeta^* \cdot \boldsymbol{u}_\zeta} \tag{10.17}$$

In addition, the eigenvalues λ_ζ are complex, and I will write them as $\lambda_\zeta = -\omega_\zeta + i\Gamma_\zeta/2$. The terms ω_ζ and Γ_ζ are identified respectively with the energy and the lifetime of the eigenmode $\boldsymbol{u}_\zeta$. To see why, we can decompose the unknown $\boldsymbol{d}$ as a sum of all the eigenmodes: $\boldsymbol{d} = \sum_\zeta d_\zeta \boldsymbol{u}_\zeta$. Injecting this form in Equation 10.16, we find that the weight of each eigenvector in the solution is given by:

$$d_\zeta = -\frac{3\pi\epsilon_0\Gamma}{k^3} \frac{E_\zeta}{\Delta - \omega_\zeta + i\Gamma_\zeta/2} \tag{10.18}$$

where E_ζ is the weight of the driving field on the eigenmodes given by Equation 10.17. In this basis, the dipole moments are directly proportional to the driving field, with a polarizability shifted by ω_ζ, and with an effective lifetime Γ_ζ. When Γ_ζ is larger than Γ, the mode considered is said to be super-radiant, and when it is smaller, it is said to be sub-radiant. When driving the system in steady-state, we thus excite several eigenmodes, each with its own frequency and linewidth. The total response of the system is thus the sum of the response of each eigenmode, with a weight that depends on how the driving field couples to the eigenmodes [SR16].

In general, to find these classical modes, one has to do a full diagonalisation of the matrix M. In the case of an infinite chain, the system has translational symetry and its eigenmodes are given by Bloch waves, or spin waves, of the form $d_i = e^{i\zeta r_i}$. In our case, while the system is finite, the atom number is large enough that we can still

expect Bloch waves to be approximate solutions, and we can look for eigenvectors as[1]:

$$\boldsymbol{u}_\zeta = \frac{1}{\sqrt{N}} \begin{bmatrix} 1 \\ e^{i\zeta d} \\ \vdots \\ e^{i\zeta(N-1)d} \end{bmatrix} \tag{10.19}$$

where ζ is an integer multiple of $2\pi/Nd$. The eigenvalues λ_ζ are then approximately given by:

$$\lambda_\zeta = \boldsymbol{u}_\zeta^* \cdot (M\boldsymbol{u}_\zeta) = i\frac{\Gamma}{2} - \frac{1}{N}\sum_{i\neq j}\frac{V_{ij}}{\hbar}e^{i\zeta d(j-i)} \tag{10.20}$$

The sum in the equation covers all ordered pairs of atoms (i, j), except the case where $i = j$. An analytical expression for these eigenvalues can be obtained in the limit of large N [Ase+17]. In particular, one finds that when the spacing d becomes smaller than half a wavelength $d < \lambda/2$, the imaginary part of λ_ζ for most modes becomes very close to zero: Most modes become strongly sub-radiant. For the results presented here for which the spacing is larger than the wavelength, an analytical expression for λ_ζ is not particularly enlightning, and I will stick to the expression given above.

We can thus understand the spectrum measurement as this: When driving the system with the laser, we excite mainly the mode that matches best the projection of the laser wavevector $\boldsymbol{k}$ on the chain, i.e. $\zeta = k_x$. This mode has eigenvalue $\lambda_{k_x} = -\omega_{k_x} + i\Gamma_{k_x}/2$, with

$$\omega_{k_x} = \frac{1}{N}\,\mathrm{Re}\left\{\sum_{i\neq j}\frac{V_{ij}}{\hbar}e^{ik_x d(j-i)}\right\} \quad \text{and} \quad \Gamma_{k_x} = \Gamma - \frac{2}{N}\,\mathrm{Im}\left\{\sum_{i\neq j}\frac{V_{ij}}{\hbar}e^{ik_x d(j-i)}\right\} \tag{10.21}$$

We thus expect to see a lorentzian spectrum[2] centered at $\Delta = \omega_{k_x}$ and with a width Γ_{k_x}. In particular, the measured shift should depend on the spacing d between the atoms and the angle between the laser and the chain. These theoretical values are plotted on Figure 10.3 a, b. One observes oscillations in the expected linewidth, but I will here focus on the frequency shift ω_{k_x}. As one can see, when driving the chain with a laser perpendicular to the chain where all atoms are excited with the same phase, the shift is close to zero in most cases, except when the spacing is a multiple of

[1] These approximate eigenmodes are actually orthogonal, but it is only true since we ignore edge effects. The exact eigenmodes are indeed not orthogonal.

[2] The spectrum is only lorentzian when a single mode is excited. This is the case in the limit of large atom number where only one eigenmode matches well the phase profile of the laser. In a small system, the spectrum deviates from a lorentzian.

λ. This is different when driving the chain with the laser parallel to its axis, where in addition to resonances at multiple of $\lambda/2$, there is also a negative trend when going to small spacings. It is not clear how to get an intuition about this behavior with the eigenmode analysis presented here.

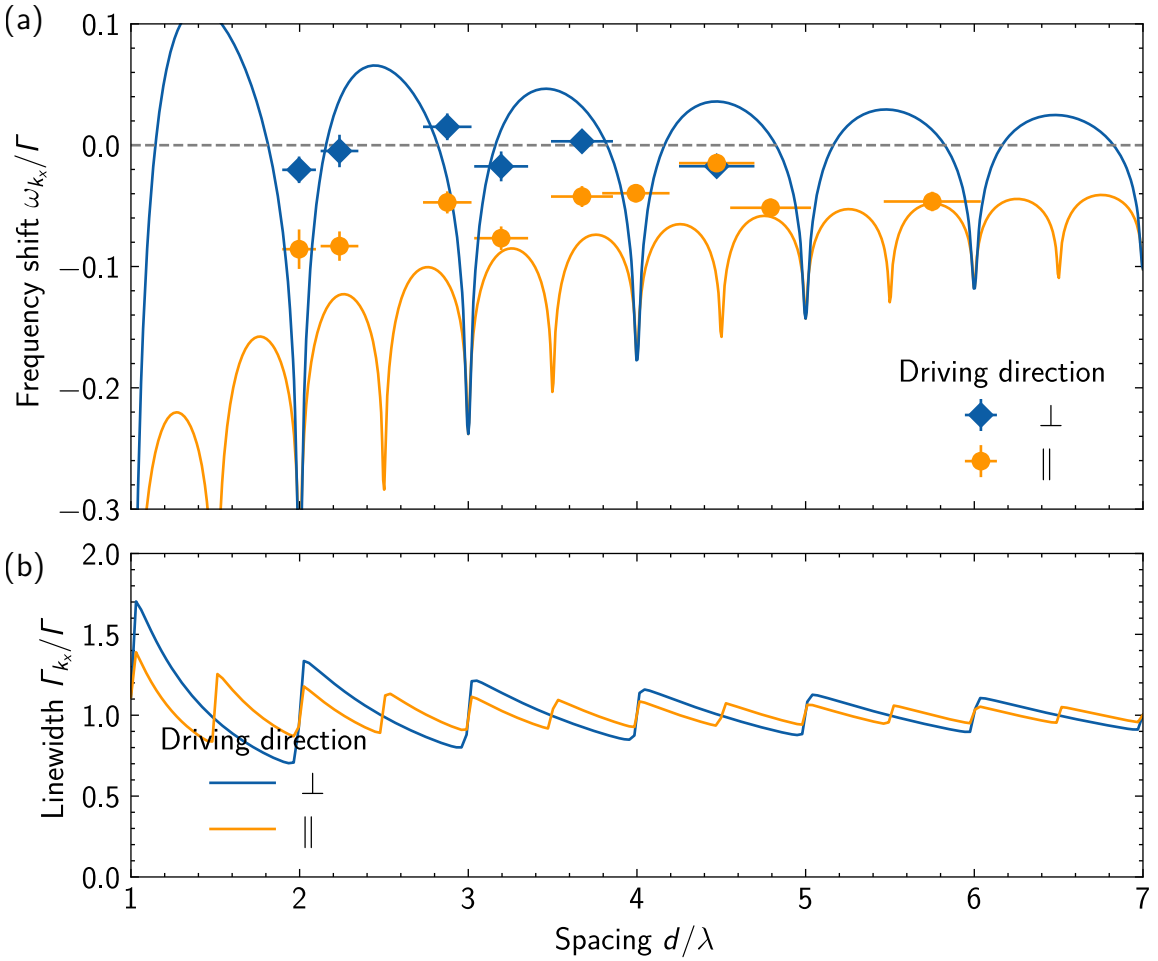

Figure 10.3. – (a) Frequency shift as a function of the spacing between the atoms. Blue diamonds and orange data points correspond to respective situations where the driving laser is perpendicular and parallel to the chain of atoms. This data is taken for a laser Rabi frequency $\Omega = 0.8\Gamma_{626}$. The solid lines are the theoretical prediction from Equation 10.21. (b) Predicted linewidth of the spectrum as a function of the spacing between the atoms using Equation 10.21.

There is also an issue when comparing the predicted values to the measured shift. The predictions largely overestimate the magnitude of the measurement. To understand this difference, we will need to add new ingredients to the theoretical predictions, such as the positional disorder of the atoms in the chain, or the fact that we are not fully in the classical limit of low atomic excitation. It is not clear how to adapt the eigenmode

analysis to include these effects. Since positional disorder breaks translational symetry, we have no idea what the modes will look like, and we have to fall back to numerical diagonalisation. Including effects of finite atomic excitation in this model is also not obvious.

10.2.3 Weakly interacting limit

Here I will present another approach to get some insight into Equation 10.10. It will, however, be limited to the case of weakly interacting atoms. This is the case when the field radiated by the atoms $G_{ij}d_j$ is small compared to the field of the laser E_l. It is the regime we can expect since $G_{ij}d_j/E_l \simeq V_{ij}/\hbar\Gamma$, which is small when the spacing between atoms is larger than the wavelength of the light. By taking the modulus square of Equation 10.10 and only keeping first order terms in G_{ij}, we find:

$$|d_i|^2 \approx \epsilon_0^2|\alpha|^2 \left(|E_l(\boldsymbol{r_i})|^2 + 2\,\mathrm{Re}\left\{ E_l(\boldsymbol{r_i})^* \sum_{j\neq i} G_{ij}d_j \right\} \right) \tag{10.22}$$

At first order, the dipole d_j is mostly driven by the laser field, such that in the right-hand side of the equation, we can replace d_j by $\epsilon_0\alpha E_l(\boldsymbol{r}_j)$. We thus get:

$$|d_i|^2 \approx \epsilon_0^2|\alpha|^2 \left(|E_l(\boldsymbol{r_i})|^2 + 2\epsilon_0\,\mathrm{Re}\left\{ \alpha \sum_{j\neq i} G_{ij}E_l(\boldsymbol{r_i})^* E_l(\boldsymbol{r}_j) \right\} \right) \tag{10.23}$$

It is more natural to rewrite this equation for the excitation probability using Equation 10.14:

$$\rho_i^{ee} = \frac{\Omega^2/\Gamma^2}{1+4\Delta^2/\Gamma^2} \left(1 - 4\,\mathrm{Re}\left[\sum_{j\neq i} \frac{iV_{ij}/\hbar\Gamma}{1-2i\Delta/\Gamma} e^{i\boldsymbol{k}\cdot(\boldsymbol{r}_j-\boldsymbol{r}_i)} \right] \right) \tag{10.24}$$

Equation 10.24 gives us the spectrum of each atom i in the chain, which is not simple to get in the eigenmode analysis. To get the global spectrum, we can average these individual terms:

$$\rho_{ee} = \frac{1}{N}\sum_{i=1}^{N} \rho_i^{ee} = \frac{\Omega^2/\Gamma^2}{1+4\Delta^2/\Gamma^2} \left(1 - 4\,\mathrm{Re}\left[\frac{1}{N}\sum_{i\neq j} \frac{iV_{ij}/\hbar\Gamma}{1-2i\Delta/\Gamma} e^{i\boldsymbol{k}\cdot(\boldsymbol{r}_j-\boldsymbol{r}_i)} \right] \right) \tag{10.25}$$

As expected, when the atoms are isolated, $V_{ij} = 0$, and we recover the lorentzian spectrum with amplitude Ω^2/Γ^2, centered at $\Delta = 0$ and with width Γ. But now, when

interactions are present, the spectrum is modified by the term proportional to V_{ij} that depends on Δ. To see how this term affects the spectrum, let us compute the real part of the sum [SR16]:

$$\rho_{ee} = \frac{\Omega^2/\Gamma^2}{1+4\Delta^2/\Gamma^2}\left[1+\frac{4}{1+4\Delta^2/\Gamma^2}\left(\frac{2\Delta_C\Delta}{\Gamma^2}+\frac{\gamma_C}{\Gamma}\right)\right] \tag{10.26}$$

where I introduced

$$\hbar\Delta_C = \frac{1}{N}\,\mathrm{Re}\left[\sum_{i\neq j} V_{ij}e^{i\boldsymbol{k}\cdot(\boldsymbol{r}_j-\boldsymbol{r}_i)}\right] \quad \text{and} \quad \hbar\gamma_C = \frac{1}{N}\,\mathrm{Im}\left[\sum_{i\neq j} V_{ij}e^{i\boldsymbol{k}\cdot(\boldsymbol{r}_j-\boldsymbol{r}_i)}\right] \tag{10.27}$$

One can see that there is an odd term in Δ that is proportional to Δ_C. This term adds a skew to the spectrum, and will tend to shift it. In this regime of weak interaction, we can define the shift of the spectrum by looking how its maximum is displaced. By finding the detuning at which the derivative of Equation 10.26 cancels, we can find the position of the maxima of the spectrum. We find that at first order, the spectrum is shifted by Δ_C. This collective shift is also sometimes called the *collective Lamb shift*. It is worth noting that while Δ_C can be defined in all situations, it cannot always be identified with a simple shift of the transition. Even in this regime of weak excitation, the spectrum is not a lorentzian shifted by Δ_C but presents a skew. From the eigenmodes analysis, we expect that when going to larger interactions, the spectrum will be the sum of several lorentzians and might even present several maxima.

When we measure a spectrum experimentally, we need to be careful how to extract the shift from the data. Simply fitting the points with a shifted and rescaled lorentzian will not give the correct value of the shift. Indeed, because of the skew of the spectrum, a shift extracted this way is ill-defined, and it will actually depend on the size of the frequency window over which the fit is performed. To avoid this problem, I instead fit the data with the functional form given in Equation 10.26.

In addition to this shift, there is also a term proportional to γ_C, and that is even in Δ. Depending on the sign of γ_C, this term will either broaden or narrow the spectrum. While it could be interesting to try and measure γ_C, there are several experimental quantities that influence the width by an amount comparable or larger than γ_C, and that make the interpretation challenging. Examples of such factors are power broadening, the laser linewidth, thermal Doppler broadening, or even the finite

duration of the light pulse. These parameters would need to be characterized carefully to ensure that they do not affect the estimated width of the spectrum. For this reason, we did not explore the modification of the linewidth in the results presented here, and instead, we focused on the shift of the spectrum Δ_C.

In the eigenmodes analysis, we obtained a similar expression for the shift. With this new approach, we can also provide a physical picture for the different behaviors observed depending on the driving direction. In particular, why is there an increasingly negative shift as d gets smaller when driving the chain parallel to its axis? One way to see this, is to estimate the phase relationship between the laser and the radiated fields [SR16]. The field on the atom j is the sum of the laser field with phase kx_j, and the sum of all the fields radiated by the other atoms i. Depending on the phase of the polarizability α, the atom i either oscillates in phase or out of phase with the laser, such that the phase of this atom is $kx_i + \arg\alpha$. Taking into account propagation, the field radiated by the atom i on the atom j has a phase $kx_i + \arg\alpha + k|x_j - x_i|$.

For an atom $i > j$ down the chain, the phase of the field it radiates on j is $k(2x_i - x_j) + \arg\alpha$. When summing up the field of the atoms downstream of j, their contributions tend to add up incoherently such that the total radiated field for $i > j$ average to zero. This is not the case for an atom $i < j$ upstream the chain. The phase of its radiated field on j is $kx_j + \arg\alpha$, and in particular, it is independent of the position of the emitting atom x_i. The radiated fields of all atoms placed before j in the chain thus sum up coherently together and with the laser field. Whether the interference is constructive or destructive with the laser depends on the sign of α.

For negative detunings, the radiated fields interfere constructively with the laser down the chain, while they interfere destructively with it for positive detunings. This spatially coherent or incoherent buildup depending on the scattering direction is illustrated on Figure 10.4 a. We thus expect the intensity of the total electric field to increase (decrease) down the chain when driving parallel to its axis for a detuning $\Delta < 0$ ($\Delta > 0$). As a result, the probability that an atom is excited will also increase (decrease) along the position in the chain. This is illustrated on Figure 10.4 b where we measured the probability ρ_i^{ee} that an atom is excited when driving parallel to the chain for two different detunings. As a result of this effect, the average probability ρ_{ee} is increased compared to isolated atoms for $\Delta < 0$, while it is decreased for $\Delta > 0$. This creates an asymmetry in the spectrum $\rho_{ee}(\Delta)$, that we can interpret as a negative shift of the transition. The explanation given above does not apply when the laser is perpendicular to the direction of the chain, such that we do not expect a coherent buildup in that case.

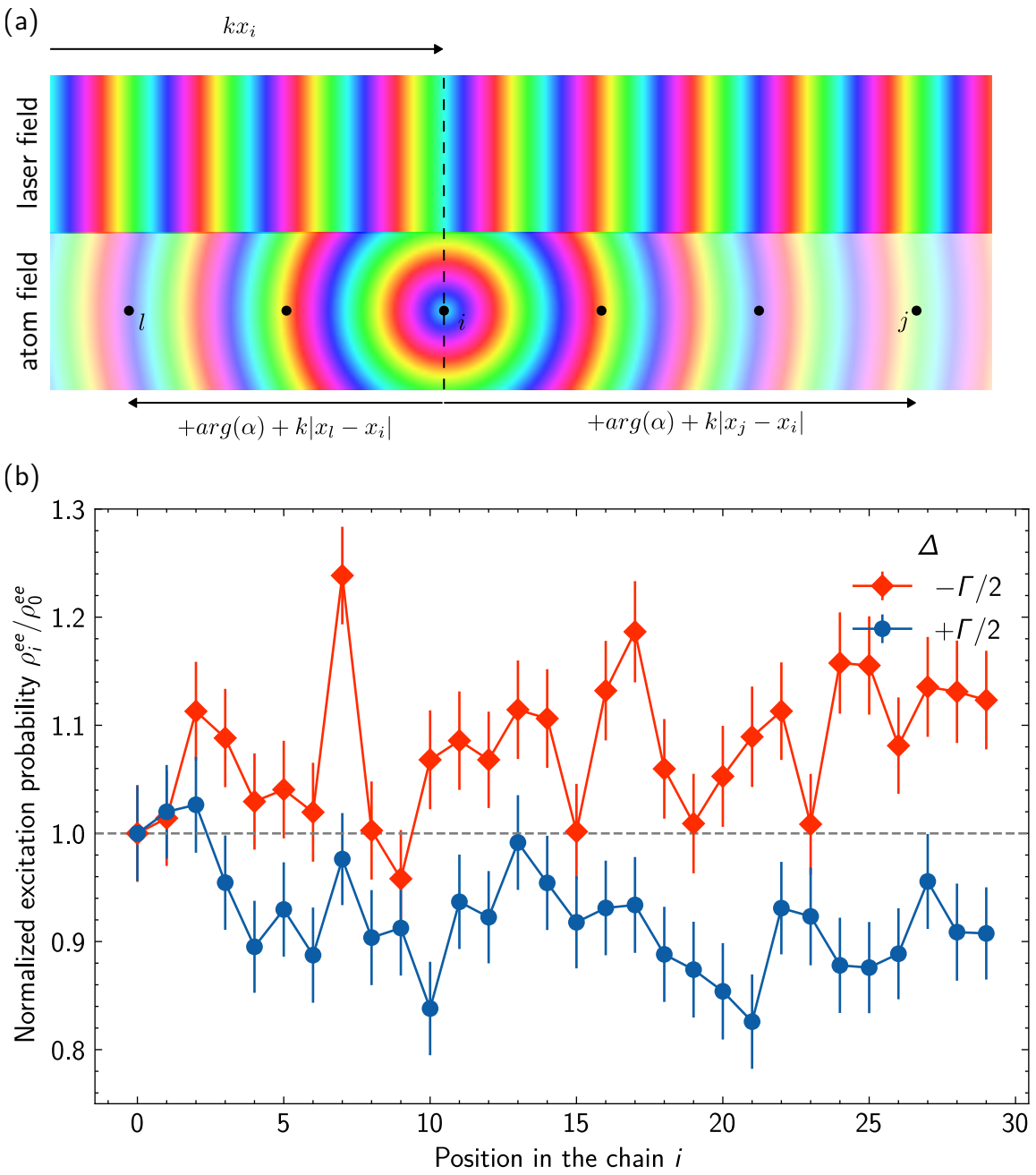

Figure 10.4. – (a) Illustration of the interference effect between the laser field and the field radiated by an atom. In this plot, the colormap represents the phase of the electric field. Towards the right, in the forward direction of laser, the field radiated by the atoms stays coherent with the laser. This is not the case in the backward direction, where the field radiated by the atoms is spatially incoherent with the laser. (b) Measured excitation probability ρ_i^{ee} of the atom i in the chain when driving the chain parallel to its axis for both negative and positive detunings.

When the spacing between the atoms is a multiple of $\lambda/2$, this explanation needs to be corrected as the back-scattered fields now also add up coherently, since $k|x_i - x_j| = \pi|i - j|$. It results in a Fabry-Perot like effect where the field is scattered back-and-forth the chain. We can thus expect the magnitude of the shift to become large at multiple of $\lambda/2$. This indeed corresponds to the resonances that are predicted for a perfectly ordered chain on Figure 10.3 a.

10.2.4 Influence of disorder

The result obtained in the weakly interacting case reduces to the same expression than the one obtained using the eigenmode analysis. However, the value obtained for the shift Δ_C in Equation 10.27 makes no assumption on the location $\boldsymbol{r}_i$ of the atoms. As long as the interactions are weak, the formula is valid whether the atoms form a chain, a circle, a grid, or a random ensemble. In particular, we can use it to estimate the influence of the positional disorder in the chain on the expected shift. For one realization of the experiment, the disorder is nearly frozen since the linewidth of the transition $\Gamma = 2\pi \times 135\,\mathrm{kHz}$ is much larger than the timescale at which the atoms move in the tweezers $\omega \approx 2\pi \times 30\,\mathrm{kHz}$[3]. To include the effect of positional disorder, we can then just average the shift for many random positions sampled according to the Boltzmann distribution. The result is shown on Figure 10.5.

One first observes that the resonances are washed out. The Fabry-Perot effect we expect when the spacing d is multiple of λ or $\lambda/2$ is very sensitive to the actual spacing between the atoms. Even though the fluctuations of position are only about 70 nm, i.e. much smaller than λ, this is enough to totally remove the effect. If we underestimate a bit the disorder on the experiment, the resonances would be even more suppressed than on the plot. For this reason, we did not observe any resonance in the measured frequency shift.

Still, even taking into account disorder, the predicted magnitude of the shift in the axial case is still much larger that what is measured. In fact, the negative trend in that case is barely affected by disorder. This is actually expected. In the discussion in the previous section on the origin of the negative shift, we do not rely on the fact that

[3] Since we are doing the experiment in time-of-flight, the atoms do not oscillate, but instead spread over time. Still, the duration of this expansion is given by the frequencies in the traps before they are turned off.

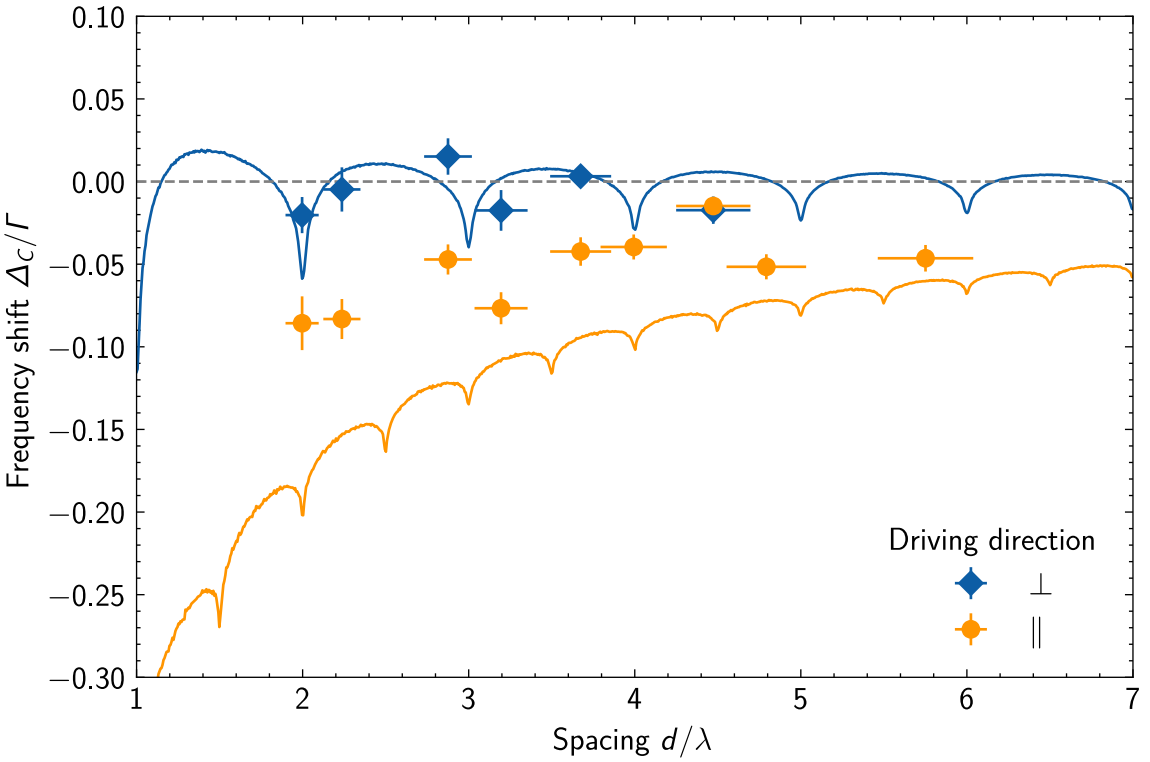

Figure 10.5. – Frequency shift as a function of the spacing between the atoms after averaging over positional disorder.

the atoms are located at equal spacing. The explanation only requires them to be placed in 1D. Thanks to this, the shift with axial driving is resilient to disorder. It has even been observed in chains with random filling [Gli+20].

While this has the advantage to make the effect robust, it means that we still need additional considerations to explain the discrepancy between what we predict and what we observe.

10.3 Mean field

10.3.1 Non-linear coupled dipoles

The previous analysis cannot fully explain what is observed since it is only valid in the classical limit. This is the situation where the atomic excitation is small $\rho_{ee} \ll 1$, or equivalently $\Omega \ll \Gamma$. In practice, we have to work at finite Rabi frequency to get a non-negligible signal, since the amplitude of the spectrum is Ω^2/Γ^2.

In the case of a single atom, we can take into account its two-level structure by

writing its master equation, or equivalently the optical Bloch equations [Ste12]:

$$\frac{\mathrm{d}\rho_{ee}}{\mathrm{d}t} = i\frac{\Omega}{2}\rho_{eg} - i\frac{\Omega}{2}\rho_{ge} - \Gamma\rho_{ee} \tag{10.28}$$

$$\frac{\mathrm{d}\rho_{eg}}{\mathrm{d}t} = \left(i\Delta - \frac{\Gamma}{2}\right)\rho_{eg} + i\frac{\Omega}{2}(\rho_{ee} - \rho_{gg}) \tag{10.29}$$

This is a simple system of two coupled linear equations that can be solved relatively easily.

For more than one atom, one has to deal with the master equation presented in Section 8.1.2. Solving this equation exactly is usually impossible when the number of particles becomes large. Instead, a common technique that generalizes the Bloch equations to several atoms is the *mean-field* approximation [KR15; Esp+20]. In this approximation, there is no correlation between two different atoms. If two operators A_i and B_j act on two different atoms $i \neq j$, we assume that $\langle A_i B_j\rangle = \langle A_i\rangle \langle B_j\rangle$. In a sense, this is still a weakly interacting approximation, since one can expect strong interactions to create some entanglement between particles that cannot be described by the mean-field approximation. For this reason, it is a plausible approximation to make in our case, since the interactions are smaller than the single atom deexcitation rate, so correlations will decay before they build up to large level.

To derive the mean-field equations, let us first derive for an operator $\hat{\mathcal{O}}$ the evolution of its expectation value $\left\langle\hat{\mathcal{O}}\right\rangle = \mathrm{tr}\left\{\hat{\rho}\hat{\mathcal{O}}\right\}$. From the master equation Equation 8.3, we obtain:

$$\begin{aligned}\frac{\mathrm{d}\left\langle\hat{\mathcal{O}}\right\rangle}{\mathrm{d}t} = \frac{i}{\hbar}\left\langle\left[\hat{H},\hat{\mathcal{O}}\right]\right\rangle + \sum_i \Gamma\left\langle\hat{\sigma}_i^+\hat{\mathcal{O}}\hat{\sigma}_i^- - \frac{1}{2}\left\{\hat{\sigma}_i^+\hat{\sigma}_i^-,\hat{\mathcal{O}}\right\}\right\rangle \\ + \sum_{i\neq j}\Gamma_{ij}\left\langle\hat{\sigma}_i^+\hat{\mathcal{O}}\hat{\sigma}_j^- - \frac{1}{2}\left\{\hat{\sigma}_i^+\hat{\sigma}_j^-,\hat{\mathcal{O}}\right\}\right\rangle\end{aligned} \tag{10.30}$$

By applying this equation to the population operator $\hat{\pi}_i^e$ and the dipole operator $\hat{\sigma}_i^-$, one finds:

$$\frac{\mathrm{d}\left\langle\hat{\pi}_i^e\right\rangle}{\mathrm{d}t} = i\frac{\Omega_i^*}{2}\left\langle\hat{\sigma}_i^-\right\rangle - i\frac{\Omega_i}{2}\left\langle\hat{\sigma}_i^+\right\rangle - \Gamma\left\langle\hat{\pi}_i^e\right\rangle + \frac{i}{\hbar}\sum_{j\neq i}\left[V_{ij}^*\left\langle\hat{\sigma}_j^+\hat{\sigma}_i^-\right\rangle - V_{ij}\left\langle\hat{\sigma}_j^-\hat{\sigma}_i^+\right\rangle\right] \tag{10.31}$$

$$\frac{\mathrm{d}\left\langle\hat{\sigma}_i^-\right\rangle}{\mathrm{d}t} = \left(i\Delta - \frac{\Gamma}{2}\right)\left\langle\hat{\sigma}_i^-\right\rangle + i\frac{\Omega_i}{2}\left\langle\hat{\pi}_i^e - \hat{\pi}_i^g\right\rangle + \frac{i}{\hbar}\sum_{j\neq i}V_{ij}\left\langle\hat{\sigma}_j^-(\hat{\pi}_i^e - \hat{\pi}_i^g)\right\rangle \tag{10.32}$$

These equations are not a closed set, since the derivative of the expectation values $\langle\hat{\pi}_i^e\rangle$

and $\left\langle \hat{\sigma}_i^- \right\rangle$ are related to the expectation value of products of operators like $\left\langle \hat{\sigma}_i^+ \hat{\sigma}_j^- \right\rangle$. To bypass this issue, we now make the mean field assumption that the expectation value of a product of operators for two different atoms can be factorized as the product of the operator for each atom. This way we get:

$$\frac{\mathrm{d}\left\langle \hat{\pi}_i^e \right\rangle}{\mathrm{d}t} = i\frac{\Omega_i^*}{2}\left\langle \hat{\sigma}_i^- \right\rangle - i\frac{\Omega_i}{2}\left\langle \hat{\sigma}_i^+ \right\rangle - \Gamma\left\langle \hat{\pi}_i^e \right\rangle + \frac{i}{\hbar}\sum_{j\neq i}\left[V_{ij}^*\left\langle \hat{\sigma}_j^+ \right\rangle\left\langle \hat{\sigma}_i^- \right\rangle - V_{ij}\left\langle \hat{\sigma}_j^- \right\rangle\left\langle \hat{\sigma}_i^+ \right\rangle\right] \tag{10.33}$$

$$\frac{\mathrm{d}\left\langle \hat{\sigma}_i^- \right\rangle}{\mathrm{d}t} = \left(i\Delta - \frac{\Gamma}{2}\right)\left\langle \hat{\sigma}_i^- \right\rangle + i\frac{\Omega_i}{2}\left\langle \hat{\pi}_i^e - \hat{\pi}_i^g \right\rangle + \frac{i}{\hbar}\sum_{j\neq i} V_{ij}\left\langle \hat{\sigma}_j^- \right\rangle\left\langle \hat{\pi}_i^e - \hat{\pi}_i^g \right\rangle \tag{10.34}$$

With the additional consideration $\langle \pi_i^e \rangle + \langle \pi_i^g \rangle = 1$, and $\left\langle \hat{\sigma}_i^+ \right\rangle = \left\langle \hat{\sigma}_i^- \right\rangle^*$, this forms a closed set of differential equations. These are the mean field equations for the problem of light-scattering. They are a generalization of the linear coupled dipole equations to the regime of non-negligible excitation. In particular, we recover the linear-coupled dipoles if we make the assumption $\langle \pi_i^e \rangle \approx 0$, and if we identify $d_i = 2\left\langle \hat{\sigma}_i^- \right\rangle \langle e|\boldsymbol{\epsilon}^* \cdot \hat{\boldsymbol{d}}|g\rangle$. The generalization to large excitation fraction, however, comes at the cost that the equations are now non-linear. For these reasons, these equations are sometimes called *non-linear coupled dipole equations*.

Another way to derive these equations is to assume that the density matrix can be factorized as a product a single particle density matrices:

$$\rho = \bigotimes_i \rho_i \tag{10.35}$$

By reinjecting this into the master equation, one gets equations over each ρ_i that are equivalent to Equation 10.33.

10.3.2 Influence of saturation

With Equation 10.33, we can now see what is the effect of a large driving field on the collective spectrum. Similarly to what was done for the linear coupled dipoles, we can solve for the total excitation probability in steady state by performing a first order expansion in $V_{ij}/\hbar\Gamma$. Again, this approximation is only valid for distances large enough that interactions are small. One can show that the expected spectrum is now

given by:

$$\langle\hat{\pi}_e\rangle \approx \frac{\Omega^2/\Gamma^2}{1+2\Omega^2/\Gamma^2+4\Delta^2/\Gamma^2}\left[1+4\frac{(1+4\Delta^2/\Gamma^2)(1+2\Omega^2/\Gamma^2)}{(1+2\Omega^2/\Gamma^2+4\Delta^2/\gamma^2)^2}\left(2\frac{\Delta_{C,\Omega}\Delta}{\Gamma^2}+\frac{\gamma_{C,\Omega}}{\Gamma}\right)\right] \tag{10.36}$$

with

$$\Delta_{C,\Omega}=\frac{\Delta_C}{1+2\Omega^2/\Gamma^2} \quad \text{and} \quad \gamma_{C,\Omega}=\frac{\gamma_C}{1+2\Omega^2/\Gamma^2} \tag{10.37}$$

where Δ_C and γ_C are the terms given in Equation 10.27 and derived in the classical regime. This spectrum is a lorentzian, with again an additional skew proportional to $\Delta_{C,\Omega}$. The maximum of this curve is approximately located at $\Delta_{C,\Omega}$. Its width is power broadened by $\sqrt{1+2\Omega^2/\Gamma^2}$, and is also modified by γ_C. Essentially, we find that collective effects give rise to behaviors very similar to the low excitation case, except now, the collective terms are divided by a factor $1+2\Omega^2/\Gamma^2$.

This is confirmed by measuring the spectrum as a function of driving field Ω as shown in Figure 10.6. One indeed observes that the shift vanishes for large driving field as $1/(1+2\Omega^2/\Gamma^2)$.

While a bit disappointing, it seems that collective effects on the steady-state spectrum do not survive for large atomic excitation. This behavior can actually be expected. Indeed, in steady-state, the mean atomic dipole $\langle\hat{\sigma}^-\rangle$ has a finite value and saturates for large driving field, scaling as:

$$\left\langle\hat{\sigma}^-\right\rangle = -i\frac{\Omega}{\Gamma}\frac{1+2i\Delta/\Gamma}{1+2|\Omega|^2/\Gamma^2+4\Delta^2/\Gamma^2} \tag{10.38}$$

At resonance, the ratio of the mean radiated field $V_{ij}\left\langle\hat{\sigma}_i^-\right\rangle$ over the laser field Ω thus scales as $1/(1+2\Omega^2/\Gamma^2)$, which is exactly the observed scaling law. For strong driving, the mean field radiated by the atoms becomes negligible compared to the laser field. It thus seems that the collective frequency shift observed only exists in the classical limit, for small population inversion.

To finish this section, Figure 10.7 shows the expected shift as function of spacing, taking into account both disorder and the saturation factor $1/(1+2\Omega^2/\Gamma^2)$. With these corrections, the predictions are now compatible with the measured shift.

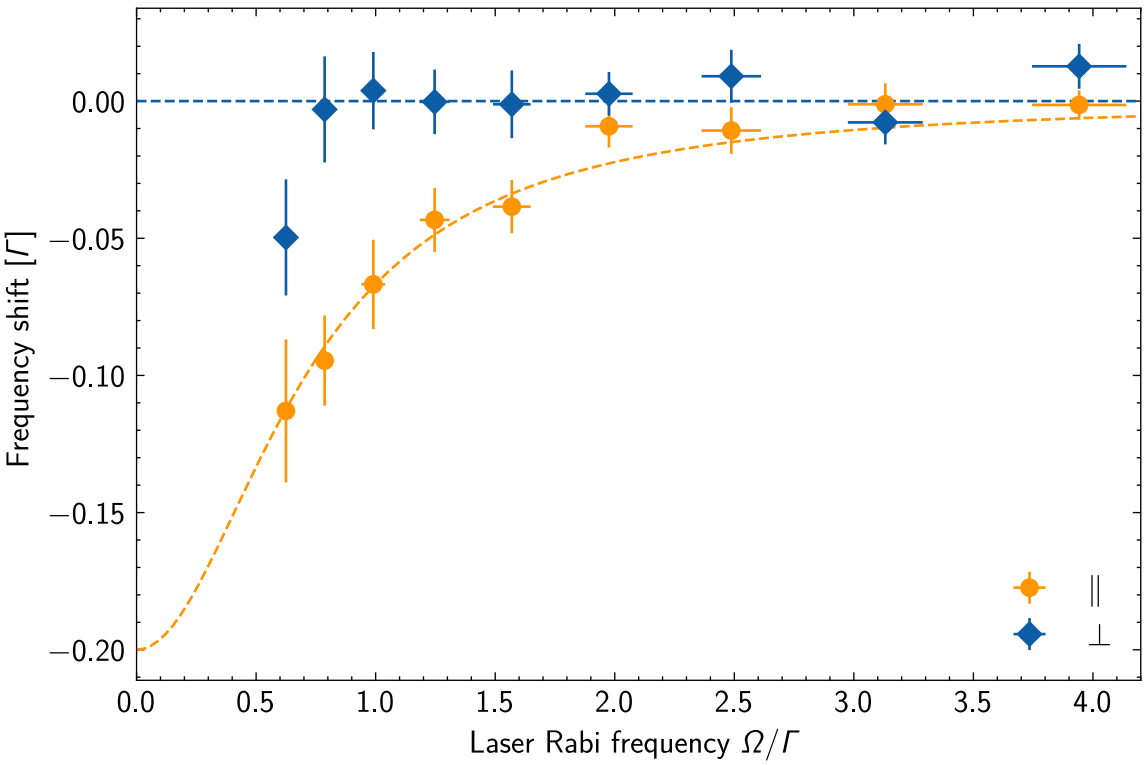

Figure 10.6. – Frequency shift of the spectrum as a function of the amplitude of the driving field. Blue diamonds and orange dots indicate the measured value of the shift respectively for perpendicular and axial driving directions. These measurements are obtained for a spacing $d = 1.25\,\mu\text{m}$. Dashed orange curve is the theoretical value from Equation 10.37, taking also into account positional disorder.

10.4 Beyond mean field?

10.4.1 Second order quantum cumulants

For all the results presented in this thesis, the spacing between the atoms is larger than the wavelength, such that interactions are relatively weak compared to the single atom lifetime. As a result, the interactions cannot build entanglement, since the system decays before it can build up to a noticeable level. For this reason, the mean field equations are enough to explain all experiments presented in this thesis. However, we plan to upgrade the setup to be able to reach spacings smaller than the wavelength of the light. In that case, interactions will be larger, and some richer effects might start to appear, even when driving in steady state. This is an interesting regime that we could probe with the same detection schema presented above. Indeed, by measuring coincidences of atoms in a picture after projecting the state with 421 nm light, we

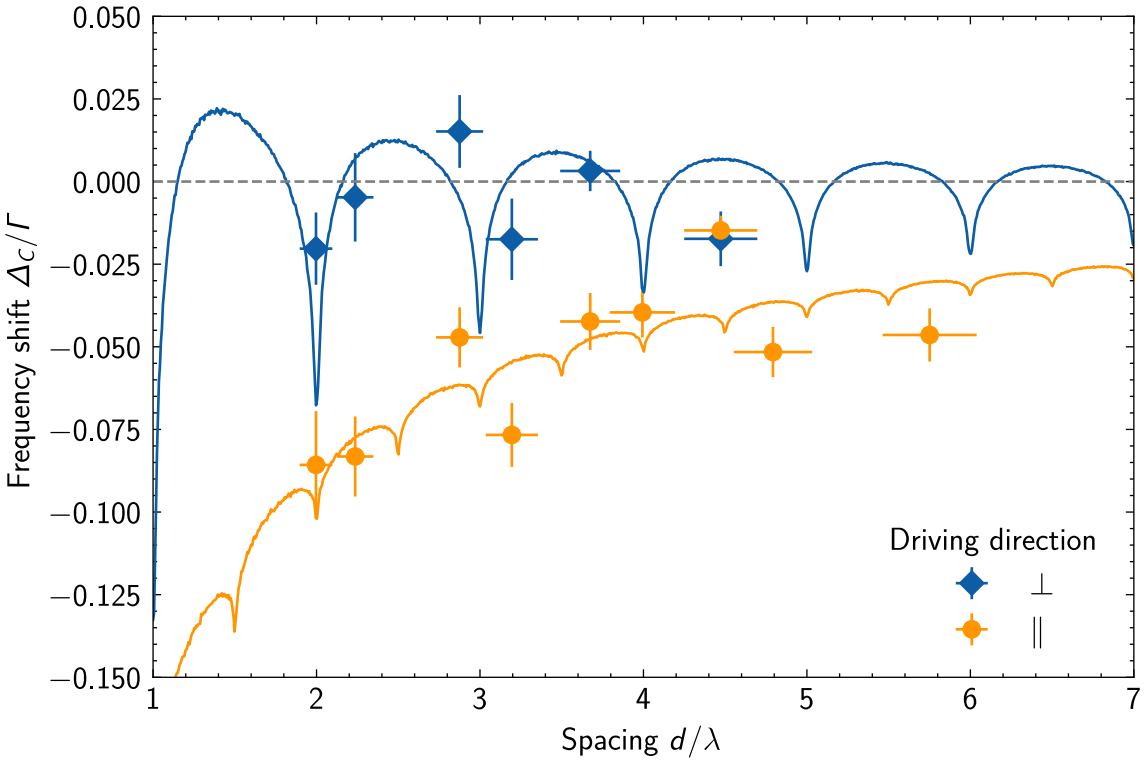

Figure 10.7. – Frequency shift of the spectrum as a function of spacing taking into account saturation according to Equation 10.37.

can access correlations between atomic populations $\left\langle \pi_i^e \pi_j^e \right\rangle$. If we apply laser rotation pulses, we can also have access to correlations between dipoles $\left\langle \hat{\sigma}_i^X \hat{\sigma}_j^X \right\rangle$ and $\left\langle \hat{\sigma}_i^Y \hat{\sigma}_j^Y \right\rangle$.

Measuring such quantities can be challenging. Notably, it requires a relatively long acquisition time since one needs to repeat the experiment many times to collect enough coincidence events. That is why it would be useful to have some idea of which regime of parameters to explore. For example, what are the most promising detuning, spacing, and probe direction to observe interesting effects?

We cannot use the mean field equations described in the previous section to explore this regime, since these equations assume that no quantum correlations exist between atoms, i.e. $\langle A_i B_j \rangle = \langle A_i \rangle \langle B_j \rangle$. The direct approach is to solve numerically the full master equation to compute the total density matrix ρ in order to extract the expectation value $\langle A_i B_j \rangle = \mathrm{Tr}\{\rho A_i B_j\}$. Unfortunately, this approach becomes technically challenging when considering more than about 10 atoms, due to the exponential scaling of the state to represent. Instead, I will present here another method, the *second order quantum cumulants* [Kub62; RS21; PHR22; ROY23], that can be used to compute quantities such as $\langle A_i B_j \rangle$. This method is the next order of approximation after the mean field equations. In the previous section, we obtained the equation for

the evolution of single particle operators, for example:

$$\frac{\mathrm{d}\left\langle\hat{\pi}_i^e\right\rangle}{\mathrm{d}t} = i\frac{\Omega_i^*}{2}\left\langle\hat{\sigma}_i^-\right\rangle - i\frac{\Omega_i}{2}\left\langle\hat{\sigma}_i^+\right\rangle - \Gamma\left\langle\hat{\pi}_i^e\right\rangle + \frac{i}{\hbar}\sum_{j\neq i}\left[V_{ij}^*\left\langle\hat{\sigma}_j^+\hat{\sigma}_i^-\right\rangle - V_{ij}\left\langle\hat{\sigma}_j^-\hat{\sigma}_i^+\right\rangle\right] \quad (10.39)$$

But now, let us keep the expectation of the product of operators, and we write its time-derivative using Equation 10.30:

$$\begin{aligned}\frac{\mathrm{d}\left\langle\hat{\sigma}_i^+\hat{\sigma}_j^-\right\rangle}{\mathrm{d}t} &= i\frac{\Omega_j}{2}\left\langle\hat{\sigma}_i^+\hat{\sigma}_j^Z\right\rangle - i\frac{\Omega_i^*}{2}\left\langle\hat{\sigma}_j^-\hat{\sigma}_i^Z\right\rangle - \Gamma\left\langle\hat{\sigma}_i^+\hat{\sigma}_j^-\right\rangle \\ &+ 2\Gamma_{j,i}\left\langle\hat{\pi}_i^e\hat{\pi}_j^e\right\rangle - \frac{i}{\hbar}V_{j,i}\left\langle\hat{\pi}_i^e\right\rangle + \frac{i}{\hbar}V_{j,i}^*\left\langle\hat{\pi}_j^e\right\rangle + \frac{i}{\hbar}\sum_{k\neq i,j}\left[V_{jk}\left\langle\hat{\sigma}_k^-\hat{\sigma}_i^+\hat{\sigma}_j^Z\right\rangle - V_{ik}^*\left\langle\hat{\sigma}_k^+\hat{\sigma}_j^-\hat{\sigma}_i^Z\right\rangle\right]\end{aligned} \quad (10.40)$$

We can do this for every product of two operators, with all equations summarized in Appendix D. We obtain a system of differential equations, but like for the mean field case, they depend on the value of higher order terms like $\left\langle\hat{\sigma}_k^+\hat{\sigma}_j^-\hat{\sigma}_i^Z\right\rangle$. To get a closed set of equations, we assume that the *third order cumulants* for different atoms vanish. The third order cumulant is defined for three operators A, B and C as:

$$\langle ABC\rangle_C = \langle ABC\rangle - \langle AB\rangle\langle C\rangle - \langle AC\rangle\langle B\rangle - \langle A\rangle\langle BC\rangle + 2\langle A\rangle\langle B\rangle\langle C\rangle \quad (10.41)$$

It can be shown that this quantity is indeed zero when one of the operator is independent of the others [Kub62]. By making the approximation $\langle ABC\rangle_C = 0$, we can express the mean value of the product of three operators as a function of only the expectation value of the product of two operators. This way, we can close the system of equations that can then be solved numerically. At this order of approximation, the number of equations scales as N^2, making it tractable for several tens of atoms, up to hundreds.

It is worth noting that this approximation is only still valid for small interactions between the atoms, and presents errors that scale as $(V_{ij}/\hbar\Gamma)^3$. Deep in the sub-wavelength regime, this assumption breaks, and one has either to go to higher order cumulant equations [ROY23], or even switch to other methods. Still, this can be a first approximation to try to predict the interesting regime to explore.

10.4.2 Correlations between dipoles

Using this method, I calculated the correlations between atoms in a chain of 30 atoms in steady-state. Here I give examples of the kind of correlations that can

be observed, to show that a large variety of behaviours can emerge. For example, Figure 10.8 a shows the correlations between the in-phase $\left\langle \hat{\sigma}_i^X \hat{\sigma}_j^X \right\rangle$ and out-of phase $\left\langle \hat{\sigma}_i^Y \hat{\sigma}_j^Y \right\rangle$ components of the dipoles for a spacing $d = \lambda$ and a detuning $\Delta = -0.5\Gamma$. All figures in this plot correspond to a driving perpendicular to the chain. One observes long-range ferromagnetic order for the in-phase component of the dipoles. In Figure 10.8 b, I plot the same for a spacing $d = \lambda/2$. In this case, there is a long-range anti-ferromagnetic order between the dipoles. When changing the detuning to $\Delta = +\Gamma/2$ in Figure 10.8 c, there is now stronger nearest neighbors correlations, but the long-range order disappears. What is maybe surprising is that increasing the Rabi frequency in Figure 10.8 d can change the behavior qualitatively. For example, while the out-of-phase correlations increase, there are now no in-phase correlations between nearest neighbors, it is only when going to $|i - j| \geq 2$ that correlations appear.

This collection of behaviors shows that there is a rich structure that appears when driving the atoms to steady-state [OYL14; PC18; PC20; PR20]. This variety of phenomenas is maybe not surprising, since even the XY hamiltonian in the absence of dissipation presents a complex behaviour [Che+23]. Adding dissipation and interactions that oscillate with distance probably only makes the system more complex. Studying the emergence of the different phases that appear in our driven dissipative chains could be interesting, and one could for example explore if the effects mentioned above are coming from the real part of the interaction or if they are caused by collective dissipation. Measuring the correlations between atoms can be used to probe this phenomenon. If we are able to reach smaller spacings, this is something that could be readily explored with the platform presented here.

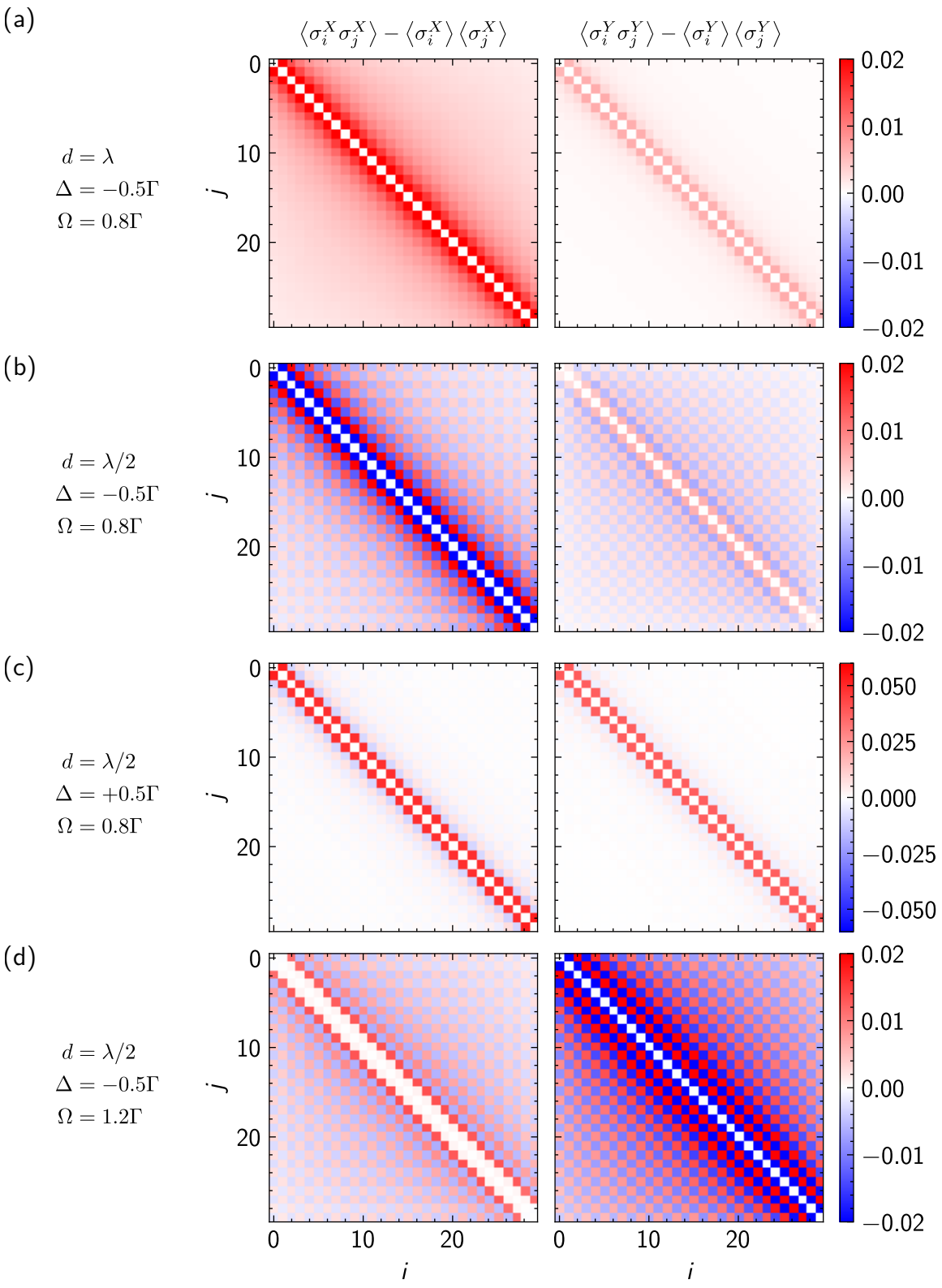

Figure 10.8. – Correlations between atomic dipoles in a steady-state chain driven perpendicular to its axis.

Summary

In this chapter, I have shown the effect of collective dipole-dipole interactions on the steady state spectrum of a chain of atoms. When the chain is being driven axially, a coherent buildup develops between the field radiated by the atoms down the chain. This results in a shift of the spectrum towards negative detunings. This shift can be understood classically by approximating the atoms with linear dipoles. In fact, the shift is maximal in the low-driving regime, and vanishes for strong field. This is because the mean atomic dipole saturates in steady-state at large intensity.

In addition to this buildup effect, we also expect Fabry-Perot resonances when the spacing between the atoms is a multiple of λ or $\lambda/2$. However, this phenomenon is very sensitive to positional disorder in the chain, and for this reason, we were not able to observe it. Still, this could be an interesting effect to explore in the future. We could observe these resonances if we manage to reduce the thermal disorder in the chain. In addition, it seems that it could be a regime where quantum correlations start to emerge. We have recently achieved near ground state cooling of the atoms in the tweezers using the narrow 741 nm transition. This strongly reduces the effect of disorder such that it should be possible to observe what happens near these resonances.

Chapter 11

Ramsey spectroscopy with collective dissipation

Contents

While in the previous chapter we have explored collective effects in steady-state, I will here discuss some Ramsey spectroscopy measurements in time dependent regime. Can we observe collective effects in this case, and if so, how do they relate to the results obtained in steady-state? The results presented here can also be found in the publication [Hof+24].

11.1 Rabi oscillations

First, to observe non-stationary effects, a simple experiment consists in driving the atoms continuously with a laser and to observe how the system evolves over time. If we measure the population of the excited state as a function of the duration for which the laser pulse is applied, we observe Rabi oscillations. Figure 11.1 shows such oscillations in the case of independent atoms. As one can see, the population oscillates between the ground and excited state at frequency $\Omega = 2\pi \times 3.6\,\mathrm{MHz}$. Neglecting dissipation, the atoms oscillate between the ground and the excited state coherently at frequency Ω:

$$|\psi\rangle = \cos(\Omega t/2)\,|g\rangle + \sin(\Omega t/2) e^{i\boldsymbol{k}\cdot\boldsymbol{r}}\,|e\rangle \tag{11.1}$$

where one has to also take into account the phase of the laser at the position of the atom. This is only true for the first few oscillations during a time $t \ll 1/\Gamma$. At

longer time, the amplitude of these oscillations damps out with timescale Γ due to the intrinsic decoherence induced by spontaneous emission. For $t \gg 1/\Gamma$, the system reaches the steady state, which was discussed in the previous chapter.

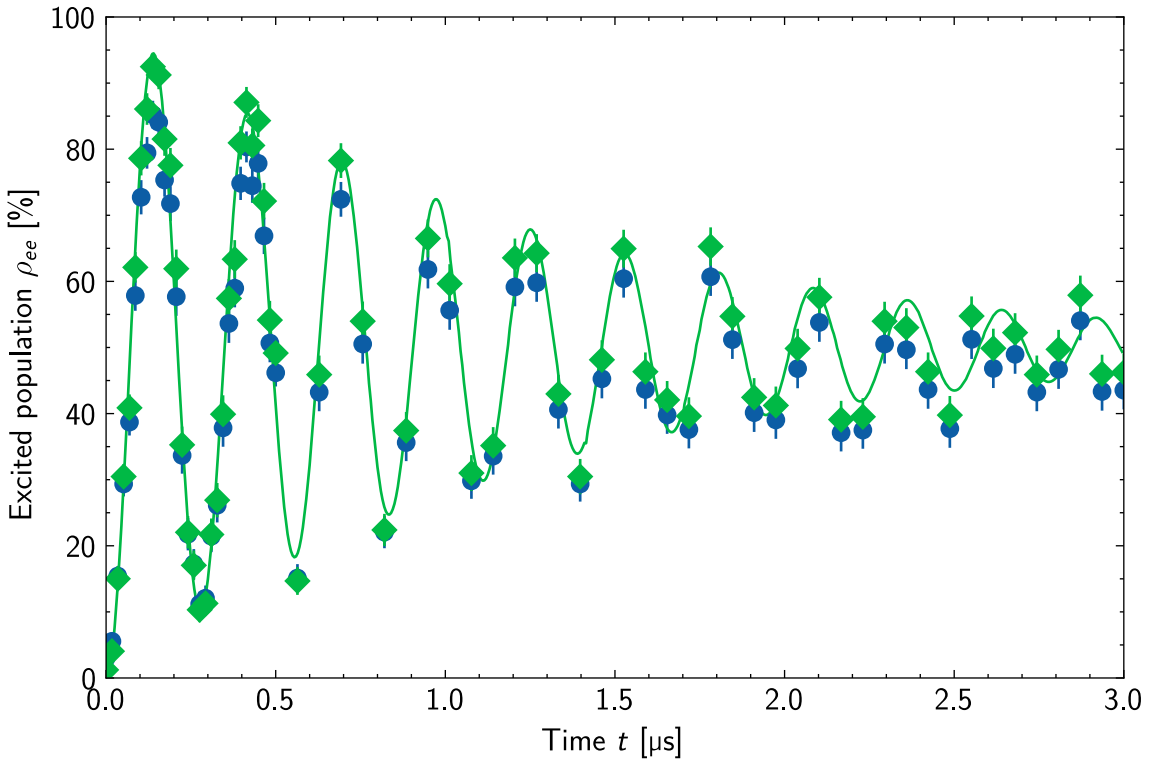

Figure 11.1. – Rabi oscillations on the excited state population. Blue points are raw experimental data, while the green diamonds are the corrected data taking into account the finite fidelity of the measurement as explained in Section 9.2.2. The green line is a fit to the corrected data obtained by solving the Bloch equations for independent atoms.

In principle, it could be possible to look at the effect of interactions on the Rabi oscillations to try to observe a variation of their amplitude, frequency or damping rate. However, for our situation at large spacings, we expect the interaction to be small compared to both the Rabi frequency and the single atom lifetime that dictates respectively the oscillation frequency and the damping rate. Because of this, the effect of interactions on the shape of the Rabi oscillations is small, and it would be difficult to observe it. In addition, if the laser is kept on for the whole duration of the evolution, we expect to see similar saturation of the dipoles than in steady state at large driving field. For these reasons, we did not explore the modification of Rabi oscillations by the presence of interactions.

11.2 Ramsey spectroscopy

Instead of having the laser continuously on, one can observe how the dipoles interact after they have been excited, and are then left to evolve freely without a driving field. One measurement for which this applies is *Ramsey spectroscopy*. This experiment probes the evolution of a two-level system in the absence of external field [Ram83; Ram90].

In this scheme, the atoms are first prepared in a coherent superposition of the ground and excited state. This is done by applying a short pulse of laser light with duration τ such that $\Omega\tau = \pi/2$. This creates the state $|\psi_i\rangle = \left(|g\rangle + e^{i\boldsymbol{k}\cdot\boldsymbol{r}_i}|e\rangle\right)/\sqrt{2}$, which is a state with a maximal dipole moment. The laser is then shut down, and the dipoles precess at their natural frequency. Then, in the classical Ramsey experiment, the amount by which the atoms have precessed is measured by comparing the accumulated phase of the atoms to that of the laser. This is done by again applying a $\pi/2$ laser pulse to map the phase acquired by the atoms into a population difference that can be measured. This technique is used for example to measure the frequency of atomic transitions with very high precision [Lud+15].

In our case, in addition to the coherent precession of the dipoles during the free evolution, the atoms can also decay by spontaneous emission. The field they radiate will then drive the other atoms, even in the absence of laser light. As this driving field will modify the evolution of the internal state of the atoms during the free evolution, we can expect to see a modification of the measured frequency by the interactions. However, it is not so obvious what the modification will be. We have seen in the previous chapter that a direct spectrum presents a collective frequency shift Δ_C in the classical limit, but that this shift vanishes for large atomic excitation. Therefore, since Ramsey spectroscopy is performed with half-probability for the atoms to be in the excited state, what would be the shift observed, if any? In addition, even if the initial population inversion is zero at the beginning of the interrogation, an imbalance will appear over time as the atoms decay back to the ground state. Can we thus expect to see a frequency shift that depends on the interrogation time? To try to answer these questions, I will first discuss in more detail the Ramsey spectroscopy experiments that we performed, and I will then discuss the results obtained.

11.2.1 Isolated atoms

To start, I will here describe more formally the Ramsey experiment that we performed. To keep the interpretation of the results simple, we performed here the simplest version of the Ramsey experiment, with only two pulses of laser light. However, in real spectroscopy experiments, it is instead usual to have additional steps, such as spin echo, to improve the performance of the measurement, as was done for instance to measure the collective Ramsey shift in optical clocks [Hut+24].

We start by applying a short and intense pulse of 626 nm light to put the atoms in a coherent state with a non-zero dipole moment. During this pulse, the laser has Rabi frequency $\Omega = 2\pi \times 3.6\,\mathrm{MHz}$ and detuning Δ. The pulse has a duration τ between 50 ns to 150 ns, which is a duration much smaller than the lifetime of the excited state. This corresponds to the first half-period of a Rabi oscillation shown in Figure 11.1.

To represent the evolution of the atomic state, it is useful to subtract the position-dependent phase of the laser that applies the pulses. To do so, let us introduce the operators:

$$\tilde{\sigma}_i^- = e^{-i\boldsymbol{k}\cdot\boldsymbol{r}_i}\hat{\sigma}_i^- \quad \text{and} \quad \tilde{\pi}_i^e = \hat{\pi}_i^e \tag{11.2}$$

where $\boldsymbol{k}$ is the wavevector of the light. In addition, to represent the state on the Bloch sphere, we define the three operators:

$$\tilde{\sigma}_i^X = \tilde{\sigma}_i^+ + \tilde{\sigma}_i^- \tag{11.3}$$

$$\tilde{\sigma}_i^Y = i\left(\tilde{\sigma}_i^- - \tilde{\sigma}_i^+\right) \tag{11.4}$$

$$\tilde{\sigma}_i^Z = 2\tilde{\pi}_i^e - 1 \tag{11.5}$$

The operator $\tilde{\sigma}_i^X$ represents the component of the atomic dipole in phase with the laser, while $\tilde{\sigma}_i^Y$ is the out-of-phase component. $\tilde{\sigma}_i^Z$ is the operator for the population inversion. For a single atom, any state mixture can be described fully by the mean value of these operators, forming a 3D vector:

$$\tilde{\boldsymbol{\sigma}}_{\boldsymbol{i}} = \left[\left\langle\tilde{\sigma}_i^X\right\rangle, \left\langle\tilde{\sigma}_i^Y\right\rangle, \left\langle\tilde{\sigma}_i^Z\right\rangle\right] \tag{11.6}$$

This makes it possible to plot the state using the Bloch sphere representation, as

shown in Figure 11.2 a, b, c. During the pulse of light, these values evolve as:

$$\frac{\mathrm{d}\left\langle\tilde{\sigma}_i^X\right\rangle}{\mathrm{d}t} = \Delta\left\langle\tilde{\sigma}_i^Y\right\rangle - \frac{\Gamma}{2}\left\langle\tilde{\sigma}_i^X\right\rangle \tag{11.7}$$

$$\frac{\mathrm{d}\left\langle\tilde{\sigma}_i^Y\right\rangle}{\mathrm{d}t} = -\Delta\left\langle\tilde{\sigma}_i^X\right\rangle - \Omega\left\langle\tilde{\sigma}_i^Z\right\rangle - \frac{\Gamma}{2}\left\langle\tilde{\sigma}_i^Y\right\rangle \tag{11.8}$$

$$\frac{\mathrm{d}\left\langle\tilde{\sigma}_i^Z\right\rangle}{\mathrm{d}t} = \Omega\left\langle\tilde{\sigma}_i^Y\right\rangle - \Gamma\left[\left\langle\tilde{\sigma}_i^Z\right\rangle + 1\right] \tag{11.9}$$

During the pulses, the Rabi frequency Ω is much larger than the detuning Δ, and their duration is much shorter than the lifetime $1/\Gamma$. In this case, we can neglect the terms proportional to Δ and Γ and keep only the terms proportional to Ω[1]. The laser performs a rotation of the state in the Bloch sphere around the X axis, with angle $\theta = \Omega\tau$. In the canonical Ramsey experiment $\theta = \pi/2$, and the atomic state is brought on the equator of the Bloch sphere. This is also the situation where the atomic dipole is the largest, and where one might expect the largest interactions. This rotation is illustrated on Figure 11.2 a. For the following discussion, I will keep an arbitrary angle θ so that we can see how the result depends on the initial population inversion $\tilde{\sigma}^Z(0) = -\cos(\theta)$.

After this pulse, the atoms evolve freely for a time T. During this evolution, the coherences follow Equation 11.7 and Equation 11.8 with $\Omega = 0$. The coherences therefore rotate around the Z axis with frequency Δ, while also decaying at a rate $\Gamma/2$:

$$\left\langle\tilde{\sigma}_i^X\right\rangle = \sin(\theta)\sin(\Delta T)e^{-\Gamma T/2} \tag{11.10}$$

$$\left\langle\tilde{\sigma}_i^Y\right\rangle = \sin(\theta)\cos(\Delta T)e^{-\Gamma T/2} \tag{11.11}$$

For $\Omega = 0$, the population inversion decouples from the coherences in Equation 11.9, and simply decays at a rate Γ. In particular, its evolution does not depend on the detuning Δ:

$$\left\langle\tilde{\sigma}_i^Z\right\rangle = \left[1 - \cos(\theta)\right]e^{-\Gamma T} - 1 \tag{11.12}$$

This is illustrated on Figure 11.2 b. After that, we perform a last laser rotation around the X axis with angle θ, similarly to the first pulse. This maps the precession along the equator in an observable population inversion, as illustrated on Figure 11.2 c.

[1] These approximations can be relaxed, it would make the analytical expressions more complicated, but it does not fondamentally change the results presented here.

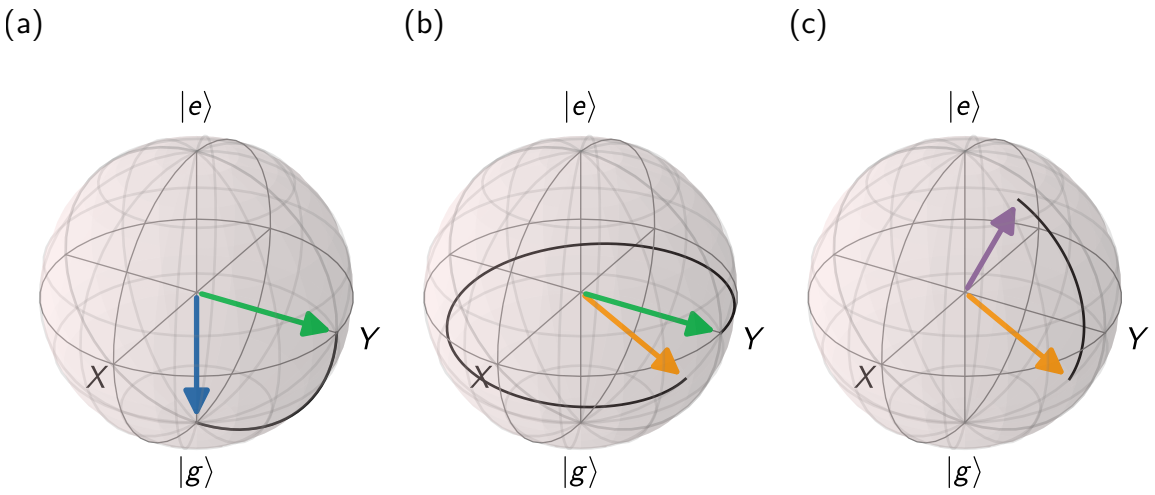

Figure 11.2. – Illustration of the evolution of the Bloch vector during the Ramsey sequence. (a) A first laser rotation with an angle $\theta = \pi/2$ puts the Bloch vector on the equator. (b) Free evolution of the Bloch vector during a time T. The vector rotates around the Z axis at a rate Δ. In addition, its transverse components decay at a rate $\Gamma/2$, while its Z component decays at a rate Γ. (c) A second laser rotation with an angle $\theta = \pi/2$ maps the precession along the equator into a population inversion.

Equation 11.13 below summarizes the evolution of the Bloch vector at each step.

$$\begin{bmatrix} 0 \\ 0 \\ -1 \end{bmatrix} \xrightarrow{R_X(\theta)} \begin{bmatrix} 0 \\ \sin(\theta) \\ -\cos(\theta) \end{bmatrix} \xrightarrow{T} \begin{bmatrix} \sin(\theta)\sin(\Delta T)e^{-\Gamma T/2} \\ \sin(\theta)\cos(\Delta T)e^{-\Gamma T/2} \\ (1-\cos(\theta))e^{-\Gamma T} - 1 \end{bmatrix}$$
$$\xrightarrow{R_X(\theta)} \begin{bmatrix} \sin(\theta)\sin(\Delta T)e^{-\Gamma T/2} \\ \cos(\theta)\sin(\theta)\cos(\Delta T)e^{-\Gamma T/2} - \sin(\theta)\left[(1-\cos(\theta))e^{-\Gamma T} - 1\right] \\ \cos(\theta)\left[(1-\cos(\theta))e^{-\Gamma T} - 1\right] + \sin(\theta)^2\cos(\Delta T)e^{-\Gamma T/2} \end{bmatrix} \quad (11.13)$$

The quantity that we measure as the end of the experiment is excited state fraction:

$$\rho_{ee} = \frac{1}{2}\left[\cos(\theta)\left[(1-\cos(\theta))e^{-\Gamma T} - 1\right] + 1\right] + \frac{1}{2}\sin(\theta)^2\cos(\Delta T)e^{-\Gamma T/2} \quad (11.14)$$

There are two terms in this expression. There is first a constant offset that does not depend on the detuning Δ, and that will not matter for the discussion here. More importantly, there is a term with a dependency on the detuning Δ. This term presents oscillations as $\cos(\Delta T)$ with a contrast $\sin(\theta)^2 e^{-\Gamma T/2}$. This is the typical Ramsey fringe. By finding the position Δ_R of the maximum of this curve, one can measure

the frequency of the transition.

Since the contrast of the fringes scales as $\sin(\theta)^2$, it is advantageous to have $\theta = \pi/2$. In addition, one usually wants to extend the interrogation time T. This way, the sensibility of the frequency measurement is increased as it produces narrower fringes. However, in our case where decay is present, the contrast is also reduced over time by $e^{-\Gamma T/2}$ as the coherences decay. For this reason, the interrogation time cannot be made arbitrarily large. This is illustrated in Figure 11.3. For short interrogation times, the fringes have a large contrast, but they are wide. For long interrogation times, the fringes are narrow, but their contrast is small.

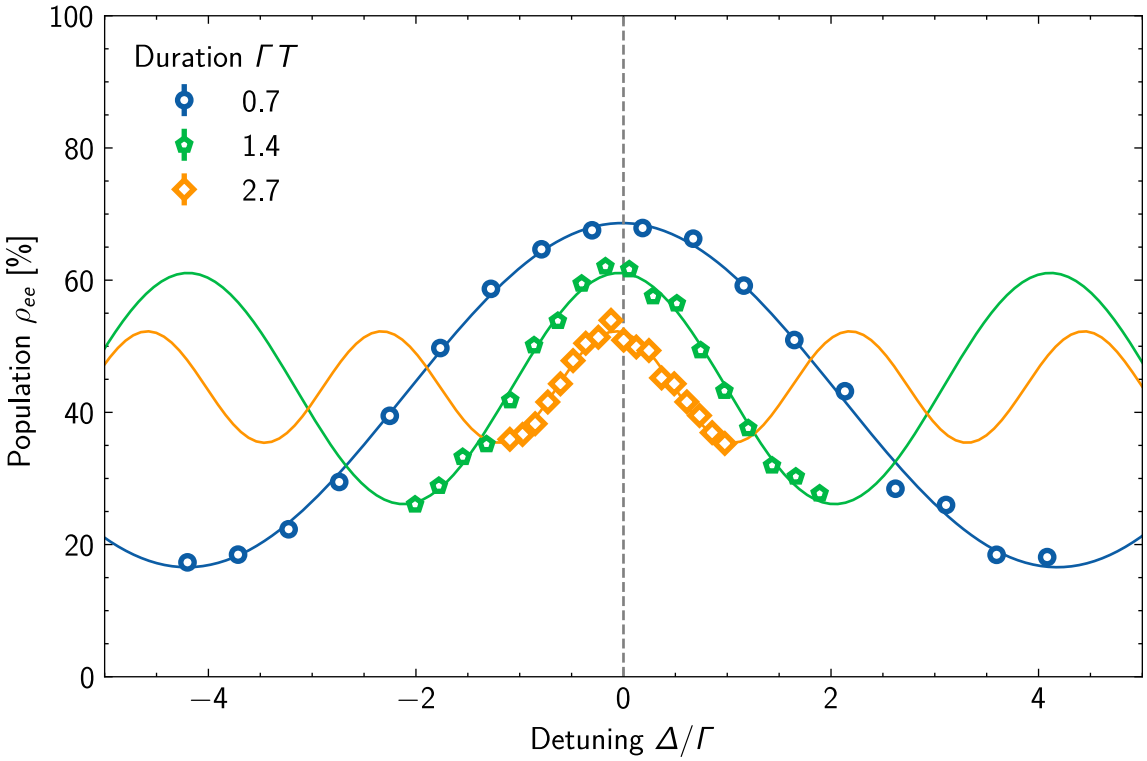

Figure 11.3. – Ramsey fringes for different interrogation times T. This data corresponds to the ideal Ramsey sequence, with θ close to $\pi/2$. As the interrogation time T increases, the fringes become narrower, but their contrast decreases. Note that the data showed here is taken in the interacting case, which is why all fringes do not line up exactly, and it will be discussed later.

For the non-interacting case where atoms are far apart, we fit the fringes obtained to extract the frequency of the transition. This is shown in Figure 11.4, where the measurement is taken for different interrogation times and different initial population inversions. We observe that in all cases, the measured shift is compatible with zero. This is not surprising since for isolated atoms, the interrogation time T and amplitude

θ of the initial pulse only influence the amplitude of the fringes and not the position of their maxima according to Equation 11.14.

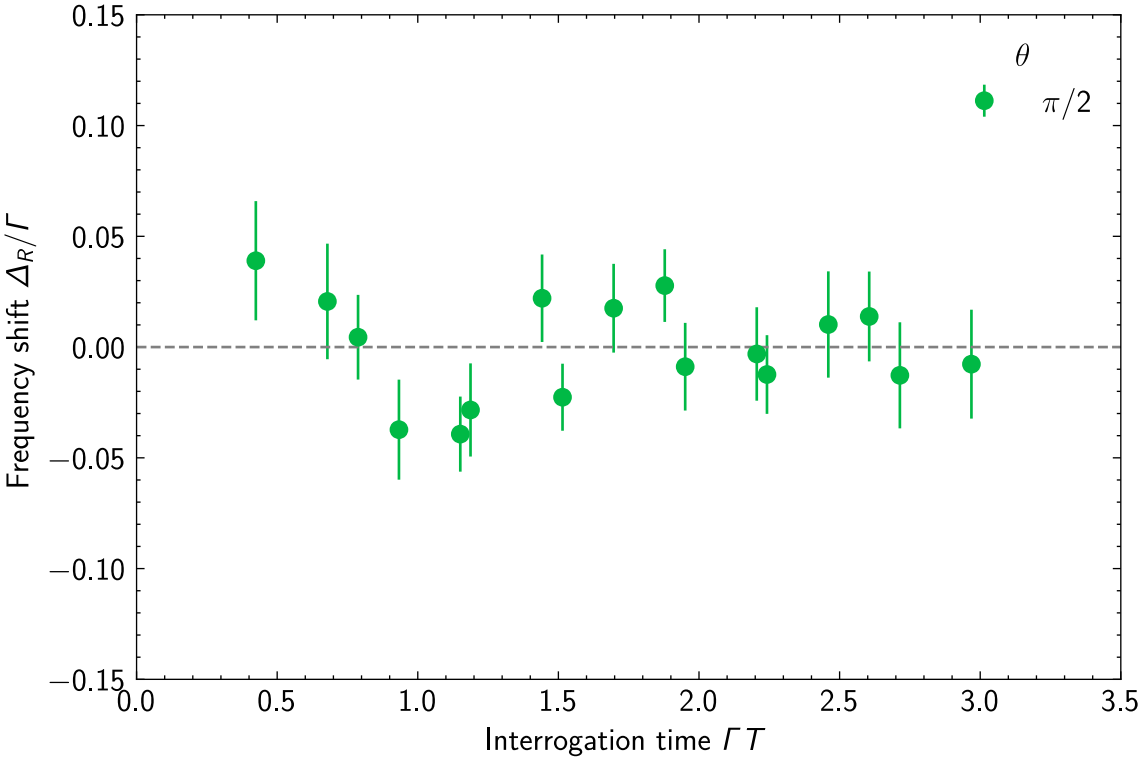

Figure 11.4. – Ramsey spectroscopy for non-interacting atoms. The spacing between the traps is 2.5 µm, but the traps are not rearranged such that the average spacing is 5.0 µm. No detuning from the bare transition is measured. We unfortunately did not perform this experiment in the non-interacting case for different pulse areas θ.

We initially performed the experiment with the 532 nm lattice to increase the axial confinement of the atoms in the chain. However, we observed that the lattice creates time-dependent shifts of the transition when it is turned off and on during the Ramsey sequence. This dynamics occurs over the first 2 µs and disappear for longer times. The reason why switching the lattice on and off creates a shift is not clear. One possibility is that it accelerates the atoms with respect to the probe laser beam, resulting in a Doppler shift. Because of this issue, the results presented above and in the next section were performed *without* the lattice, to make sure that it does not perturb the measurement. For this reason, the shifts measured are smaller than those obtained in the previous chapter in steady state.

11.2.2 With interactions

Experimental results

Let us now look at what happens when the atoms are close. In Figure 11.5, I show the results of the Ramsey spectroscopy when the atoms are arranged in a chain with a spacing $d = 1.4\,\mu\text{m} = 2.2\lambda$. The procedure to prepare this chain is similar to the one explained in Chapter 10, with the only difference being that the lattice is not turned on for the measurements presented here.

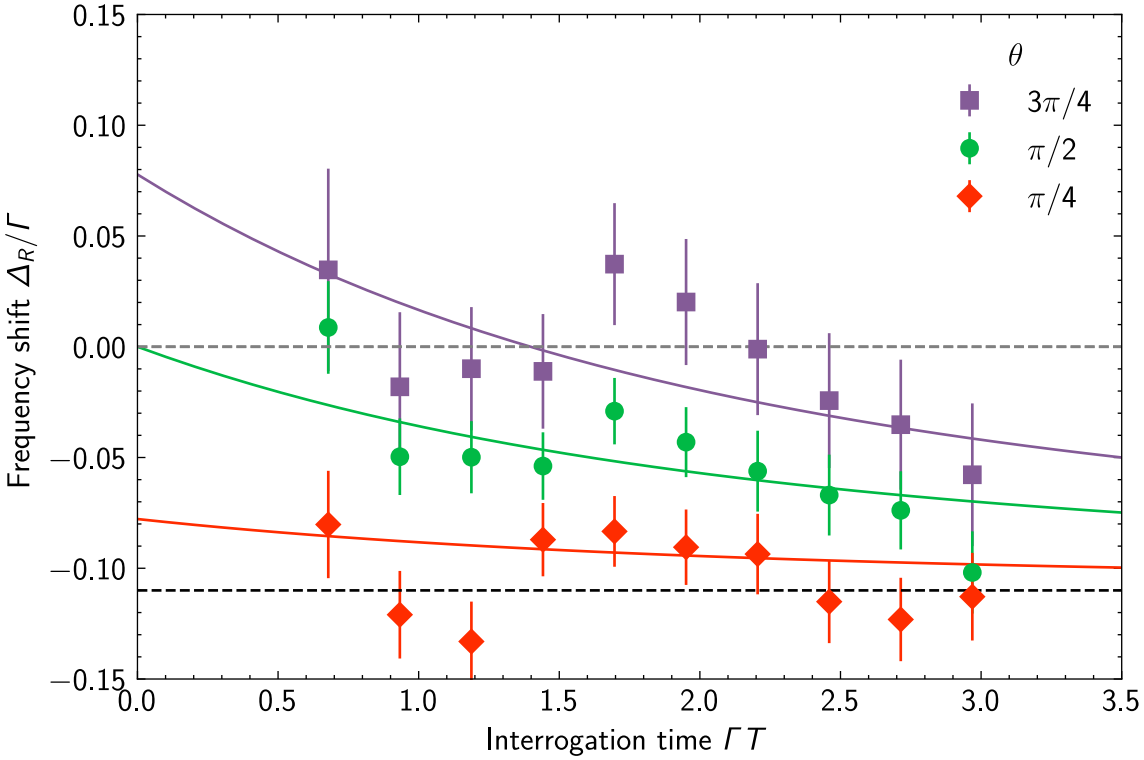

Figure 11.5. – Ramsey spectroscopy for atoms at spacing $d = 1.4\,\mu\text{m}$, with an interrogation laser sent along the direction of the chain. Each set of points corresponds to an initial population inversion $\cos(\theta)$. For each set, the extracted detuning is plotted as a function of the Ramsey interrogation time T. The dashed black line indicates the theoretical value of the classical shift Δ_C for this chain spacing and disorder. The colored lines correspond to the expected behviours using the model of Equation 11.19.

We can observe several features on Figure 11.5. One can see that the measured shift depends on the initial pulse area θ. For a small population inversion $\theta = \pi/4$, there is a negative frequency shift $\Delta_R \approx -0.1\Gamma$. The value of this shift is close to the predicted classical shift $\Delta_C = -0.11\Gamma$ derived in the previous chapter for the steady-state spectrum. It is maybe not surprising that we get a value similar to Δ_C

when θ is small, as it corresponds to the limit of low atomic excitation. In the case where the initial population inversion is zero $\theta = \pi/2$, the shift at small interrogation time T is compatible with zero, but then decreases towards Δ_C as T increases. For an initially large population inversion $\theta = 3\pi/4$, the measured shift starts at a value slightly above 0, and then also decays over time towards Δ_C.

It is not totally unexpected that all values converge to Δ_C for long interrogation times, since the population decays over time, and the system approaches the low excitation limit. What is maybe more surprising is the initial value of the shift depending on θ.

The data presented on Figure 11.5 is quite noisy, making it difficult to see very small shifts. To reduce the errorbars by a factor two, one would need to quadrupule the duration of the experiment. However, the data presented here already corresponds to 200 000 repetitions of the experiment, or a bit more than two full days of continuous acquisition at a repetition rate of 1 Hz. Ensuring the upmost stability of the setup for durations longer than this starts to become challenging. This relatively low repetition rate is a limitation of cold atom plateforms, but efforts to improve the repetition rate or to develop non-destructive measurement technique could improve the situation.

Mean-field model

I will try here to provide an explanation for the behaviour of the Ramsey frequency shift as a function of the interrogation time T and the initial population inversion θ. The dependency on θ has been studied, both theoretically [CYL04] and experimentally [Hut+24], in the case of optical lattice clocks. Indeed, for these experiments, it is crucial to understand how the interactions can modify the frequency measured. Since these experiments use ultra-narrow transitions, with millihertz linewidths, the collective shift has only been studied in the regime where the lifetime $1/\Gamma$ is very long compared to the interrogation time T. In this case, it is predicted that the initial frequency shift indeed has a dependency on the initial population inversion as:

$$\Delta_R = \Delta_C \cos(\theta) \tag{11.15}$$

In the limit of low atomic excitation $\theta \approx 0$, one indeed recovers the classical shift Δ_C. For a perfect Ramsey sequence with $\theta = \pi/2$, the shift is zero. In the limit of large

atomic excitation $\theta \approx \pi$, the shift is now equal to $-\Delta_C$: Somehow the frequency shift when the atoms are fully inverted is still related to the value in the classical limit.

To explain this behavior, let us try to predict the measured shift by adapting the derivation presented in [CYL04]. When doing so, we will also relax the approximation $\Gamma T \ll 1$, and instead we will assume that interactions are weak, i.e. $V_{ij}/\hbar\Gamma \ll 1$. There is no need to take interactions into account during the laser pulses, since the Rabi frequency involved is large and their duration is much shorter than the time for interactions to take place. To a good approximation, we then only need to take account interactions during the free evolution for the duration T. To compute the evolution of the dipole during this time, we can use the mean field equation introduced in Section 10.3:

$$\frac{\mathrm{d}\left\langle\tilde{\sigma}_i^-\right\rangle}{\mathrm{d}t} = \left(i\Delta - \frac{\Gamma}{2}\right)\left\langle\tilde{\sigma}_i^-\right\rangle + \frac{i}{\hbar}\sum_{j\neq i}\tilde{V}_{ij}\left\langle\tilde{\sigma}_j^-\right\rangle\left\langle\tilde{\sigma}_i^Z\right\rangle \tag{11.16}$$

where the position-dependent phase applied by the laser is taken into account in the interaction potential $\tilde{V}_{ij} = V_{ij}e^{i\boldsymbol{k}\cdot(\boldsymbol{r}_j-\boldsymbol{r}_i)}$.

Equation 11.16 can be solved at first order in V_{ij} using perturbation theory. To do so, we assume that the solution corresponds to the non-interacting case given in Equation 11.10 and Equation 11.12 with a small correction proportional to V_{ij}. In the term $\sum_{j\neq i}\tilde{V}_{ij}\left\langle\tilde{\sigma}_j^-\right\rangle\left\langle\tilde{\sigma}_i^Z\right\rangle$, we can thus replace $\left\langle\tilde{\sigma}_j^-\right\rangle$ and $\left\langle\tilde{\sigma}_i^Z\right\rangle$ by their value in the non-interacting case to get the first order solution. Integrating the differential equation obtained this way, one finds for the total dipole:

$$\left\langle\tilde{\sigma}^-\right\rangle = \frac{1}{N}\sum_i\left\langle\tilde{\sigma}_i^-\right\rangle = \sin(\theta)e^{\left(i\Delta-\frac{\Gamma}{2}\right)T}\left[1 + \frac{i}{N\hbar}\sum_{i\neq j}\tilde{V}_{ij}\int_0^T\left\langle\tilde{\sigma}_0^Z(t)\right\rangle\mathrm{d}t\right] \tag{11.17}$$

where $\left\langle\tilde{\sigma}_0^Z\right\rangle$ is the population inversion in the case where the atoms are not interacting, and is given by Equation 11.12. This can also be approximately rewritten as:

$$\left\langle\tilde{\sigma}^-\right\rangle = \sin(\theta)\exp\left[\left(i(\Delta-\Delta_R) - \frac{\Gamma_R}{2}\right)T\right] \tag{11.18}$$

with

$$\Delta_R = \Delta_C \times S_\theta(T) \quad \text{and} \quad \Gamma_R = \Gamma - 2\gamma_C \times S_\theta(T) \tag{11.19}$$

where Δ_C and γ_C are the classical collective terms introduced in the previous chapter

and

$$S_\theta(T) = -\frac{1}{T}\int_0^T \left\langle \tilde{\sigma}_0^Z(t) \right\rangle \mathrm{d}t = 1 + \frac{\cos(\theta)-1}{\Gamma T}(1-e^{-\Gamma T}) \tag{11.20}$$

It is worth noting that we only need to take into account interactions for the dipole moment of the atoms $\hat{\sigma}^-$, and we do not have to compute what happens to the population inversion $\hat{\sigma}^Z$. This is because the evolution of $\hat{\sigma}^Z$ does not depend explicitly on the detuning Δ. Because of this, at first order, its evolution only influences the vertical offset of the Ramsey fringes, but not their position or their contrast [CYL04].

Looking at Equation 11.18, we see that taking into account interactions is similar to shifting the frequency of the transition by Δ_R and changing the linewidth by Γ_R. However, Δ_R and Γ_R are not simple constants: They depend on the integrated population inversion during the Ramsey sequence. As such, they depend both on the initial population inversion θ and on the interrogation time T. This is illustrated Figure 11.5 where the predicted value for Δ_R is plotted as a function of T for different initial pulse area θ. These predictions are free of any fitting parameter, and are indeed compatible with the observed shift.

At short times, Equation 11.19 recovers the prediction from Equation 11.15. In particular, to understand why the shift cancels for $\theta = \pi/2$, we can notice that the field radiated by the atoms j apply a torque to the Bloch vector of the atom i with an axis in the XY plane. If the Bloch vector of the atom i is also in the equatorial plane, this torque cannot cause the Bloch vector to precess around the Z direction, and the Ramsey sequence is not affected by the interactions. For optical clock applications, it means that as long as the initial pulse is around $\pi/2$, the frequency measured is insensitive to interactions. However, as the atoms decay from the equator of the Bloch sphere, the field radiated by their neighbors can now cause them to precess along Z, resulting in a shift that builds up over time.

To understand why the shift at full inversion is the opposite of the classical limit at short time, one can notice the hamiltonian part flips sign under excitation-hole exchange. This symmetry is however broken by the dissipative part when T becomes comparable to Γ.

Besides the shift of the frequency, there is also a modification of the decay rate of the Ramsey fringes Γ_R. In the case presented here of small V_{ij}/Γ, the contrast decay of the Ramsey fringes is only modified by a small amount: $\Gamma_R \approx \Gamma$, and the damping of the fringe contrast is still dominated by spontaneous emission of single atoms. However, in the case of strong interactions, the decay rate of the Ramsey

fringes can be significantly modified. For example, it might be possible to engineer states for which this decay is much longer than isolated atoms. This would make it possible to interrogate the atoms for much longer time, with potential gain for metrology measurements [ORG13; Ost+14].

Summary

In this chapter, I presented the effect that collective dissipation can have on Ramsey frequency measurement in the limit of weak interactions. A collective frequency shift can be observed as the field radiated by an atom can drive another during the interrogation of the system. This shift is related to the classical frequency shift presented in the previous chapter, but also depends on the instantaneous population inversion of the atoms. Since the excitation decays over time, it results in a time-dependent shift that converges to the classical limit for long times.

The experiment presented here is done for large spacing, and therefore is well described by a mean field theory. If we are able to reach the subwavelength regime in the future, this kind of measurement could be useful to get insights into how interactions affect the measured frequency and the decay of Ramsey fringes [Hen+19; Cid+21].

Chapter 12

Conclusion and outlook

To conclude this manuscript, I summarize below the work that I have performed during my PhD. I finish by mentioning the next improvements that will be done on the setup and some experiments that could be explored in the future.

Building a tweezer experiment

The first part of my PhD was dedicated to the design and construction of a new optical tweezer experiment using dysprosium atoms. As detailed in Chapter 3, the setup was built from scratch, and we first had to decide on the laser cooling scheme to use. The very first task I did was to perform simulations of the possibility to load a 3D MOT in a glass cell using for the first time a 2D MOT for dysprosium. It turned out to be a viable solution for the requirement of a tweezer experiment, and we designed and built the vacuum system around this idea.

Once we were able to produce clouds of cold atoms in a magneto-optical trap, we built the optical tweezers components as explained in Chapter 4. For this, we use a commercial microscope objective with a 0.5 numerical aperture in combination with an acousto-optical deflector to create the tweezers. This technology has been demonstrated in several experiments, and we adapted it to our needs. We now use the AOD to create arrays of up to 75 tweezers in 1D, and we can move the traps at will to rearrange the atoms or to dynamically change the spacing.

Trapping and imaging single dysprosium atoms

A major milestone of the experiment was the first demonstration of trapping and imaging of single dysprosium atoms in tweezers. This opened the door to optical tweezers experiments using lanthanide species, with potential applications beyond light scattering experiments, for example by exciting lanthanide atoms to Rydberg states [Tra+21; Grü+24].

One critical point we had to characterize, as explained in Chapter 5, is the influence of the anisotropic polarizability of Dy on the differential light-shift when imaging on the narrow intercombination line at 626 nm. In particular, we found that cooling during imaging only works when the transition is magic, and the ground and excited states experience the same trapping potential. We demonstrated that for Dy, this situation can be reached by tuning the polarization of the tweezer light. In this case, it is possible to image non-destructively single atoms with good fidelity.

In Chapter 7, I perform a detailed analysis of the performance of the imaging scheme, and show that we reach fidelity of about 99 %. The fidelity is limited by losses during the imaging. We identified that these losses are due to two-photon absorption processes where an atom in the excited state of the 626 nm transition absorbs a trap photon at 532 nm and is sent to dark metastable states. Because of this, we lose about 2.5 % of the atoms when taking a picture. Potential ways to mitigate this effect could be to use a repumper to bring back atoms from dark states [Cov+19], or to use a different trapping wavelength, for example in the infrared [Cha+18; Rav+18]. On the shorter term, the setup is being upgraded to use a larger 0.7 numerical aperture objective. With the increased collection efficiency, we expect to be able to image the atoms with fewer losses and better fidelity.

In Chapter 6, we also perform an experimental study of light-assisted collisions on the intercombination line. Magic tweezers give us very good control to study this effect, and we measured the two-body loss rate in systems of a few atoms. I also performed Monte-Carlo simulations to compare the extracted two-body loss rates to simple models such as the Gallagher-Pritchard model and the Landau-Zener model. The data is in relatively good agreement with these calculations, but we observe some deviation at large detuning. It could be interesting to explore this effect in more detail in the future, for example by performing an extensive study over a wider range of experimental parameters.

First light scattering experiments

I also present in the manuscript the first collective light scattering experiments we performed. To do so, I explain in Chapter 8 how we prepare chains of 30 atoms with spacing between 2 to 5 times the wavelength of the 626 nm transition.

To diagnose the state of the atoms, I present in Chapter 9 a state readout protocol

on an optical transition. This scheme uses shelving on the 626 nm transition while depumping the atoms to other Zeeman states with the fast 421 nm transition. With it, we are able to measure the internal state on the 626 nm transition for individual atoms in a single shot. This scheme gives us direct access to the atomic state during light-scattering experiments, and it can give complementary insights compared to experiments that measure the light emitted by the atoms. The fidelity of the scheme is about 90 %, and is limited by the ratio between the linewidth of the science transition and the readout transition. It could be improved significantly when using the narrower 741 nm transition instead of the 626 nm one. In addition, this scheme is non-destructive, and it could be used to increase the repetition rate of the experiment.

Using this technique, in Chapter 10 we measured the frequency excitation spectrum of the atoms in steady-state. When the atoms are close and the laser driving them is parallel to the chain, we observe a shift of the resonance towards lower frequency. This modification of the frequency, also called collective Lamb-shift, can be understood as a classical effect caused by the coherent buildup of the field radiated by the atoms along the chain. In particular, we observe that, in steady-state, this effect only exists in the classical limit of low atomic excitation, and vanishes at large driving field due to the saturation of the atomic dipole.

When the spacing between the atoms is a multiple of the half-wavelength of the light, one also expects a Fabry-Perot like effect with the field being reflected back and forth the chain. However, this effect is very sensitive to thermal positional disorder, and we did not observe it in the experiments presented here. It could be interesting to explore this situation after reaching lower temperatures in the tweezers [Bia+25].

In Chapter 11, we compare the spectroscopic shift observed to the shift obtained in Ramsey spectroscopy, which is relevant to optical clocks. This is a situation of large atomic population, outside of the classical regime. Still, we measure a collective frequency shift, related to the collective Lamb shift observed in the classical limit. The effect observed however is also proportional to the population inversion of the atoms. Since the excited state population decays over time, we observe a frequency shift that additionally depends on the interrogation time of the Ramsey sequence.

All the results presented here are obtained with a spacing between the atoms larger than the wavelength of the light being scattered. Because of this, the interactions are weak compared to the single atom lifetime. As a result, all the experiments are well described by a mean-field theory, and there is no strong entanglement between the

atoms. Still, these experiments act as a benchmark of the setup, and demonstrate the capabilities of the tweezer platform to perform light-scattering experiments in ordered ensembles with a high degree of control.

The next upgrade of the setup is to reach the subwavelength regime, where collective effects become important, and we can expect beyond mean-field effect to become important. To do so, an optical accordion lattice with tunable spacing is being implemented on the setup, similarly to the technique demonstrated in [Su+23]. We plan to load the lattice with perfect filling using the optical tweezers, and then to dynamically reduce the lattice spacing below the wavelength of the light. The diagnostic tools developed here, in particular the state readout protocol, can then be used to explore the interesting physics in this regime. For example, one could explore the rich variety of phases presented in Section 10.4.

Another kind of experiment, closer to the study of light-induced collisions presented here, could be to prepare small Dicke ensembles with several atoms trapped in the same tweezer inside a volume smaller than a wavelength. To build such systems, a possible approach could be to merge two tweezers after having cooled the atoms in the motional ground state [Rut+23].

All-in-all the microscopic control provided by the optical tweezers platform and the techniques associated seem promising to learn more about light-induced effects in ensembles of many atoms. Even though reaching the subwavelength regime might prove challenging, many perspectives can be explored once this is achieved. In addition, combining the optical tweezer platform with the rich structure of lanthanide atoms, and their large spin and magnetic moment, could also lead to other interesting applications in the fields of quantum optics and quantum simulation [Du+24].

Appendices

Chapter A

Magnetic fields

A.1 2D MOT magnets

To create the magnetic field gradient for the 2D MOT, we use stacks of permanent magnets mounted around the chamber. The magnets are held in place by a 3D-printed holder that lets us change the number of magnets in the stack. They have dimension $25\,\mathrm{mm} \times 10\,\mathrm{mm} \times 3\,\mathrm{mm}$, and their magnetization is $8.0(1) \times 10^5\,\mathrm{A\,m^{-1}}$. The stacks of magnets are located at the corners of the square $(\pm\Delta_x, 0, \pm\Delta_z)$ with $\Delta_x = 70\,\mathrm{mm}$ and $\Delta_z = 75\,\mathrm{mm}$.

To estimate the field produced by the magnets at the position of the 2D MOT, we approximate them as point dipoles with a magnetic moment equal to the product of the volume of the magnets and their magnetization. To check that the field produced is indeed the one we expect, we measured it using a Hall probe, as shown in Figure A.1.

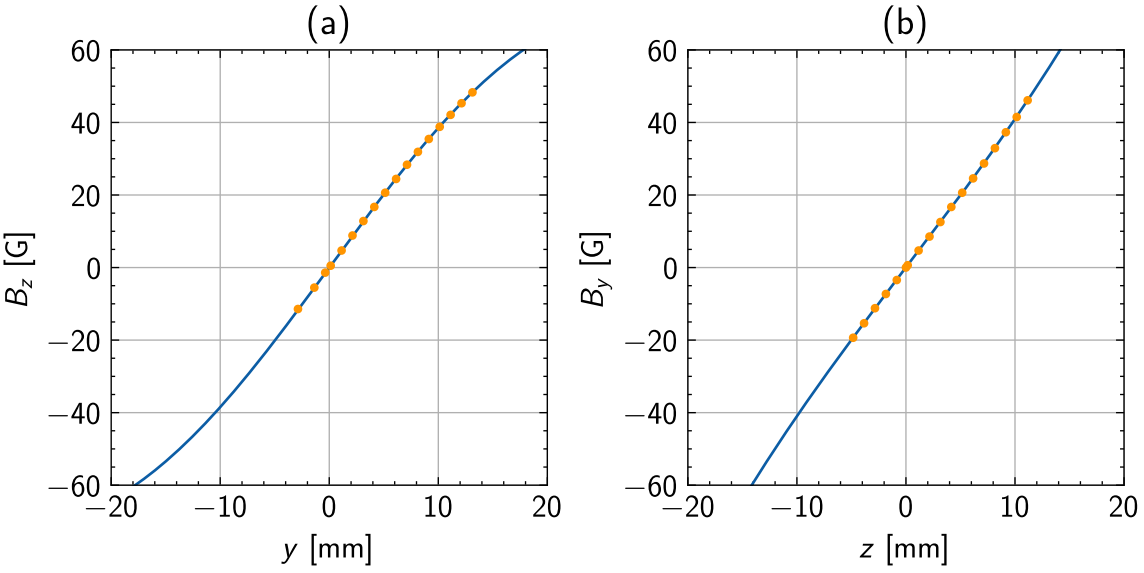

Figure A.1. – (a, b) Magnetic field for the 2D MOT produced by permanent magnets along the two principal axes. Orange points are measured field values using a Hall probe. Blue curves are the theoretical fields calculated using the model of point dipoles.

The data plotted on Figure A.1 was obtained with stacks of 9 magnets resulting in a field gradient of $40\,\mathrm{G\,cm^{-1}}$. Instead, we now use only 5 magnets per stack, and a field gradient of $22\,\mathrm{G\,cm^{-1}}$.

A.2 MOT coils

A pair of coils in the anti-Helmholtz configuration is used to generate the magnetic field gradient for the MOT. They are made of 60 turns of wire. They generate a theoretical magnetic field gradient of $1.7\,\mathrm{G\,cm^{-1}\,A^{-1}}$. Their dimensions are plotted on Figure A.2.

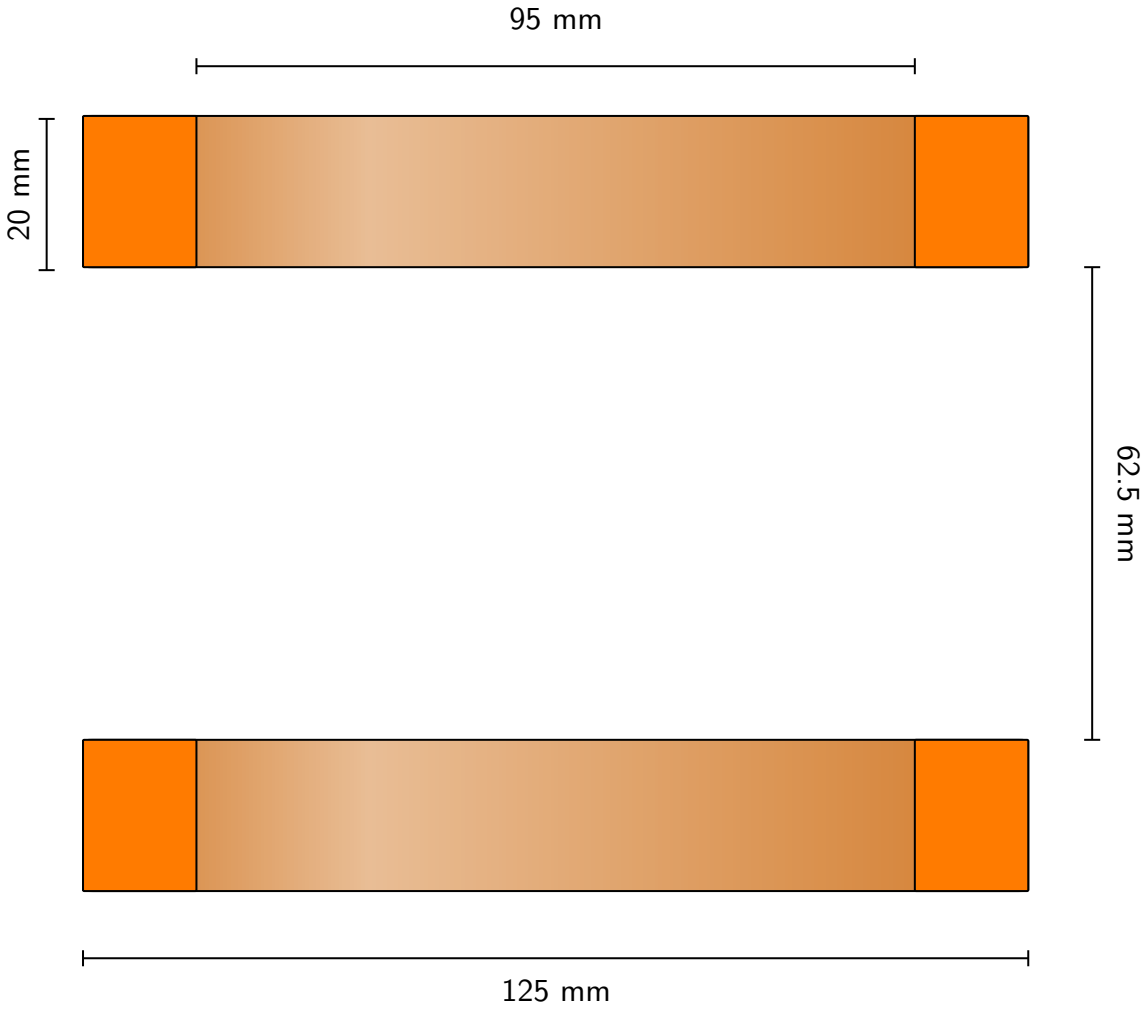

Figure A.2. – Dimensions of the coils used to produce the magnetic field for the 3D MOT.

Direction	X	Y	Z
Number of turns	15	24	10
Dimensions [mm]	120x120	80x120	80x120
Spacing [mm]	108	134	134
Field strength [$\mathrm{G\,A^{-1}}$]	1.55	1.5(1)	1.194(1)

Table A.1. – Properties of the coils used to produced uniform magnetic field on the setup.

A.3 Offset coils

In addition to the gradient coils, we also use a pair of coils in Helmholtz configuration in each direction to apply homogenous magnetic fields on the atoms. These are rectangular coils placed around the glass cell. Their properties are summarized in Table A.1.

Chapter B

Paraxial optics

For an optical system described by an $ABCD$ matrix between two planes, the electric field in the image plane $\boldsymbol{r}$ can be linked to the electric field in the object plane $\boldsymbol{s}$ by:

$$E(\boldsymbol{r}) = \frac{e^{idr^2/2b}}{2i\pi b} \int e^{-i\boldsymbol{r}\cdot\boldsymbol{s}/b} e^{ias^2/2b} E(\boldsymbol{s}) \mathrm{d}^2 s \tag{B.1}$$

where the coefficients are defined from the $ABCD$ matrix as:

$$M = \begin{pmatrix} a & bk \\ c/k & d \end{pmatrix} \tag{B.2}$$

For an input beam with radial symmetry, the electric field in the image plane can be written as:

$$E(r) = \frac{e^{idr^2/2b}}{ib} \int_0^{+\infty} J_0\left(\frac{rs}{b}\right) e^{ias^2/2b} E(s) s \mathrm{d}s \tag{B.3}$$

In particular, this can be used to describe the field at the focus of a lens with focal length f and input radius R, for which $M = \begin{pmatrix} -z/f & f+z \\ -1/f & 1 \end{pmatrix}$. The peak intensity of the beam is given by:

$$I_0 = 2c\epsilon_0 |E(r=0, z=0)|^2 = \frac{2c\epsilon_0}{b^2} \left| \int_0^R E(s) s \mathrm{d}s \right|^2 \tag{B.4}$$

For an input collimated gaussian beam with waist w and power P, this gives:

$$I_0 = \frac{k^2 P}{2\pi} \frac{R^2}{f^2} x^2 \left(1 - e^{-1/x^2}\right)^2 \tag{B.5}$$

where we introduced $x = w/R$.

We can do the same for the radial intensity curvature at the focus:

$$\frac{\partial^2 I}{\partial r^2} = \frac{k^4 P}{2\pi} \frac{R^4}{f^4} x^2 \left(1 - e^{1/x^2}\right) \left(x^2 e^{1/x^2} - x^2 - 1\right) e^{-2/x^2} \tag{B.6}$$

and the axial intensity curvature:

$$\frac{\partial^2 I}{\partial z^2} = -4\pi^3 \frac{P}{\lambda^4} \left(\frac{R}{f}\right)^6 x^2 \left(x^4 - 2x^4 e^{-1/x^2} + x^4 e^{-2/x^2} - e^{-1/x^2}\right) \tag{B.7}$$

Chapter C

Signal generation for tweezers

This appendix contains some technical details about the signal sent to the acousto-optic deflector used to generate arrays of traps.

C.1 Static traps

To generate arrays of traps, we feed the AOD with a signal that is the sum of several sinusoidal signals:

$$V(t) = V_0 \sum_{i=1}^{N} a_i \sin(2\pi\nu_i t + \varphi_i) \tag{C.1}$$

Here V_0 is a global scaling amplitude that is constant for the whole duration of the experiment, a_i is the relative amplitude of the trap i, ν_i is its frequency and φ_i is its phase.

C.1.1 Signal generation

This signal is generated by an arbitrary waveform generator (AWG). It is computed for each timestep $t_i = i/\nu_S$, where the sampling frequency is $\nu_S = 625\,\mathrm{MHz}$. With a typical number of traps $N = 75$, we would then need to compute about $50\,\mathrm{GSa\,s^{-1}}$ if we were to compute $V(t)$ on the fly. This is challenging to do in real-time with regular computers. To avoid this issue, we simply precompute the signal over a short duration $T_b = N_b/\nu_S \approx 1\,\mathrm{ms}$ and then loop over this block to generate the full signal. When doing so, it is however critical that $V(t)$ is truly periodic over a block. If this is not the case, the tweezer's intensity would glitch at every repetition of the block, which heats up the atoms and eventually leads to their loss. To ensure this, we enforce the frequency of each trap to be a multiple of the block frequency $\nu_i = m_i/T_b$ where m_i is an integer. With this, we only need to precompute a small number of samples, and we can then produce the signal for an arbitrarily long duration. A potential drawback is that it limits the frequency resolution of the traps to $\Delta\nu = 1/T_b$, which translates

to a spatial resolution $\Delta x = 2.5\,\mathrm{nm}$. This is small enough to not be an issue for our purposes.

C.1.2 Choice of phases

The choice of the relative phases φ_i might not seem important at first, since it should have no influence on the intensity or position of the tone $a_i \sin(2\pi\nu_i t + \varphi_i)$. However, the choice of phases influences strongly the amplitude of the total signal $V(t)$. For example, if we pick all phases to be equal, the resulting signal presents large bursts of amplitude. This is an issue if some components in the RF setup present some non-linearity that distorts large signals. To avoid this issue, we use a different choice of phases to minimize the envelope of the signal [Sch70]. The phases are defined by the recursive relation:

$$\varphi_i = 2\pi \sum_{j<i} (m_i - m_j)\rho_j \tag{C.2}$$

where $\rho_i = a_i^2 / \sum_j a_j^2$ is the relative power of each tone.

C.1.3 Equalization

When using equal amplitude a_i for each trap in a chain, the intensities of the tweezers are typically not perfectly equal but fluctuate by some tens of percent from trap to trap. This is due to the finite bandwidth of the AOD and non-linearity in the system. To equalize the intensity of the tweezers, we apply an iterative correction algorithm. We start by measuring the relative intensity of the traps r_i. These intensities can be measured in different ways, for example, by sampling the tweezers on a camera or by using an atomic signal, such as the differential light-shift of a transition in non-magic traps.

We then compute new amplitudes for the different tones to compensate for inhomogeneities:

$$a_i' = a_i / r_i^\beta \tag{C.3}$$

Here β is a parameter between 0.1 and 0.5 that controls the speed of the equalization process. The total RF power after this correction step is typically different from the

initial value, so we renormalize the amplitudes obtained:

$$a_i'' = a_i' \sqrt{\frac{\sum_i a_i^2}{\sum_i a_i'^2}} \tag{C.4}$$

We then repeat these steps, each time by measuring the intensity of the tweezers and computing corrected amplitudes. After repeating this procedure to convergence, we reduce fluctuations of intensity between different tweezers to about 2 %.

C.2 Moving tweezers

To move the tweezers, we change the frequency of the signal over time. A signal with a time-varying amplitude $a(t)$ and frequency $\nu(t)$ is defined as:

$$s(t) = a(t)\sin(\phi(t)) \tag{C.5}$$

with

$$\frac{\mathrm{d}\phi(t)}{\mathrm{d}t} = \nu(t) \tag{C.6}$$

We want to interpolate the frequency $\nu(t)$ between two times t_1 and t_2, such that $\nu(t_1) = \nu_1$ and $\nu(t_2) = \nu_2$. One way to do so is to choose:

$$\nu(t) = \frac{\nu_f + \nu_i}{2} + \frac{\nu_f - \nu_i}{2} F\left(\frac{t - t_i}{t_f - t_i}\right) \tag{C.7}$$

where $F(x)$ is an interpolation function such that $F(0) = -1$ and $F(1) = 1$. We indeed have $\nu(t_i) = \nu_i$ and $\nu(t_f) = \nu_f$. The issue is that we cannot ensure phase continuity at the two boundaries. We can only choose one integration constant for ϕ, and therefore, we can only ensure phase continuity at one of the boundaries.

To circumvent this issue, we can substitute F by a new interpolation function F_ϵ with an extra tuning parameter ϵ:

$$F_\epsilon(x) = \begin{cases} F\left(\frac{x}{1-\epsilon}\right) & \text{if } x < 1 - \epsilon \\ 1 & \text{if } x \geq 1 - \epsilon \end{cases} \tag{C.8}$$

This function is also a valid interpolation function, and we can choose ϵ to have phase

continuity at both boundaries. The phase is then given by:

$$\phi(t) = \phi_i + \int_{t_i}^{t} \nu(t')\,\mathrm{d}t' \tag{C.9}$$

We use the extra degree of freedom ϵ to have arbitrary control over the phase accumulated during the move:

$$\frac{\phi(t_f) - \phi(t_i)}{2\pi} = \frac{\nu_f + \nu_i}{2}(t - t_i) + \frac{\nu_f - \nu_i}{2}(t_f - t_i)\left[(1-\epsilon)\int_0^1 F(x)\,\mathrm{d}x + \epsilon\right] \tag{C.10}$$

If we do not have this additional degree of freedom, the phase of the signal will jump discontinuously at the end of a move, which might lead to loss of atoms.

Chapter D

Second order cumulants

In this appendix, I provide the set of equations used to perform the second order beyond mean-field cumulants presented in Section 10.4. The first two equations are used to derive the evolution of the expectation value of the single body operators:

$$\begin{aligned}\frac{\mathrm{d}\left\langle\hat{\pi}_i^e\right\rangle}{\mathrm{d}t} &= i\frac{\Omega_i^*}{2}\left\langle\hat{\sigma}_i^-\right\rangle - i\frac{\Omega_i}{2}\left\langle\hat{\sigma}_i^+\right\rangle - \Gamma\left\langle\hat{\pi}_i^e\right\rangle \\ &\quad + \frac{i}{\hbar}\sum_{k\neq i}\left[V_{ik}^*\left\langle\hat{\sigma}_k^+\hat{\sigma}_i^-\right\rangle - V_{ik}\left\langle\hat{\sigma}_k^-\hat{\sigma}_i^+\right\rangle\right]\end{aligned} \tag{D.1}$$

$$\frac{\mathrm{d}\left\langle\hat{\sigma}_i^-\right\rangle}{\mathrm{d}t} = \left(i\Delta - \frac{\Gamma}{2}\right)\left\langle\hat{\sigma}_i^-\right\rangle + i\frac{\Omega_i}{2}\left\langle\hat{\sigma}_i^Z\right\rangle + \frac{i}{\hbar}\sum_{k\neq i}V_{ik}\left\langle\hat{\sigma}_k^-\hat{\sigma}_i^Z\right\rangle \tag{D.2}$$

These equations depend on the expectation value of products of operators. To complete them, we compute the evolution of these products. For $i \neq j$, we have:

$$\begin{aligned}\frac{\mathrm{d}\left\langle\hat{\sigma}_i^+\hat{\sigma}_j^-\right\rangle}{\mathrm{d}t} &= i\frac{\Omega_j}{2}\left\langle\hat{\sigma}_i^+\hat{\sigma}_j^Z\right\rangle - i\frac{\Omega_i^*}{2}\left\langle\hat{\sigma}_i^Z\hat{\sigma}_j^-\right\rangle - \Gamma\left\langle\hat{\sigma}_i^+\hat{\sigma}_j^-\right\rangle \\ &\quad + 2\Gamma_{ji}\left\langle\hat{\pi}_i^e\hat{\pi}_j^e\right\rangle + \frac{i}{\hbar}V_{ji}^*\left\langle\hat{\pi}_j^e\right\rangle - \frac{i}{\hbar}V_{ji}\left\langle\hat{\pi}_i^e\right\rangle \\ &\quad + \frac{i}{\hbar}\sum_{k\neq i,j}\left[V_{jk}\left\langle\hat{\sigma}_i^+\hat{\sigma}_k^-\hat{\sigma}_j^Z\right\rangle - V_{ik}^*\left\langle\hat{\sigma}_k^+\hat{\sigma}_i^Z\hat{\sigma}_j^-\right\rangle\right]\end{aligned} \tag{D.3}$$

$$\begin{aligned}\frac{\mathrm{d}\left\langle\hat{\pi}_i^e\hat{\pi}_j^e\right\rangle}{\mathrm{d}t} &= i\frac{\Omega_i^*}{2}\left\langle\hat{\pi}_j^e\hat{\sigma}_i^-\right\rangle + i\frac{\Omega_j^*}{2}\left\langle\hat{\pi}_i^e\hat{\sigma}_j^-\right\rangle - i\frac{\Omega_i}{2}\left\langle\hat{\pi}_j^e\hat{\sigma}_i^+\right\rangle - i\frac{\Omega_j}{2}\left\langle\hat{\pi}_i^e\hat{\sigma}_j^+\right\rangle - 2\Gamma\left\langle\hat{\pi}_i^e\hat{\pi}_j^e\right\rangle \\ &\quad + \frac{i}{\hbar}\sum_{k\neq i,j}\left[V_{ki}^*\left\langle\hat{\pi}_j^e\hat{\sigma}_k^+\hat{\sigma}_i^-\right\rangle + V_{kj}^*\left\langle\hat{\pi}_i^e\hat{\sigma}_k^+\hat{\sigma}_j^-\right\rangle - V_{ik}\left\langle\hat{\pi}_j^e\hat{\sigma}_i^+\hat{\sigma}_k^-\right\rangle - V_{jk}\left\langle\hat{\pi}_i^e\hat{\sigma}_j^+\hat{\sigma}_k^-\right\rangle\right]\end{aligned} \tag{D.4}$$

$$\frac{\mathrm{d}\left\langle \hat{\pi}_i^e \hat{\sigma}_j^- \right\rangle}{\mathrm{d}t} = i\frac{\Omega_i^*}{2}\left\langle \hat{\sigma}_i^- \hat{\sigma}_j^- \right\rangle - i\frac{\Omega_i}{2}\left\langle \hat{\sigma}_i^+ \hat{\sigma}_j^- \right\rangle + i\frac{\Omega_j}{2}\left\langle \hat{\pi}_i^e \hat{\sigma}_j^Z \right\rangle + \left(i\Delta - \frac{3}{2}\Gamma\right)\left\langle \hat{\pi}_i^e \hat{\sigma}_j^- \right\rangle + \frac{i}{\hbar}V_{ij}^*\left\langle \hat{\pi}_j^e \hat{\sigma}_i^- \right\rangle + \frac{i}{\hbar}\sum_{k\neq i,j}\left[V_{ik}^*\left\langle \hat{\sigma}_k^+ \hat{\sigma}_i^- \hat{\sigma}_j^- \right\rangle - V_{ik}\left\langle \hat{\sigma}_k^- \hat{\sigma}_i^+ \hat{\sigma}_j^- \right\rangle + V_{jk}\left\langle \hat{\pi}_i^e \hat{\sigma}_k^- \hat{\sigma}_j^Z \right\rangle\right] \quad \text{(D.5)}$$

$$\frac{\mathrm{d}\left\langle \hat{\sigma}_i^- \hat{\sigma}_j^- \right\rangle}{\mathrm{d}t} = (2i\Delta - \Gamma)\left\langle \hat{\sigma}_i^- \hat{\sigma}_j^- \right\rangle + i\frac{\Omega_i}{2}\left\langle \hat{\sigma}_i^Z \hat{\sigma}_j^- \right\rangle + i\frac{\Omega_j}{2}\left\langle \hat{\sigma}_i^- \hat{\sigma}_j^Z \right\rangle + \frac{i}{\hbar}\sum_{k\neq i,j} V_{ik}\left\langle \hat{\sigma}_k^- \hat{\sigma}_i^Z \hat{\sigma}_j^- \right\rangle + V_{jk}\left\langle \hat{\sigma}_i^- \hat{\sigma}_k^- \hat{\sigma}_j^Z \right\rangle \quad \text{(D.6)}$$

This total set of equations is still not closed since the products of two operators depend on the expectation of three operators. To get a closed system of equations, we assume that the third order cumulants are zero, and we replace $\langle A_i B_j C_k \rangle$ by $\langle A_i B_j \rangle \langle C_k \rangle + \langle A_i C_k \rangle \langle B_j \rangle + \langle A_i \rangle \langle B_j C_k \rangle - 2 \langle A_i \rangle \langle B_j \rangle \langle C_k \rangle$. We thus obtain a non-linear system of differential equations that can be solved numerically.

Bibliography

[AL85] M. P. V. Albada and A. Lagendijk. "Observation of Weak Localization of Light in a Random Medium". *Physical Review Letters* **55.24** (1985), 2692–2695. DOI: 10.1103/PhysRevLett.55.2692.

[And+21] F. Andreoli et al. "Maximum Refractive Index of an Atomic Medium". *Physical Review X* **11.1** (2021), 011026. DOI: 10.1103/PhysRevX.11.011026.

[Ara+16] M. O. Araújo et al. "Superradiance in a Large and Dilute Cloud of Cold Atoms in the Linear-Optics Regime". *Physical Review Letters* **117.7** (2016), 073002. DOI: 10.1103/PhysRevLett.117.073002.

[Ase+17] A. Asenjo-Garcia et al. "Exponential Improvement in Photon Storage Fidelities Using Subradiance and "Selective Radiance" in Atomic Arrays". *Physical Review X* **7.3** (2017), 031024. DOI: 10.1103/PhysRevX.7.031024.

[Ash70] A. Ashkin. "Acceleration and Trapping of Particles by Radiation Pressure". *Physical Review Letters* **24.4** (1970), 156–159. DOI: 10.1103/PhysRevLett.24.156.

[Bar+16] D. Barredo et al. "An atom-by-atom assembler of defect-free arbitrary two-dimensional atomic arrays". *Science* **354.6315** (2016), 1021–1023. DOI: 10.1126/science.aah3778.

[Bar+20] M. Barbiero et al. "Sideband-Enhanced Cold Atomic Source for Optical Clocks". *Physical Review Applied* **13.1** (2020), 014013. DOI: 10.1103/PhysRevApplied.13.014013.

[Bec+18] J. H. Becher et al. "Anisotropic polarizability of erbium atoms". *Physical Review A* **97.1** (2018), 012509. DOI: 10.1103/PhysRevA.97.012509.

[Ber97] P. R. Berman. "Resonant interaction between identical atoms including recoil". *Physical Review A* **55.6** (1997), 4466–4476. DOI: 10.1103/PhysRevA.55.4466.

[BGA16a] R. J. Bettles, S. A. Gardiner, and C. S. Adams. "Enhanced Optical Cross Section via Collective Coupling of Atomic Dipoles in a 2D Array". *Physical Review Letters* **116.10** (2016), 103602. DOI: 10.1103/PhysRevLett.116.103602.

[BGA16b] Robert J. Bettles, Simon A. Gardiner, and Charles S. Adams. "Cooperative eigenmodes and scattering in one-dimensional atomic arrays". *Physical Review A* **94.4** (2016), 043844. DOI: 10.1103/PhysRevA.94.043844.

[Bia+25] G. Biagioni et al. "Narrowline cooling of dysprosium atoms in optical tweezers arrays". *To be published* (2025).

[BL20] A. Browaeys and T. Lahaye. "Many-body physics with individually controlled Rydberg atoms". *Nature Physics* **16.2** (2020), 132–142. DOI: 10.1038/s41567-019-0733-z.

[Blo+23] D. Bloch et al. "Trapping and Imaging Single Dysprosium Atoms in Optical Tweezer Arrays". *Physical Review Letters* **131.20** (2023), 203401. DOI: 10.1103/PhysRevLett.131.203401.

[Blo+24] D. Bloch et al. "Anisotropic polarizability of Dy at 532 nm on the intercombination transition". *Physical Review A* **110.3** (2024), 033103. DOI: 10.1103/PhysRevA.110.033103.

[Bor+23] G. Bornet et al. "Scalable spin squeezing in a dipolar Rydberg atom array". *Nature* **621.7980** (2023), 728–733. DOI: 10.1038/s41586-023-06414-9.

[Bro+19] M. O. Brown et al. "Gray-Molasses Optical-Tweezer Loading: Controlling Collisions for Scaling Atom-Array Assembly". *Physical Review X* **9.1** (2019), 011057. DOI: 10.1103/PhysRevX.9.011057.

[BW99] M. Born and E. Wolf. *Principles of Optics: Electromagnetic Theory of Propagation, Interference and Diffraction of Light*. 7th ed. Cambridge, Cambridge University Press. DOI: 10.1017/CBO9781139644181.

[CD72] C. Cohen-Tannoudji and J. Dupont-Roc. "Experimental Study of Zeeman Light Shifts in Weak Magnetic Fields". *Physical Review A* **5.2** (1972), 968–984. DOI: 10.1103/PhysRevA.5.968.

[Cha+11] M. Chalony et al. "Coherent flash of light emitted by a cold atomic cloud". *Physical Review A* **84.1** (2011), 011401. DOI: 10.1103/PhysRevA.84.011401.

[Cha+18] T. Chalopin et al. “Anisotropic light shift and magic polarization of the intercombination line of dysprosium atoms in a far-detuned dipole trap”. *Physical Review A* **98.4** (2018), 040502. DOI: 10.1103/PhysRevA.98.040502.

[Cha+20] T. Chalopin et al. “Probing chiral edge dynamics and bulk topology of a synthetic Hall system”. *Nature Physics* **16.10** (2020), 1017–1021. DOI: 10.1038/s41567-020-0942-5.

[Che+23] C. Chen et al. “Continuous symmetry breaking in a two-dimensional Rydberg array”. *Nature* **616.7958** (2023), 691–695. DOI: 10.1038/s41586-023-05859-2.

[Cho+22] L. Chomaz et al. “Dipolar physics: a review of experiments with magnetic quantum gases”. *Reports on Progress in Physics* **86.2** (2022), 026401. DOI: 10.1088/1361-6633/aca814.

[Chr+19] A. Christianen et al. “Photoinduced Two-Body Loss of Ultracold Molecules”. *Physical Review Letters* **123.12** (2019), 123402. DOI: 10.1103/PhysRevLett.123.123402.

[Cid+21] A. Cidrim et al. “Dipole-Dipole Frequency Shifts in Multilevel Atoms”. *Physical Review Letters* **127.1** (2021), 013401. DOI: 10.1103/PhysRevLett.127.013401.

[Coo18] A. Cooper. “Alkaline-Earth Atoms in Optical Tweezers”. *Physical Review X* **8.4** (2018). DOI: 10.1103/PhysRevX.8.041055.

[Cot+19] F. Cottier et al. “Microscopic and Macroscopic Signatures of 3D Anderson Localization of Light”. *Physical Review Letters* **123.8** (2019), 083401. DOI: 10.1103/PhysRevLett.123.083401.

[Cov+19] J. P. Covey et al. “2000-Times Repeated Imaging of Strontium Atoms in Clock-Magic Tweezer Arrays”. *Physical Review Letters* **122.17** (2019), 173201. DOI: 10.1103/PhysRevLett.122.173201.

[CYL04] D. E. Chang, Jun Ye, and M. D. Lukin. “Controlling dipole-dipole frequency shifts in a lattice-based optical atomic clock”. *Physical Review A* **69.2** (2004), 023810. DOI: 10.1103/PhysRevA.69.023810.

[CZ95] J. I. Cirac and P. Zoller. “Quantum Computations with Cold Trapped Ions”. *Physical Review Letters* **74.20** (1995), 4091–4094. DOI: 10.1103/PhysRevLett.74.4091.

[DC89] J. Dalibard and C. Cohen-Tannoudji. “Laser cooling below the Doppler limit by polarization gradients: simple theoretical models”. *JOSA B* **6.11** (1989), 2023–2045. DOI: 10.1364/JOSAB.6.002023.

[Dic54] R. H. Dicke. “Coherence in Spontaneous Radiation Processes”. *Physical Review* **93.1** (1954), 99–110. DOI: 10.1103/PhysRev.93.99.

[DLR77] A. P. Dempster, N. M. Laird, and D. B. Rubin. “Maximum Likelihood from Incomplete Data Via the EM Algorithm”. *Journal of the Royal Statistical Society: Series B (Methodological)* **39.1** (1977), 1–22. DOI: 10.1111/j.2517-6161.1977.tb01600.x.

[Dre+17] D. Dreon et al. “Optical cooling and trapping of highly magnetic atoms: the benefits of a spontaneous spin polarization”. *Journal of Physics B: Atomic, Molecular and Optical Physics* **50.6** (2017), 065005. DOI: 10.1088/1361-6455/aa5db5.

[Dre17] Davide Dreon. “Designing and building an ultracold Dysprosium experiment : a new framework for light-spin interaction”. PhD Thesis. Paris Sciences et Lettres (ComUE), 2017.

[Du+24] L. Du et al. “Atomic physics on a 50-nm scale: Realization of a bilayer system of dipolar atoms”. *Science* **384.6695** (2024), 546–551. DOI: 10.1126/science.adh3023.

[Eck+22] S. Eckel et al. “PyLCP: A Python package for computing laser cooling physics”. *Computer Physics Communications* **270** (2022), 108166. DOI: 10.1016/j.cpc.2021.108166.

[End+16] M. Endres et al. “Atom-by-atom assembly of defect-free one-dimensional cold atom arrays”. *Science* **354.6315** (2016), 1024–1027. DOI: 10.1126/science.aah3752.

[Esc+21] R. G. Escudero et al. “Steady-state magneto-optical trap of fermionic strontium on a narrow-line transition”. *Physical Review Research* **3.3** (2021), 033159. DOI: 10.1103/PhysRevResearch.3.033159.

[Esp+20] T. S. do Espirito Santo et al. “Collective excitation dynamics of a cold atom cloud”. *Physical Review A* **101.1** (2020), 013617. DOI: 10.1103/PhysRevA.101.013617.

[Fab+22] A. Fabre et al. “Simulating two-dimensional dynamics within a large-size atomic spin”. *Physical Review A* **105.1** (2022), 013301. DOI: 10.1103/PhysRevA.105.013301.

[Fai24] F. Faisant. “Building a strontium quantum gas microscope”. PhD Thesis. 2024.

[Fer+21] G. Ferioli et al. “Laser-Driven Superradiant Ensembles of Two-Level Atoms near Dicke Regime”. *Physical Review Letters* **127.24** (2021), 243602. DOI: 10.1103/PhysRevLett.127.243602.

[Fer+24] G. Ferioli et al. “Non-Gaussian Correlations in the Steady State of Driven-Dissipative Clouds of Two-Level Atoms”. *Physical Review Letters* **132.13** (2024), 133601. DOI: 10.1103/PhysRevLett.132.133601.

[FJR16] G. Facchinetti, S. D. Jenkins, and J. Ruostekoski. “Storing Light with Subradiant Correlations in Arrays of Atoms”. *Physical Review Letters* **117.24** (2016), 243601. DOI: 10.1103/PhysRevLett.117.243601.

[Foo05] C. J. Foot. *Atomic physics*. Oxford University Press, USA.

[FSA16] Y. H. Fung, P. Sompet, and M. F. Andersen. “Single Atoms Preparation Using Light-Assisted Collisions”. *Technologies* **4.1** (2016), 4. DOI: 10.3390/technologies4010004.

[FT02] Z. Ficek and R. Tanaś. “Entangled states and collective nonclassical effects in two-atom systems”. *Physics Reports* **372.5** (2002), 369–443. DOI: 10.1016/S0370-1573(02)00368-X.

[Fuh+12] A. Fuhrmanek et al. “Light-assisted collisions between a few cold atoms in a microscopic dipole trap”. *Physical Review A* **85.6** (2012), 062708. DOI: 10.1103/PhysRevA.85.062708.

[Fuh11] A. Fuhrmanek. “From single to many atoms in a microscopic optical dipole trap”. Theses. Université Paris Sud - Paris XI, 2011.

[GAK16] W. Guerin, M. O. Araújo, and R. Kaiser. “Subradiance in a Large Cloud of Cold Atoms”. *Physical Review Letters* **116.8** (2016), 083601. DOI: 10.1103/PhysRevLett.116.083601.

[GB21] C. Gross and W. S. Bakr. “Quantum gas microscopy for single atom and spin detection”. *Nature Physics* **17.12** (2021), 1316–1323. DOI: 10.1038/s41567-021-01370-5.

[GH82] M. Gross and S. Haroche. “Superradiance: An essay on the theory of collective spontaneous emission”. *Physics Reports* **93.5** (1982), 301–396. DOI: 10.1016/0370-1573(82)90102-8.

[Gli+20] A. Glicenstein et al. "Collective Shift in Resonant Light Scattering by a One-Dimensional Atomic Chain". *Physical Review Letters* **124.25** (2020), 253602. DOI: 10.1103/PhysRevLett.124.253602.

[GP89] A. Gallagher and D. E. Pritchard. "Exoergic collisions of cold Na-Na". *Physical Review Letters* **63.9** (1989), 957–960. DOI: 10.1103/PhysRevLett.63.957.

[GRK17] W. Guerin, M.T. Rouabah, and R. Kaiser. "Light interacting with atomic ensembles: collective, cooperative and mesoscopic effects". *Journal of Modern Optics* **64.9** (2017), 895–907. DOI: 10.1080/09500340.2016.1215564.

[Grü+10] T. Grünzweig et al. "Near-deterministic preparation of a single atom in an optical microtrap". *Nature Physics* **6.12** (2010), 951–954. DOI: 10.1038/nphys1778.

[Grü+24] D. Grün et al. "Optical Tweezer Arrays of Erbium Atoms". *Physical Review Letters* **133.22** (2024), 223402. DOI: 10.1103/PhysRevLett.133.223402.

[GWO00] R. Grimm, M. Weidemüller, and Y. B. Ovchinnikov. "Optical Dipole Traps for Neutral Atoms". *Advances In Atomic, Molecular, and Optical Physics*. Ed. by Benjamin Bederson and Herbert Walther. Vol. 42. Academic Press, 95–170. DOI: 10.1016/S1049-250X(08)60186-X.

[Hen+19] L. Henriet et al. "Critical open-system dynamics in a one-dimensional optical-lattice clock". *Physical Review A* **99.2** (2019), 023802. DOI: 10.1103/PhysRevA.99.023802.

[Hof+24] B. Hofer et al. *Single-atom resolved collective spectroscopy of a one-dimensional atomic array*. arXiv:2412.02541 [quant-ph]. 2024. DOI: 10.48550/arXiv.2412.02541.

[Hof22] B. Hofer. *M2 internship report*. Tech. rep. 2022.

[Höl23] C. Hölzl. "Motional ground-state cooling of single atoms in state-dependent optical tweezers". *Physical Review Research* **5.3** (2023). DOI: 10.1103/PhysRevResearch.5.033093.

[HTK12] A. A. Houck, H. E. Türeci, and J. Koch. "On-chip quantum simulation with superconducting circuits". *Nature Physics* **8.4** (2012), 292–299. DOI: 10.1038/nphys2251.

[Hui+23] W. Huie et al. “Repetitive Readout and Real-Time Control of Nuclear Spin Qubits in ^{171}Yb Atoms”. *PRX Quantum* **4.3** (2023), 030337. DOI: 10.1103/PRXQuantum.4.030337.

[Hut+24] R. B. Hutson et al. “Observation of millihertz-level cooperative Lamb shifts in an optical atomic clock”. *Science* **383.6681** (2024), 384–387. DOI: 10.1126/science.adh4477.

[IG11] V. V. Ivanov and S. Gupta. “Laser-driven Sisyphus cooling in an optical dipole trap”. *Physical Review A* **84.6** (2011), 063417. DOI: 10.1103/PhysRevA.84.063417.

[Jac99] J. D. Jackson. *Classical electrodynamics*. 3rd ed. New York, NY, Wiley. ISBN: 978-0-471-30932-1.

[Jen+22] A. Jenkins et al. “Ytterbium Nuclear-Spin Qubits in an Optical Tweezer Array”. *Physical Review X* **12.2** (2022), 021027. DOI: 10.1103/PhysRevX.12.021027.

[Jin+23] S. Jin et al. “Two-dimensional magneto-optical trap of dysprosium atoms as a compact source for efficient loading of a narrow-line three-dimensional magneto-optical trap”. *Physical Review A* **108.2** (2023), 023719. DOI: 10.1103/PhysRevA.108.023719.

[Joy94] A. Joye. “Proof of the Landau–Zener formula”. *Asymptotic Analysis* **9.3** (1994), 209–258. DOI: 10.3233/ASY-1994-9302.

[Kea+12] J. Keaveney et al. “Cooperative Lamb Shift in an Atomic Vapor Layer of Nanometer Thickness”. *Physical Review Letters* **108.17** (2012), 173601. DOI: 10.1103/PhysRevLett.108.173601.

[Kja+20] M. Kjaergaard et al. “Superconducting Qubits: Current State of Play”. *Annual Review of Condensed Matter Physics* **11.Volume 11, 2020** (2020), 369–395. DOI: 10.1146/annurev-conmatphys-031119-050605.

[KP11] S. Kotochigova and A. Petrov. “Anisotropy in the interaction of ultracold dysprosium”. *Physical Chemistry Chemical Physics* **13.42** (2011), 19165–19170. DOI: 10.1039/C1CP21175G.

[KR15] S. Krämer and H. Ritsch. “Generalized mean-field approach to simulate the dynamics of large open spin ensembles with long range interactions”. *The European Physical Journal D* **69.12** (2015), 282. DOI: 10.1140/epjd/e2015-60266-5.

[Kre+21] M. Kreyer et al. “Measurement of the dynamic polarizability of Dy atoms near the 626-nm intercombination line”. *Physical Review A* **104.3** (2021), 033106. DOI: 10.1103/PhysRevA.104.033106.

[Kub62] R. Kubo. “Generalized Cumulant Expansion Method”. *Journal of the Physical Society of Japan* **17.7** (1962), 1100–1120. DOI: 10.1143/JPSJ.17.1100.

[Lee+15] J. Lee et al. “Core-shell magneto-optical trap for alkaline-earth-metal-like atoms”. *Physical Review A* **91.5** (2015), 053405. DOI: 10.1103/PhysRevA.91.053405.

[Leh70] R. H. Lehmberg. “Radiation from an N-Atom System. I. General Formalism”. *Physical Review A* **2.3** (1970), 883–888. DOI: 10.1103/PhysRevA.2.883.

[Li+16] H. Li et al. “Optical trapping of ultracold dysprosium atoms: transition probabilities, dynamic dipole polarizabilities and van der Waals C6 coefficients”. *Journal of Physics B: Atomic, Molecular and Optical Physics* **50.1** (2016), 014005. DOI: 10.1088/1361-6455/50/1/014005.

[LSR13] F. Le Kien, P. Schneeweiss, and A. Rauschenbeutel. “Dynamical polarizability of atoms in arbitrary light fields: general theory and application to cesium”. *The European Physical Journal D* **67.5** (2013), 92. DOI: 10.1140/epjd/e2013-30729-x.

[Lu+11] M. Lu et al. “Strongly Dipolar Bose-Einstein Condensate of Dysprosium”. *Physical Review Letters* **107.19** (2011), 190401. DOI: 10.1103/PhysRevLett.107.190401.

[Lud+15] A. D. Ludlow et al. “Optical atomic clocks”. *Reviews of Modern Physics* **87.2** (2015), 637–701. DOI: 10.1103/RevModPhys.87.637.

[LWD14] M. Lepers, J.-F. Wyart, and O. Dulieu. “Anisotropic optical trapping of ultracold erbium atoms”. *Physical Review A* **89.2** (2014), 022505. DOI: 10.1103/PhysRevA.89.022505.

[Mad21] I. S. Madjarov. “Entangling, Controlling, and Detecting Individual Strontium Atoms in Optical Tweezer Arrays”. PhD thesis. California Institute of Technology, 2021. DOI: 10.7907/d1em-dt34.

[Mai+14] T. Maier et al. “Narrow-line magneto-optical trap for dysprosium atoms”. *Optics Letters* **39.11** (2014), 3138–3141. DOI: 10.1364/OL.39.003138.

[Mei+14] Z. Meir et al. “Cooperative Lamb Shift in a Mesoscopic Atomic Array”. *Physical Review Letters* **113.19** (2014), 193002. DOI: 10.1103/PhysRevLett.113.193002.

[Mon+95] C. Monroe et al. “Resolved-Sideband Raman Cooling of a Bound Atom to the 3D Zero-Point Energy”. *Physical Review Letters* **75.22** (1995), 4011–4014. DOI: 10.1103/PhysRevLett.75.4011.

[NF21] M. A. Norcia and F. Ferlaino. “Developments in atomic control using ultracold magnetic lanthanides”. *Nature Physics* **17.12** (2021), 1349–1357. DOI: 10.1038/s41567-021-01398-7.

[Nos+17] I. Nosske et al. “Two-dimensional magneto-optical trap as a source for cold strontium atoms”. *Physical Review A* **96.5** (2017), 053415. DOI: 10.1103/PhysRevA.96.053415.

[NYK18] M. Norcia, A. Young, and A. Kaufman. “Microscopic Control and Detection of Ultracold Strontium in Optical-Tweezer Arrays”. *Physical Review X* **8.4** (2018), 041054. DOI: 10.1103/PhysRevX.8.041054.

[ORG13] L. Ostermann, H. Ritsch, and C. Genes. “Protected State Enhanced Quantum Metrology with Interacting Two-Level Ensembles”. *Physical Review Letters* **111.12** (2013), 123601. DOI: 10.1103/PhysRevLett.111.123601.

[Ost+14] L. Ostermann et al. “Protected subspace Ramsey spectroscopy”. *Physical Review A* **90.5** (2014), 053823. DOI: 10.1103/PhysRevA.90.053823.

[OYL14] B. Olmos, D. Yu, and I. Lesanovsky. “Steady-state properties of a driven atomic ensemble with nonlocal dissipation”. *Physical Review A* **89.2** (2014), 023616. DOI: 10.1103/PhysRevA.89.023616.

[Pam+25] S. K. Pampel et al. “Quantifying Light-Assisted Collisions in Optical Tweezers across the Hyperfine Spectrum”. *Physical Review Letters* **134.1** (2025), 013202. DOI: 10.1103/PhysRevLett.134.013202.

[PC18] C. D. Parmee and N. R. Cooper. “Phases of driven two-level systems with nonlocal dissipation”. *Physical Review A* **97.5** (2018), 053616. DOI: 10.1103/PhysRevA.97.053616.

[PC20] C. D. Parmee and N. R. Cooper. “Steady states of a driven dissipative dipolar XXZ chain”. *Journal of Physics B: Atomic, Molecular and Optical Physics* **53.13** (2020), 135302. DOI: 10.1088/1361-6455/ab8949.

[Per+17] J. Perczel et al. “Topological Quantum Optics in Two-Dimensional Atomic Arrays”. *Physical Review Letters* **119.2** (2017), 023603. DOI: 10.1103/PhysRevLett.119.023603.

[Pey+18] T. Peyrot et al. “Collective Lamb Shift of a Nanoscale Atomic Vapor Layer within a Sapphire Cavity”. *Physical Review Letters* **120.24** (2018), 243401. DOI: 10.1103/PhysRevLett.120.243401.

[Phi98] W. D Phillips. “Laser cooling and trapping of neutral atoms”. *Rev. Mod. Phys.* **70.3** (1998).

[PHR22] D. Plankensteiner, C. Hotter, and H. Ritsch. “QuantumCumulants.jl: A Julia framework for generalized mean-field equations in open quantum systems”. *Quantum* **6** (2022), 617. DOI: 10.22331/q-2022-01-04-617.

[PR20] C. D. Parmee and J. Ruostekoski. “Signatures of optical phase transitions in superradiant and subradiant atomic arrays”. *Communications Physics* **3.1** (2020), 1–11. DOI: 10.1038/s42005-020-00476-1.

[Raa+87] E. L. Raab et al. “Trapping of Neutral Sodium Atoms with Radiation Pressure”. *Physical Review Letters* **59.23** (1987), 2631–2634. DOI: 10.1103/PhysRevLett.59.2631.

[Ral+06] Y. Ralchenko et al. *NIST Atomic Spectra Database (version 3.1.0),* 2006.

[Ram83] N. F. Ramsey. “History of Atomic Clocks”. *Journal of Research of the National Bureau of Standards* **88.5** (1983), 301. DOI: 10.6028/jres.088.015.

[Ram90] N. F. Ramsey. “Experiments with Separated Oscillatory Fields and Hydrogen Masers”. *Science* **248.4963** (1990), 1612–1619. DOI: 10.1126/science.248.4963.1612.

[Rav+18] C. Ravensbergen et al. “Accurate Determination of the Dynamical Polarizability of Dysprosium”. *Physical Review Letters* **120.22** (2018), 223001. DOI: 10.1103/PhysRevLett.120.223001.

[Roo+16] S. J. Roof et al. “Observation of Single-Photon Superradiance and the Cooperative Lamb Shift in an Extended Sample of Cold Atoms”. *Physical Review Letters* **117.7** (2016), 073003. DOI: 10.1103/PhysRevLett.117.073003.

[Ros+24] P. Rosario et al. “Detecting Entanglement from Macroscopic Measurements of the Electric Field and Its Fluctuations”. *Physical Review Letters* **133.5** (2024), 050203. DOI: 10.1103/PhysRevLett.133.050203.

[ROY23] O. Rubies-Bigorda, S. Ostermann, and S. F. Yelin. "Characterizing superradiant dynamics in atomic arrays via a cumulant expansion approach". *Physical Review Research* **5.1** (2023), 013091. DOI: 10.1103/PhysRevResearch.5.013091.

[RS21] F. Robicheaux and Deepak A. Suresh. "Beyond lowest order mean-field theory for light interacting with atom arrays". *Physical Review A* **104.2** (2021), 023702. DOI: 10.1103/PhysRevA.104.023702.

[RSC21] C. C. Rusconi, T. Shi, and J. I. Cirac. "Exploiting the photonic nonlinearity of free-space subwavelength arrays of atoms". *Physical Review A* **104.3** (2021), 033718. DOI: 10.1103/PhysRevA.104.033718.

[Rui+20] J. Rui et al. "A subradiant optical mirror formed by a single structured atomic layer". *Nature* **583.7816** (2020), 369–374. DOI: 10.1038/s41586-020-2463-x.

[Rut+23] D. K. Ruttley et al. "Formation of Ultracold Molecules by Merging Optical Tweezers". *Physical Review Letters* **130.22** (2023), 223401. DOI: 10.1103/PhysRevLett.130.223401.

[RWG97] B. Richards, E. Wolf, and D. Gabor. "Electromagnetic diffraction in optical systems, II. Structure of the image field in an aplanatic system". *Proceedings of the Royal Society of London. Series A. Mathematical and Physical Sciences* **253.1274** (1997), 358–379. DOI: 10.1098/rspa.1959.0200.

[Sas19] S. Saskin. "Narrow-Line Cooling and Imaging of Ytterbium Atoms in an Optical Tweezer Array". *Physical Review Letters* **122.14** (2019). DOI: 10.1103/PhysRevLett.122.143002.

[Sat+21] T. Satoor et al. "Partitioning dysprosium's electronic spin to reveal entanglement in nonclassical states". *Physical Review Research* **3.4** (2021), 043001. DOI: 10.1103/PhysRevResearch.3.043001.

[Sch+01] N. Schlosser et al. "Sub-poissonian loading of single atoms in a microscopic dipole trap". *Nature* **411.6841** (2001), 1024–1027. DOI: 10.1038/35082512.

[Sch70] M. Schroeder. "Synthesis of low-peak-factor signals and binary sequences with low autocorrelation (Corresp.)" *IEEE Transactions on Information Theory* **16.1** (1970), 85–89. DOI: 10.1109/TIT.1970.1054411.

[Sem+21] G. Semeghini et al. “Probing topological spin liquids on a programmable quantum simulator”. *Science* **374.6572** (2021), 1242–1247. DOI: 10.1126/science.abi8794.

[Sha+17] E. Shahmoon et al. “Cooperative Resonances in Light Scattering from Two-Dimensional Atomic Arrays”. *Physical Review Letters* **118.11** (2017), 113601. DOI: 10.1103/PhysRevLett.118.113601.

[Som+13] P. Sompet et al. “Dynamics of two atoms undergoing light-assisted collisions in an optical microtrap”. *Physical Review A* **88.5** (2013), 051401. DOI: 10.1103/PhysRevA.88.051401.

[Sor+12] Y. R. P. Sortais et al. “Sub-Poissonian atom-number fluctuations using light-assisted collisions”. *Physical Review A* **85.3** (2012), 035403. DOI: 10.1103/PhysRevA.85.035403.

[SOT97] T. A. Savard, K. M. O’Hara, and J. E. Thomas. “Laser-noise-induced heating in far-off resonance optical traps”. *Physical Review A* **56.2** (1997), R1095–R1098. DOI: 10.1103/PhysRevA.56.R1095.

[SR16] R. T. Sutherland and F. Robicheaux. “Collective dipole-dipole interactions in an atomic array”. *Physical Review A* **94.1** (2016), 013847. DOI: 10.1103/PhysRevA.94.013847.

[SRG02] N. Schlosser, G. Reymond, and P. Grangier. “Collisional Blockade in Microscopic Optical Dipole Traps”. *Physical Review Letters* **89.2** (2002), 023005. DOI: 10.1103/PhysRevLett.89.023005.

[SSC13] M. Segev, Y. Silberberg, and D. N. Christodoulides. “Anderson localization of light”. *Nature Photonics* **7.3** (2013), 197–204. DOI: 10.1038/nphoton.2013.30.

[Ste12] D. A. Steck. *Quantum and Atom Optics*.

[Su+23] L. Su et al. “Dipolar quantum solids emerging in a Hubbard quantum simulator”. *Nature* **622.7984** (2023), 724–729. DOI: 10.1038/s41586-023-06614-3.

[Su+25] L. Su et al. “Fast single atom imaging for optical lattice arrays”. *Nature Communications* **16.1** (2025), 1017. DOI: 10.1038/s41467-025-56305-y.

[Suo+95] K.-A. Suominen et al. “Optical shielding of cold collisions”. *Physical Review A* **51.2** (1995), 1446–1457. DOI: 10.1103/PhysRevA.51.1446.

[Suo96] K.-A. Suominen. “Theories for cold atomic collisions in light fields”. *Journal of Physics B: Atomic, Molecular and Optical Physics* **29.24** (1996), 5981. DOI: 10.1088/0953-4075/29/24/008.

[Taï+94] R. Taïeb et al. “Cooling and localization of atoms in laser-induced potential wells”. *Physical Review A* **49.6** (1994), 4876–4887. DOI: 10.1103/PhysRevA.49.4876.

[Tan+19] L. Tanzi et al. “Observation of a Dipolar Quantum Gas with Metastable Supersolid Properties”. *Physical Review Letters* **122.13** (2019), 130405. DOI: 10.1103/PhysRevLett.122.130405.

[Tao+24] R. Tao et al. “High-Fidelity Detection of Large-Scale Atom Arrays in an Optical Lattice”. *Physical Review Letters* **133.1** (2024), 013401. DOI: 10.1103/PhysRevLett.133.013401.

[Tho+13] J. D. Thompson et al. “Coherence and Raman Sideband Cooling of a Single Atom in an Optical Tweezer”. *Physical Review Letters* **110.13** (2013), 133001. DOI: 10.1103/PhysRevLett.110.133001.

[Tra+21] A. Trautmann et al. “Spectroscopy of Rydberg states in erbium using electromagnetically induced transparency”. *Physical Review Research* **3.3** (2021), 033165. DOI: 10.1103/PhysRevResearch.3.033165.

[Vet+10] E. Vetsch et al. “Optical Interface Created by Laser-Cooled Atoms Trapped in the Evanescent Field Surrounding an Optical Nanofiber”. *Physical Review Letters* **104.20** (2010), 203603. DOI: 10.1103/PhysRevLett.104.203603.

[Vil+17] J. L. Ville et al. “Loading and compression of a single two-dimensional Bose gas in an optical accordion”. *Physical Review A* **95.1** (2017), 013632. DOI: 10.1103/PhysRevA.95.013632.

[WI79] D. J. Wineland and W. M. Itano. “Laser cooling of atoms”. *Physical Review A* **20.4** (1979), 1521–1540. DOI: 10.1103/PhysRevA.20.1521.

[WMS11] Y. Waseda, E. Matsubara, and K. Shinoda. *X-Ray Diffraction Crystallography*. ISBN: 978-3-642-16634-1. DOI: 10.1007/978-3-642-16635-8.

[Yam+16] R. Yamamoto et al. “An ytterbium quantum gas microscope with narrow-line laser cooling”. *New Journal of Physics* **18.2** (2016), 023016. DOI: 10.1088/1367-2630/18/2/023016.

[YLL10] S. H. Youn, M. Lu, and B. L. Lev. "Anisotropic sub-Doppler laser cooling in dysprosium magneto-optical traps". *Physical Review A* **82.4** (2010), 043403. DOI: 10.1103/PhysRevA.82.043403.

[You+10] S. H. Youn et al. "Dysprosium magneto-optical traps". *Physical Review A* **82.4** (2010), 043425. DOI: 10.1103/PhysRevA.82.043425.

[You+22] A. W. Young et al. "Tweezer-programmable 2D quantum walks in a Hubbard-regime lattice". *Science* **377.6608** (2022), 885–889. DOI: 10.1126/science.abo0608.

[You23] A. Young. "Programmable arrays of alkaline earth atoms: qubits, clocks, and the Bose-Hubbard model". Publication Title: Department of Physics Volume: Ph.D. PhD Thesis. Boulder: University of Colorado Boulder, 2023.